Stony Brook University

Nitrogen-containing CUBICON ceramics and their applications for rechargeable batteries

A Dissertation Presented

by

Jue Liu

to

The Graduate School

in Partial Fulfillment of the

Requirements

for the Degree of

Doctor of Philosophy

in

Chemistry

Stony Brook University

December 2015

Stony Brook University

The Graduate School

Jue Liu

We, the dissertation committee for the above candidate for the

Doctor of Philosophy degree, hereby recommend

acceptance of this dissertation.

Peter G. Khalifah, Ph.D., Advisor
Associate Professor, Department of Chemistry, Stony Brook University

Xiao-Qing Yang, Ph.D., Co-advisor
Scientist, Chemistry Department, Brookhaven National Laboratory

John B. Parise, Ph.D., Chairperson of Defense
Professor, Department of Chemistry, Department of Geosciences, Stony Brook University

Katherine B. Aubrecht, Ph.D., Third Member
Assistant Professor, Department of Chemistry, Stony Brook University

Hong Gan, Ph.D., Outside Member
Scientist, Sustainable Energy Technologies Department, Brookhaven National Laboratory

This dissertation is accepted by the Graduate School

Charles Taber
Dean of the Graduate School

Abstract of the Dissertation

Nitrogen-containing CUBICON ceramics and their applications for rechargeable batteries

by

Jue Liu

Doctor of Philosophy

in

Chemistry

Stony Brook University

2015

High energy density rechargeable batteries have been widely investigated and optimized for portable electronics applications. However, research into novel electrode materials with higher energy densities and better ionic transport is needed to develop next-generation rechargeable batteries that can satisfy the requirements of the emerging technologies of electric vehicles and grid-scale energy storage. These needs motivate the present investigation of a new class of nitridophosphate ceramics for use as cathodes or solid state electrolytes in rechargeable batteries.

Nitridophosphate compounds with general formula of $A_2M_2P_3O_9N$ and $A_3MP_3O_9N$ (A = monopositive cation, M = divalent or trivalent cation) are demonstrated to be the first N^{3-}-containing cathode materials for rechargeable batteries, exhibiting a variety of advantages over conventional O^{2-}-based cathodes. $Na_3TiP_3O_9N$ and $Na_3VP_3O_9N$ have the highest Ti^{4+}/Ti^{3+} and V^{4+}/V^{3+} redox potentials ever reported for Na-ion batteries, and have remarkably small volume changes during cycling. The Li-ion analogues of these compounds cannot be directly synthesized, but can be prepared through new non-molten solid ion exchange methods developed in the course of this work. In addition to having higher capacities, the Li-ion analogues ($Li_2Fe_2P_3O_9N$, $Li_2TiP_3O_9N$, and $Li_3VP_3O_9N$) have higher ionic conductivities and better rate performance. Additionally, metastable nitridophosphate systems with redox-inactive M cations

($Li_2Mg_2P_3O_9N$, $Li_3AlP_3O_9N$ and $Li_3GaP_3O_9N$) are demonstrated to have high ionic conductivities which are promising for applications as solid state electrolytes. The isotropic three-dimensional ion transport pathways in these cubic compounds have been mapped out and quantified using a combination of structural, electrochemical and theoretical methods.

New structure characterization tools have been developed in support of these materials design efforts. The first-ever in situ neutron diffraction study of Li^+/Na^+ ion exchange was successfully carried out, allowing the detailed mechanism of the ion exchange reaction to produce $Li_2Mg_2P_3O_9N$ to be resolved. Additionally, quantitative studies of stacking faults in technologically important honeycomb-ordered transition metal oxide cathodes were carried out, allowing kinetic and thermodynamic aspects of the order-disorder transition to be distinguished. These results highlight the importance of structure knowledge when designing materials for rechargeable batteries.

Table of Contents

List of Figures

List of Tables

Acknowledgments

Frist, I would like to thank my advisors Professor Peter Khalifah and Dr. Xiao-Qing Yang. I would not be where I am today without their guidance in the last five years. Their attitudes toward the precision and accuracy in scientific research will be the greatest inspiration in my research career. I would like to say I am the lucky student who got two greatest mentors instead of one.

Second, I would like to thank my committee members Professor John Parise and Professor Katherine Aubrecht for all the guidance and encouragement they gave me within the last five years. I am also indebted to Dr. Hong Gan, my defense outside member, for carefully reading my thesis and giving me suggestions on my future directions.

I would also like to thank all current and past Khalifah and Yang group members. It is my great pleasure to work with you guys. I would like to give special thanks to Dr. Yuri Janssen and Dr. Xiqian Yu for teaching me many aspects about crystallography and Li-ion batteries. I would also like to thank Dr. Enyuan Hu for all wonderful scientific chats we had throughout these years. I am also indebted to all my collaborators, it would be impossible to collect all these beautiful data without you guys.

I would also like to thank all of my friends for their support in the last five years. I would like to say a special thank you to all members of 70 Admiral Street, for all the great memories we share.

Last but not least, I would like to thank all of my family, especially my parents and my girlfriend, for your trust and encouragement.

Chapter 1 Introduction

1.1 Rechargeable Li/Na-ion batteries

The wide use of the electronic devices such as cell phones and laptops in the last decades has led to the fast development of rechargeable batteries with high energy densities[1,2]. More recently, with the increasing price of gasoline and environment concerns, it becomes urgent to develop a new generation of rechargeable batteries with energy density that can satisfy the requirements for hybrid electronic vehicles (HEV) or electronic vehicles (EV)[2]. Lithium-ion batteries are promising candidates for these applications due to their higher gravimetric and volumetric energy density compared to other rechargeable battery systems such as lead-acid, nickel-cadmium and nickel metal – hydride batteries[2-4].

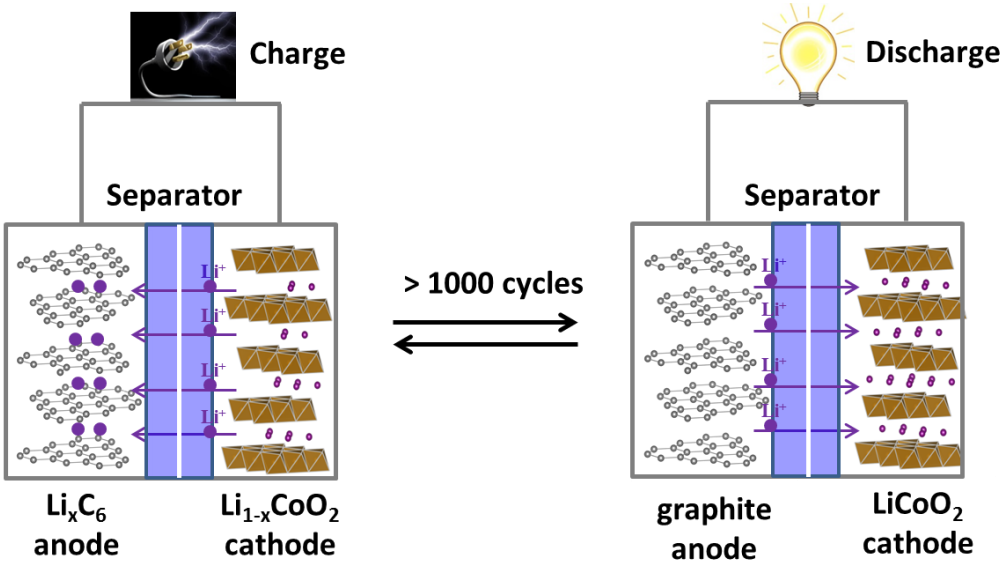

Figure 1.1 Schematic illustration of charge/discharge process of rechargeable Li-ion batteries.

The operation of rechargeable lithium-ion batteries involves the reversible extraction/insertion of lithium ions from the host compounds (cathode or anode) during charge/discharge process. The shuttle of lithium ions between cathode and anode can form a flow of lithium ions through the electrolyte which is accompanied by the oxidation/reduction reaction of the host compounds. The amount of lithium that can be extracted or inserted into the host compounds determines the theoretical capacity of this material. Although metallic lithium has a huge capacity of 3860 mAh/g as an anode electrode[4], for

safety consideration, commercial lithium-ion cells were assembled with $LiCoO_2$ cathode and graphite anode[1]. A schematic illustration of the working mechanism of this type of cell is shown in Figure 1.1, during the charge process, lithium ions are extracted from $LiCoO_2$ and inserted into graphite layers, whereas the reverse process is carried out during discharge.

Li-ion batteries have gained broad attentions in the last three decades, whereas the analogue Na-ion batteries did not attract much attention due to its lower energy density. However, the situation has changed recently due to the consideration of global lithium reserves. The abundance of lithium is less than 0.01% in Earth's crust while sodium is 2.3%, as can be seen in Figure 1.2. The elemental abundance and price become practically important in terms of large scale grid energy storage, e.g. energy storage for solar panels or wind mills etc[5]. The basic working mechanism for sodium ion batteries is similar to that of lithium ion batteries except that charge carriers are replaced by Na-ions. However, it is worthwhile to note that Na^+ has much large ionic radii (1.02 Å) than that of Li^+ (0.74 Å)[6] , resulting in somewhat unique charge/discharge behaviors of sodium ion batteries, details will be discussed in chapter 6.

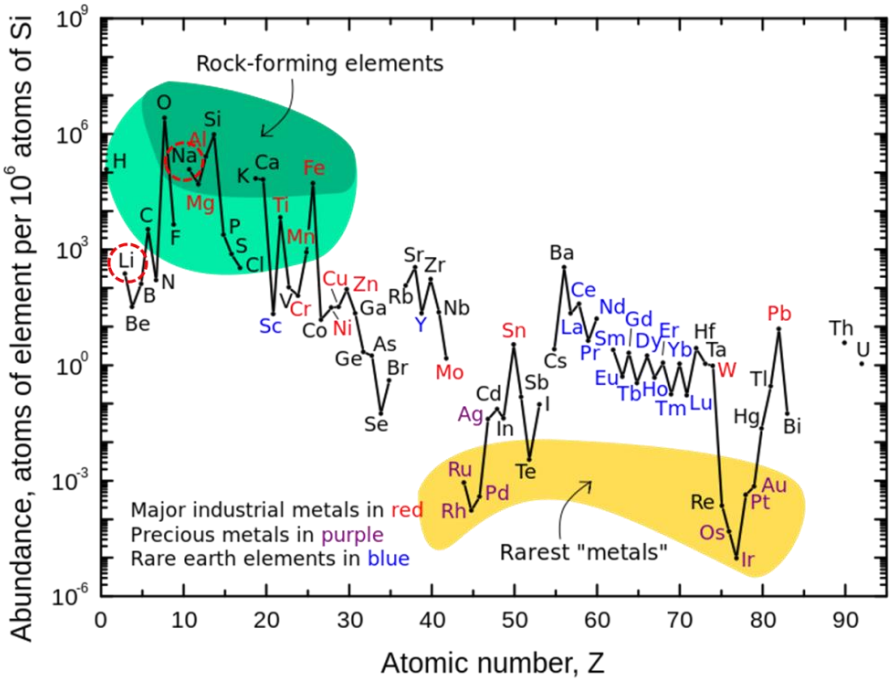

Figure 1.2 Abundance (in atomic fraction) of the chemical elements in Earth's upper continental crust as a function of atomic number[7].

After two decades' optimization, the energy density of today's commercialized lithium ion (or even sodium ion) batteries can well satisfy the requirements of portable electronics such as cell phones or laptops. However, great hindrance exists to further increase energy densities to meet the requirements for electric vehicle applications. Both cathode and anode need further modification to increase the energy density of Li/Na-ion batteries to a similar level of today's gasoline based combustion engine. Among these modifications, exploring new types of cathode materials played a key role in further developed of the rechargeable Li/Na-ion batteries[2]. Therefore, it is worthwhile to give a brief introduction of the development of cathode materials for rechargeable Li/Na-ion batteries.

1.1.1 Cathode materials for Li-ion batteries

1.1.1.1 Early days: the sulfide based materials

The concept of intercalation reaction of Li^+ into host structure can be traced back to the 1970s. The first intercalation system studied is the binary and ternary sulfide compounds, such as TiS_2 and $FePS_3$[8-11]. The reversible Li^+ intercalation/deintercalation into/from TiS_2 has also been viewed as the first example of rechargeable Li-ion battery. Interestingly, the first assembled Li/TiS_2 cell (in the 1970s) is still operational and displays more than 2/3 of its original capacity[12], demonstrating the high reversibility of this type of reaction in host structure. The structure of TiS_2 is shown in Figure 1.3, it can be seen that this compound has large interlayer distance of 2.85 Å which can provide fast two dimensional Li^+ transport.

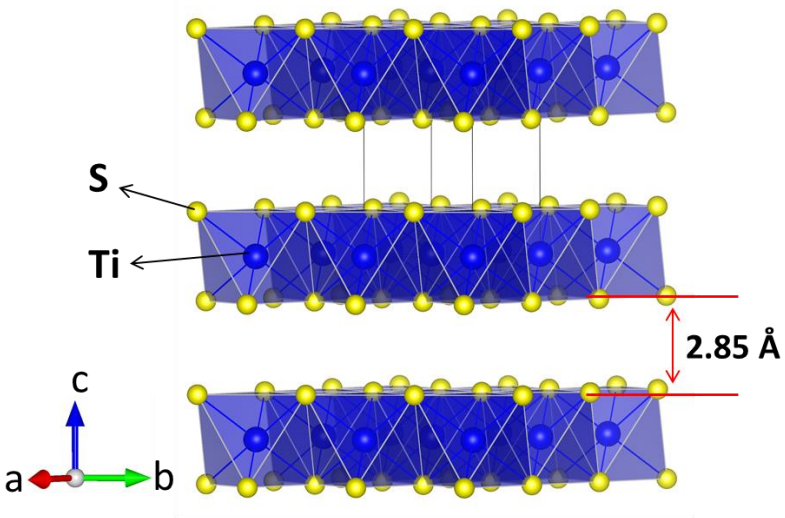

Figure 1.3 Crystal structure of TiS_2 (S.G. *P-3m*, a = b = 3.407 Å, c = 5.695 Å).

1.1.1.2 Commercialization: lithium transition metal oxides

The highly reversible cycling of Li^+ in TiS_2 proved the plausibility of utilizing intercalation reaction for rechargeable battery applications. However, this initial system suffered from low redox potential and limited capacity and thus resulted in a limited energy density. Several years later, Goodenough's group proposed the utilization of $LiCoO_2$ as cathode material[13], leading to the commercialization of Li-ion batteries by Sony in 1991. Since then, lithium transition metal oxides with general formula of Li*M*O_2 (*M* = Al, Co, Ni and Mn etc.) dominated the market of cathode materials[14,15]. A typical Li*M*O_2 crystallizes in *R-3m* space with three slabs of transition metal *M*O_2 layer and three slabs of LiO_2 layer, as can be seen in Figure 1.4. All Li and transition metal *M* sits in edge sharing LiO_6 or *M*O_6 octahedra, for this reason, this type of layered oxides is also referred as O_3-type structure[16]. It is expected that the electronic and Li-ionic conductivity of these compounds are appreciable due to the edge sharing nature of *M*O_6 octahedra and relative large inter slab distance of LiO_2 (~2.6 Å). However, it should be noted that the peculiar pseudo two dimensional structure of Li*M*O_2 can easily lead to stacking modification and slab gliding after specific amount of Li^+ ions are extracted from the structure. Some of these changes, such as transition metal migration or oxygen release can result in irreversible structure change/decomposition and thus lead to capacity loss or battery failure. It is for this reason, a broad exploration of lithium transition metal oxides with three dimensional structure types was carried out in in the 1980s[17-20], which led to the discovery of several technologically important cathode/anode materials, including $LiMn_2O_4$[19], $LiNi_{0.5}Mn_{1.5}O_4$[21,22] and $Li_4Ti_5O_{12}$[23,24]. Interestingly, all of these compounds have spinel ($MgAl_2O_4$) type structure, as can be seen in Figure 1.5. $LiMn_2O_4$ displays a redox potential of 4.1 V versus Li^+/Li by utilizing the $Mn^{3+/}Mn^{4+}$ redox couple[18]; $LiNi_{0.5}Mn_{1.5}O_4$ is the so-called "high voltage" spinel with very high operating potential of 4.7 V due to the $Ni^{2+}/Ni^{3+}/Ni^{4+}$ multi-electron transfer redox couples; $Li_4Ti_5O_{12}$ shows much lower operating potential of 1.5 V due to the lower redox potential of Ti^{3+}/Ti^{4+} and thus is often used as anode material, the most interesting character of this compound is the near zero-volume change during Li^+ insertion/extraction which makes this compound ultra-stable during cycling process[24].

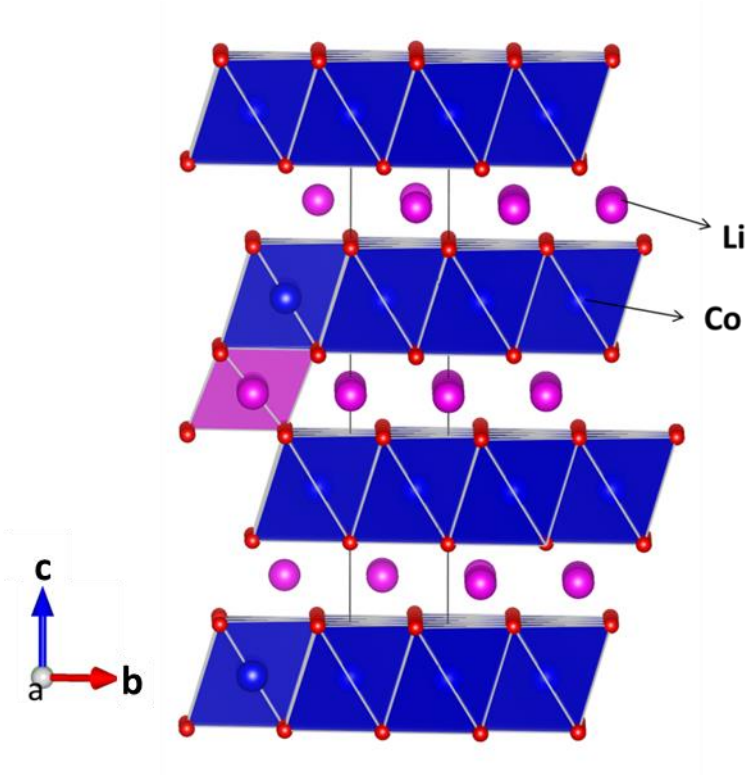

Figure 1.4 Crystal structure of $LiCoO_2$ (S.G. *R-3m*, a = b = 2.818 Å, c = 14.064 Å)

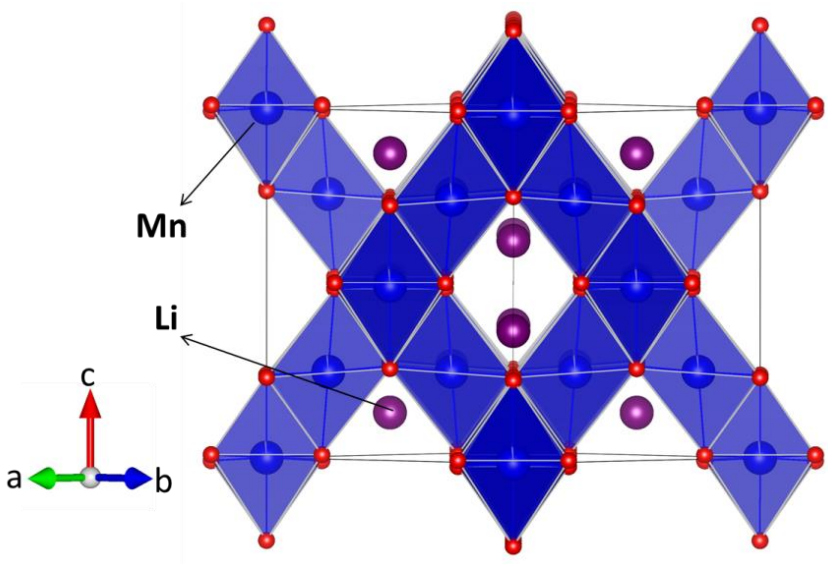

Figure 1.5 Crystal structure spinel-type $LiMn_2O_4$ (S.G. *Fd-3m*, a = 8.25 Å)

More recently, tremendous efforts have been spent on improving the performance of a series of so-called "lithium rich" oxides with general formula of xLi_2MnO_3 $(1-x)Li\mathit{M}O_2$, which has been treated as either the composite of honeycomb ordered Li_2MnO_3 and traditional lithium transition metal oxides $Li\mathit{M}O_2$ (M = Co, Ni and Mn etc.)[25,26], or a solid solution between these two components. Although these materials showed very high capacity (> 200 mAh/g) between specific voltage windows, the serious voltage fading hinders their commercialization. It is worthwhile to note that Li_2MnO_3 plays an important role for the high capacity of these lithium rich materials, there exists a so called "activation" process (> 4.5V) to gain excess capacity which is believed to be associated with activation of Li_2MnO_3. Curiously, after more than two decades study of Li_2MnO_3[27-29], the exact structure of this honeycomb ordered compound is still under debate. Therefore, a quantitative investigation is in urgent need for this structure type, which will be thoroughly presented in chapter 6 of this thesis.

1.1.1.3 Polyanion based frameworks for recharge Li-ion batteries

During the exploration of three dimensional structures for cathode application, another important structure type attracted broad interests. These structures are built on three dimensional frameworks of transition metal polyanions, which can be viewed as basic structure skeletons. Lithium/sodium ions are filled in the large vicinity formed by these polyanion motifs. This subject has been intensively investigated after the demonstration of electrochemical activity of $LiFePO_4$ by Goodenough's group[30]. In principle, there are several advantages for utilizing polyanion based compounds for rechargeable Li-ion batteries though the energy density of these compounds are often lower than those of transition metal oxides: first, the polyanion framework is more stable than those of lithium transition metal oxides especially at lithium extraction states, and thus they can provide better long-term cyclability; second, the potential of transition metal redox couples (M^{n+}/M^{n+1}) can be dramatically increased related to the corresponded oxides, this has been effectively explained using inductive effect introduce by Goodenough et al.[31,32]. It is almost impossible to introduce the whole area of the polyanion-based cathode materials considering the amount of publications. Therefore, several milestone-type examples will be addressed here.

NASICON-type structures shall come first. NASICON (Na-super-ionic-conductors) were first discovered by Goodenough's group in the later 1970s[33,34]. At that time, major efforts were spent on searching for fast ceramic Na-ionic conductors that can be used for high temperature Na-S batteries,

NASICON and β''-Al_2O_3[35] are among the most famous ones. Later on, facile reversible alkali ion insertion/deinsertion was demonstrated in $Fe_2(MoO_4)_3$[36,37] and $Li(Na)Ti_2(PO_4)_3$[38-41]. These findings stimulated the battery filed to further explore Li^+ cyclability of other NASICON or anti-NASICON type structures, such as $Fe_2(WO_4)_3$[31,36], $Fe_2(SO_4)_3$[32,42] and $Li_3Fe_2(PO_4)_3$[42,43]. It was also during this period of time, inductive effect was introduced to explain the redox potential difference of Fe^{2+}/Fe^{3+} among compounds with general formula of $Li_xFe_2(XO_4)_3$ (*X* = P, W, Mo and S), as can be seen in Figure 1. 6. This theory takes advantage of the electronegativity difference among different X (*X* = P, W, Mo and S). It stated that the electronegativity of *X* could weaken the covalency of Fe-O bonds related to that in pure oxides, e.g. $LiFeO_2$, which can therefore lower the antibonding states of $Li_xFe_2(XO_4)_3$ compounds and increase the redox potential of Fe^{2+}/Fe^{3+}. The amount of increase depends qualitatively on how electronegative X is, therefore, $Fe_2(SO_4)_3$ has the highest redox potential due to the strongest electronegativity of S compared to P, W and Mo.

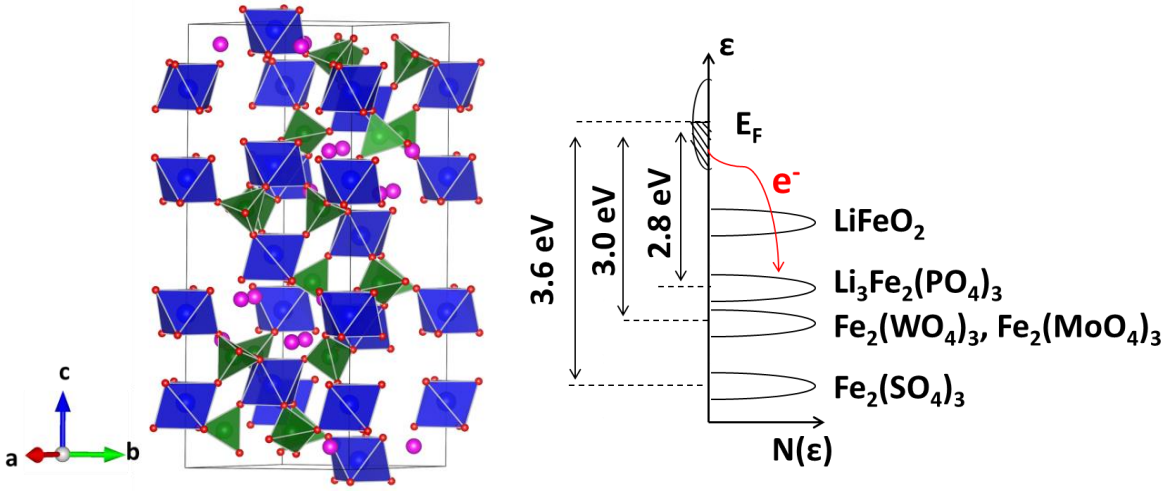

Figure 1.6 Left, crystal structure of $Li_3Fe_2(PO_4)_3$ (S.G. *R-3*, a = b = 8.301 Å, c= 22.502 Å). Right, relative $Fe^{3+/}Fe^{2+}$ redox positions versus Li^+/Li in NASICON-type $LixFe_2(XO_4)_3$ (*X* = P, W, Mo and S).

The demonstration of reversible Li^+ intercalation/deintercaltion in NASICON type structure proved the feasibility of utilizing polyanion-based three dimensional frameworks as cathode materials. The later discovery of electrochemical activity of $LiFePO_4$[30] opened the door for commercialization of polyanion-based compounds. Since the first publication by Padhi et al.[30], this olivine structure has attracted numerous attentions. The triphylite $LiFePO_4$ adopts an olivine-type structure, as can be seen in Figure 1.7. It should be noted that $LiMO_2$ adopts edge sharing MO_6 octahedra (Figure 1. 4) and thus electrons

are delocalized within the transition metal plane to enable fast two dimensional electronic transport, whereas the FeO_6 octahedron in $LiFePO_4$ shares corner oxygen with each other and thus hinders the delocalization of electrons and resulted in poor electronic conductivity. It has also been noticed that the Li-ionic conductivity in $LiFePO_4$ was found to be one dimensional[44,45], which can also be estimated by using difference bond valence sum map calculation, as can be seen in Figure 1.7. This one dimensional Li-ionic diffusion channel may be easily blocked by anti-site defects and led to limited ionic conductivity in the synthesized sample[44]. To overcome the poor intrinsic kinetic properties of $LiFePO_4$, various modifications such as nanosizing[46,47], carbon coating[48] and doping[49] were utilized.

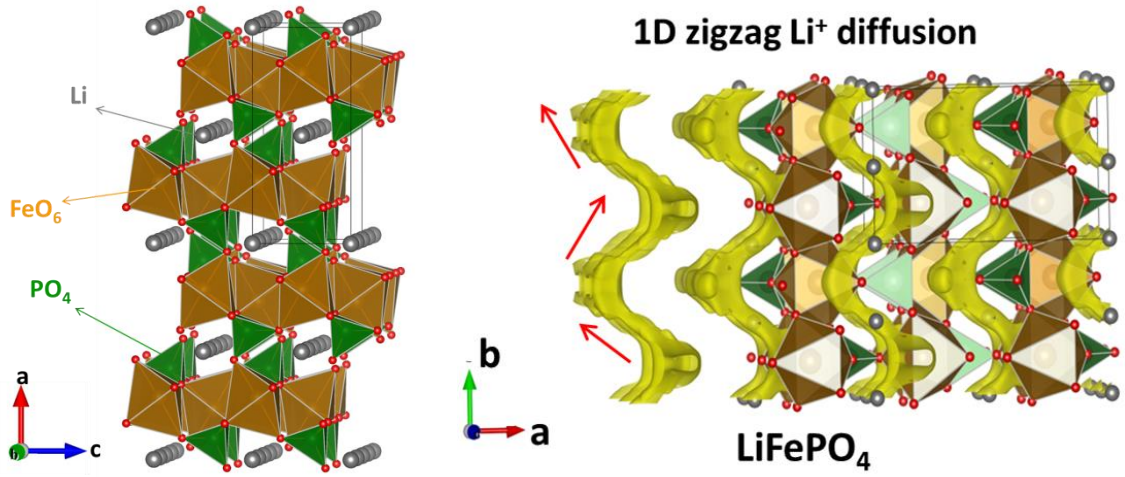

Figure 1.7 Left, crystal structure of olivine $LiFePO_4$ (S.G. *Pnma*, a = 10.392 Å, b = 6.049 Å, c = 4.726 Å). Right, lithium ion bond valence difference map ($|\Delta V|$ = 0.08) used to estimate the potential lithium ion diffusion pathway, an one dimensional zigzag Li-ion diffusion pathway has been identified. Details about this method will be presented in chapter 2.

Aside from olivine-type Li*M*PO_4, several other oxide-based polyanion compounds also attracted broad attentions due to their high theoretical capacity or low cost. One is the lithium transition metal silicates with general formula of Li_2MSiO_4 (*M* = Mn, Fe and Co)[50-54]. For economic and environmental consideration, it is obvious that cathode materials such as Li_2FeSiO_4 or Li_2MnSiO_4 should be most desirable due to the low cost and environment benign nature of Fe, Mn and Si, this compound also provide the potential of utilizing multi-electron transfer redox couple ($Fe^{2+/}Fe^{3+}/Fe^{4+}$ or $Mn^{2+}/Mn^{3+}/Mn^{4+}$) and hence can double the theoretical capacity[55]. The crystal structure of Li_2FeSiO_4 is complicated and different synthetic temperatures may result in different polymorphs[51,56-58], the detailed

structure description will be omitted here and can be found in related references. It should be noted that these silicates suffer from very low intrinsic conductivity. Lithium transition metal borates are a more recent example, the optimized $LiFeBO_3$ was reported to deliver a reversible capacity as high as 190 mAh/g at C/20 rate[59]. However, this compound suffers from easy degradation when exposed to air and thus prevents its further application[60]. More complex structure types can be formed by introducing other elements such as F^- into the phosphate or sulfate-based polyanion motifs, for example, tavorite-type $LiVPO_4F$[61,62] and $LiFeSO_4F$[63]. These materials benefits particularly from the additional inductive effect from F^-, resulting in relatively higher redox potential related to that of pure phosphate compounds (e.g. NASICON type phosphates or sulfates).

1.1.2 Cathode materials for Na-ion batteries

The investigation of Na^+ and Li^+ as charge carriers started at the same time. Later on, Li^+ system attracted more attention due to its higher energy density compared to that of Na^+ system. However, intensive efforts have been put on investigating the Na-ion system recently due to the much lower cost and higher abundance of Na resources related to that of Li. Although Na^+ shows a variety of similarities as charge carriers as that of Li^+, the tremendous ionic radii difference (0.74 Å for Li^+ and 1.02 for Na^+)[6] between these two ions often lead to different electrochemical performance for Na/Li analogue compounds, for instance, O3-type $NaCrO_2$ has been demonstrated to be able to effectively cycle Na^+ in Na-ion batteries[64,65], whereas its lithium analogue $LiCrO_2$[65] is barely electrochemical active in Li-ion batteries. In particular, Na^+ has been found to easily form Na^+- vacancy ordering in layered oxides during charge/discharge, as exemplified by P2-type $NaCoO_2$[66]. Therefore, it is worthwhile to give a brief introduction about the development of Na-ion cathode materials, especially sodium transition metal oxides, for rechargeable Na-ion batteries.

1.1.2.1 Classification of layered sodium (lithium) transition metal oxides

As mentioned in the introduction of layered lithium transition metal oxides, these layered compounds consist of edge-sharing MO_6 and AO_6 (A is the alkali ion) octahedral layers. Different polymorphs can form by staking these octahedra layers in different orientations along stacking direction (or c axis direction). Two major polymorphs existed for sodium transition metal oxides, which can be referred as O3-type and P2-type according to the notation system proposed by Delmas[16]. It has been found that samples synthesized with high sodium concentration (typically > 0.7) adopt O3-type

structure, whereas the ones synthesized with low sodium concentration preferred P2-type structure[16]. O3-type sodium transition metal oxides contain cubic close packed (ccp) oxygen arrays (AB CA BC…) with Na^+ and transition metal ions fully occupy the as-formed octahedral vicinities. Details about the structure evolution of normal rock salt (FeO) to ordered rock salt (O3-type $NaFeO_2$) can be found in chapter 6. In contrast to the three layer configuration of O3-type $NaMO_2$, P2-type Na_xMO_2 consists of only two MO_2 and two NaO_2 layers in AB BA… stacking configuration, as can be seen in Figure 1.8. Extraction appreciable amounts of Na^+ from O3 and P2-type sodium transition metal oxides generally induces phase transitions. For O3-type structure, Na^+ ions are initially stable at edge shared octahedral sites, however, the prismatic sites become energetic more favorable after Na^+ ions are partially removed from the structure, resulting in a phase transition to the P3-type structure. The formation of this P3-type structure is associated with the gliding of MO_2 slabs, resulting in the change of oxygen packing to "AB BC CA…". Similarly, sodium removal from P2-type sodium transition metal oxides leads to the formation of O2-type structure. However, it should be noted that the phase transition between O3 phase and O2 phase, or P2 and P3 phase will be difficulty since these transitions require breaking and reforming M-O bonds.

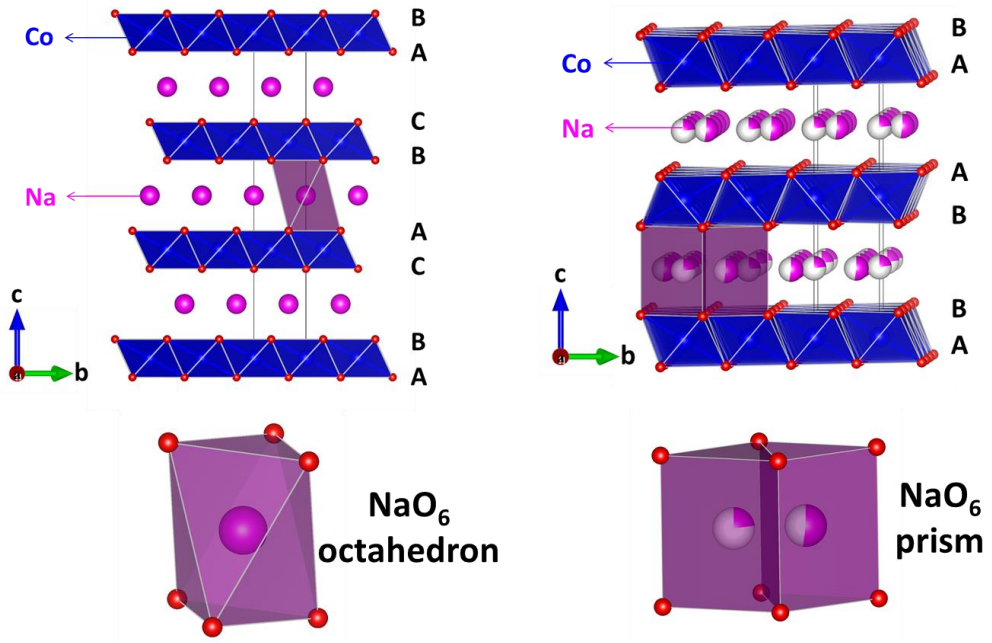

Figure 1.8 Left, structure of O3-type $NaCoO_2$ (S.G. *R-3m*, a = b = 2.88 Å, c = 15.58 Å). Right, structure of P2-type $Na_{0.72}CoO_2$ (S.G. *P6₃/mm*, a = b = 2.8408 Å, c = 10.8115 Å). Na^+ sits in NaO_6 octahedron in O3-type $NaCoO_2$, whereas Na^+ occupies trigonal prims in P2-type $Na_{0.72}CoO_2$.

1.1.2.2 Layered sodium transition metal oxides as cathode materials

Various O3-type sodium transition metal oxides can work as promising cathode materials for rechargeable sodium ion batteries. In this introduction, a list of the reported compounds and their electrochemical performance will be given. Detailed working mechanism of these materials can be found in recent review articles[67]. O3-type $NaFeO_2$, $NaMnO_2$, $NaCoO_2$ and $NaCrO_2$ are among the first transition metal oxides to be investigated, these compounds showed limited reversible capacity (typically less than 120 mAh/g). P2-type sodium transition metal oxides typically showed higher reversible capacity (up to 170 mAh/g) compared to related O3-type compounds, and thus are proposed to be better candidates for real battery applications[5,67]. Among these P2-type oxides, $Na_xFe_{0.5}Mn_{0.5}O_2$ is of particular interest due to the low cost and environmental friendly nature of Fe and Mn[68].

1.1.2.3 Polyanion compounds as cathode materials

NASICON-type $Na_xM_2(PO_4)_3$ compounds were the first to be investigated as potential cathode for Na-ion batteries, as exemplified by $NaTi_2(PO_4)_3$[39,41]. More recently, phosphates and pyrophosphates with Fe(II) or Mn(II) have been demonstrated to be able to reversibly cycle Na^+ in Na-ion cells[69,70]. Interestingly, sodium ion structures can be more complex than related lithium ion structures, for example, the mixed $(PO_4)^{3-}$ and pyrophosphate $(P_2O_7)^{4-}$ ions can be stabilized in the Na system, forming $Na_4M_3(PO_4)_2(P_2O_7)$ (M = Mn, Fe, Co and Ni) type structure[71,72], however, its lithium analogue is not known and is very likely to be metastable. $NaFePO_4$ is another interesting example. Thermodynamically stable $NaFePO_4$ phase crystallizes in maricite-type structure. The sodium ions are found to be located at large tetrahedral sties which are isolated in the structure, thus the energy barrier for sodium diffusion is very high and no obvious electrochemical activity has been observed for the system[70]. In contrast, the metastable triphylite-type $NaFePO_4$, which can be obtained from re-sodiation of the chemical or electrochemically dilithiated olivine-type $LiFePO_4$, has been demonstrated to be electrochemically active[73].

1.1.3 Research motivation

Sodium/lithium transition metal phosphates or fluorophosphates have been widely investigated as cathode materials for rechargeable Na/Li-ion batteries. However, limited attention has been paid to the nitrogen-incorporated phosphates (nitriphophates). This may due to the difficulties associated with pure sample synthesis. However, incorporating N^{3-} into phosphate anion has several advantages. In particular,

N^{3-} has much higher charge to mass ratio (3/14 e^-/atom) than that of O^{2-} (2/16 e^-/atom), indicating that higher amount of cations (e.g. Li^+/Na^+ or transition metal ions) can be introduced into the structure without increasing the molar mass of related compounds, and thus can lead to higher specific capacity. It is also worth to notice that the triple valent character N^{3-} may lead to the formation of novel three dimensional nitridophosphate frameworks that may have interesting Na^+/Li^+ transport properties. Therefore, Chapters 2 to 5 of this thesis focus on exploring novel nitridophosphates and their potential applications in rechargeable Na^+/Li^+ batteries.

New structure characterization tools are of great importance in support of materials designing. Therefore, several novel characterization techniques have been developed during the exploration for promising cathode/solid state electrolyte materials for rechargeable batteries. The first-ever *in situ* neutron diffraction study of Li^+/Na^+ ion exchange was successfully carried out, allowing the detailed mechanism of the ion exchange reaction to produce $Li_2Mg_2P_3O_9N$ to be resolved, which will addressed in Chapters 4 and 5. Chapter 6 of this thesis will focus on the quantitatively study of stacking (or coloring) faults in honeycomb ordered sodium transition metal oxides. This type of stacking faults were previously recognized and studied in some technologically important cathode materials, such as Li_2MnO_3[27,28], $LiNi_{0.5}Mn_{0.5}O_2$[74,75] and Li-rich cathode materials[25,26]. However, no quantitative result has been reported and the accurate structure is still under debate today. In this specific chapter, a thorough quantitative local and average structure study of $Na_3Ni_2BiO_6$ will be presented, which we believe is generally applicable to stacking faults study of other honeycomb ordered oxides system. These results highlight the importance of structure knowledge when designing materials for rechargeable batteries.

1.2 Structure characterization techniques

1.2.1 X-ray, neutron and electron scattering

1.2.1.1 Introduction of the nature of X-ray

X-rays were first discovered by Röntgen in 1896, the electromagnetic nature of X-rays was later demonstrated: it propagates in the vacuum with a velocity of 3×10^8 m/s; the electric field vector and magnetic field vector are both orthogonal to the direction of wave propagation; the wavelengths of X-rays are between that of ultraviolet rays and γ-rays with typical values between 0.1 Å and 100 Å, as can be seen in Figure 1.9, and with this short wavelength, the refractive index of X-rays are almost near to

unit. Thus, X-rays cannot be focused using lenses as that for ordinary lights or electrons (magnetic lenses), and therefore cannot be used directly to image individual atoms (the case changed as specific devices such as plating zones are developed to focus X-rays), however, by transforming an ordered atomic structure into reciprocal space, X-ray diffraction can be used to precisely observe atomic periodicity in specific structures.

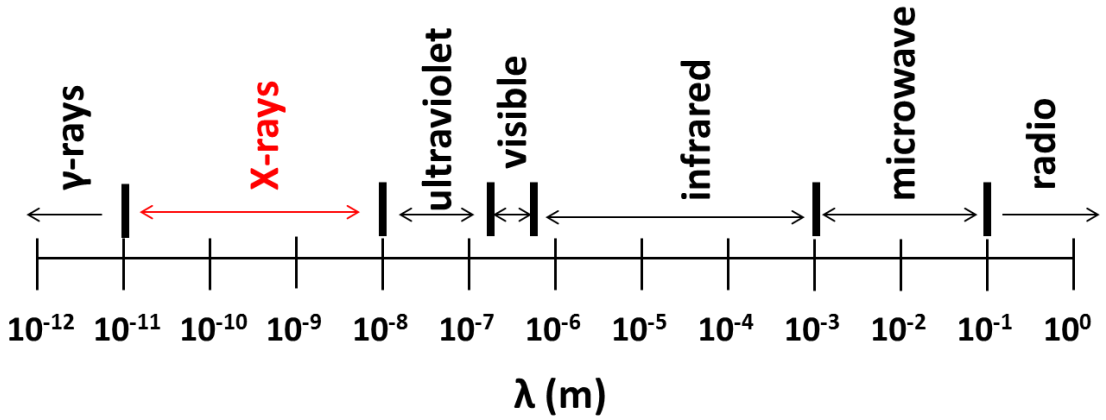

Figure 1.9 Spectrum of electromagnetic waves, the region of X-rays is marked with red color.

1.2.1.2 X-ray scattering

For a diffraction experiment, we shine an incident beam such as X-ray or neutron onto the sample and collect the scattered beam as a function of scattered angle (*2θ)* or time-of-flight (TOF). The as-collected data was then analyzed to unravel the structure information. X-rays and neutrons interact relatively weakly with matter (i.e. atoms or molecules), which satisfies the kinematic approximation and makes the analysis relatively simple compared to multiple scattered systems such as electron. In this chapter, only the X-ray scattering theory will be introduced.

1.2.1.3 Scattering by a free electron: Thomson scattering

When a X-ray beam interacts with a sample, two process happen: first, the X-ray could be absorbed by the sample, for instance, it can lead to the ejection of inner core electrons of specific atoms which can be used to design a very important technique - X-ray absorption spectroscopy (XAS), which we shall discuss later in this chapter; second, the X-ray beam can be scattered. The scattering can result in both unmodified scattered beam (same wavelength as the incident beam and also has specific phase

relation) and modified scattered beam (Compton scattering). Here, we shall only focus on the theory related to unmodified scattering.

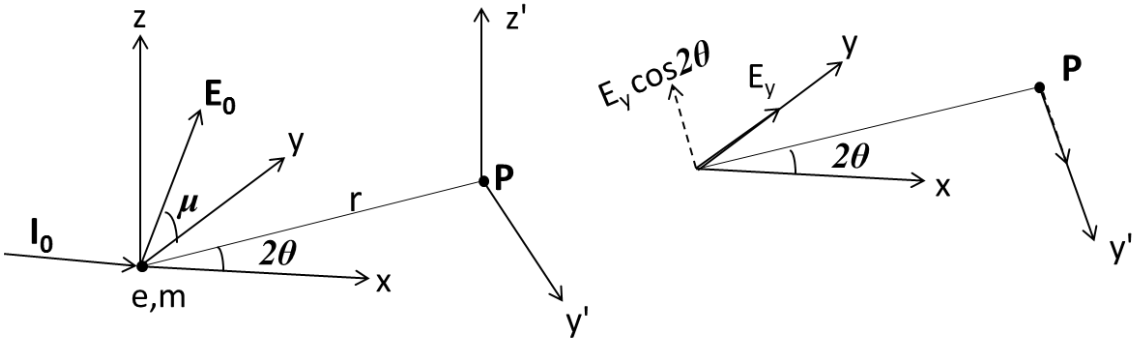

Figure 1.10 Left, a free electron sits at O, a monochromatic and polarized (μ is the polarization angle) X-ray wave propagates along x axis with amplitude of E_0 and frequency of ν. The observation is set to P, which locates on the xy plane with a distance of r from the original position (O), 2θ is the angle between wave propagation direction (along x axis) and the observation direction. Right, the effective electric field of y component ($E_y \cos 2\theta$).

As mentioned in the previous part, X-ray is an electromagnetic wave, thus the electric vector of X-ray beam should varying sinusoidally with time and perpendicular to the wave propagation direction. For clarification, we assume a free electron with mass of *m* and charge of *e* sits on the wave propagation direction of an incident X-ray beam, as can be seen in Figure 1. 10. The electric field introduced by X-ray should put forces on the electron and result in the acceleration of the electron. Based on the classical electromagnetic theory, an accelerated electron is a source of radiation. This radiation shall have the same frequency as the primary beam and it also has a phase relation with the primary beam. Let's assume a monochromatic and polarized X-ray beam propagates along x axis with amplitude of E_0 and frequency of ν, the electric field can be described as:

$$\boldsymbol{E_{0x}} = \boldsymbol{E_0}\exp 2\pi i\nu\left(t - \frac{x}{c}\right)$$

Where E_0 is the amplitude of the incident beam, ν is the frequency, t is the time of propagation and x is the location of the free electron. It can be seen that the acceleration on the free electron should be:

$$\mathbf{a} = e\boldsymbol{E_{0x}}/m = (e\boldsymbol{E_0}\exp 2\pi i\nu(t - \tfrac{x}{c}))/m,$$

Thus, the electron field at point P is:

$$\mathbf{E_p} = \mathbf{E_{0p}}\exp[2\pi i\nu\left(t - \frac{r}{c}\right) - i\alpha]$$

$$\mathbf{E_{0p}} = \mathbf{E_0}\frac{e^2}{mc^2}\frac{1}{r}\,sin\varphi$$

Where φ is the angle between primary electric field E_0 and the observation direction OP. For further clarity, we assume the incident beam is polarized with a polarization angle of μ, therefore the E_0 (only considering the amplitude here) can be decoupled into E_{0y} and E_{0z} components as:

$$E_{0y} = E_0 cos\mu$$

$$E_{0z} = E_0 sin\mu$$

Similarly, the electric filed at observer position can also be decoupled into y' and z' components:

$$E_{pz'} = \frac{e^2}{mc^2}\frac{1}{r}E_0 sin\mu$$

$$E_{py'} = \frac{e^2}{mc^2}\frac{1}{r}E_0 cos\mu cos2\theta$$

Here, 2θ is the angle between wave propagation direction and observation direction. Thus, the intensity of electric field at observation P point should be:

$$E_p^2 = E_{pz'}^2 + E_{py'}^2 = E_0^2\frac{e^4}{m^2c^4r^2}(sin^2\mu + cos^2\mu cos^2 2\theta)$$

For a non-polarized beam, $< sin^2\mu > = < cos^2\mu > = ½$, then the intensity can be written as:

$$I_p = I_0\frac{e^4}{m^2c^4r^2}\frac{1+cos^2 2\theta}{2}$$

This equation describes the intensity associated with a unit solid angle of 2θ. Thus the total scattering power can be integrated as:

$$I_{total} = \int_0^\pi I_p 2\pi r^2 sin2\theta\, d(2\theta) = I_0\frac{e^4}{m^2c^4r^2}\int_0^\pi \frac{1+cos^2 2\theta}{2}\, sin2\theta\, d(2\theta) = \frac{8\pi e^4}{3m^2c^4}I_0$$

It can be figured out that I_{total}/I_0 is at the scale of 7×10^{-25} cm^2/e, a very small number. However, it is worth to noted that the amount of atoms (or electrons) within one scattering experiment is also appreciable($\gg 10^{20}$), that is why scattered radiation from a sample is not necessary to be too small.

1.2.1.4 Scattering by an atom: atomic scattering factor

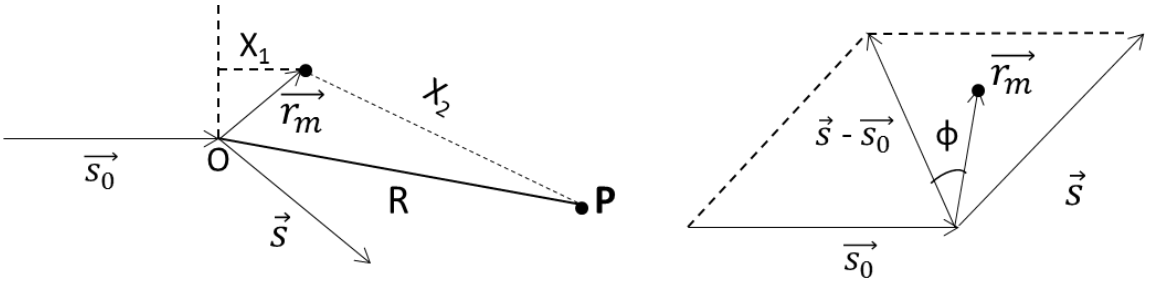

Figure 1.11 Left, schematic illustration of the scattering of a group of electrons located at r_m, s_0 and s are the incident beam and scattered beam, the observation point is set to P. Right, schematic illustration of the unmodified scattering of the *m*th electron.

The scattering by an atom can be treated as the scattering of a group of electrons that are confined into small volume. Let's first consider the scattering from the *m*th electron, as can be seen in Figure 1.11. The electric field introduced by the incident beam on the *m*th electron can be expressed as:

$$E_m = E_0 \exp(2\pi\nu i\left(t - \frac{X_1}{c}\right))$$

Thus, the electric field at P caused by the radiation of the *m*th electron is:

$$E_{pm} = E_0 \frac{e^2}{mc^2 X_2} \exp(2\pi\nu i\left(t - \frac{X_1 + X_2}{c}\right))$$

Considering the small dimension of an atom compared to the distance R, X_2 can be treated as R. Using the plane wave approximation, (X_1+X_2) is approximated to (R- $\overrightarrow{r_m}(\vec{s} - \overrightarrow{s_0})$). Therefore, the electric field at position P can be expressed as:

$$E_{pm} = E_0 \frac{e^2}{mc^2 R} \exp\left(2\pi\nu i\left(t - \frac{R}{c}\right)\right) \exp\left(2\pi\nu i \frac{\overrightarrow{r_m}(\vec{s} - \overrightarrow{s_0})}{c}\right)$$

The next step is to calculate the total unmodified scattering from an atom, which shall be the sum of all electrons in the atom, and thus can be expressed as:

$$E_{total} = E_0 \frac{e^2}{mc^2 R} \exp\left(2\pi\nu i\left(t - \frac{R}{c}\right)\right) \sum_m \exp\left(2\pi\nu i \frac{\overrightarrow{r_m}(\vec{s} - \overrightarrow{s_0})}{c}\right)$$

For a good approximation, the electrons in an atom can be treated as homogenously distributed electron density clouds, thus for one electron there should be $\int \rho \, dV = 1$. Therefore, E_{total} can be expressed as following:

$$E_{total} = E_0 \frac{e^2}{mc^2 R} \exp\left(2\pi\nu i\left(t - \frac{R}{c}\right)\right) \int \exp\left(2\pi\nu i \frac{\vec{r}(\vec{s} - \overrightarrow{s_0})}{c}\right) \rho(r) dV$$

As can be seen in the right side of Figure 1.11, for an unmodified scattering, $\vec{r}(\vec{s} - \overrightarrow{s_0})$ can be expressed as 2rsinθcosφ. Here, we will introduce transfer momentum Q = $\frac{4\pi sin\theta}{\lambda} = \frac{4\pi\nu sin\theta}{c}$, using this abbreviation, E_{total} can be expressed as:

$$E_{total} = E_0 \frac{e^2}{mc^2 R} \exp\left(2\pi\nu i\left(t - \frac{R}{c}\right)\right) \int \exp(Qicos\varphi)\, \rho(r) dV$$

The integral part is the scattering factor per electron (f_e). Assuming the electron density has spherical symmetry, f_e can then be expressed as:

$$f_e = \int_{r=0}^{\infty} \int_{\varphi=0}^{\pi} \exp(Qicos\varphi)\rho(r) 2\pi r^2 sin\varphi d\varphi dr = \int_{r=0}^{\infty} 4\pi r^2 \rho(r) \frac{\sin(Qr)}{Qr} dr$$

Therefore, the unmodified atomic scattering factor can be expressed as:

$$f_m = \sum_m \int_{r=0}^{\infty} 4\pi r^2 \rho_m(r) \frac{\sin(Qr)}{Qr} dr$$

It can be seen that for X-ray scattering, the atomic scattering factor decreases as Q increasing. It is worth to note that Z (atomic number) = $\sum_m \int_{r=0}^{\infty} 4\pi r^2 \rho_m(r)\, dr$, therefore, f_m is approaching Z at very small Q.

For the above treatment, we made the assumption that X-ray beam energy is much lower than the absorption edges of the atom, which is not often satisfied. Thus, a dispersion correction is needed:

$$f = f_m + \Delta f' + i\Delta f''$$

The treatment of modified scattering will be omitted in this introduction, but it should be noted that the intensity of modified (Compton scattering) atomic scattering can be expressed as $i_e = Z - \sum_m f_m^2$.

1.2.1.5 Scattering by a small crystal

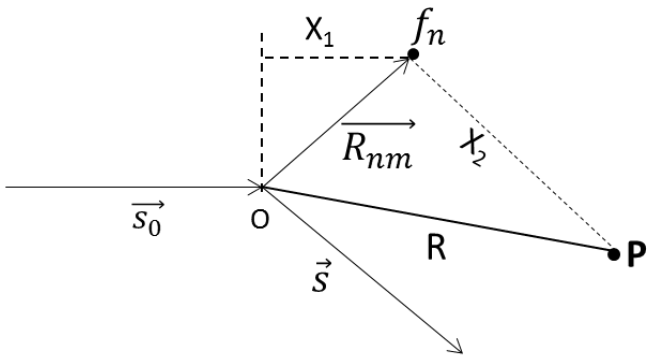

Figure 1.12 Illustration of scattering by a small crystal by parallel beam.

A small crystal can be viewed as a confined system with n atoms and the size (R_{nm}) of the crystal shall be considered as point related to the observation distance of R (R_{OP}), as can be seen in Figure 1.12. Assuming a monochromatic and fully polarized X-ray beam $\overrightarrow{s_0}$ shining on this small crystal with crystal origin located at O. The *n*th atom is located at the *m*th unit cell ($m_1\overrightarrow{a_1} + m_2\overrightarrow{a_2} + m_3\overrightarrow{a_3}$) with inter unit cell position of $\overrightarrow{r_n}$, therefore, $\overrightarrow{R_{nm}}$ can be written as $m_1\overrightarrow{a_1} + m_2\overrightarrow{a_2} + m_3\overrightarrow{a_3} + \overrightarrow{r_n}$. Similar to the treatment of scattering by an atom, we still use the plane wave approximation in the current case. Thus the electric field at observation position P can be expressed by,

$$\epsilon_p = \frac{E_0 e^2}{mc^2 R} f_n \exp\left\{2\pi i\nu\left(t - \frac{R - (\vec{s} - \overrightarrow{s_0})\overrightarrow{R_{nm}}}{c}\right)\right\}$$

Replacing $\overrightarrow{R_{nm}}$ by $m_1\overrightarrow{a_1} + m_2\overrightarrow{a_2} + m_3\overrightarrow{a_3} + \overrightarrow{r_n}$, we can get,

$$\epsilon_p = \frac{E_0 e^2}{mc^2 R} f_n \exp\left\{2\pi i\nu\left(t - \frac{R}{c}\right)\right\} \exp\left(2\pi i\nu \frac{(\vec{s} - \overrightarrow{s_0})(m_1\overrightarrow{a_1} + m_2\overrightarrow{a_2} + m_3\overrightarrow{a_3} + \overrightarrow{r_n})}{c}\right)$$

Separating the $\overrightarrow{r_n}$ term out, it can be written as following,

$$\epsilon_p = \frac{E_0 e^2}{mc^2 R} \exp\left\{2\pi i\nu\left(t - \frac{R}{c}\right)\right\} f_n \exp\left(2\pi i\nu \frac{(\vec{s} - \overrightarrow{s_0})\overrightarrow{r_n}}{c}\right) \exp\left(2\pi i\nu \frac{(\vec{s} - \overrightarrow{s_0})(m_1\overrightarrow{a_1} + m_2\overrightarrow{a_2} + m_3\overrightarrow{a_3})}{c}\right)$$

Thus, the total electric field at P should be the summation over all atoms in all unit cells. For simplicity, it is assumed that the small crystal has N_1a_1, N_2a_2 and N_3a_3 unit cells with crystal edges parallel to unit cell axis $\overrightarrow{a_1}$, $\overrightarrow{a_2}$ *and* $\overrightarrow{a_3}$. Hence the summation can be written as,

$$\epsilon_{total} = \frac{E_0 e^2}{mc^2 R} \exp\left\{2\pi i\nu\left(t - \frac{R}{c}\right)\right\} \sum_n f_n \exp\left(2\pi i\nu \frac{(\vec{s} - \overrightarrow{s_0})\overrightarrow{r_n}}{c}\right) \sum_{m_1=0}^{N_1-1} \exp(2\pi i\nu \frac{(\vec{s} - \overrightarrow{s_0})m_1\overrightarrow{a_1}}{c})$$

$$\sum_{m_2=0}^{N_2-1} \exp(2\pi i\nu \frac{(\vec{s} - \overrightarrow{s_0})m_2\overrightarrow{a_2}}{c}) \sum_{m_3=0}^{N_2-1} \exp(2\pi i\nu \frac{(\vec{s} - \overrightarrow{s_0})m_3\overrightarrow{a_2}}{c})$$

The term $\sum_n f_n \exp\left(2\pi i\nu \frac{(\vec{s}-\overrightarrow{s_0})\overrightarrow{r_n}}{c}\right)$ is called the structure factor F, which is very important in terms of crystal structure determination and we will revisit it later in this section. It is useful to introduce the complex conjugate of ϵ^*_{total}, taking the product of $\epsilon_{total}\epsilon^*_{total}$, and use the relation of $\lambda = \frac{\nu}{c}$, the expression can be simplified as,

$$\epsilon_{total}\epsilon^*_{total} = \frac{\mathrm{E_0^2 e^4}}{\mathrm{m^2 c^4 R^2}} \mathrm{FF^*} \frac{sin^2 \frac{\pi(\vec{s} - \overrightarrow{s_0})\, N_1\overrightarrow{a_1}}{\lambda}}{sin^2 \frac{\pi(\vec{s} - \overrightarrow{s_0})\overrightarrow{a_1}}{\lambda}} \frac{sin^2 \frac{\pi(\vec{s} - \overrightarrow{s_0})\, N_2\overrightarrow{a_2}}{\lambda}}{sin^2 \frac{\pi(\vec{s} - \overrightarrow{s_0})\overrightarrow{a_2}}{\lambda}} \frac{sin^2 \frac{\pi(\vec{s} - \overrightarrow{s_0})\, N_3\overrightarrow{a_3}}{\lambda}}{sin^2 \frac{\pi(\vec{s} - \overrightarrow{s_0})\overrightarrow{a_3}}{\lambda}}$$

By timing $\frac{8\pi}{c}$ on each side of the equation, we can get the scattering intensity from a polarized beam (perpendicular to the paper):

$$I_{total} = I_0 \frac{\mathrm{e^4}}{\mathrm{m^2 c^4 R^2}} \mathrm{FF^*} \frac{sin^2 \frac{\pi(\vec{s} - \overrightarrow{s_0})\, N_1\overrightarrow{a_1}}{\lambda}}{sin^2 \frac{\pi(\vec{s} - \overrightarrow{s_0})\overrightarrow{a_1}}{\lambda}} \frac{sin^2 \frac{\pi(\vec{s} - \overrightarrow{s_0})\, N_2\overrightarrow{a_2}}{\lambda}}{sin^2 \frac{\pi(\vec{s} - \overrightarrow{s_0})\overrightarrow{a_2}}{\lambda}} \frac{sin^2 \frac{\pi(\vec{s} - \overrightarrow{s_0})\, N_3\overrightarrow{a_3}}{\lambda}}{sin^2 \frac{\pi(\vec{s} - \overrightarrow{s_0})\overrightarrow{a_3}}{\lambda}}$$

For an unpolarized beam, it is easy to figure out that I_0 term shall be written as $\frac{1+cos^2 2\theta}{2} I_0$. Interestingly, aside from the structure factor term ($\mathrm{FF^*}$), the condition that I_{total} is non-zero is when the last three terms in the equation are non-zero. It can be seen that when N is a large number, which is validated in the current situation, these terms are essentially zero at positions that $\frac{\pi(\vec{s}-\overrightarrow{s_0})\overrightarrow{a_x}}{\lambda} \neq n_x\pi$ ($\mathrm{n_x}$ is an integer), hence, we can generate the three Laue equations:

$$\frac{\pi(\vec{s} - \overrightarrow{s_0})\overrightarrow{a_1}}{\lambda} = h'\pi;\ \frac{\pi(\vec{s} - \overrightarrow{s_0})\overrightarrow{a_1}}{\lambda} = k'\pi;\ \frac{\pi(\vec{s} - \overrightarrow{s_0})\overrightarrow{a_1}}{\lambda} = l'\pi$$

It is obvious that these three equations are essentially the same as that of the famous Bragg's law: $(\vec{s} - \overrightarrow{s_0}) = \overrightarrow{H_{hkl}}\lambda$. However, it is worth to note that the Laue equations demonstrate that the scattering peak intensities from a small crystal are proportional to the square of the number of unit cells (N^2), which explains why the Bragg diffraction peaks are strong and sharp.

Last but not least, let's go back to the structure factor $F = \sum_n f_n \exp\left(2\pi i\nu \frac{(\vec{s}-\overrightarrow{s_0})\overrightarrow{r_n}}{c}\right)$, $\overrightarrow{r_n}$ can be expressed in fraction of unit cell coordinates ($\overrightarrow{a_1}$, $\overrightarrow{a_2}$ *and* $\overrightarrow{a_3}$) as $x_n\overrightarrow{a_1} + y_n\overrightarrow{a_2} + z_n\overrightarrow{a_3}$. As mentioned in the Laue equation part, the scattering is non-zero only under the condition of $(\vec{s} - \overrightarrow{s_0}) = \overrightarrow{H_{hkl}}\lambda$, hence, $F = \sum_n f_n \exp 2\pi i\overrightarrow{H_{hkl}}(x_n\overrightarrow{a_1} + y_n\overrightarrow{a_2} + z_n\overrightarrow{a_3}) = \sum_n f_n \exp 2\pi i(hx_n + ky_n + lz_n)$. If the structure factor F is zero, then the diffraction intensity associated with (hkl) peak should also be zero. This type of vanishing is called systematic absence. For instance, in a crystal with fcc lattice, the structure factor F_{hkl} is non-zero only when hkl is all even or all odd. It should also be noted that temperature vibration also played an important role in the structure factor and scattering intensity, which we will discuss in the diffuse scattering part.

1.2.1.6 Integrated intensity from scattering of a small crystal

As mentioned in the previous chapter, if the three Laue equations are satisfied, the maximum scattering intensity should be:

$$I_{max} = I_0 \frac{e^4}{m^2c^4R^2} F_T^2 N_1^2 N_2^2 N_3^2$$

However, it should be noted that the peaks in the three Laue equations have a finite breadth, thus there is intensity at $(\vec{s} - \overrightarrow{s_0})$ that slightly varies from the ideal $\overrightarrow{H_{hkl}}\lambda$. And the incident beam is not perfectly parallel. Considering these situations, it is unrealistic to measure the scattering intensity I_{total}. Instead, we will measure the "integrated intensity", a quantity that can be both measured and calculated. Here, the tedious math work will be omitted, details can be found in various text books[76]. The diffracted energy that can be measured is given by

$$E = I_0\left(\frac{e^4}{m^2c^4}\right)\frac{\lambda^3\delta V F_T^2}{\omega v_a^2}\left(\frac{1+cos^2 2\theta}{2sin2\theta}\right)$$

It can be seen that the Lorentz-polarization (LP) factor for a single crystal diffraction from a non-polarized beam is $(1+\cos^2 2\theta)/2\sin 2\theta$. The diffraction energy is proportional to the volume of the single

crystal. By carefully measuring the value of E/I_0, we can obtain F_T^2(hkl) which is the key for structure determination.

1.2.1.7 Integrated intensity from scattering of powder sample

A powder sample can be treated as the combination of enormous amount of small single crystals with random orientations. In this condition, it is easy to figure out that there is a cone of diffracted beam for each d spacing that satisfy the three Laue equations. Similar to the previous treatment of the single crystal, only the final result will be presented here. The power per unit length of diffraction circle at distance R has the form of

$$P = \frac{I_0}{16\pi R}\left(\frac{e^4}{m^2c^4}\right)\frac{V\lambda^3 n_{hkl}F_T^2}{v_a}\left(\frac{1+cos^2 2\theta}{sin\theta sin2\theta}\right)$$

The Lorentz-polarization factor of powder diffraction is then $(1+\cos^2 2\theta)/ \sin\theta\sin 2\theta$.

1.2.1.8 Neutron scattering

In contrast to photon, neutron is a heavy particle with appreciable amount of mass. A neutron has a spin of ½ and magnetic moment of 1.913 nuclear magnetons. Therefore, the neutron beams can be viewed as mass waves. Details about how to produce neutrons and how they behave as a wave will be omitted here. The introduction will be confined to the interaction of neutron beams with matters, in particular, the neutron- nucleus interaction. It should be noted that neutrons (spin) can also interact with the magnetic momentum associated with atoms and thus result in magnetic scattering, the introduction of this type of scattering will not be presented but can be found in related references[77,78].

The interactions between neutrons and nucleus are governed by the short-range nuclear forces ($\sim 10^{-15}$ m or fm). The nuclear radius (~fm) is much smaller than the wavelength of incident nuclear beam (~Å).Therefore, the nucleus can be treated as point and thus the atomic nuclear scattering length (b) is isotropic and does not depend on the wave transfer moment (Q). As mentioned in the previous X-ray scattering section, there is a 180 ºphase change for the scattering beam related to the incident beam. By convention, a phase change of 180 º means the scattering amplitude is positive, therefore, X-ray scattering amplitude is always positive. However, when neutrons are very close to nucleus, a metastable system is formed and which will decay and reemit the neutron. Thus, the nuclear scattering factor is assumed to have the form of $b = b_0 - \Delta b$, if Δb is larger than b_0, it is possible to have a negative scattering factor. Therefore, one of the greatest advantages of neutron diffraction lies in the elemental sensitive

character. In great contrast to the X-ray or electron diffraction, which are more sensitive to heavy atoms (Z contrast). Thus, combined X-ray and neutron diffraction study will be extremely useful for structure clarity.

1.2.1.9 Electron scattering

Unlike neutrons or X-rays, which interact weakly with matter, electrons can be strongly absorbed by even very thin layer of matter (~10^{-7} cm). Therefore, the kinematic approximation that used for treat X-ray and neutron scattering is not validated for the case of electron diffraction. Detailed dynamic scattering theory of electron scattering falls out of the scope of current introduction. Here, we will only make a simple comparison between the X-ray atomic scattering factor (f_{ax}) and electron atomic scattering factor (f_{ae}).

The scattering of electron is caused by the interaction of electron beam with the electrostatic field φ(r) of the atom. φ(r) can be divided into the field of nucleus and the field of electron clouds. φ(r) can be expressed in terms of charge density by Pisson equation

$$\nabla^2\varphi(r) = -4\pi\big(\rho_n(r) - \rho_e(r)\big)$$

$\rho_n(r)$ is the nuclear charge density while $\rho_e(r)$ is the electron density. Let's set $\frac{\vec{s}-\vec{s_0}}{\lambda} = r^*$, then the Mott formula can be written as:

$$f_{ae}(r^*) = \frac{\pi^{-1}(Z - f_{ax}(r^*))}{r^{*2}}$$

Based on this equation, it can be seen that f_{ae} shall be more efficient than that of f_{ax} at lower r* or Q, that's why the electron diffraction can be easily detected with small volume samples (~100Å). f_{ae} is also less sensitive to Z value and therefore electron diffraction is more sensitive to light atoms than the X-rays. However, it should be noted that f_{ae} decreases tremendously at higher Q. And multiple scattering is common for electron diffraction, which makes the analysis more complex related to that of X-ray and neutron diffraction.

1.2.1.10 Rietveld refinement

The goal of structure study is to gain the atomic positions (or environments) in the periodic unit cell. However, it should be noted that we cannot directly observe the "atoms" by diffraction experiments, what we are trying to locate is actually the positions of atomic electron or nuclei densities.

Unfortunately, we cannot gain this information directly from the diffraction experiment because only the magnitude of the diffraction beam is observed, the phase information is lost. Therefore, we are facing the so-called phase problem in crystallography. This also indicates that the solution obtained from the diffraction experiments is not necessary unique. However, in principle we can at least obtain a reasonable structure model because the measured scattering intensity is proportional to the square of the structure factor. The typical strategy utilized is to first gain an approximate structure model or the so-called initial structure model. Then this structure model is refined until a good agreement is reached between the calculated diffraction intensity (from structure model) and that of experimental observation. Different methods can be used to obtain the initial structure model, which can typically be divided into two categories. For the biased method, the previous known analogue structure types are usually used as initial model. For the unbiased method, an initial model can be obtained by methods such as direct methods (from reciprocal space), electron density modification method and charge flipping method (in direct space), the detailed mathematics behind these methodologies fall out of the scope of the current study and can be found in numerous crystallography books[79]. The second stage of structure study is to refine the initial structure model to obtain a physic meaningful final structure solution. Rietveld refinement is one of the most popular refinement techniques for this purpose. Thus, it is worth to give a brief introduction about this refinement method.

For a typical powder X-ray or neutron diffraction experiment, the one dimensional diffraction pattern (only considering the one dimension case here) contains thousands of data points. Each of these measured points have the same increments (or step size) Δx with a specific observed (or measured) scattering intensity y_i. For simplicity, assuming we are using X-ray or neutron beam with constant wavelength, then the increment is in scattering angle (or 2θ). The traditional way to interpret the one dimensional powder diffraction is by integrating the well-defined Bragg diffraction peaks separately, these integrated diffraction intensities were then used to solve and refine the crystal structure. However, this approach became problematic in case of complex structures with lower symmetry and high amount of atoms within the unit cell, which often showed serious peak overlapping especially at high diffraction angles. The solution was to refine structure using the whole series of Bragg diffraction peaks simultaneously instead of just integrating/refining them one by one, this whole pattern structure refinement technique was first developed by Dr. Rietveld in 1966[80] and was since called Rietveld refinement.

Typically, the calculated intensities y_{calc} in Rietveld refinement can be expressed as

$$y_{calc} = s_0 \sum_H L_H F_H^2 \varphi(2\theta_i - 2\theta_H) P_H A + y_{bi}$$

Where s_0 is the scale factor, H is the Miller indices for Bragg diffraction. L_H is the summation of multiplicity and polarization factors, F_H is the temperature dependent structure factor, φ is the peak profiles, P_H represents the preferred orientation and A is the absorption correction, y_{bi} is the background intensity which may come from air scattering and sample specimens etc.

Rietveld refinement utilized the least square minimization procedure, which can be expressed as a series of equations containing derivatives of all calculated intensities y_{cal}, and can be written as a normal two dimensional m ×m matrix,

$$m_{jk} = -\sum_i 2\frac{1}{y_i}\left[(y_i - y_{calc})\frac{\partial^2 y_{calc}}{\partial x_k \partial x_j} - \left(\frac{\partial y_{calc}}{\partial x_j}\right)\left(\frac{\partial y_{calc}}{\partial x_k}\right)\right]$$

Deleting the first term in this equation, we can obtain

$$m_{jk} = -\sum_i 2\frac{1}{y_i}\left[\left(\frac{\partial y_{calc}}{\partial x_j}\right)\left(\frac{\partial y_{calc}}{\partial x_k}\right)\right]$$

Since the residual function is non-linear, thus the shift can be calculated

$$\Delta = \sum_k m_{jk}^{-1} \frac{\partial(\sum_i \frac{1}{y_i}(y_i - y_{calc})^2)}{\partial x_k}$$

The calculated shifts of parameters are then applied to the initial model and the whole procedure was then repeated until a minimum is reached. It should be noted that the starting model in the Rietveld refinement (or other non-linear least square refinement) shall be close to the correct model otherwise the refinement procedure may lead to the local minimum instead of a global minimum. The model parameters (or refinement parameters) can be the structure related parameters such as unit cell lattice parameters, atomic positions, occupancies and thermal displacements, and it can also be background parameters, instrumental geometrics, specimen or sample aberrations. It should be noted that there are variety approaches for peak shape function modeling for different samples or different experimental configurations, details will not be presented here and can be referenced to many text books[79] or manuals of Rietveld refinement software such as GSAS, JANA, Fullprof and TOPAS.

Here, I will just briefly introduce the criteria of Rietveld refinement. Since Rietveld refinement is a process that will adjust the refinement parameters until a minimum is reached for the residual. Therefore, it is important to have some type of "criteria" of fit, and it is also important to have indicators at each cycle so that it can used to judge whether the refinement is sufficiently near completion. Thus, several "R-values" are introduced in Rietveld refinement.

$$R_{Bragg} = \frac{\sum_H |I_H('obs') - I_H(calc)|}{\sum_H I_H('obs')}$$

$$R_P = \frac{\sum_i |y_i(obs) - y_i(calc)|}{\sum_i y_i(obs)}$$

$$R_{wP} = \sqrt{\frac{\sum_i w_i (y_i(obs) - y_i(calc))^2}{\sum_i w_i\, y_i(obs)^2}} \quad w_i = \frac{1}{y_i}$$

$$R_{exp} = \sqrt{\frac{N - P}{\sum_i w_i y_i(obs)^2}}$$

$$d_{WD} = \frac{\sum_{i=2}^{N} (\Delta y_i - \Delta y_{i-1})^2}{\sum_{i=1}^{N} \Delta y_i^2} \quad \Delta y_i = y_i(obs) - y_i(calc)$$

The "observed" intensities used to calculate R_{Bragg} is not the real intensities of Bragg diffraction peaks but is actually extracted based on the structure model used for the refinement. Therefore, this R value is seriously biased by the model used. However, it is still useful since it will not be influenced by the mismatch of data points that are not associated with Bragg diffraction. R_p reflects the non-weighted residual progress, whereas R_{wp} reflects the weighted residual progress and should be most meaningful R-value to evaluate the progress of refinement. R_{exp} is the smallest expected R index. The ratio of R_{wp}/R_{exp} is referred as goodness of fit (or χ factor) and is reflecting how well the model fits account for the observed data. Another important statistic parameter is the so-called Durbin-Watson statistic d_{WD}, this value reflects the serial correlation between successive y_i values.

1.2.1.11 Diffuse scattering in reciprocal space and models of disorder

Since defects, such as point defects, stacking faults or dislocation are important structure characters for many battery cathode materials. The simple Bragg diffraction theory based on perfect structure geometric progression is not adequate to explain the scattering behavior any more. It is worthwhile to give a brief introduction about the diffuse scattering and related techniques to study this phenomenon.

We shall confine this introduction to the static structure, treatment of dynamics of the local structure falls out of the scope of current study.

As mentioned in the previous introduction of scattering by a small crystal, the scattering intensity can be expressed by summing the amplitude of scattering from different atoms and then multiplying that by the summation of its complex conjugate, thus,

$$I(\vec{Q}) = \sum_m b_m e^{i\vec{Q}\overrightarrow{r_m}} \sum_n b_n e^{-i\vec{Q}\overrightarrow{r_n}}$$

b_m and b_n are the atomic scattering factors for the *m*th and *n*th atom separately. Let $\overrightarrow{r_{mn}} = \overrightarrow{r_m} - \overrightarrow{r_n}$, then,

$$I(\vec{Q}) = \sum_m \sum_n b_m b_n e^{-i\vec{Q}\overrightarrow{r_{mn}}}$$

Assuming $\overrightarrow{r_{mn}}$ takes equal probability over the entire sphere with radius of $|\overrightarrow{r_{mn}}|$, therefore I(Q) can be written as,

$$I(Q) = \sum_m \sum_n b_m b_n \frac{\sin(Qr_{mn})}{Qr_{mn}}$$

This is often called Debye scattering equation[81]. Here, no geometric relation was assumed for the atoms in the structure, it could be gases, liquids, amorphous or crystalline solids. For further clarity, we will introduce Laue monotonic scattering term ($<b>^2$ - $<b^2>$) into the I(Q) equation,

$$I(\vec{Q}) = \sum_m \sum_n b_m b_n e^{-i\vec{Q}\overrightarrow{r_{mn}}} + < b >^2 - < b^2 >$$

Then, we define the so-called total scattering structure function S(Q),

$$S(\vec{Q}) = \frac{I(\vec{Q})}{< b >^2}$$

As mentioned previously, the assumption of perfect periodicity of atoms in the structure is the basis for developing Bragg diffraction theory. However, it should be noted that a crystal structure cannot be perfect: first, the crystal cannot be perfect, there is more or less defects in the structure; second, the atomic positions are never fixed due to the thermal vibration. For simplicity, we will first deal with the second situation: a perfect crystal structure with lattice (or atom) vibration.

Assuming the position of the *m*th atom is $\overrightarrow{r_m}$(t), it can be expressed as the summation of the time-averaged position $<\overrightarrow{r_m}>$ and position deviation $\vec{u}(t)$. Thus, the time-averaging $e^{-i\vec{Q}\overrightarrow{r_m}}$ can be expressed as

$$< e^{-i\vec{Q}\overrightarrow{r_m}} > = e^{i\vec{Q}<\overrightarrow{r_m}>} < e^{i\vec{Q}\vec{u}} >$$

If the term $\vec{Q}\vec{u}$ is small, which is usually correct for thermal vibration, the second average term can be expanded as

$$< e^{i\vec{Q}\vec{u}} > = 1 + i < \vec{Q}\vec{u} > -\frac{1}{2} < \overrightarrow{(Q\vec{u})^2} > -\frac{1}{6} i < \overrightarrow{(Q\vec{u})^3} >$$

All odd terms are averaged to zero considering about the symmetry of vibration (positive and negative), therefore,

$$< e^{i\vec{Q}\vec{u}} > = 1 + i < \vec{Q}\vec{u} > -\frac{1}{2} < \overrightarrow{(Q\vec{u})^2} > -\frac{1}{6} i < \overrightarrow{(Q\vec{u})^3} > \cong e^{-\frac{<\overrightarrow{(Qu)}^2>}{2}}$$

$$< e^{-i\vec{Q}\overrightarrow{r_m}} > = e^{i\vec{Q}<\overrightarrow{r_m}>} e^{-\frac{<\overrightarrow{(Qu)}^2>}{2}} = e^{i\vec{Q}<\overrightarrow{r_m}>} e^{-W}$$

e^{-W} term is called the Debye-Waller factor. It is worth to note that this approximation is still validated if $\vec{u}(t)$ follows Gaussian distribution even if the value is not small[76]. Combining this approximation into the total scattering function, then (inelastic scattering is neglected here),

$$S(\vec{Q}) = e^{-W} S_0(\vec{Q})$$

Where $S_0(\vec{Q})$ shall be the total structure function of Bragg diffraction with average atomic positions. Since Debye-Waller factor has the value smaller than one, it can be seen that the intensity of Bragg diffraction peak decreases due to the vibration of atoms, and it can also be seen that the intensity will be finally diminished at very high Q.

The reduced intensities of Bragg diffraction peaks due to the Debye-Waller factor are not really disappeared, they becomes part of the diffuse scattering, which are the so-called thermal diffuse scattering. This type of diffuse scattering becomes predominate at high Q. In the following section, we will consider a more general situation of diffuse scattering in a crystalline material with small deviations. Let's assume the position of *m*th atom $\overrightarrow{r_m}$ deviates from the ideal site by the amount of $\vec{u}$. Using similar methodology as that for the thermal vibration, the amplitude of the total scattering amplitude can be expressed as,

$$\Psi(\vec{Q}) = \Psi_{Bragg}(\vec{Q}) + \Psi_{Diffuse}(\vec{Q}, \vec{q})$$

$$\Psi_{Diffuse}(\vec{Q},\vec{q}) = \frac{i}{< b > \sqrt{N}} \sum_{n} b_n \, e^{2\pi i \vec{H}\vec{r}} (\vec{Q}\overrightarrow{u_q}) \delta(\vec{Q} - \vec{q} - 2\pi\vec{H})$$

It should be noted that the condition for non-zero value of $\Psi_{Bragg}(\vec{Q})$ is when $\vec{Q} = 2\pi\vec{H}$ (Bragg equation, $\frac{\vec{s}-\vec{s_0}}{\lambda} = \vec{H}$). Whereas for the diffuse scattering, it is when $\vec{Q} = \vec{q} + 2\pi\vec{H}$, which is at a quantity of $\vec{q}$ out of the idea Bragg peak positions. Interestingly, if there is only one $\vec{q}$ where deviation $\overrightarrow{u_q}$ is non-zero, there is a modulated structure. However, if the deviation is local, then the diffuse scattering is spread over the whole Q space.

Until here, the treatment we used is by separating the Bragg diffraction from diffuse scattering. This approach is reasonable when the atomic position deviation is small from the ideal periodicity. However, this approach fails in practice when the structure is extensively disordered. Therefore, it is worthwhile to treat Bragg diffraction and diffuse scattering on equal basis. The most trivial and obvious way is to analyze the as collected total scattering structure function S(Q) in reciprocal Q space, this method has been well adopted in the traditional crystallography community, especially for the study of single crystal diffuse scattering. Here, I will only discuss about the treatment of one-dimensional disorder in the reciprocal Q space, this type of disorder will be further addressed in studying stacking (or coloring) faults of $Na_3Ni_2BiO_6$ in chapter 6.

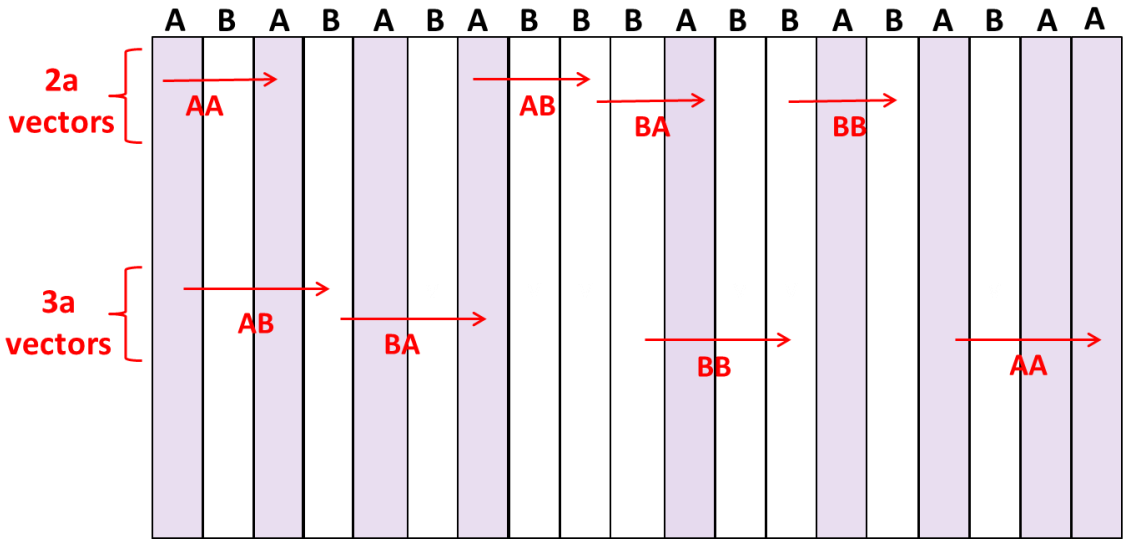

Figure 1.13 The schematic of one dimensional stacking disorder of a system consists of two different layers A and B, the layers are separated by the same layer spacing of a.

Assuming there are two types of layers A and B, as can be seen in Figure 1.13, and the atoms within a specific layer remains perfect periodicity. Thus, during the calculation of the summation over all atoms for Debye scattering equation, we can first carry out the summation over the atoms within a specific layer so that the atomic scattering factors can be replaced by layer form factors, then the summation can be carried out in an one-dimensional array. In this specific case, there shall be two types of layer form factors F_A and F_B, these layers are stacked in one dimensional array with layer spacing of a. Let's also assume that within these N layers array, the A type layer has a fraction of n_A and B type layer has the fraction of n_B=1-n_A. Suppose all unit cells have the same layer dimensions (na), for instance, 3 layers in cubic closed packing (ccp) stacking. Therefore, four different types of layer pair configuration can be generated A…A, A…B, B…A and B…B, as can be seen in Figure 1.13. Suppose the probability of these configurations are P_n^{AA}, P_n^{AB}, P_n^{BA} and P_n^{BB} separately, the relationship between different probabilities can be expressed as,

$$P_n^{AA} + P_n^{AB} + P_n^{BA} + P_n^{BB} = 1$$

$$P_n^{AA} + P_n^{AB} = m_A$$

$$P_n^{AA} + P_n^{BA} = m_A$$

Using this notation, the scattering intensity $I(\vec{Q})$ can be rewritten as

$$I(\vec{Q}) = \sum_{1-N}^{N-1} (N-n)^2 (P_n^{AA} F_A F_A^* + P_n^{BB} F_B F_B^* + P_n^{AB} F_A F_B^* + P_n^{BA} F_B F_A^*) \exp(i\vec{Q} n\vec{a})$$

Let's define a correlation parameter: $C_n = \frac{P_n^{AA} - m_A^2}{m_A m_B}$, then

$$I(\vec{Q}) = (m_A F_A + m_B F_B)(m_A F_A^* + m_B F_B^*) \sum_{1-N}^{N-1} \exp(i\,\vec{Q} n\vec{a})$$

$$+ m_A m_B (F_A - F_B)(F_A^* - F_B^*) \sum_{1-N}^{N-1} C_n \exp(i\,\vec{Q} n\vec{a})$$

The first term expresses the diffraction from a perfect layered crystal with average scattering factor of $\bar{F} = m_A F_A + m_B F_B$, the second term in the equation depends on the difference between the two layer form factors and is related to the diffuse scattering intensity due to the A, B layer disordering. This treatment is fairly straight forward for one dimensional disordering with limited layer types. The

treatment of disordering in higher dimensions will not be covered in this introduction, they can be found in many well written books[82].

The above layer correlation approach of one dimensional disorder is practically applicable for the situation of small numbers of layers. However, this explicit summation will become unrealistic when there are multiple layer types and the layer number N is enormously large (or infinite for many cases). Here, we will briefly go through a recursion method[83] that can be used to analytically analyze one dimensional planar faults.

Suppose there is a layer compound contains a total of N layers with M distinct layer types. Assuming there is a probability of P_{ij} that an i-type layer will be followed by a j-type layer with a layer connection vector of $\overrightarrow{R_{\mathrm{ij}}}$, and j-type layer is then followed by a k-type layer etc. Therefore, for a configuration that i-layer type at origin followed by j-type layer and then followed by k-type layer etc., the total scattering potential can be expressed as

$$V^{N}_{\mathrm{i,j,k..}}(\vec{r}) = \rho_{\mathrm{i}}(\vec{r}) + \rho_{\mathrm{j}}\left(\vec{r} - \overrightarrow{R_{\mathrm{ij}}}\right) + \rho_{\mathrm{k}}\left(\vec{r} - \overrightarrow{R_{\mathrm{ij}}} - \overrightarrow{R_{\mathrm{jk}}}\right) + \cdots$$

The probability for this type of sequence can be written as $g_i P_{ij}\, P_{jk}\ldots$, where g_i is the probability that i-type layer will be the first origin layer, which should be equal to summation of transition probability between i-type layer and other types of layers,

$$g_{\mathrm{i}} = \sum_{j} g_{\mathrm{j}} P_{\mathrm{ji}}$$

The scattered wave function can then be expressed as the Fourier transform of the corresponded total potential function,

$$\phi^{N}_{\mathrm{i,j,k..}}\left(\vec{Q}\right) = \int V^{N}_{\mathrm{i,j,k..}}(\vec{r}) e^{-i\vec{Q}\vec{r}}\, d\, r$$

Here, we have to introduce Born approximation,

$$\int \rho_{\mathrm{j}}\left(\vec{r} - \overrightarrow{R_{\mathrm{ij}}}\right) e^{-i\vec{Q}\vec{r}} dr \cong e^{-i\vec{Q}\overrightarrow{R_{\mathrm{ij}}}} \int \rho_{\mathrm{j}}(\vec{r})\, e^{-i\vec{Q}\vec{r}} dr = e^{-i\vec{Q}\overrightarrow{R_{\mathrm{ij}}}} F_j(\vec{Q})$$

Therefore, $\phi^{N}_{\mathrm{i,j,k..}}(\vec{r})$ can be expressed as

$$\phi^{N}_{\mathrm{i,j,k..}}\left(\vec{Q}\right) = F_i(\vec{Q}) + e^{-i\vec{Q}\overrightarrow{R_{\mathrm{ij}}}} F_j\left(\vec{Q}\right) + e^{-i\vec{Q}\left(\overrightarrow{R_{\mathrm{ij}}} + \overrightarrow{R_{\mathrm{jk}}}\right)} F_k\left(\vec{Q}\right) + \cdots$$

$$= F_i(\vec{Q}) + e^{-i\vec{Q}\overrightarrow{R_{\mathrm{ij}}}}\left[F_j\left(\vec{Q}\right) + e^{-i\vec{Q}\overrightarrow{R_{\mathrm{jk}}}}\left[F_k\left(\vec{Q}\right) + \cdots\right]\right]$$

Here, we can clearly see the recursive nature of the scattered wave function $\phi^{N}_{\mathrm{i,j,k..}}(\vec{r})$. We can further introduce the ensemble average scattered wave function $\phi^{N}_{\mathrm{i}}(\vec{Q})$ that has the layer configurations that begin with i-type layer,

$$\phi^{N}_{\mathrm{i}}(\vec{Q}) = F_i(\vec{Q}) + \sum_j P_{\mathrm{ij}}\, e^{-i\vec{Q}\overrightarrow{R_{\mathrm{ij}}}}[F_j(\vec{Q}) + \sum_k P_{\mathrm{jk}}\, e^{-i\vec{Q}\overrightarrow{R_{\mathrm{jk}}}}[F_k(\vec{Q}) + \cdots]]$$

It is obvious that this function has a recursion nature and can be expressed as,

$$\phi^{N}_{\mathrm{i}}(\vec{Q}) = F_i(\vec{Q}) + \sum_j P_{ij} e^{-i\vec{Q}\overrightarrow{R_{\mathrm{ij}}}}\, \phi^{N-1}_{\mathrm{i}}(\vec{Q})$$

Therefore, the scattering intensity $I(\vec{Q})$ can be written as

$$I(\vec{Q}) = \sum_{m=0}^{N-1} \sum_i g_i(F_i^*(\vec{Q})\, \phi^{N-m}_{\mathrm{i}}(\vec{Q}) + F_i(\vec{Q})\phi^{N-m}_{\mathrm{i}}(\vec{Q})^* - \left|F_i(\vec{Q})\right|^2)$$

Further treatment of $I(\vec{Q})$ in this form can be found in the references[83,84]. This is also the fundamental algorithm implemented for the software Diffax[83], which has been widely used for stacking faults simulation.

1.2.1.12 Total scattering in real space and pair distribution function (PDF)

In the previous section, we defined the total scattering function S(Q) in reciprocal space which contains the information of both Bragg diffraction and diffuse scattering. And we also mentioned the analysis of S(Q) in reciprocal space for structures with perfect periodicity and those with defects (or disorder) . In this section, we will introduce another convenient tool that can be used to analyze the total scattering function: Fourier transformation. And this technique is known as atomic pair distribution function (PDF).

As mentioned in the diffuse scattering section, the scattering amplitude can be written as

$$\phi(\vec{Q}) = \frac{1}{< b >} \sum_n b_n e^{i\vec{Q}\overrightarrow{r_n}}$$

Here, assuming there is only one type of atom in the structure, then

$$\phi(\vec{Q}) = \int \rho(\vec{r})\, e^{i\vec{Q}\vec{r}} dr$$

The total scattering structure function can be expressed as

$$S(\vec{Q}) = \frac{1}{N}\phi(\vec{Q})\phi^*(\vec{Q}) = \frac{1}{N}\iint \rho(\overrightarrow{r_1})\rho(\overrightarrow{r_2})\, e^{i\vec{Q}(\overrightarrow{r_1}-\overrightarrow{r_2})} dr_1 dr_2$$

Let's carry out Fourier transformation of $S(\vec{Q})$

$$F^{-1}(\vec{R}) = \frac{1}{8\pi^3}\int S(\vec{Q})e^{i\vec{Q}\vec{R}}dQ = \frac{1}{8N\pi^3}\iiint \rho(\overrightarrow{r_1})\rho(\overrightarrow{r_2})\, e^{i\vec{Q}(\overrightarrow{r_1}-\overrightarrow{r_2}+\vec{R})} dr_1 dr_2 dQ$$

$$= \frac{1}{N}\iint \rho(\overrightarrow{r_1})\rho(\overrightarrow{r_2})\delta(\overrightarrow{r_1}-\overrightarrow{r_2}+\vec{R})dr_1 dr_2 = \frac{1}{N}\int \rho(\overrightarrow{r_1})\rho(\overrightarrow{r_1}+\vec{R})dr_1$$

Note that $\int \rho(\overrightarrow{r_1})dr_1 = N$, hence,

$$\frac{1}{N}\int \rho(\overrightarrow{r_1})\rho(\overrightarrow{r_1}+\vec{R})dr_1 = \rho_0 g(\vec{R})$$

$g(\vec{R})$ is defined as pair distribution function. For powder samples or isotropic amorphous materials, this function can be further simplified to

$$\rho_0 g(R) = \frac{1}{2\pi^2 R}\int_0^\infty S(Q)sin(QR)QdQ$$

It should be noted that in practical experiments, this integral is not extended to infinite but instead terminated at a limited Q_{max}. And as mentioned previously, S(Q) is approaching unit at high Q. Therefore, this integration will varies wildly as a function of Q_{max}. To solve this problem, a reduced pair distribution function is introduced,

$$\rho_0(g(R)-1) = \frac{1}{2\pi^2 R}\int_0^{Q_{max}}(S(Q)-1)sin(QR)QdQ$$

Multiplying 4πR on each side of the equation, the equation can be rewritten as

$$G(R) = 4\pi\rho_0 R(g(R)-1) = \frac{2}{\pi}\int_0^{Q_{max}}(S(Q)-1)sin(QR)QdQ$$

G(R) is the reduced pair distribution function and is most commonly used form for PDF. It can be seen that the function g(r) gives the probability of finding two atoms separated by a distance of r. It should also be noted that both Bragg intensity and diffuse scattering intensity are used in generating pair distribution function g(r), and there is no requirement for any periodicity of r in describing PDF.

We have shown that experimentally measured total scattering structure function S(Q) can be Fourier transformed into the real space pair distribution function (g(r) or G(r)). The next step is to interpret the data and connect it to a physical meaningful structure model. It is obvious that the peak positions, peak widths or corresponding integrated peak intensities contain valuable information about the studied

structure, for instance, the peak positions in G(r) are related to the atom-atom distance and the integrated intensity of a specific peak is associated with coordination number of atom-atom pairs. However, it should be noted that more quantitatively reliable information can be obtained by carrying out modeling PDF data.

The first method is to calculate G(r) from a reasonable initial model and compare the calculated the $G_c(r)$ to the measured data $G_o(r)$, then some model parameters such as atomic positions are allowed to vary and refine by using regression techniques such as least square refinement. The refined result was further compared to the measured data until a reasonable minimum difference is found between these two. This process is quite similar as the Rietveld refinement of powder X-ray or neutron diffraction data except that the refinement of G(r) is carried out in real space instead of reciprocal space. Therefore, it can be seen that for a well-ordered crystalline structure, the refinement of G(r) shall be essentially the same of refinement of Bragg diffraction. It has been pointed out[85] that thermal displacement factors refined from PDF is more reliable than that from Bragg diffraction due to the higher Q space utilized in corresponded total scattering experiments (> 25 $Å^{-1}$). However, it should be noted that the lattice parameter refined from PDF data is less accurate than that from reciprocal space. The advantage of utilizing PDF becomes preferred when local atomic deviations exist. These deviations will lead to the formation of significant amount of diffuse scattering. Modeling of these diffuse scattering can be carried out in either reciprocal space (see section 1.2.1.5) or in real space, which is the PDF.

Real space least square refinement is useful modeling technique when the studied compound is well crystalline with a reasonable initial crystal structure. However, this becomes unrealistic for amorphous compound or crystalline compounds with extensive disorder. Techniques such as Reverse Monte Carlo are widely used for modeling these systems, the detailed methodology falls out of the scope of current introduction and can be found in related references[86].

1.2.2 X-ray absorption

When shining X-ray beams on a sample, the beam can be either absorbed or scattered. The theory of X-ray scattering and its application have been thoroughly introduced in the previous section. Here, a brief introduction of X-ray absorption will be presented. X-ray absorption spectroscopy measures the absorption coefficient of X-ray beam as a function of photon energy E. If the absorption coefficient is plotted as a function of photon energy, the overall trend is that the absorption coefficient decrease as E

increasing, however, sharp increase of absorptions can be identified at specific photon energies and these are called absorption edges. It should also be noted that at energies above the absorption edges, there are series of wiggles and oscillates. The appearance of strong absorption edges can be explained by Fermi's "golden rule", and this edge region is often referred as X-ray absorption near-edge structure (XANES). The appearance of the oscillation region above absorption edge is due to the scattering of excited photoelectron with neighboring atoms. It is worthwhile to note that the theory of XANES is not fully quantitative (compared to that for EXAFS) yet although it contains useful electronic structure information. Thus, only brief qualitative introduction of XANES and its application will be given from a chemist point of view. A more rigorous physic treatment can be found in related reference and textbooks[87]. Quantitatively interpretation of EXAFS data will be introduced based on the single absorber-scatter approximation, corrections for multiple scattering effects fall out of the scope of this introduction.

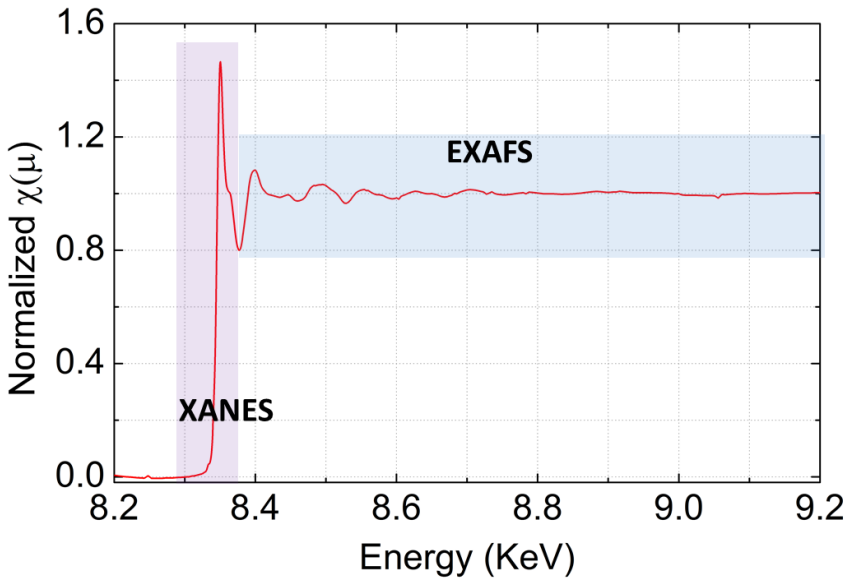

Figure 1.14 Ni K-edge XAS of $Na_3Ni_2BiO_6$, details can be found in chapter 6.

1.2.2.1 X-ray absorption near-edge structure (XANES)

The definition of XANES (near-edge) implies that the kinetic energy of excited photoelectrons is low and thus leaves it with long mean-free path. This character makes XANES sensitive to long distance absorber-scatter interactions rather than the short distance interactions as that in EXAFS. This

longer distance interactions results in the difficult of quantitative analysis of XANES data although some progress has been made in recent years. Here, we will confine ourselves to qualitative analysis of XANES data.

XANES is sensitive to oxidative states. It is generally right to state that the energy of absorption edges increases as the oxidation state of the absorber increases. This can be explained by using simple electrostatic model, since more oxidized sample is more positively charged and thus require higher energy to further eject core electrons.

The pre-edge peak is associated with bound state transition and is sensitive to coordination environments of the studied atoms. The most common observed pre-edge transition is for the K-edge of first row transition metal with open 3d shell. This pre-edge transition is associated with the 1s to 3d transition, it should be noted that 1s to 3d transition is forbidden transition by dipole selection rule. Theoretically, there should be no observable intensity for this type of transition. However, the existence of d(transition metal)-p(ligand) mixing and quadrupole coupling effect will result in partially permitted pre-edge transitions. Since the pre-edge transition is associated with d-p mixing, it is obvious that this pre-edge 1s to 3d transition is sensitive to the local geometry. For example, the 3d-4p mixing shall be very weak for centrosymmetric coordination environments such as MO_6 (*M* is a first row transition metal) octahedron, however, appreciable amount of 3d-4p mixing can be formed in non-centrosymmetric environments such as MO_4 tetrahedron or MO_5 trigonal bipyramid. Thus, it is expected that transition metal ions sit in non-centrosymmetric environments can give much stronger pre-edge transitions than the centrosymmetric ones. A more effective way to gain these local coordination environments is by measuring the L edge transitions (transition metal ions or ligands), the lower energy associated with these transitions (L_1, L_2 and L_3) make the corresponded edge-transition much sharper than that of K edge pre-edge transition. However, it should be noted that the measurement of these low energy transitions should be carried out in high vacuum and thus limit the availability of these techniques. What we considered above is the single electron transitions, it is worthwhile to note that multi-electron transitions is also observable for some elements at higher photon energy (e.g. Mn^{2+}), the detailed theory about this phenomenon will not be introduced here and can be found in related references[88].

1.2.2.2 Extended X-ray absorption fine structure (EXAFS)

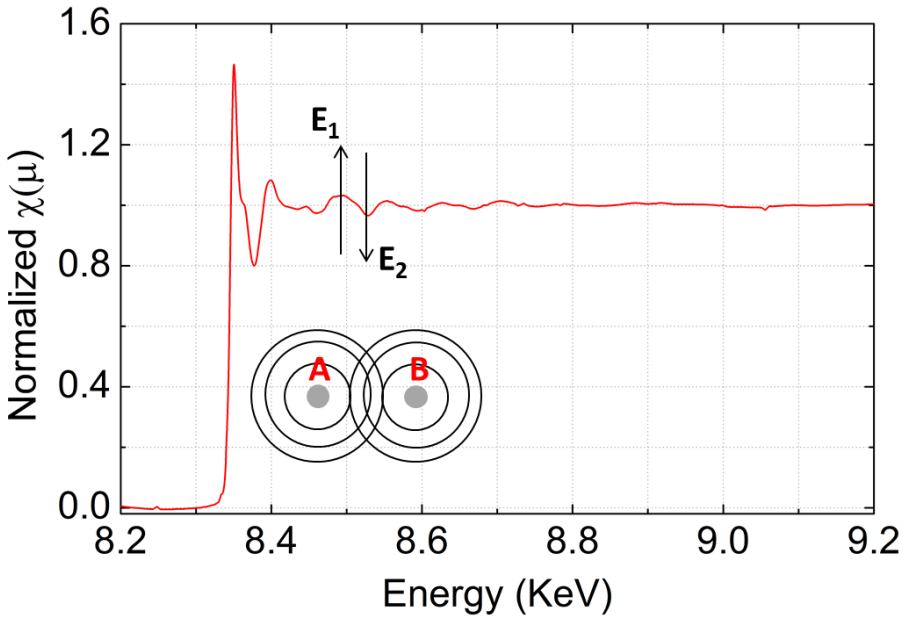

Figure 1.15 Ni K-edge EXAFS of $Na_3Ni_2BiO_6$, insertion shows the single scattering process of the nearest absorber-scatter pair.

The EXAFS part of XAS starts at 20-30 eV above the absorption edge, as can be seen in Figure 1.15. Therefore, the excited photoelectrons have reasonably high kinetic energies and thus would be treated as electron wave with wavelength at the scale of interatomic distances. For simplicity, let's first consider the situation of single absorber-scatter. Suppose the interatomic distances are fixed (a good approximation), as mentioned in the scattering part, the interference of the incident beam and the scattering (i.e. backscattering) beam will depend on the wavelength (or kinetic energy) of the excited photoelectric wave: if the interference is in phase, we see the absorption cross section oscillates toward the local maximum, as represented by E_1 in Figure 1.15; whereas if the interference is destructive (or in opposite phase), then the oscillation is toward local minimum, as represented by E_2. Thus, the oscillation contains information about local atomic information, such as atomic species, interatomic distances and coordination environments etc.

In the following section, I'll give a brief introduction about the semi-quantitative analysis of EXAFS data. For simplicity, we will first consider the single scattering situation, as shown in Figure 1.15.

Similar to the wave vector ($\vec{s}$) used in X-ray or neutron scattering, here, we define a photoelectron wave vector ($\vec{k}$), the absolute value of this wave vector is given by

$$k = \sqrt{\frac{2m_e(E - E_0)}{h^2}}$$

In the EXAFS interpretation, the scanning energy dependent $\chi_\mu(E)$ is converted into the photoelectron wave vector depended EXAFS function $\chi(k)$. The conversion can be expressed as

$$\chi(k) = \frac{\chi_\mu(E) - \chi_{\mu 0}(E)}{\chi_{\mu 0}(E)}$$

$\chi_\mu(E)$ is the measured absorption coefficient as a function of photon energy E, $\chi_{\mu 0}(E)$ is the ideal absorption coefficient without the contribution from interatomic photoelectron scattering. It should be noted that $\chi_{\mu 0}(E)$ is not directly measureable and is obtained by fitting the XAS data with a spline function. A typical $\chi(k)$ as a function of k is shown in Figure 1.16, and $\chi(k)$ is often multiplied by k^2 or k^3 to emphasize the high k signal, as can be seen in Figure 1.16.

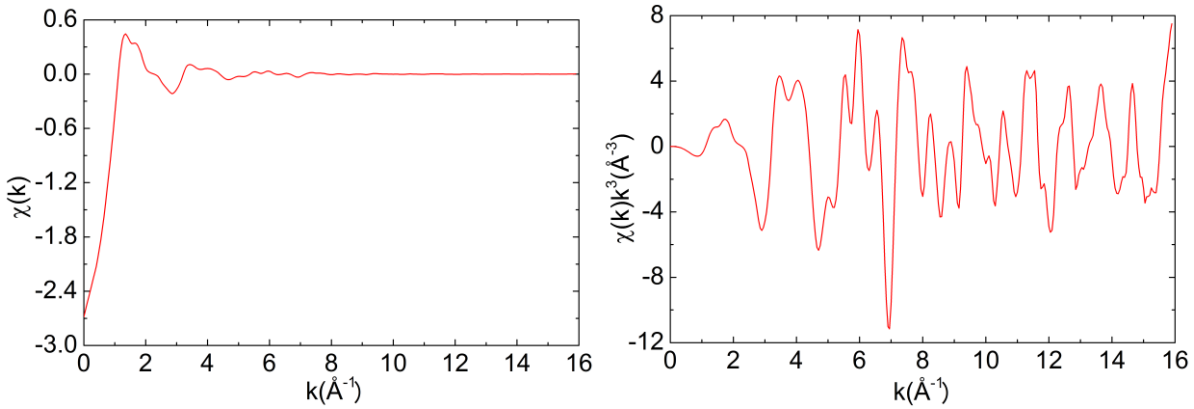

Figure 1.16 The as collected Ni K-edge EXAFS of $Na_3Ni_2BiO_6$ (left) $\chi(k)$ as a function of k (right) $\chi(k)k^3$ as a function of k.

Qualitative interpretation of EXAFS function can be first carried out by observing the amplitude and frequency of oscillation, which are associated with the number of scattering atoms (total scattering power) and the absorber-scatter interatomic distances separately. Quantitative analysis requires more rigorous quantum mechanics treatment of photoelectron scattering function, which will not be introduced here but can be found in related references[87]. $\chi(k)$ can be expressed as

$$\chi(k) = \sum_m \frac{N_m \varphi_m(k) S_0^2}{kR^2} \exp\left(-\frac{R}{\lambda(k)}\right) \exp(-2k^2\sigma^2) \sin(2kR + \tau(k))$$

In which, N_m is the coordination number of the absorber, R is the interatomic distance between absorber and scatter atoms, λ(k) is the mean free path of the photoelectron. σ is the Deybe-Waller factor, $\varphi_m(k)$ and τ(k) is the photoelectron scattering function and phase shift separately. It should be noted that the EXAFS falls off as $1/R^2$, and the second and third term in the summation can also be viewed as damping factors of χ(k). These terms determine that χ(k) will fall out quickly at high k. In practice, $\varphi_m(k)$, τ(k) and λ(k) can be obtained using ab initio calculations from a model structure.

A more practical and intuitive way to carry out EXAFS analysis is by Fourier transforming χ(k) into real space as a pseudo radial distribution function χ(r). It should be noted that the peak position in χ(r) is not equal to the corresponded absorber-scatter pair distance as that in PDF, it actually shifts a specific distance (~ 0.5 Å for the first shell) due to the phase shift term τ(k) in $\chi(k)$. Once an initial model is provided, the non-linear least square refinement can be carried out in both k space and r space, variables such as absorber-scatter interatomic distance R, absorber coordination number and Debye-Waller factors σ are simultaneously refined until a minimum difference between calculated pattern and observed data is found. A typical fitting in r space is shown in Figure 1.17.

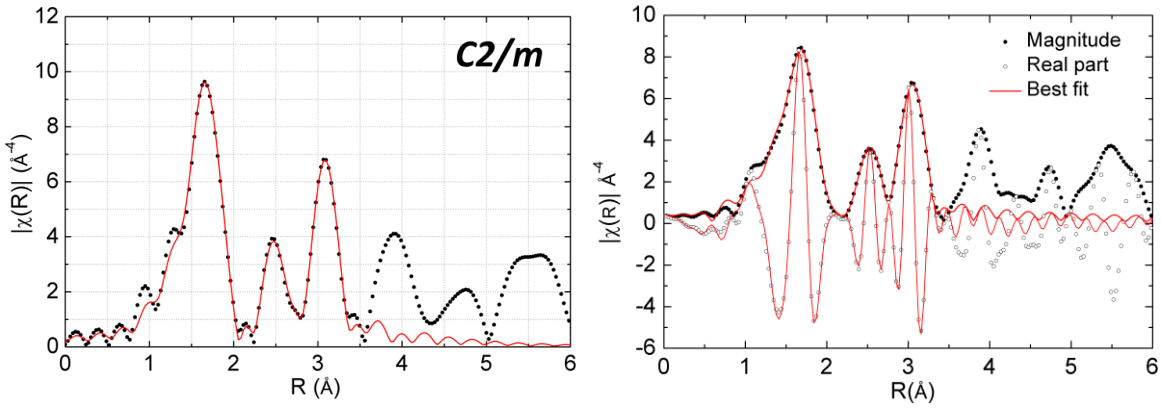

Figure 1.17 Fitting of Ni K-edge EXAFS of $Na_3Ni_2BiO_6$ in *r* space with experiment data in black dots, calculated curve in red.

Last but not least, it is worthwhile to note that the number of independent data points in EXAFS is not equal to the measured data points as those for X-ray and neutron diffraction. The EXAFS spectra are often oversampled and hence the independent parameter information (N_i) should be much less than the measured data points N. For a good approximation, the N_i can be evaluated as

$$N_i = \frac{2\Delta k \Delta R}{\pi}$$

For the case of Ni K-edge EXAFS of $Na_3Ni_2BiO_6$, as can be seen in Figure 1.XX. If we choose a k window between 2 $Å^{-1}$ and 15 $Å^{-1}$ and confine the refined R range between 1 to 3.5 Å (third shell), a maximum of 20 independent parameters can be refined, which is significant but not comparable to other structure study techniques such as Bragg diffraction or pair distribution function. However, it should be noted that EXAFS is elemental specified, indicating that the as collected data is partial radial distribution function of the absorber atoms instead of total pair distribution function as that in PDF. This unique character makes EXAFS to be a convenient tool to study the local coordination chemistry.

References

(1) Nagaura, T.; Tozawa, K. *Prog. Batteries Solar Cells* **1990**, *9*, 209.
(2) Armand, M.; Tarascon, J. M. *Nature* **2008**, *451*, 652.
(3) Linden, D.; Reddy, T. B.; McGraw-Hill: 2002.
(4) Tarascon, J. M.; Armand, M. *Nature* **2001**, *414*, 359.
(5) Pan, H. L.; Hu, Y. S.; Chen, L. Q. *Energy & Environmental Science* **2013**, *6*, 2338.
(6) Shannon, R. D.; Prewitt, C. T. *Acta Crystallographica Section B-Structural Crystallography and Crystal Chemistry* **1969**, *B 25*, 925.
(7) http://pubs.usgs.gov/fs/2002/fs087-02/.
(8) Whittingham, M. S. *Prog. Solid State Chem.* **1978**, *12*, 41.
(9) Thompson, A. H.; Whittingham, M. S. *Mater. Res. Bull.* **1977**, *12*, 741.
(10) Whittingham, M. S. *Science* **1976**, *192*, 1126.
(11) Whittingham, M. S. *J. Electrochem. Soc.* **1976**, *123*, 315.
(12) Whittingham, M. S. *Chem. Rev.* **2014**, *114*, 11414.
(13) Mizushima, K.; Jones, P. C.; Wiseman, P. J.; Goodenough, J. B. *Mater. Res. Bull.* **1980**, *15*, 783.
(14) Guilmard, M.; Pouillerie, C.; Croguennec, L.; Delmas, C. *Solid State Ionics* **2003**, *160*, 39.
(15) Ohzuku, T.; Makimura, Y. *Chem. Lett.* **2001**, 744.
(16) Delmas, C.; Fouassier, C.; Hagenmuller, P. *Physica B & C* **1980**, *99*, 81.
(17) Goodenough, J.; Thackeray, M.; David, W.; Bruce, P. *Revue de Chimie minerale* **1984**, *21*, 435.
(18) Thackeray, M.; David, W.; Bruce, P.; Goodenough, J. *Mater. Res. Bull.* **1983**, *18*, 461.
(19) Thackeray, M. M.; David, W. I. F.; Bruce, P. G.; Goodenough, J. B. *Mater. Res. Bull.* **1983**, *18*, 461.
(20) Thackeray, M.; Johnson, P.; De Picciotto, L.; Bruce, P.; Goodenough, J. *Mater. Res. Bull.* **1984**, *19*, 179.
(21) Ohzuku, T.; Ariyoshi, K.; Yamamoto, S.; Makimura, Y. *Chem. Lett.* **2001**, 1270.
(22) Ariyoshi, K.; Iwakoshi, Y.; Nakayama, N.; Ohzuku, T. *J. Electrochem. Soc.* **2004**, *151*, A296.

(23) Colbow, K.; Dahn, J.; Haering, R. *J. Power Sources* **1989**, *26*, 397.
(24) Ohzuku, T.; Ueda, A.; Yamamoto, N. *J. Electrochem. Soc.* **1995**, *142*, 1431.
(25) Lu, Z.; MacNeil, D.; Dahn, J. *Electrochem. Solid-State Lett.* **2001**, *4*, A191.
(26) Thackeray, M. M.; Johnson, C. S.; Vaughey, J. T.; Li, N.; Hackney, S. A. *J. Mater. Chem.* **2005**, *15*, 2257.
(27) Strobel, P.; Lambertandron, B. *J. Solid State Chem.* **1988**, *75*, 90.
(28) Breger, J.; Jiang, M.; Dupre, N.; Meng, Y. S.; Shao-Horn, Y.; Ceder, G.; Grey, C. P. *J. Solid State Chem.* **2005**, *178*, 2575.
(29) Boulineau, A.; Croguennec, L.; Delmas, C.; Weill, F. *Chem. Mater.* **2009**, *21*, 4216.
(30) Padhi, A. K.; Nanjundaswamy, K. S.; Goodenough, J. B. *J. Electrochem. Soc.* **1997**, *144*, 1188.
(31) Manthiram, A.; Goodenough, J. *J. Solid State Chem.* **1987**, *71*, 349.
(32) Manthiram, A.; Goodenough, J. *J. Power Sources* **1989**, *26*, 403.
(33) Goodenough, J. B.; Hong, H. Y. P.; Kafalas, J. A. *Mater. Res. Bull.* **1976**, *11*, 203.
(34) Hong, H. Y. P. *Mater. Res. Bull.* **1976**, *11*, 173.
(35) Yao, Y. F. Y.; Kummer, J. T. *Journal of Inorganic & Nuclear Chemistry* **1967**, *29*, 2453.
(36) Reiff, W.; Zhang, J.; Torardi, C. *J. Solid State Chem.* **1986**, *62*, 231.
(37) Torardi, C.; Prince, E. *Mater. Res. Bull.* **1986**, *21*, 719.
(38) NADIRI, A.; Delmas, C.; Salmon, R.; Hagenmuller, P. *Revue de chimie minérale* **1984**, *21*, 537.
(39) Delmas, C.; Cherkaoui, F.; Nadiri, A.; Hagenmuller, P. *Mater. Res. Bull.* **1987**, *22*, 631.
(40) Delmas, C.; Nadiri, A. *Mater. Res. Bull.* **1988**, *23*, 65.
(41) Delmas, C.; Nadiri, A.; Soubeyroux, J. *Solid State Ionics* **1988**, *28*, 419.
(42) Nanjundaswamy, K.; Padhi, A.; Goodenough, J.; Okada, S.; Ohtsuka, H.; Arai, H.; Yamaki, J. *Solid State Ionics* **1996**, *92*, 1.
(43) Masquelier, C.; Padhi, A.; Nanjundaswamy, K.; Goodenough, J. *J. Solid State Chem.* **1998**, *135*, 228.
(44) Islam, M. S.; Driscoll, D. J.; Fisher, C. A.; Slater, P. R. *Chem. Mater.* **2005**, *17*, 5085.
(45) Morgan, D.; Van der Ven, A.; Ceder, G. *Electrochem. Solid-State Lett.* **2004**, *7*, A30.
(46) Huang, H.; Yin, S.-C.; Nazar, L. s. *Electrochem. Solid-State Lett.* **2001**, *4*, A170.
(47) Yamada, A.; Chung, S.-C.; Hinokuma, K. *J. Electrochem. Soc.* **2001**, *148*, A224.
(48) Ravet, N.; Chouinard, Y.; Magnan, J.; Besner, S.; Gauthier, M.; Armand, M. *J. Power Sources* **2001**, *97*, 503.
(49) Chung, S.-Y.; Bloking, J. T.; Chiang, Y.-M. *Nat. Mater.* **2002**, *1*, 123.
(50) Armand, M.; Michot, C.; Ravet, N.; Simoneau, M.; Hovington, P. *There is no corresponding record for this reference*.
(51) Nytén, A.; Abouimrane, A.; Armand, M.; Gustafsson, T.; Thomas, J. O. *Electrochem. Commun.* **2005**, *7*, 156.
(52) Dominko, R.; Conte, D. E.; Hanzel, D.; Gaberscek, M.; Jamnik, J. *J. Power Sources* **2008**, *178*, 842.
(53) Gong, Z.; Li, Y.; Yang, Y. *Electrochem. Solid-State Lett.* **2006**, *9*, A542.
(54) Gong, Z.; Li, Y.; Yang, Y. *J. Power Sources* **2007**, *174*, 524.
(55) Masquelier, C.; Croguennec, L. *Chem. Rev. (Washington, DC, U. S.)* **2013**, *113*, 6552.
(56) Nishimura, S.-i.; Hayase, S.; Kanno, R.; Yashima, M.; Nakayama, N.; Yamada, A. *J. Am. Chem. Soc.* **2008**, *130*, 13212.
(57) Boulineau, A.; Sirisopanaporn, C.; Dominko, R.; Armstrong, A. R.; Bruce, P. G.; Masquelier, C. *Dalton Trans.* **2010**, *39*, 6310.
(58) Sirisopanaporn, C.; Boulineau, A.; Hanzel, D.; Dominko, R.; Budic, B.; Armstrong, A. R.; Bruce, P. G.; Masquelier, C. *Inorg. Chem.* **2010**, *49*, 7446.
(59) Yamada, A.; Iwane, N.; Harada, Y.; Nishimura, S. i.; Koyama, Y.; Tanaka, I. *Adv. Mater. (Weinheim, Ger.)* **2010**, *22*, 3583.
(60) Bo, S.-H.; Wang, F.; Janssen, Y.; Zeng, D.; Nam, K.-W.; Xu, W.; Du, L.-S.; Graetz, J.; Yang, X.-Q.; Zhu, Y. *J. Mater. Chem.* **2012**, *22*, 8799.
(61) Barker, J.; Gover, R. K. B.; Burns, P.; Bryan, A.; Saidi, M. Y.; Swoyer, J. L. *J. Power Sources* **2005**, *146*, 516.

(62) Barker, J.; Gover, R. K. B.; Burns, P.; Bryan, A. *Electrochemical and Solid State Letters* **2005**, *8*, A285.
(63) Recham, N.; Chotard, J. N.; Dupont, L.; Delacourt, C.; Walker, W.; Armand, M.; Tarascon, J. M. *Nat. Mater.* **2010**, *9*, 68.
(64) Zhou, Y. N.; Ding, J. J.; Nam, K. W.; Yu, X. Q.; Bak, S. M.; Hu, E. Y.; Liu, J.; Bai, J. M.; Li, H.; Fu, Z. W.; Yang, X. Q. *Journal of Materials Chemistry A* **2013**, *1*, 11130.
(65) Komaba, S.; Takei, C.; Nakayama, T.; Ogata, A.; Yabuuchi, N. *Electrochem. Commun.* **2010**, *12*, 355.
(66) Berthelot, R.; Carlier, D.; Delmas, C. *Nat. Mater.* **2011**, *10*, 74.
(67) Yabuuchi, N.; Kubota, K.; Dahbi, M.; Komaba, S. *Chem. Rev. (Washington, DC, U. S.)* **2014**, *114*, 11636.
(68) Yabuuchi, N.; Kajiyama, M.; Iwatate, J.; Nishikawa, H.; Hitomi, S.; Okuyama, R.; Usui, R.; Yamada, Y.; Komaba, S. *Nat. Mater.* **2012**, *11*, 512.
(69) Zaghib, K.; Trottier, J.; Hovington, P.; Brochu, F.; Guerfi, A.; Mauger, A.; Julien, C. *J. Power Sources* **2011**, *196*, 9612.
(70) Sun, A.; Beck, F. R.; Haynes, D.; Poston, J. A.; Narayanan, S.; Kumta, P. N.; Manivannan, A. *Materials Science and Engineering: B* **2012**, *177*, 1729.
(71) Kim, H.; Park, I.; Seo, D.-H.; Lee, S.; Kim, S.-W.; Kwon, W. J.; Park, Y.-U.; Kim, C. S.; Jeon, S.; Kang, K. *J. Am. Chem. Soc.* **2012**, *134*, 10369.
(72) Sanz, F.; Parada, C.; Rojo, J.; Ruiz-Valero, C. *Chem. Mater.* **2001**, *13*, 1334.
(73) Moreau, P.; Guyomard, D.; Gaubicher, J.; Boucher, F. *Chem. Mater.* **2010**, *22*, 4126.
(74) Breger, J.; Dupre, N.; Chupas, P. J.; Lee, P. L.; Proffen, T.; Parise, J. B.; Grey, C. P. *J. Am. Chem. Soc.* **2005**, *127*, 7529.
(75) Makimura, Y.; Ohzuku, T. *J. Power Sources* **2003**, *119*, 156.
(76) Warren, B. E. *X-ray Diffraction*; Courier Corporation, 1969.
(77) Giacovazzo, C.; Monaco, H.; Viterbo, D.; Scordari, F.; Gilli, G.; Zanotti, G.; Catti, M. *Acta Cryst* **1993**, *49*, 373.
(78) Willis, B. T. M.; Carlile, C. J. *Experimental neutron scattering*; Oxford Univ. Press, 2009.
(79) Young, R. A. *Cryst. Res. Technol.* **1995**, *30*.
(80) Rietveld, H. M. *J. Appl. Crystallogr.* **1969**, *2*, 65.
(81) Debye, P. *The Journal of Physical Chemistry* **1947**, *51*, 18.
(82) Welberry, T. R. *Diffuse x-ray scattering and models of disorder*; Oxford Univ. Press Oxford, 2004; Vol. 16.
(83) Treacy, M.; Newsam, J.; Deem, M. In *Proceedings of the Royal Society of London A: Mathematical, Physical and Engineering Sciences*; The Royal Society: 1991; Vol. 433, p 499.
(84) Hendricks, S.; Teller, E. *The Journal of Chemical Physics* **1942**, *10*, 147.
(85) Egami, T.; Billinge, S. J. *Underneath the Bragg peaks: structural analysis of complex materials*; Elsevier, 2003; Vol. 16.
(86) McGreevy, R. L. *J. Phys.: Condens. Matter* **2001**, *13*, R877.
(87) Koningsberger, D.; Prins, R. *X-ray absorption: principles, applications, techniques of EXAFS, SEXAFS, and XANES* **1988**.
(88) Rehr, J.; Ankudinov, A. *Coord. Chem. Rev.* **2005**, *249*, 131.

Chapter 2 $Na_3TiP_3O_9N$ as zero volume change cathode material for rechargeable Na-ion batteries[1]

2.1 Introduction

The rapid growth of the mobile electronic industry has been facilitated by the development of Li-ion batteries. The development of next-generation batteries which can meet the demands of the grid energy storage and electrical utilities may similarly revolutionize these sectors, though these batteries might not use Li^+ as the mobile ion due to its high price. The batteries required for these emerging industries are very large, and therefore necessitate inexpensive compounds which can still meet desired performance metrics of power, safety, and lifetime. There has therefore been a renewed interest in Na-ion batteries due to the reduced cost and enhanced availability of sodium relative to lithium[2-4], and depending on the needs of the particular application, the minimum metrics for energy density and rate performance may be relaxed relative to those of the mobile electronics industry.

Although Na-ion battery is an old battery system which can date back to the 1980s[5], however, it is much less explored than Li-ion batteries. Until today, only limited amount of compounds have been reported to be promising sodium insertion electrode materials. In regards of oxide-based electrode materials, it is worth to mention the sodium based layered compounds, which can be categorized into O3-type and P2-type[6], in which sodium ions accommodate octahedral and prismatic sites specifically: O3-type compounds are analogues of α-$NaFeO_2$ structure family such as Na_xMO_2 (M= V, Cr, Co and Ni etc.)[5,7-10]; recently, it was found P2-type sodium based layered structure seems to show higher capacity than O3-type structure, as exemplified by P2-$Na_{0.6}MnO_2$[11], P2-$Na_{0.7}CoO_2$[12] and P2-$Na_x[Fe_{1/2}Mn_{1/2}]O_2$ [13]. Similarly, some classic Li-ion battery structures have also been revisited and tested for their ability to serve as Na-ion batteries. For example, secondary batteries based on the Na-ion analogues of the one-dimensional (1D) Li-ion conductors with the olivine structure (such as $NaFePO_4$, $NaFe_{0.5}Mn_{0.5}PO_4$) have been developed [14,15]. However, good Na-ion based electrode materials of the important 3D cubic spinel class of Li-ion batteries have not yet been found; perhaps the Na-ion battery cathode systems that come closest to achieving isotropic 3D Na-ion conduction are those based on the NASICON structure framework first developed ($Na_{1+x}Zr_2P_{3-x}Si_xO_{12}$)[16] for superionic conduction applications, such as $NaTi_2(PO_4)_3$[17] and $Na_3V_2(PO_4)_3$[18,19]. Although there has been prior work aimed at developing a stable cubic stable framework for isotropic Na-ion conduction (such as cubic form $NaSbO_3$)[16], this classic goal

has not yet been achieved. However, there have been a number of interesting recent successes in discovering novel structural frameworks with other symmetries which do permit sufficiently rapid (of course not fast) Na-ion conduction to serve as electrode materials for secondary Na-ion batteries, resulting in the development of $NaVPO_4F$[20], $Na_3V_2(PO_4)_2F_3$[21,22], Na_2FePO_4F[23,24], $Na_3MnPO_4CO_3$[25] and $Na_2FeSO_4 \cdot 2H_2O$[26].

In order to expand the range of available structural families capable of transporting mobile ions, we have been motivated to incorporate N^{3-} anions into cathode materials. The three bonding character of N^{3-} is of particular interesting for designing three dimensional crystal structure, and the use of nitrogen also offers potential advantages in energy density since the mass charge ratio of N^{3-} (m/z = 5) is low relative to O^{2-} (m/z = 8), though the detailed structure and stoichiometry of such compounds will determine whether or not the overall capacity will exceed that of current generation materials. When nitrogen is present in the form of nitridophosphate (PO_3N) groups, inductive effects allow high voltages suitable for cathodes to be realized. We have recently demonstrated that the 2:2 cubic nitridophosphate $Na_2Fe_2P_3O_9N$ can effectively serve as a Li-ion battery at room temperature at voltages above 3 V (*vs.* Li^+/Li) after Li-ion exchange with the theoretical capacity of this compound of 144 mAh/g being mostly realized, though higher temperatures (~300 °C) are necessary to effectively remove Na ions from the framework during the ion exchange process due to the low room temperature mobility of Na in this compound. The large difference in mobility between Na and Li in this Fe-containing framework is correctly predicted by bond valence sum (BVS) maps, which give a threshold of more than 0.5 valence units (v.u.) for Na ions, but less than 0.05 v.u. for Li ions.[27] While the room temperature mobility of Na in $Na_2Fe_2P_3O_9N$ is poor, it is worthwhile to ask if higher Na mobilities can be achieved by chemical substitutions in the very intriguing cubic framework of this compound that should be conducive to isotropic Na-ion conduction, and which may be able to effectively serve as secondary battery cathode or as an isotropic solid state electrolyte, depending on the nature of cation used to replace Fe.

In addition to the 2:2 $Na_2M^{II}{}_2P_3O_9N$ compounds with divalent cations, charge balance can also be achieved in 3:1 cubic sodium nitridophosphate compounds with a trivalent cation resulting in the general formula $Na_3M^{III}P_3O_9N$ (Figure 2.1). A variety of redox-active trivalent *3d* transition metals (*M* = Ti, V, Cr etc.) can occupy the M^{III} site[28-33], giving theoretical specific gravimetric capacities of about 70 – 215 mAh/g if one to three Na ions can be cycled electrochemically. The structure of $Na_3TiP_3O_9N$ is shown in Figure 2.1.

Our simple bond valence sum map calculations suggest that 3:1 $Na_3TiP_3O_9N$ should have much higher Na-ion mobility than 2:2 $Na_2Fe_2P_3O_9N$. We demonstrate here the validity of this prediction for $Na_3TiP_3O_9N$ through a variety of electrochemical, structural, and theoretical experiments which confirm that there is very good three dimensional Na-ion mobility at room temperature in this compound. It is shown that $Na_3TiP_3O_9N$ can reversibly cycle Na-ions in a manner suitable for secondary batteries, and that the volume changes on Na-removal are remarkably small (< 1%) relative to other known Na-ion battery systems and offer unique advantages toward the development of Na-ion systems with extended lifetimes. Due to the cubic symmetry of this phase, the ionic conductivity of $Na_3TiP_3O_9N$ is fully isotropic unlike other known classes of Na-ions conductors such as beta'-alumina (two-dimensional Na^+ conductivity)[34] or NASICON (three-dimensional but anisotropic Na-ion conduction)[16], and may therefore offer unique advantages as a solid state electrolyte. This general class of cubic nitridophosphate structures will be abbreviated as CUBICONs (CUBic Ionic Conductors), in recognition of the Na^+ (and Li^+) ion conduction possible within the framework of these 3:1 and 2:2 nitridophosphate compounds.

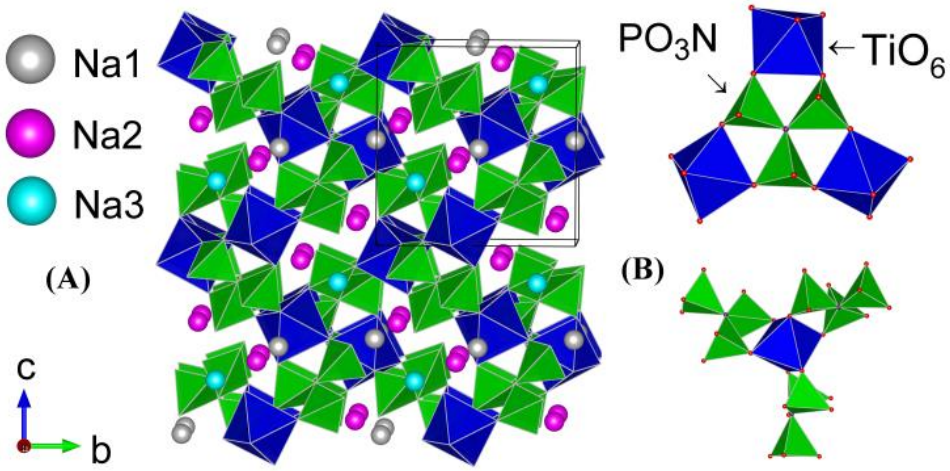

Figure 2.1 (A) Crystal structure of $Na_3TiP_3O_9N$ viewed along the (100) direction, with unit cell boundaries shown in black. (B) The connectivity of trimers of PO_3N tetrahedra (green) with isolated TiO_6 octahedra (blue).

2.2 Experimental parts

2.2.1 Synthesis of $Na_3TiP_3O_9N$

For a single-step synthesis of $Na_3TiP_3O_9N$, $NaPO_3$ (Fisher Scientific, n ~ 6), TiO_2 (<32nm, Alfa Aesar, 99.9%) were combined in a molar ratio of 3.05:1 and ball milled for 120 min in the vibratory ball mill together with 10% (molar ratio relative to Ti^{4+}) ascorbic acid. The mixture was then put into an open-ended fused quartz boat (prepared by cutting open a 15 mm diameter tube) which was then inserted into a 1 inch diameter fused quartz tube and heated at 200 ℃/h to a reaction temperature of 850 ℃ for 20 h under flowing ammonia gas (50 mL/min). A minor (less than 5%) impurity phase of NASICON-type $Na_{3-x}Ti_2(PO_4)_3$ was typically found in the final product when ascorbic acid was not used in the reaction.

2.2.2 Chemical desodiation

Powder samples obtained from a single-step solid state synthesis were oxidized with excess 1.0 M NO_2BF_4 in acetonitrile solution for 10 h to 20 h in an Ar filled glove box. The oxidized products were washed with acetonitrile (three times) and then acetone (three times), and were finally dried at room temperature in a glove box. The color of $Na_3TiP_3O_9N$ powder samples changed from violet to grey after 10 h indicating the partial oxidation of Ti^{3+}, and then to nearly white after 20 h indicating a Ti^{4+} valence in the final product which resulted from the very nearly complete sample desodiation.

2.2.3 Diffraction studies

Room temperature X-ray diffraction (XRD) data on as-prepared $Na_{3-x}TiP_3O_9N$ powders were collected on a Bruker D8 Advance diffractometer utilizing Cu K_α radiation from a fine focus X-ray tube ($K_{\alpha1}$ = 1.54053 Å, $K_{\alpha2}$ = 1.54431 Å), with a 300 mm working radius and a 1D position-sensitive LynxEye Si detector with 192 channels. Synchrotron X-ray diffraction data of powder samples were collected at beamline X14A of the National Synchrotron Light Source (NSLS) of Brookhaven National Laboratory (BNL) with a 1D linear position sensitive detector at a distance of 1433 mm and a wavelength of approximately 0.78 Å. Additional synchrotron XRD data of $Na_{2.5}TiNP_3O_9$ was collected at beamline X7B of the NSLS with a 2D area detector at a distance of 376 mm with a constant wavelength of about 0.32 Å. The software Fit2D[35] was used to convert the 2D diffraction image to a 1D diffraction pattern based on an estimated beam polarization of 90%. *In situ* XRD experiments probing

the thermal decomposition of $Na_3TiP_3O_9N$ powders were carried out at beamline X7B. The powder sample was placed in a 1.5 mm quartz capillary, and then the whole capillary was mounted thick-wire resistive heater which had been calibrated in advance of the experiment[36]. The sample was heated to 850 ℃ at 2 ℃/min, held at 850 ℃ for 30 min, and then allowed to naturally cool to room temperature. Structures were refined using the Rietveld method as implemented in the TOPAS software package (Bruker-AXS, version 4.2).

Time-of-flight (TOF) neutron diffraction experiments were performed on the NOMAD[37] and POWGEN powder diffractometers at the Spallation Neutron Source (SNS), Oak Ridge National Laboratory during the 2013-A run cycle (NOMAD) 2013-B run cycle (POWGEN). For NOMAD experiments, about 100 mg of powder were packed in a 3 mm diameter fused quartz capillary, and typical data acquisition times of 100 min were used. The detectors were calibrated using scattering from the standard diamond powder prior to the measurements. Neutron powder diffraction data were normalized against a V rod and the background was subtracted using the specific IDL routines developed for NOMAD instrument, including corrections for coherent scattering from the V rod. POWGEN diffraction data were collected with a center neutron wavelength of 1.333 Å. About 1.5 grams of sample were loaded into a 6 mm vanadium can which was inserted into a cryofurnace (JANIS) running under vacuum (pressure less than 10^{-5} bar during data collection). Powder diffraction data were collected with a typical data acquisition time of 3 hours. High temperature scans on $Na_3TiP_3O_9N$ were run at temperatures of 300 K, 400 K, 500 K, 595K, and 645 K.

The neutron diffraction data were refined using the Rietveld method as implemented in the TOPAS software package (Bruker-AXS, version 4.2). A back-to-back exponential function convoluted with a split pseudo-Voigt function was used to model the peak shape. No absorption correction was needed for the NOMAD data due to the low linear absorption coefficient of both the sample ($\mu = 0.055$ cm^{-1}, $\mu R = 0.0165$) and the thin, small diameter capillary. For POWGEN data, a cylindrical absorption correction with estimated absorption coefficient $\mu R \sim 0.35$ was used.

2.2.4 X-ray absorption spectroscopy

X-ray absorption spectroscopy (XAS) data at the Ti K-edge were collected in transmission mode at beamline X19A of the NSLS synchrotron at BNL. Ti metal foil was used as a simultaneous reference

energy calibrant. The X-ray absorption near edge structure (XANES) data was processed using the ATHENA software package[38].

2.2.5 Electrochemistry

For Na-ion battery testing, electrochemical cycling against a sodium metal anode was done in a 2032-type coin cell. Cathodes were prepared by mixing $Na_3TiP_3O_9N$ powders obtained from the ascorbic acid assisted method for producing a carbon coating during the synthesis procedure (TGA tests indicates about 4% carbon in the powder), carbon black, and PVDF in the mass ratio of 8:1:1. Mixing was done either by hand grinding (all data in main paper), or by low energy milling in a vibratory ball mill (additional data in SI) which lead to slightly enhanced electrochemical performance. Coin cells were assembled in an Ar-filled glove box using thickly cut strips of Na metal as the anode and 1M $NaClO_4$ in 3:7 (by mass) EC/DMC solution as electrolyte. The coin cells were tested at room temperature on an Arbin BTU-2000 instrument with a typical current density of 0.014 mA/cm^2 corresponding to a C/20 rate, though other rates were also investigated. Galvanostatic intermittent titration technique (GITT) experiments were carried out on coin cells by first charging for 1 hour at a constant current of 0.014 mA/cm^2 and then relaxing for 20 hours, and repeating until the potential reached 3.5 V (on charge) or 1.4 V (on the subsequent discharge).

Ionic and electronic conductivities were determined using pellets of $Na_3TiP_3O_9N$ that was synthesized without ascorbic acid (about 12.7 mm in diameter, 1.7 mm in thickness, and 85% dense) prepared by compression under a uniaxial force of 1000 to 4000 kg followed by sintering for 8 – 16 hrs at 600 ℃ under flowing NH_3. Gold contacts (~250 nm thick) were prepared on both sides of the pellet by sputter deposition (Denton Vacuum). The pellet was loaded into a Swagelok—type electrochemical cell, allowing Hebb-Wagner polarization data to be collected using Solartron SI1287 and SI1260 instruments. Cells were polarized at 20 mV for 18 hours, allowing sufficient amount of time for ions to be blocked at the gold contacts, a process followed by monitoring the current decay as a function of time. After polarization the cell was left at open circuit for 12 hours and the voltage decay was used to monitor the relaxation of the cell. Alternating current (ac) impedance measurements were also taken before and after polarization to check for consistency in conductivity calculations and to identify any changes in the cell resulting from polarization. Cells were scanned from 2 MHz to 100 mHz with a 20mV amplitude sweep. For the activation energy measurements, temperature dependent AC impedance

data were collected using a similar pellet of $Na_3TiP_3O_9N$ (about 12.7 mm in diameter / 2.5 mm thick) with contacts made by a thick Ag epoxy coating (~1 mm) applied to both faces of the pellet. The pellet was placed on a gold coated glass slide which was then heated on a hot plate. Temperatures at the top and bottom of the pellet were recorded using a thermocouple and averaged, with their temperature difference typically being less than 2°C. Data was collected both on heating (to 185 ℃) and cooling (to 75 ℃) using scans from 20 Hz to 2 MHz (5 mV amplitude) on an Agilent E4980A LCR Meter.

2.2.6 Electron microscopy

Scanning electron microscope (SEM) images were collected on a JEOL 7600 SEM operating at 5 KV in a low vacuum condition to minimize charging effects. Elemental-dispersive X-ray analysis (EDX) spectra of the as-prepared samples were collected on a JEOL 7600 SEM operating at 15 KV equipped with an Oxford EDX spectrometer. TEM images and electron diffraction patterns were recorded at 300 kV in a JEM-3000F transmission electron microscope equipped with a field emission gun and a Gatan Image Filter spectrometer.

2.2.7 Thermogravimetric analysis

Thermogravimetric analysis (TGA) was carried out between 25 ℃ and 700 ℃ on Q5000IR (TA instruments) system with a constant flow of oxygen gas (25 mL/min). A 3-4 mg sample was placed on a platinum pan and first stabilized at 50 ℃ for 2 hours to remove moisture potentially present in the powders, then heated to 700 ℃ at 2 ℃ / min, held at 700 ℃ for 4 hours, and finally cooled down to 25 ℃ in a symmetrical manner, allowing overall mass changes to be determined without requiring separate corrections for buoyancy effects when initial and final masses at equal temperatures were compared.

2.2.8 Bond valence sum maps

Bond valence sum (BVS) maps were calculated using a local computer program incorporating routines from the Crystallographic Fortran Modules Library[39]. In the BVS map calculation, the positions of oxygen and nitrogen were used to calculate the valence of Na within the unit cell using the softBV parameters provided by Adams[40]. Since the soft BVS parameters for N have not yet been determined, the nitrogen was given the same parameters as oxygen ions – a good approximation (hard BVS parameters for N give a valence contribution only 4% different from O at the same distance) that should

have negligible influence on the results since the N atoms were far from any potential Li or Na site. The absolute valence difference (ΔV) between the calculated bond valence of Li or Na at each point on a 3D grid within the unit cell and the ideal valence of 1 was then plotted as an isosurface in VESTA[41]. The likely ion diffusion pathways were estimated by increasing ΔV to the minimal values necessary to connect the mobile cation sites into a continuous network. Although there is not a simple relationship between valence and free energy, sites with higher valence differences do represent sites with higher free energies that require higher activation energies to access during diffusional processes. Although the BVS method does not include repulsions from neighboring cations, this method has been successfully applied to estimate the Li-ion diffusion pathways in $LiFePO_4$ and many other battery materials[42-45].

2.2.9 First-principles calculations

First-principles calculations were performed using the generalized gradient approximation (GGA-PBE) to density functional theory (DFT) and the Hubbard model extension (GGA+U) as implemented in the Vienna *ab initio* Simulation package (VASP)[46]. The effect of the core electrons on the valence states was treated with the projector augmented wave (PAW) method[47]. A plane wave energy cutoff of 600 eV was used. The *k*-point sampling within the Brillouin zone was performed with a 3×3×3 mesh for the primitive unit cell (containing a total 68 atoms). Equivalent *k*-point densities were used for supercells of the primitive unit cell. All calculations were performed using spin polarization with ferromagnetic ordering of the initial magnetic moments. GGA+U calculations were performed with the method of Dudarev *et al.* [48] with an effective Coulombic potential of U_{eff} = U - J (effectively, J = 0).

It was found that pure GGA calculations with U = 0 underestimated the average voltage by more than 1 V, which can be attributed to a large self-interaction error in GGA for localized electronic states. In contrast to simple oxides of Ti like TiO_2, the cubic structure and the isolated Ti octahedra within it are more likely to localize electronic states around Ti. By performing a systematic study of the dependence of the average voltage of the $Na_3TiN(PO_3)_3$–$Na_2TiN(PO_3)_3$ couple relative to a Na metal reference anode on the Hubbard U parameter, we determined that a value of U = 5.0 eV predicts an average voltage of 2.7 V, which is close to the experimentally measured average voltage. We used this value of U to further analyze phase stability and thermodynamic properties at room temperature. The energies of 5 different Na-vacancy arrangements over the Na1 sites of this structure were calculated within GGA+U. For each Na-vacancy configuration over the Na1 sites, we enumerated all

symmetrically distinct Ti^{3+}/Ti^{4+} arrangements and used these to initialize the DFT calculations (by initializing magnetic moments consistent with the particular Ti^{3+}/Ti^{4+} charge ordering). The lowest energy for each of the Na-vacancy configurations was then used to parameterize a cluster expansion[49,50] to describe the variation of the fully relaxed energy with Na-vacancy arrangement. Due to the large distance between neighboring Na1 sites, the cluster expansion Hamiltonian only includes pair, triplet and quadruplet clusters extending up to the first-nearest neighbor cell. Grand canonical Monte Carlo simulations were applied to the cluster expansion to predict the equilibrium voltage curve (which is related to negative of the Na chemical potential). Migration barriers for Na hops to vacant neighboring sites were calculated with the nudged elastic band method as implemented in VASP using both GGA and GGA+U methods.

2.3 Results and discussion

2.3.1 Synthesis and sodium ion removal

$Na_3TiP_3O_9N$ powders were prepared by a single-step solid state reaction under flowing ammonia gas similar to the method originally described by Marchand *et al.* [28], but with the addition of ascorbic acid to minimize or eliminate the amount of nitrogen-free impurities (typically of the $NaTi_2(PO_4)_3$ NASICON-type structure) that would otherwise form. Rietveld refinements of synchrotron X-ray and time-of-flight (TOF) neutron powder diffraction data confirmed the space group ($P2_13$, #198) and cation stoichiometry (nearly 3:1) expected for this structure type (details in Figures 2.2 and 2.3). The structure of this compound consists of TiO_6 octahedra which are linked by trimers of PO_3N tetrahedra that share a central N ion and together form a rigid $[P_3O_9N]^{6-}$ polyanion unit, as can be seen in Figure 2.1. Potentially mobile Na ions are found within open spaces inside the framework constructed from the TiO_6 octahedra and P_3O_9N tetrahedral trimers. Three different types of sodium sites are present in this structure, with equal abundances but with very different coordination environments despite the fact that all the Na sites are situated on 3-fold rotation axes. Na1 sits at the center of a NaO_6 trigonal prism, Na2 occupies a distorted octahedron formed by six oxygen atoms, and Na3 is closely coordinated by three oxygens (2.4 Å) with six more oxygen atoms at much longer distances (3.0 and 3.1 Å) that are at best weakly bound. The valences of Na1, Na2 and Na3 were calculated to be 0.67, 1.03, 0.72, respectively, by hard BVS methods.[51] This suggests that Na ions at Na1 and Na3 sites are weakly bound and should be quite mobile at elevated temperatures if a diffusion pathway exists. This weak bonding was

experimentally confirmed by the observation of large sodium thermal displacement values at Na1 and Na3 sites in Rietveld refinements, shown in Figure 2.2 and discussed in more detail later.

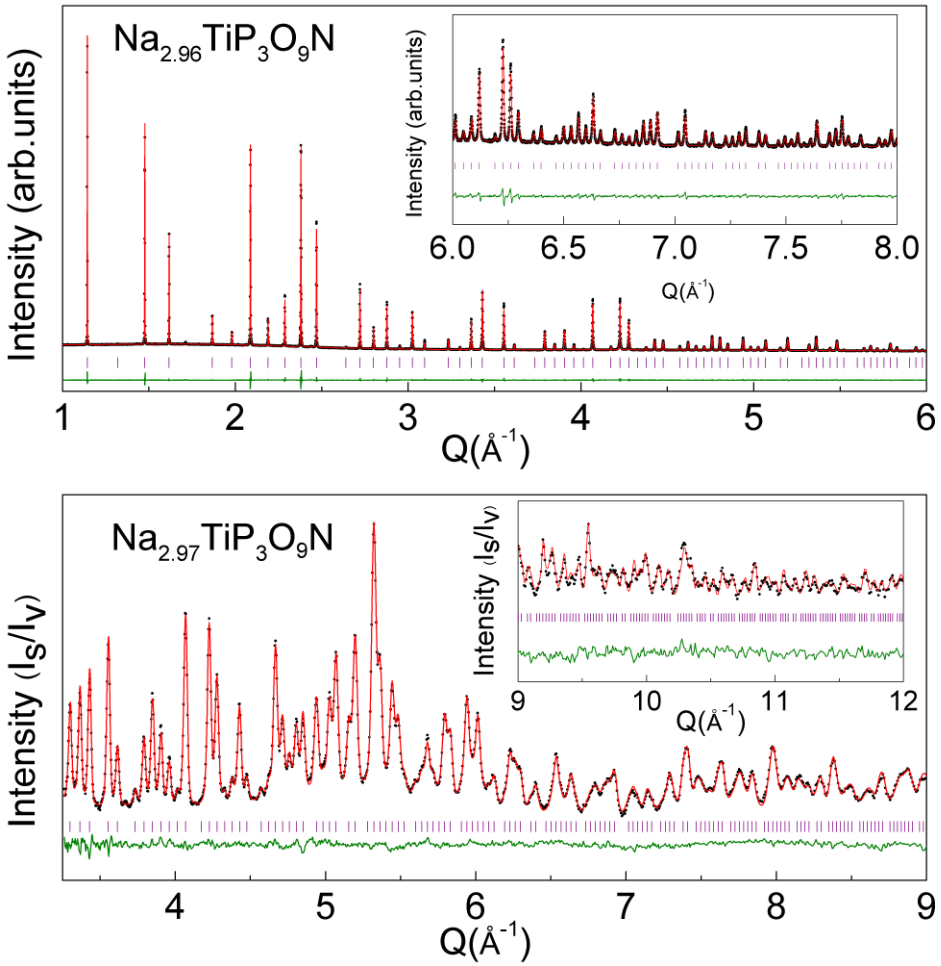

Figure 2.2 Rietveld refinement of $Na_3TiP_3O_9N$ using synchrotron XRD data (λ = 0.7788 Å, top) and TOF neutron diffraction data (2θ = 154 °bank, bottom) with experimental data in black dots, calculated pattern in red, tick marks indicating Bragg reflections in purple, and difference curves in green.

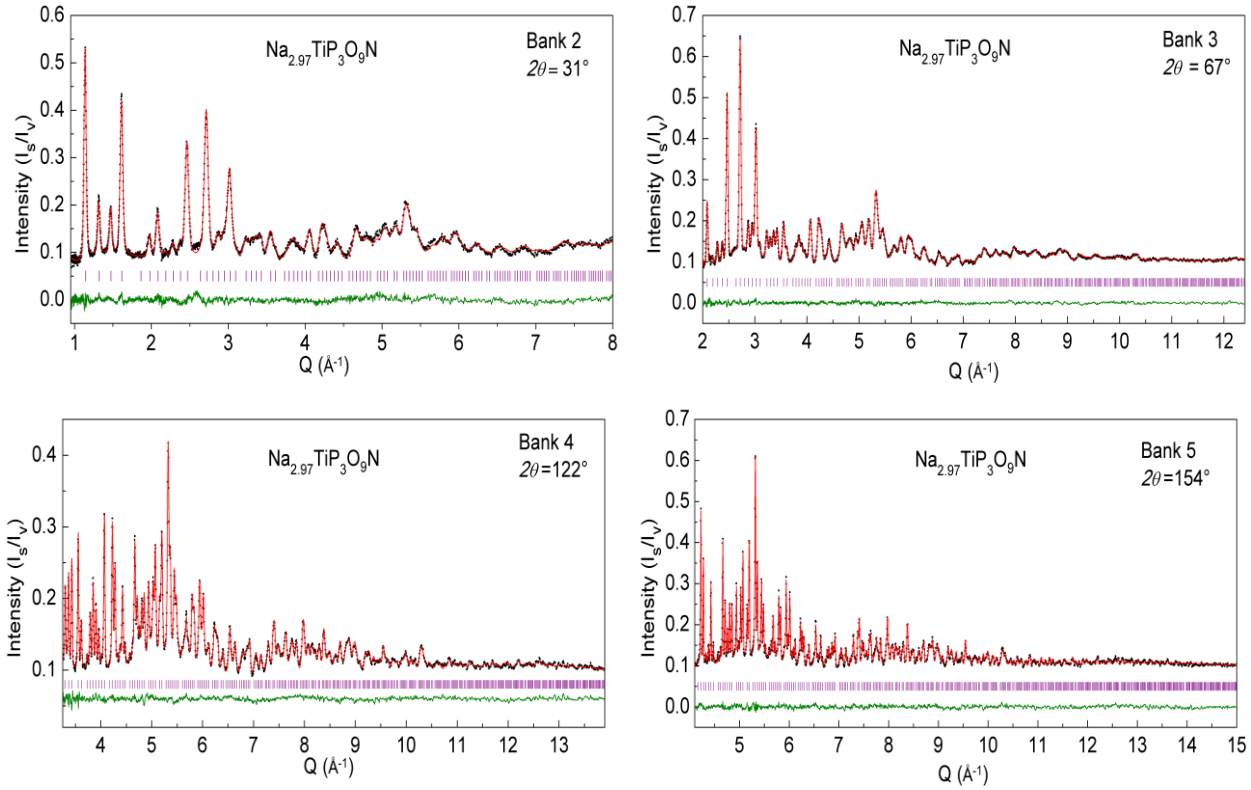

Figure 2.3 Rietveld refinement of $Na_3TiP_3O_9N$ structure with TOF neutron diffraction data.

The removal of sodium from this structure and the concomitant oxidation of Ti^{3+} to Ti^{4+} could be chemically driven by reacting $Na_3TiP_3O_9N$ with NO_2BF_4 in acetonitrile. In contrast to $Na_2Fe_2P_3O_9N$ (which requires elevated temperatures of almost 300 °C for the complete removal of Na ions), the essentially complete removal of Na could be accomplished at room temperature in $Na_3TiP_3O_9N$, indicating a large enhancement in Na-ion mobility relative to $Na_2Fe_2P_3O_9N$.[27] The robustness of the $Na_3TiP_3O_9N$ lattice during this process of chemical desodiation is demonstrated by a comparison of the powder XRD patterns of $Na_3TiP_3O_9N$, $Na_{2.5}TiP_3O_9N$, and $Na_2TiP_3O_9N$, which exhibit the same cubic structure before and after Na removal as shown in Figures 2.4. The (002) peak and (022) peak intensities are particularly sensitive to the changes in Na occupancy. The change in Ti oxidation state during Na-ion removal was reflected both in changes in sample color (violet -> gray -> white) and in the shifts in the position of the Ti *K*-edge seen in XANES spectra (Figure 2.5).

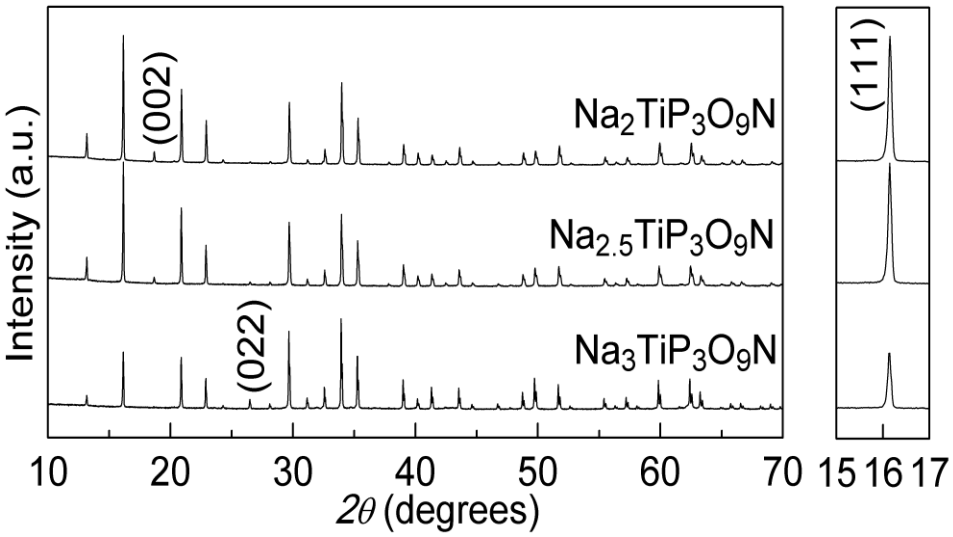

Figure 2.4 XRD patterns of $Na_{2+x}TiP_3O_9N$ (x = 0, 0.5, 1.0) phases formed by chemical desodiation.

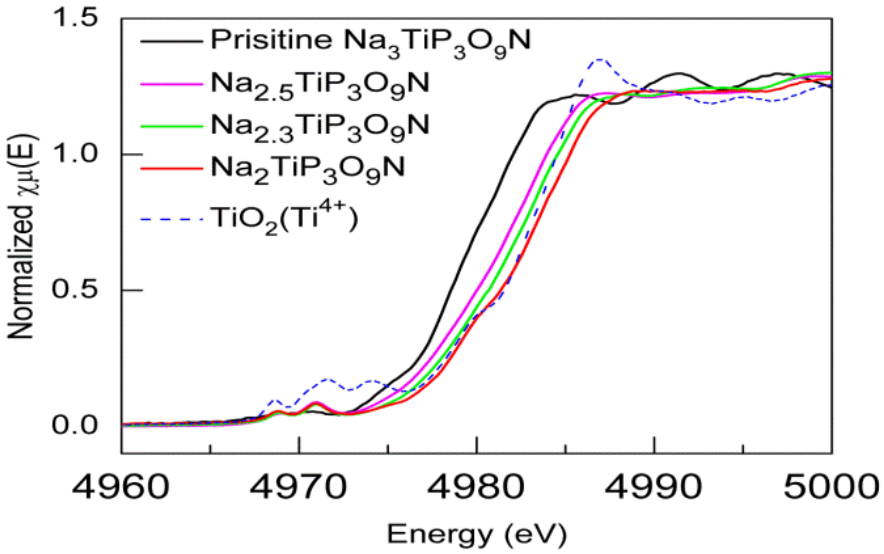

Figure 2.5 Ti *K*-edge XANES spectra compared to a Ti^{4+} reference, TiO_2.

The stoichiometry of these $Na_{3-x}TiP_3O_9N$ ($0 \leq x \leq 1$) samples were more precisely investigated through the Rietveld refinement of high resolution synchrotron (x = 0, 0.5, 1.0) and time-of-flight neutron (x = 0, 1) diffraction data. The full observed and modeled spectra, data collection parameters, atomic site information, and relevant bond distances are provided in the Figures 2.6 to 2.8, Tables 2.1 to 2.7), and will be discussed in more detail when the cycling mechanism of this system is discussed. From

these, it is found that the Na1 site is depopulated during the chemical desodiation process. First-principles density functional theory calculations done both within the generalized gradient approximations (GGA) and with a Hubbard model extension (GGA+*U*) similarly found that Na vacancies are most stable at the Na1 site. Placing the vacancies in the other sodium sites increases the energy by 210 meV (Na2) or 180 meV (Na3) per formula unit, as can be seen in Figure 2.9.

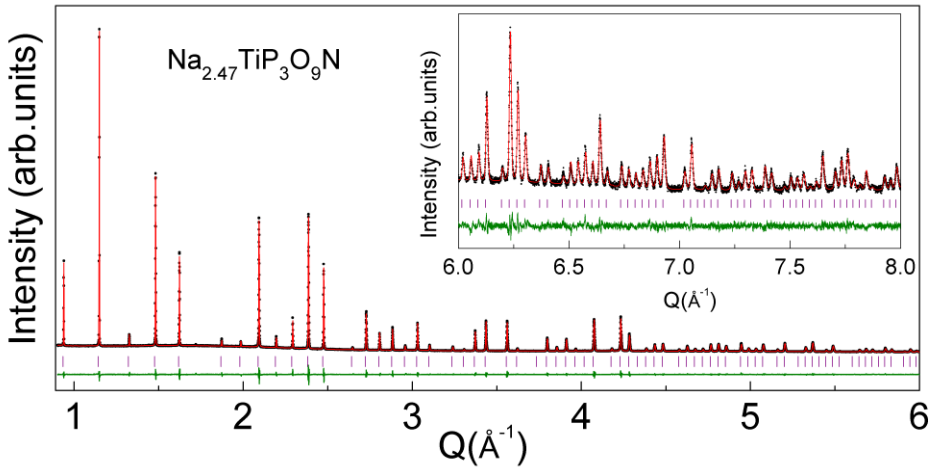

Figure 2.6 Rietveld refinement of $Na_{2.5}TiP_3O_9N$ structure using synchrotron XRD data (λ = 0.77767Å).

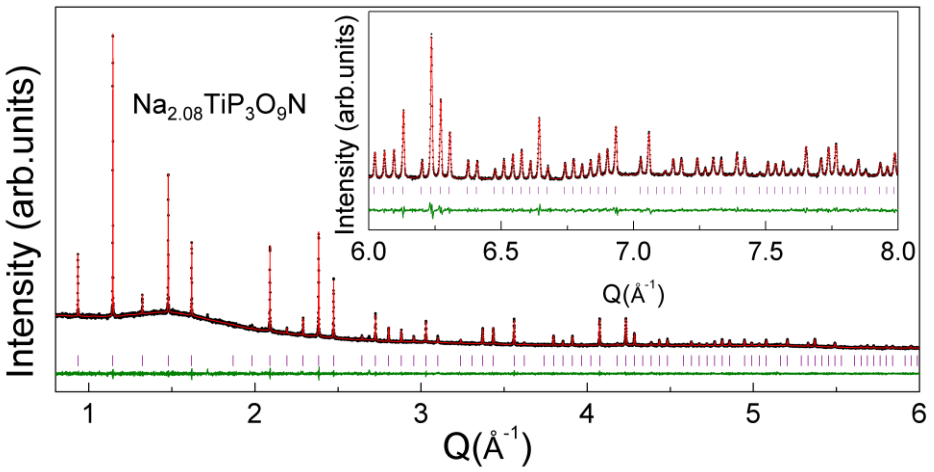

Figure 2.7 Rietveld refinement of $Na_2TiP_3O_9N$ structure using synchrotron XRD data (λ = 0.77875 Å).

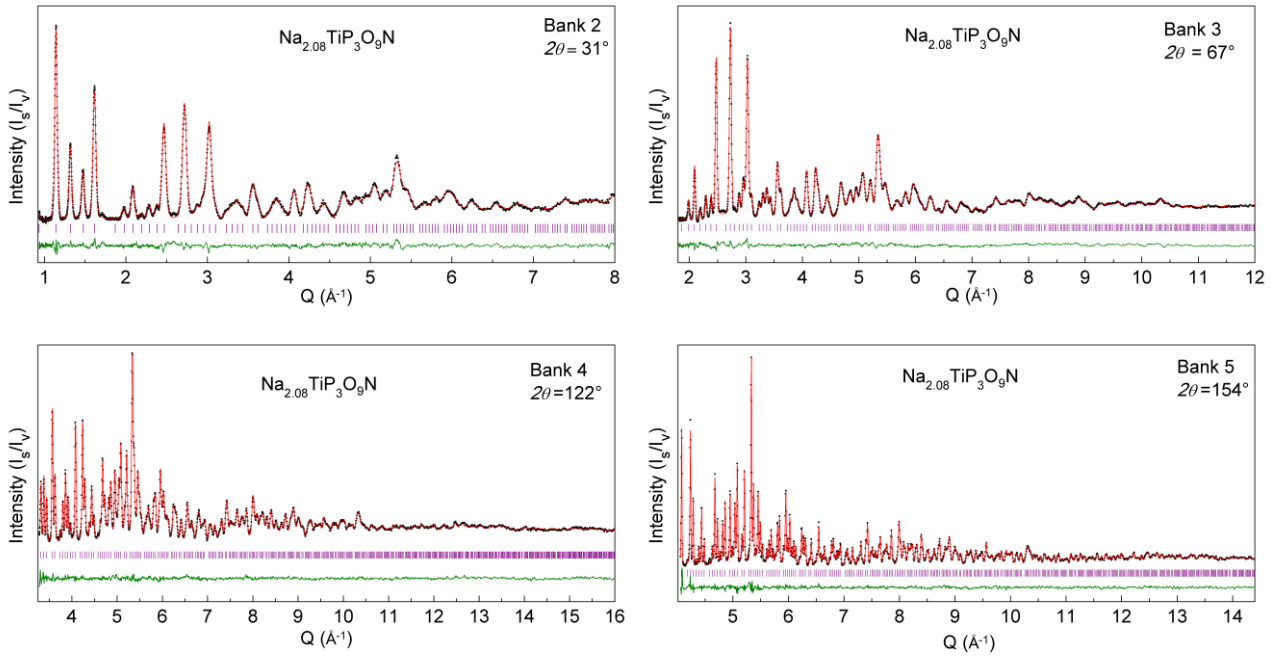

Figure 2.8 Rietveld refinement of $Na_2TiP_3O_9N$ structure using TOF neutron diffraction data.

Table 2.1 Summary of Rietveld refinement results

Radiation	XRD	XRD	XRD	TOF neutron	TOF neutron
λ	0.77878 Å	0.77767Å	0.77875 Å	0.1-3 Å	0.1-3 Å
Formula	$Na_{2.96}TiP_3O_9N$	$Na_{2.47}TiP_3O_9N$	$Na_{2.08}TiP_3O_9N$	$Na_{2.97}TiP_3O_9N$	$Na_{2.08}TiP_3O_9N$
Crystal system	Cubic	Cubic	Cubic	Cubic	Cubic
Space group	*$P2_13(198)$*	*$P2_13(198)$*	*$P2_13(198)$*	*$P2_13(198)$*	*$P2_13(198)$*
Lattice a	9.5192 (3) Å	9.5161 (4) Å	9.5046 (2) Å	9.5180 (2) Å	9.5092 (2) Å
Cell volume	862.58 (7) $Å^3$	861.74 (11) $Å^3$	858.60 (6) $Å^3$	862.26 (5) $Å^3$	859.86 (5) $Å^3$
R_{wp}	2.81%	3.68%	4.45%	2.34%	2.64%
R_p	1.88%	2.56%	2.60%	2.15%	1.59%
χ^2	3.50	3.99	3.75	1.21	1.66

Table 2.2 Rietveld refinement results for $Na_3TiP_3O_9N$ using TOF neutron diffraction data measured at 300 K in Ar (NOMAD, SNS).

Atom	Wyck.	*x*	*y*	*z*	Occ.	B_{eq} (Å^2)
Na1	4a	0.01129(34)	0.01129(34)	0.01129(34)	0.966(37)	2.49
Na2	4a	0.39430(27)	0.39430(27)	0.39430(27)	1	1.49
Na3	4a	0.80249(36)	0.80249(36)	0.80249(36)	1	2.99
Ti1	4a	0.58186(25)	0.58186(25)	0.58186(25)	1	0.95
P1	12b	0.08461(16)	0.24474(15)	0.33282(18)	1	0.74
O1	12b	0.02187(14)	0.84785(14)	0.23148(13)	1	1.12
O2	12b	0.00640(15)	0.11152(14)	0.37448(14)	1	1.26
O3	12b	0.16837(15)	0.30919(18)	0.45015(14)	1	1.43
N1	4a	0.19905(9)	0.19905(9)	0.19905(9)	1	0.79

Atom	U_{11}(Å^2)	U_{22}(Å^2)	U_{33}(Å^2)	U_{12}(Å^2)	U_{13}(Å^2)	U_{23}(Å^2)
Na1	0.0348(24)	0.0348(24)	0.0348(24)	0.0210(29)	0.0210(29)	0.0210(29)
Na2	0.0209(16)	0.0209(16)	0.0209(16)	0	0	0
Na3	0.0459(25)	0.0459(25)	0.0459(25)	0.0247(35)	0.0247(35)	0.0247(35)
Ti1	0.0131(12)	0.0131(12)	0.0131(12)	0.0045(13)	0.0045(13)	0.0045(13)
P1	0.0136(12)	0.0064(11)	0.0095(12)	0.0024(8)	0.0007(7)	-0.0007(7)
O1	0.0158(12)	0.0140(13)	0.0153(12)	-0.0102(8)	0.0012(8)	-0.0034(8)
O2	0.0153(12)	0.0120(12)	0.0157(13)	-0.0015(7)	0.0014(8)	0.0028(7)
O3	0.0207(14)	0.0280(15)	0.0110(11)	-0.0050(9)	-0.0011(8)	-0.0045(9)
N1	0.0107(8)	0.0107(8)	0.0107(8)	-0.0008(4)	-0.0008(4)	-0.0008(4)

Table 2.3 Rietveld refinement results for $Na_3TiP_3O_9N$ using synchrotron X-ray diffraction data measured at 300 K in air. (X14A, NSLS).

Atom	Wyck.	*x*	*y*	*z*	Occ.	B_{eq} (Å^2)
Na1	4a	0.01231(18)	0.01231(18)	0.01231(18)	0.963(10)	1.61(13)
Na2	4a	0.39364(21)	0.39364(21)	0.39364(21)	1	1.53(11)
Na3	4a	0.80348(25)	0.80348(25)	0.80348(25)	1	1.93(10)
Ti1	4a	0.58129(8)	0.58129(8)	0.58129(8)	1	0.59(8)
P1	12b	0.08636(12)	0.24551(13)	0.33344(13)	1	0.52(8)
O1	12b	0.02168(26)	0.84884(27)	0.23382(40)	1	1.01(10)
O2	12b	0.00552(30)	0.11398(27)	0.37635(27)	1	0.77(10)
O3	12b	0.16837(27)	0.30995(26)	0.44508(43)	1	0.90(10)
N1	4a	0.19893(32)	0.19893(32)	0.19893(32)	1	0.57(20)

Table 2.4 Rietveld refinement results for $Na_{2.5}TiP_3O_9N$ using synchrotron X-ray diffraction data measured at 300 K in air. (X14A, NSLS).

Atom	Wyck.	*x*	*y*	*z*	Occ.	B_{eq} (Å^2)
Na1	4a	0.01408(55)	0.01408(55)	0.01408(55)	0.474(10)	2.96(29)
Na2	4a	0.39080(23)	0.39080(23)	0.39080(23)	1	2.33(16)
Na3	4a	0.80829(24)	0.80829(24)	0.80829(24)	1	1.97(13)
Ti1	4a	0.58318(10)	0.58318(10)	0.58318(10)	1	0.68(11)
P1	12b	0.08461(14)	0.24248(15)	0.33057(14)	1	0.58(11)
O1	12b	0.02430(30)	0.83715(32)	0.24097(39)	1	0.75(13)
O2	12b	0.00869(31)	0.10782(44)	0.37752(38)	1	0.77(10)
O3	12b	0.16696(32)	0.30557(33)	0.44779(34)	1	0.97(13)
N1	4a	0.19730(36)	0.19730(36)	0.19730(36)	1	1.25(19)

Table 2.5Rietveld refinement results for $Na_2TiP_3O_9N$ using TOF neutron diffraction data measured at 300 K in Ar (NOMAD, SNS).

Atom	Wyck.	*x*	*y*	*z*	Occ.	B_{eq} (Å^2)
Na1	4a	0.0064(27)	0.0064(27)	0.0064(27)	0.085(4)	2.17(98)
Na2	4a	0.39123(20)	0.39123(20)	0.39123(20)	1	1.10
Na3	4a	0.81376(23)	0.81376(23)	0.81376(23)	1	2.33
Ti1	4a	0.58474(21)	0.58474(21)	0.58474(21)	1	1.10
P1	12b	0.08461(14)	0.23983(12)	0.32989(14)	1	0.62
O1	12b	0.02576(11)	0.83577(12)	0.23872(10)	1	0.94
O2	12b	0.00893(12)	0.10335(11)	0.37382(11)	1	0.89
O3	12b	0.16634(12)	0.30500(13)	0.44710(11)	1	1.40
N1	4a	0.19616(7)	0.19616(7)	0.19616(7)	1	0.72

Atom	U_{11}(Å^2)	U_{22}(Å^2)	U_{33}(Å^2)	U_{12}(Å^2)	U_{13}(Å^2)	U_{23}(Å^2)
Na1	-	-	-	-	-	-
Na2	0.0139(11)	0.0139(11)	0.0139(11)	0	0	0
Na3	0.0296(13)	0.0296(13)	0.0296(13)	0.0053(19)	0.0053(19)	0.0053(19)
Ti1	0.0140(10)	0.0140(10)	0.0140(10)	0.0013(11)	0.0013(11)	0.0013(11)
P1	0.0104(9)	0.0063(8)	0.0069(8)	-0.0008(4)	-0.0002(5)	-0.0021(6)
O1	0.0127(8)	0.0134(1)	0.0095(8)	-0.0061(5)	-0.0002(6)	-0.0022(7)
O2	0.0112(8)	0.01096(9)	0.0118(8)	-0.0053(4)	0.0016(7)	0.0005(6)
O3	0.0194(11)	0.0229(10)	0.0109(8)	-0.0067(6)	-0.0039(7)	-0.0035(7)
N1	0.0090(4)	0.0090(4)	0.0090(4)	0.0011(4)	0.0011(4)	0.0011(4)

Table 2.6 Rietveld refinement results for $Na_2TiP_3O_9N$ using synchrotron X-ray diffraction data measured at 300 K in air (X14A, NSLS).

Atom	Wyck.	*x*	*y*	*z*	Occ.	B_{eq} (Å^2)
Na1	4a	0.01232(18)	0.0026(35)	0.0026(35)	0.085*	2.17*
Na2	4a	0.39090(25)	0.39090(25)	0.39090(25)	1	1.51(15)
Na3	4a	0.81422(32)	0.81422(32)	0.81422(32)	1	1.80(15)
Ti1	4a	0.58518(10)	0.58518(10)	0.58518(10)	1	0.49(13)
P1	12b	0.08541(15)	0.23998(11)	0.33038(15)	1	0.43(14)
O1	12b	0.02451(40)	0.83665(45)	0.23960(42)	1	0.67(15)
O2	12b	0.00848(40)	0.10458(41)	0.37511(42)	1	0.68(14)
O3	12b	0.16587(47)	0.30312(46)	0.44508(43)	1	1.21(16)
N1	4a	0.19524(51)	0.19524(51)	0.19524(51)	1	0.57(20)

* fixed to refinement result of neutron diffraction data

Table 2.7 Selected bond distances (Å) for $Na_3TiP_3O_9N$, $Na_{2.5}TiP_3O_9N$ and $Na_2TiP_3O_9N$.

	$Na_{2.96}TiP_3O_9N$ (XRD)	$Na_{2.97}TiP_3O_9N$ (TOF neutron)	$Na_{2.5}TiP_3O_9N$ (XRD)	$Na_{2.08}TiP_3O_9N$ (XRD)	$Na_{2.08}TiP_3O_9N$ (TOF neutron)
Na1 – O1 (×3)	2.6220(34)	2.6120(14)	2.7397(35)	2.7661(83)	2.7480(61)
Na1 – O3 (×3)	2.6091(33)	2.5998(44)	2.6527(74)	2.577(41)	2.559(32)
Na1 – N	3.0767(60)	3.0953(58)	3.020(11)	3.112(58)	3.130(45)
Na2 – O2 (×3)	2.4358(36)	2.4465(36)	2.4737(46)	2.4832(44)	2.4991(28)
Na2 – O3 (×3)	2.3464(33)	2.3586(31)	2.3429(38)	2.3545(43)	2.3512(23)
Na3 – O1 (×3)	3.0697(43)	3.0473(52)	3.0723(45)	3.1071(48)	3.1257(34)
Na3 – O3 (×3)	2.3765(38)	2.3715(40)	2.3332(40)	2.3096(43)	2.2834(24)
Ti – O1 (×3)	1.9642(36)	1.9824(25)	1.9207(36)	1.8985(36)	1.9245(21)
Ti – O2 (×3)	2.0344(27)	2.0190(30)	1.9865(41)	1.9688(34)	1.9684(25)
P – O1	1.5614(31)	1.5378(21)	1.5327(35)	1.5449(37)	1.5361(17)
P – O2	1.5256(29)	1.5229(20)	1.5374(41)	1.5355(35)	1.5416(16)
P – O3	1.4792(30)	1.5030(21)	1.4896(35)	1.4723(40)	1.4935(17)
P – N	1.7274(15)	1.7311(17)	1.7155(17)	1.7133(18)	1.7073(13)

An intriguing feature of the $Na_{3-x}TiP_3O_9N$ X-ray diffraction patterns is the nearly imperceptible shifts in peak positions during the desodiation process. A Le Bail fitting of laboratory XRD lattice parameters shows a volume change of -0.16% after deintercalation of 0.5 Na and -0.54% after deintercalation of 1.0 Na (Table 2.8). This cubic Na-ion framework approaches the zero volume change observed for the cubic Li anode spinel, $Li_{4/3}Ti_{5/3}O_4$ [52], a remarkable result given that Na ions have an ionic volume about 150% larger than Li ions (4.4 *vs.* 2.4 Å^3). The observed small volume changes are

in good agreement with theory as GGA+*U* calculations predict a volume change of -0.6% upon removal of Na from $Na_3TiP_3O_9N$ to form $Na_2TiP_3O_9N$ (Figure 2.9). Since the cycling-induced development of stresses and subsequent cracking can be a major failure mechanism in systems with large volumetric changes, it is expected that the present system could be very suitable for extended cycling applications if other failure mechanisms (*ie* those associated with surface reactions) in the electrochemical cell can be identified and eliminated. Small volume changes are also very desirable for all solid state batteries, which would further benefit from the isotropic nature of this structure type.

Table 2.8 Volume changes on desodiation of $Na_3TiNP_3O_9N$

Compound	*a (Å)*	*V(Å^3)*	*ΔV*
$Na_{2.96}TiP_3O_9N$	9.5219(1)	863.33(1)	
$Na_{2.47}TiP_3O_9N$	9.5170(3)	861.98(7)	-0.16%
$Na_{2.08}TiP_3O_9N$	9.5048(1)	858.69(1)	-0.54%

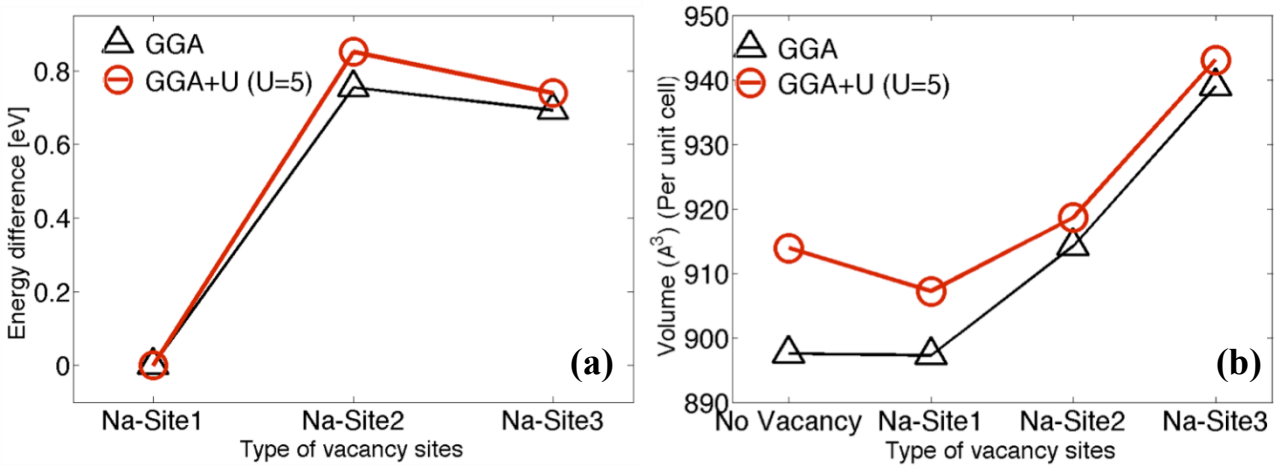

Figure 2.9 Calculated free energy (a) and volume change (b) associated with Na removal from each of the three crystallographic sites of $Na_3TiP_3O_9N$ (energies and volumes are per primitive unit cell containing four $Na_3TiP_3O_9N$ formula units).

2.3.2 $Na_3TiP_3O_9N$ as a Na-ion battery cathode

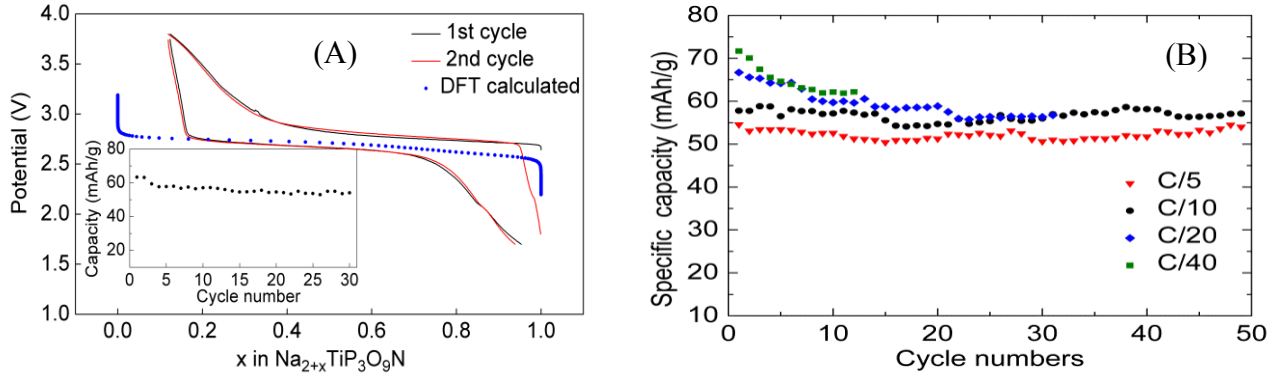

Figure 2.10 (A) Electrochemical performance of $Na_3TiP_3O_9N$ cathodes cycled against Na metal. The voltage (*vs.* Na^+/Na) charge-discharge curve of $Na_3TiP_3O_9N$ was obtained at C/20. The thermodynamic charge-discharge curve predicted by DFT calculation is overlaid (blue dotted symbols). (B) $Na_3TiP_3O_9N$ cycled against Na^+/Na at different C rates as seen in specific capacities during discharge.

The complete oxidation of $Na_3TiP_3O_9N$ during chemical desodiation and the extremely small volume change of the open cubic framework of this phase during this process indicate that $Na_3TiP_3O_9N$ may be an excellent electrode material for Na-ion batteries. Indeed, it was determined that $Na_3TiP_3O_9N$ can be very effectively cycled against a Na metal electrode using an electrolyte of 1M $NaClO_4$ in 3:7 EC/DMC with a promising Na-ion rate performance and reversibility with an average voltage of about 2.7 V vs. Na^+/Na, as shown in Figure 2.10. At a charge/discharge rate of C/20, a discharge capacity of 67 mAh/g (91% of the theoretical capacity of 74 mAh/g) is achieved in the first cycle, with discharge capacities stabilizing at 50 – 60 mAh/g over the subsequent 50 cycles, depending on the charging rate. Unlike many other Na-ion systems, no intermediate plateaus are observed during charge/discharge. This is likely a consequence of the worm-like diffusion channels within this material, which lead to a higher degree of screening of Na^+ ions from each other, thus inhibiting the formation of Coulombically stabilized intermediate phases with different types of Na-ion ordering during charge/discharge cycles. While relatively small polarization was observed in the middle of the charge/discharge curves, higher polarization was observed near the ends of these curves. This is attributed to kinetic limitations in accessing the center of particles due to limitations in the timescale of ionic or electronic conduction. IT should also be noticed that the Na^+ ionic diffusivity decreased tremendously after appreciable amount sodium ions are extracted, as can be seen in Figure 2.11b. This assignment is confirmed by GITT

experiments, which clearly demonstrate that the system relaxes to voltages close to the average potential when the system is allowed to fully equilibrate.

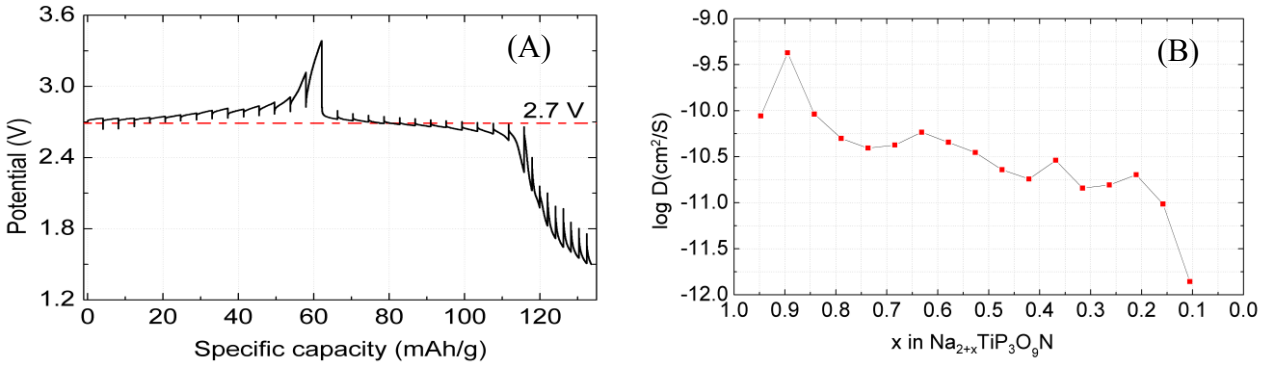

Figure 2.11 (A) GITT curve of $Na_3TiP_3O_9N$ cathode cycled against Na metal. (B) Calculated apparent chemical diffusion coefficient as a function of sodium concentration in $Na_{3-x}TiP_3O_9N$ during charge.

This is also consistent with the reduction in accessible capacity when the cycling rate is increased from C/40 to C/5. The typical particle size of $Na_3TiP_3O_9N$ observed in SEM experiments (Figure 2.12) and TEM experiments (Figure 2.13) was on the order of 1 -5 microns in diameter and 0.5 microns in the minimum dimension, suggesting that there is an opportunity to improve the electrochemical performance of this system if improved syntheses which reduce the particle size can be developed. The presence of facets on these particles suggests that partial melting of precursors may occur during the synthesis, and that smaller particle sizes cannot be achieved without switching to precursors (or reaction conditions) that promote higher melting point.

Since no evidence of a plateau is seen in the GITT data, it is concluded that the cycling occurs through a solid solution rather than a two-phase mechanism. The mechanism can be further explored through density functional theory. The voltage profile of $Na_3TiP_3O_9N$ was calculated from Monte Carlo simulations performed on a cluster expansion Hamiltonian describing the energy of Na-vacancy disorder parameterized by GGA+U total energy calculations. At zero Kelvin, GGA+U calculations predict that that there will be ordering of the Na vacancies (on Na1 sites) in partially desodiated samples resulting in a two-phase reaction mechanism at this temperature. However, this vacancy ordered structure has only slightly positive formation energies relative to $Na_2TiP_3O_9N$ and $Na_3TiP_3O_9N$, and as a result, Monte Carlo simulations predict that solid-solution behavior with a slightly sloping voltage

profile should be seen at room temperature, (blue dots, Figure 2.10A), behavior which is indeed observed in experimental GITT measurements.

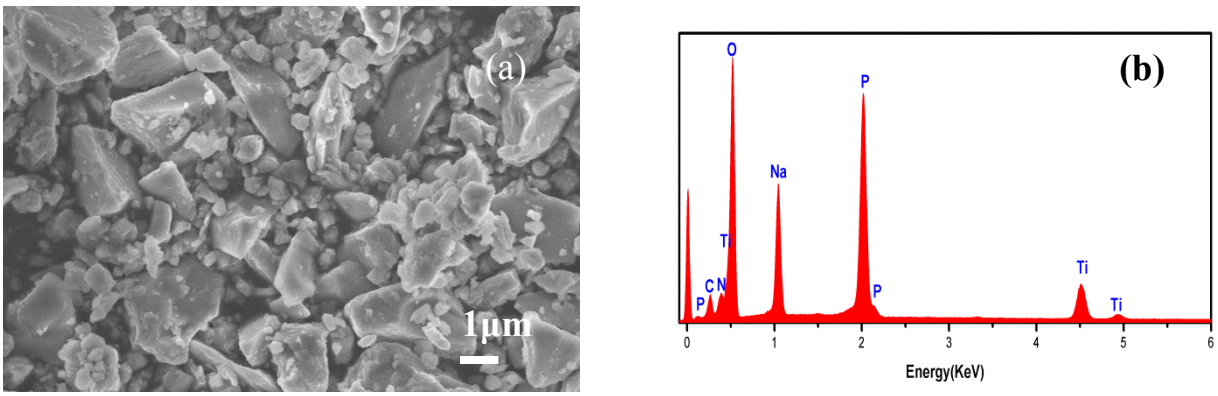

Figure 2.12 (a) SEM image and (b) EDX pattern of the as-prepared $Na_3TiP_3O_9N$.

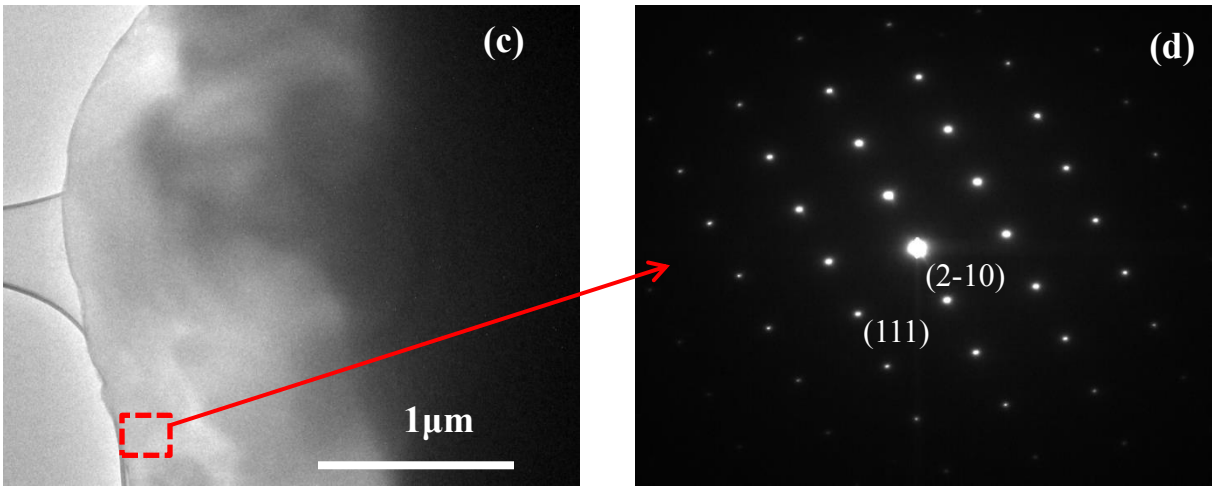

Figure 2.13 (a) TEM image and (d) selected area electron diffraction (SAED) pattern from as-prepared $Na_3TiP_3O_9N$ powder.

2.3.3 Ionic conductivity studies

2.3.3.1 Conductivity measurements

The facile chemical desodiation and reversible electrochemical cycling of $Na_3TiP_3O_9N$ suggests that the ionic conductivity within this structural framework may be good. The possibility of achieving high Na^+ ion conductivity within an isotropic cubic framework is especially intriguing, as there are not many

existing materials with this combination of properties, though some promising oxide and oxoanion cubic frameworks have previously been screened for this purpose.[16] The Na^+ mobility within the $Na_3TiP_3O_9N$ CUBICON structure was first studied by dc polarization measurements on sintered pellets (~85% dense) of $Na_3TiP_3O_9N$ with gold blocking electrodes (Figure 2.14). The current decayed by more than 98% after relaxation, indicating that the ionic conductivity (σ_I = 4.2 x 10^{-7} S/cm) of pristine $Na_3TiP_3O_9N$ far exceeds its electronic conductivity (σ_e = 6.8 × 10^{-9} S/cm) at room temperature. This ionic conductivity is quite substantial, and it is likely that the framework ionic conductivity can be enhanced considerably by the intentional introduction of Na vacancies, or by substitutions on the transition metal site. The electronic conductivity for this compound is somewhat low in a manner reminiscent of phosphate battery electrode materials. During cycling, the electrical conductivity is expected to somewhat increase relative to the integer valence pristine material, but will likely remain the limiting factor for cycling rates due to the lack of direct metal-oxygen-metal linkages between transition metal sites.

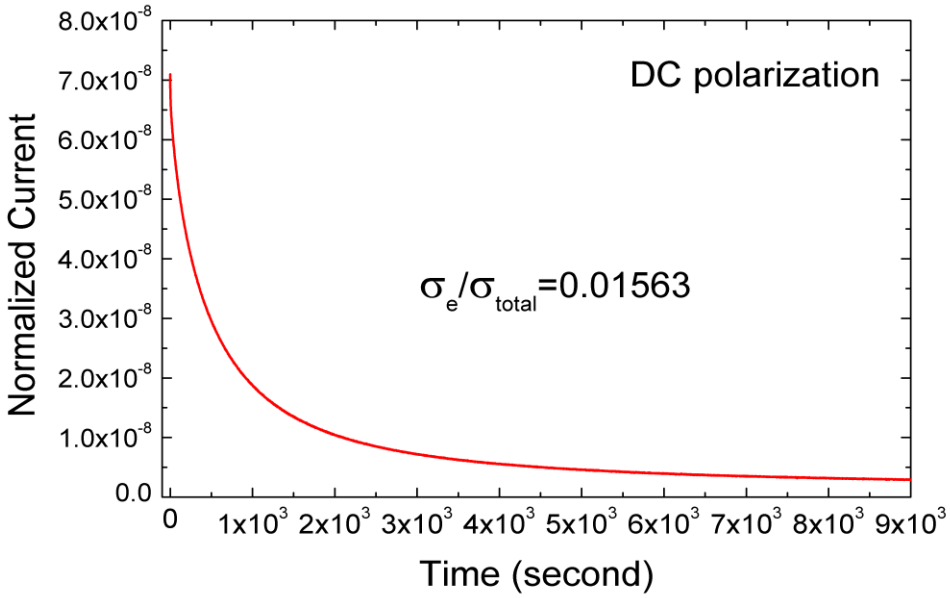

Figure 2.14 Decay of dc current for $Na_3TiP_3O_9N$ polarized at 20 mV.

Further insights into the ionic conductivity of $Na_3TiP_3O_9N$ were obtained from ac impedance measurements (Figure 2.15). The data at all temperatures were well modeled using an equivalent circuit previously proposed for solids with primarily ionic conductivity[53], and represent an upper limit for the bulk conductivity since the actual sample contains abundant grain boundaries which may also

contributed to the overall conductivity. The fit process is described in more detail in the Figure 2.16 and Table 2.9. The temperature dependence of conductivity followed a modified Arrhenius form of $\sigma T = \sigma_0 \mathrm{Exp}(-E_a/k_B T)$ with an activation energy of 0.54 eV (52 kJ/mol). The total conductivity was found to be 2.5×10^{-7} S/cm at 30 ℃ and 4.0×10^{-5} S/cm at 163 ℃. This conductivity is similar to that observed for some NASICON-type $NaM_2(PO_4)_3$ compounds[54], though it is about 2 orders of magnitude lower than for fully optimized NASICON $Na_3Zr_2PSi_2O_{12}$[16]. It is expected that the conductivity of the CUBICON framework can be similarly optimized by substitution (aliovalent doping to increase the vacancy content, or isovalent doping to tune the size of the diffusion channels). Furthermore, our prior studies on $Li_xFe_2P_3O_9N$ found that Li is substantially more mobile than Na within this framework[27], suggesting that Li conductivity in the CUBICON framework may be increased by a few orders of magnitude, and might potentially permit the observation of Li superionic conduction.

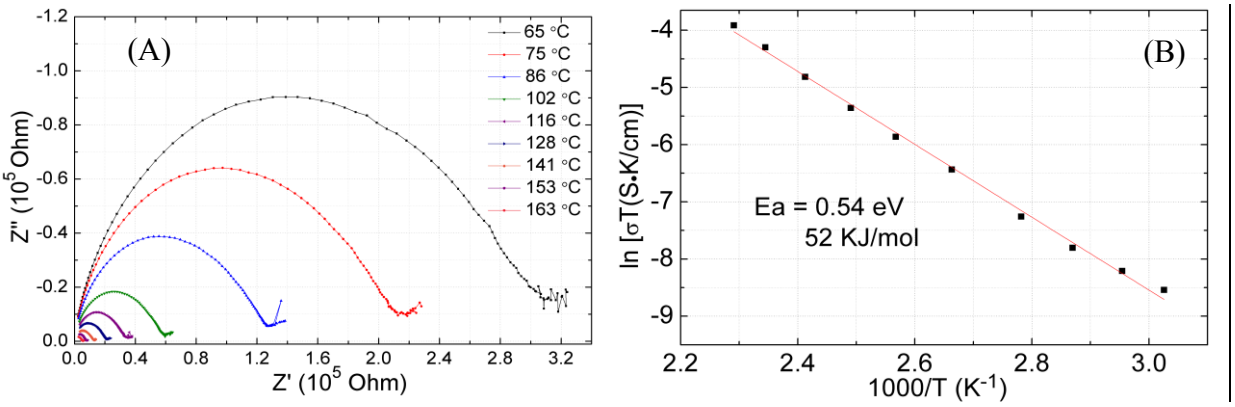

Figure 2.15 (A) $Na_3TiP_3O_9N$ ac impedance spectra and (B) the Arrhenius behavior of the derived activation energy.

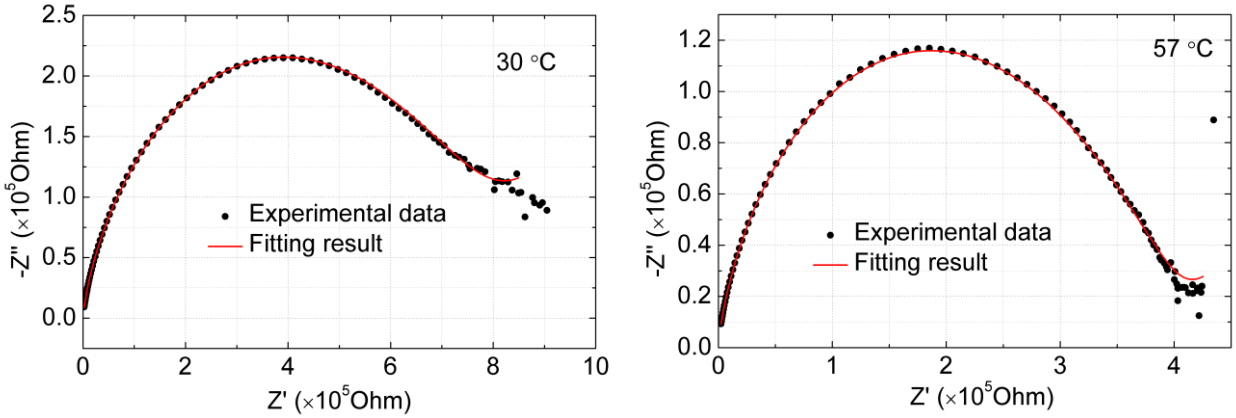

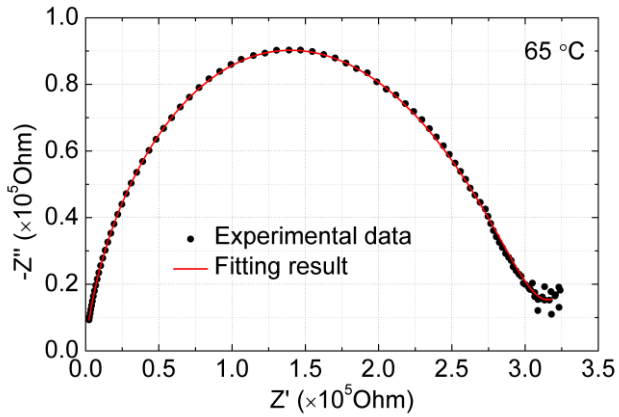
65 °C
Experimental data
Fitting result
-Z'' (×10^5Ohm)
Z' (×10^5Ohm)

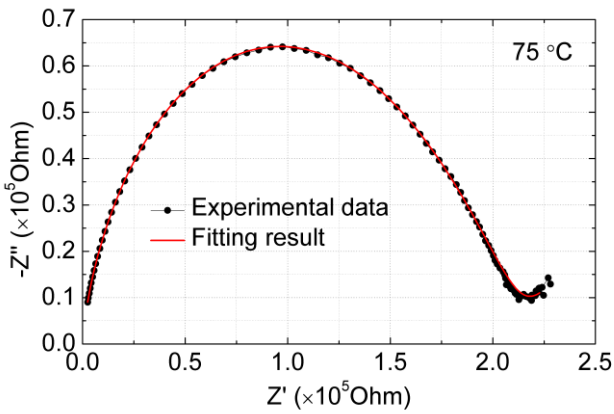
75 °C
Experimental data
Fitting result
-Z'' (×10^5Ohm)
Z' (×10^5Ohm)

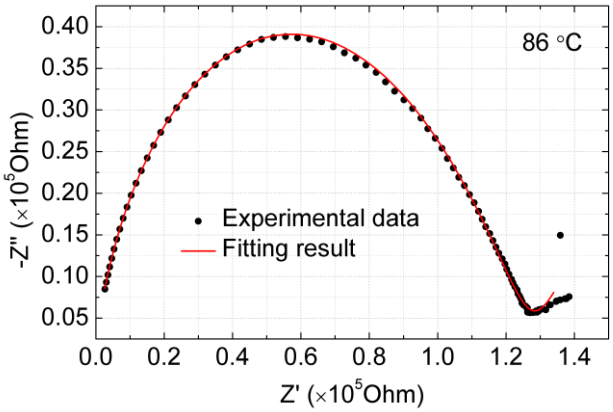
86 °C
Experimental data
Fitting result
-Z'' (×10^5Ohm)
Z' (×10^5Ohm)

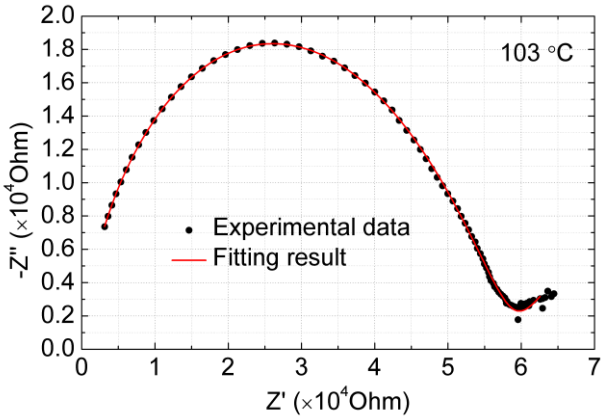
103 °C
Experimental data
Fitting result
-Z'' (×10^4Ohm)
Z' (×10^4Ohm)

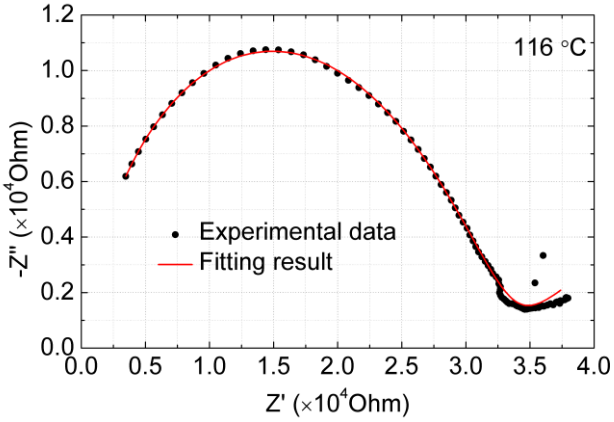
116 °C
Experimental data
Fitting result
-Z'' (×10^4Ohm)
Z' (×10^4Ohm)

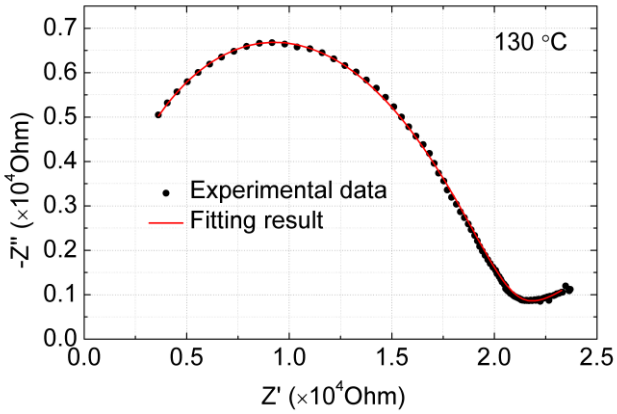
130 °C
Experimental data
Fitting result
-Z'' (×10^4Ohm)
Z' (×10^4Ohm)

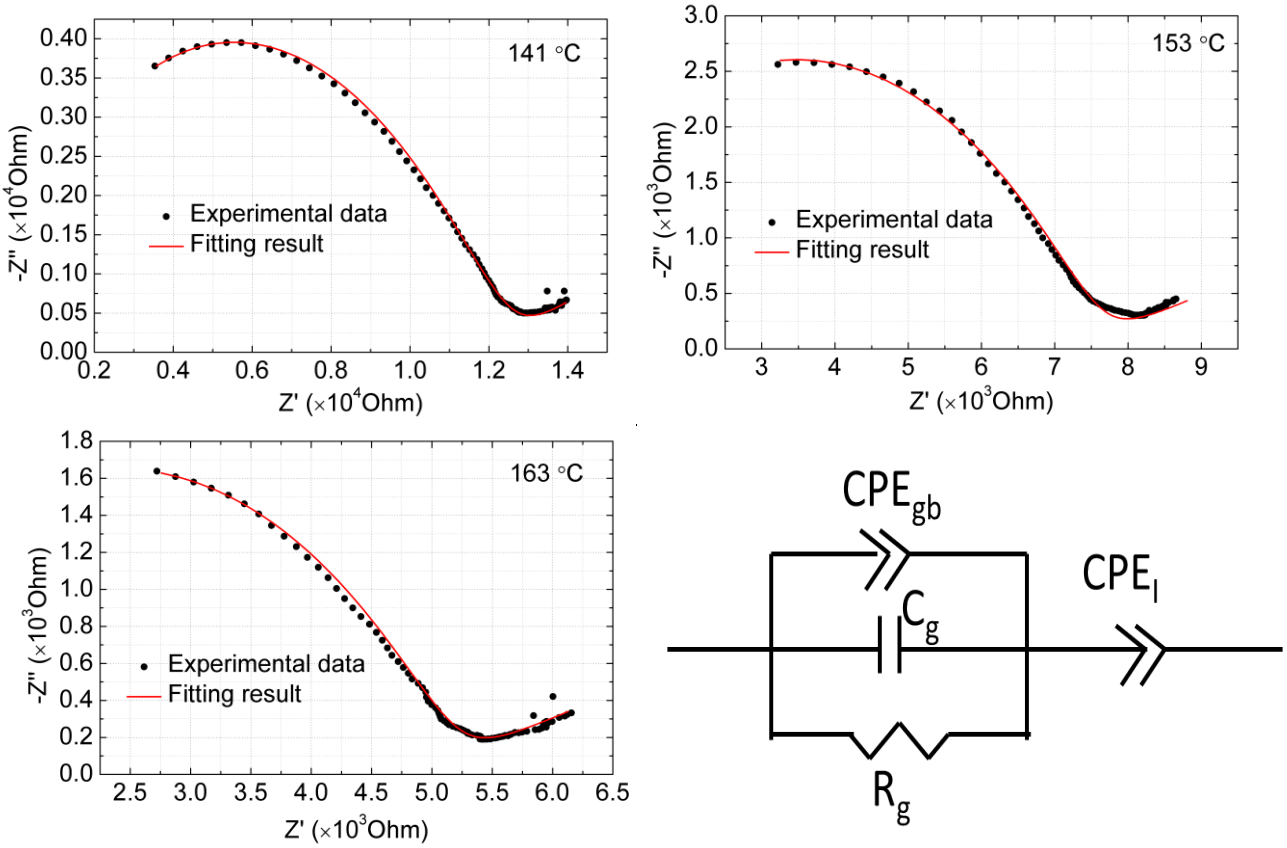

Figure 2.16 Fits of AC impedance spectra collected at temperatures from 30 – 163 °C using frequencies of 20 Hz – 2 MHz, and the equivalent circuit used for modeling the data. Refined parameters are reported in Table 2.9. The parameters in this equivalent circuit are closely associated with physical response mechanisms permitted within pellet the measurement geometry. R_g represents the bulk resistance of the $Na_3TiP_3O_9N$ electrolyte, C_g represents the capacitance between the two metal electrodes, CPE_{gb} is a constant-phase-angle element that represents sodium ions moving into (or across) grain boundaries, and CPE_I is a constant-phase-angle element used to model the diffusion of sodium ions into the contacts. The first three elements allow the high-frequency arc to be described, while the CPE_I is required to model the low frequency tail of the spectrum.

Table 2.9 Fit results of T-dependent ac impedance data.

T (°C)	R_g (Ω)	Δ R_g (%)	C_g (F)	CPE_{gb} B1 (Ω S^{-n1})	CPE_{gb} n1	CPE_I B2 (Ω S^{-n2})	CPE_I n2
30	794790	0.226	6.97E-12	4.33E-09	0.5449	6.37E-07	0.45228
57	402160	0.485	6.23E-12	3.20E-09	0.5682	3.40E-06	0.40031
65	306230	0.106	6.28E-12	3.30E-09	0.5635	7.22E-06	0.36441
75	211990	0.119	6.28E-12	3.46E-09	0.5628	8.72E-06	0.36990

86	127070	0.377	6.06E-12	3.77E-09	0.5670	7.39E-06	0.47269
103	58355	0.266	6.30E-12	5.60E-09	0.5547	2.62E-05	0.36451
116	32646	0.510	7.00E-12	7.88E-09	0.5424	5.07E-05	0.24503
130	20074	0.257	7.41E-12	1.11E-08	0.5311	0.000101	0.19595
141	12105	0.748	6.81E-12	1.38E-08	0.5336	0.000172	0.19916
153	7319	0.108	7.42E-12	9.99E-09	0.5558	0.000269	0.17713
163	4929	1.184	5.48E-12	8.93E-09	0.5860	0.00034	0.17380

2.3.3.2 Conductivity mechanism

Good insights into the potential wells associated with the three sodium sites in $Na_3TiP_3O_9N$ can be gained from the displacement parameters refined using high resolution time-of-flight neutron diffraction data (d_{min} ~ 0.3 Å) acquired on the POWGEN diffractometer. The very large room temperature displacement parameters refined for Na1 (U_{eq} = 0.033 Å^2) and Na3 (0.039 Å^2) far exceed that of Na2 (0.015 Å^2) and the other non-sodium atoms (Figure 2.17). These displacements are strongly enhanced by increasing temperature, confirming that they represent dynamic rather than static displacements. The average displacement inferred from these parameters increases from about 0.2 Å at room temperature to 0.3 Å at 650 K. This indicates that Na1 and Na3 have very shallow potential wells which are conducive to fast ionic diffusion if a suitable diffusion pathway exists.

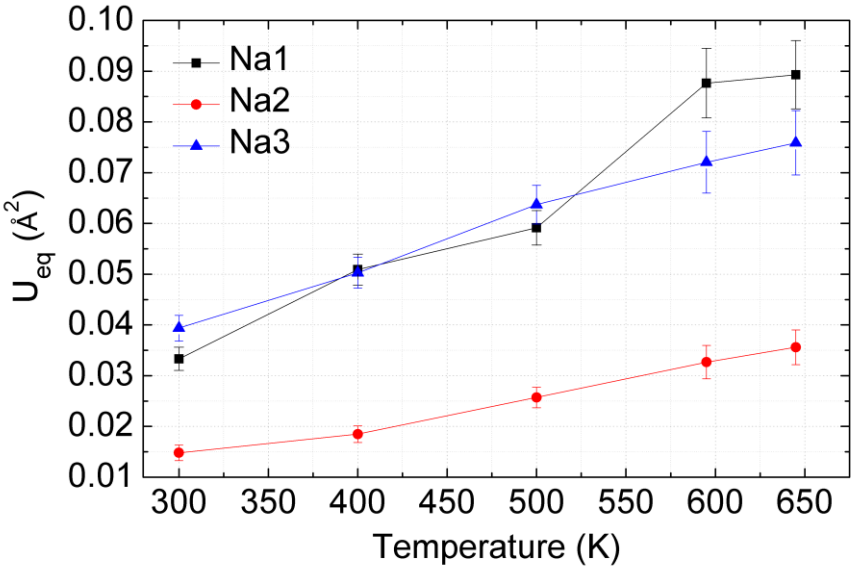

Figure 2.17 Temperature-dependent displacement parameters for the sodium sites of $Na_3TiP_3O_9N$ from neutron diffraction data.

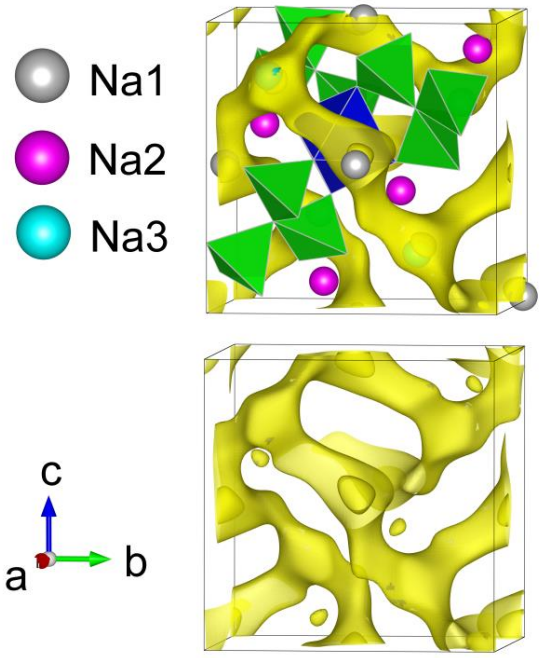

Figure 2.18 Na difference bond valence sum (|ΔV|) map of $Na_3TiP_3O_9N$ (top) and $Na_2TiP_3O_9N$ (bottom) drawn with an isosurface level of 0.12. The Na1 and Na3 sites (white and blue spheres, respectively) are predicted to be part of a three dimensional ion conduction network, while the Na2 sites (purple) are expected to be isolated from this network.

In order to visualize possible diffusion paths for Na ions within this structure type, bond valence sum (BVS) difference maps [55] were calculated. It is expected that all positions within the cell where the absolute value of the valence difference (|ΔV|) between the BVS-calculated valence and the ideal valence of +1 is small represent low free energy positions that are accessible to Na at modest activation energies. The likely diffusion paths of Na ions are represented by the |ΔV| isosurfaces shown in Figure 2.18, which were calculated based on the refined structures for stoichiometric $Na_3TiP_3O_9N$ (top) and desodiated $Na_2TiP_3O_9N$ (bottom). The Na1 and Na3 sites of $Na_3TiP_3O_9N$ first become connected in a continuous network when a very small |ΔV| threshold of 0.03 is chosen, and Na ions at these two sites are therefore predicted to be mobile and to form an isotropic three-dimensional ion transport network. The Na2 site requires a much larger threshold of 0.45 valence units to be connected, and it is therefore expected to be difficult to access these sites at room temperature. A comparison of threshold |ΔV| values for network formation of $Na_{3-x}TiP_3O_9N$ structures determined in this work (Table 2.10) suggests that

similar behavior will be observed for structures with different sodium concentration, though the barrier for accessing Na2 is lowered when Na is partially or fully removed. The relative barriers to diffusion predicted for the three Na sites are in very consistent with the displacement parameters associated with these sights, suggesting that the primary barrier to motion in the diffusional process is directly associated with the potential well in the immediate vicinity of the Na atoms.

Table 2.10 Threshold values for sodium bond valence difference (|ΔV|) map.

Linkage type	$Na_3TiP_3O_9N$	$Na_{2.5}TiP_3O_9N$	$Na_2TiP_3O_9N$
Na1-Na3	0.03	0.02	0.05
Na1-Na2-Na3	0.45	0.24	0.29

Although BVS maps have been found to be a convenient and effective method to visualize possible diffusion pathways, they do not include cation-cation repulsions and only qualitatively correspond to the potential energy surface associated with the mobile ions. Careful crystal structure analysis of the local environments of the sodium ions may provide further insights into the possible diffusion paths. From the refined crystal structure of $Na_3TiP_3O_9N$, it can be seen that the shortest direct paths between two Na1 sites or two Na3 sites are forbidden due to the presence of intervening TiO_6 octahedra and PO_3N tetrahedra, consistent with the BVS predictions. The most likely diffusion pathways instead involve heterogeneous migration paths in which ions consecutively access both Na1 and Na3 sites. Two possible paths of this type through open space have been identified, and will be referred to as S13 and L13 for the shorter (3.44 Å) and longer path (4.44 Å), respectively. As seen in Figure 2.19, the S13 path involves migration through an equilateral triangle formed by three O3 atoms (with O3-O3 bond lengths of 3.10 Å) which are part of the coordination sphere of both Na1 and Na3. The S13 path is located directly on the three-fold axis on which both the Na1 and Na3 sites are found. In contrast, the L13 path radiates away from each site in three different directions since it is not collinear with a 3-fold symmetry axis. This path allows Na ions to pass through a much more open triangle formed by two O1 ions associated with the Na1 coordination shell and one O3 ion that is part of the Na2 octahedral environment.

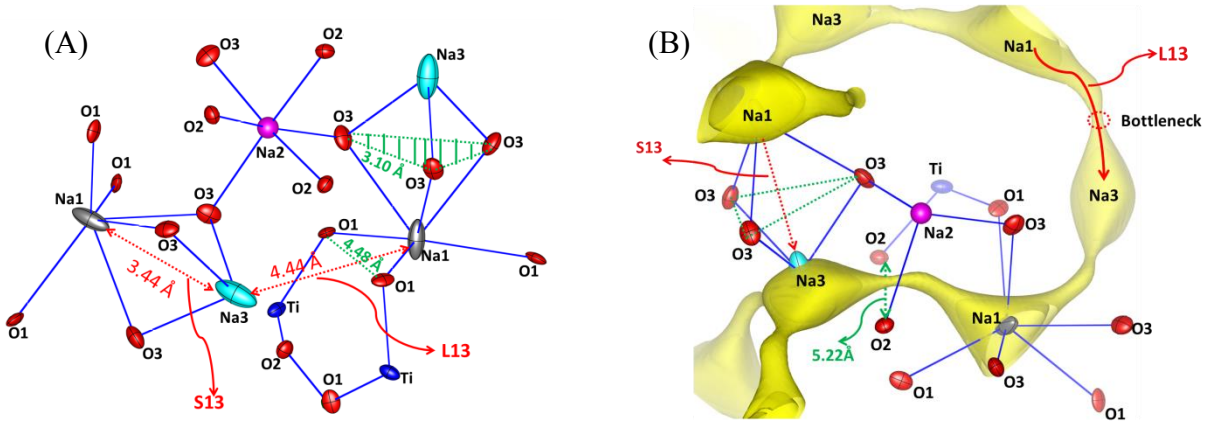

Figure 2.19 (A) Thermal ellipsoids (50% probability) of ions near the two most plausible sodium ionic diffusion paths (S13 and L13) in $Na_3TiP_3O_9N$. (B) Plot of the Na difference bond valence map ($|\Delta V|=0.05$) suggests that the barrier for moving between the Na1 and Na3 sites is low along the longer L13 type path but is high along the S13 type path (remains disconnected even for $|\Delta V|=0.5$).

While BVS maps provide a rapid method for identifying potential diffusion paths, DFT calculations are better able to quantify hopping energies and are more directly comparable with experimental results. In order to understand the diffusion process, it is necessary to understand which sites have kinetically accessible hopping pathways, and which sites have an occupancy that varies with the state of charge (only the Na1 site of $Na_3TiP_3O_9N$). It is interesting to note that the desodiation of 2:2 $Na_2Fe_2P_3O_9N$ removes twice as many Na ions per formula unit,[27] and that these two Na ions are removed from sites which correspond to the Na1 and Na3 sites of $Na_3TiP_3O_9N$, supporting the BVS prediction that the diffusion path connects Na1 and Na3 sites. First-principles density functional theory calculations done both within the generalized gradient approximations (GGA) and the Hubbard model extension (GGA+*U*) also indicate a fully three-dimensional diffusion path that links both Na1 and Na3 but not Na2 sites.

The energy barriers of three possible diffusion pathways (illustrated in Figure 2. 20) were calculated by DFT+U methods upon introduction of one Na vacancy in the 68 atom primitive cell. The lowest energy pathway was found to be along the L13 path from Na1 to Na3. As Na migrates along the long paths, it will pass through an intermediate local minimum where it is likely to thermalize before hopping further into either the Na1 or Na3 sites. This local minimum coincides with a four-fold oxygen coordinated site, similar to the intermediate tetrahedral sites of Li hops in many Li intercalation compounds.[56] The topology of the structure is such that the long path (L13) will allow fully isotropic

three-dimensional diffusion. Two barriers of 0.5 eV and 0.29eV need to be overcome when migrating from the Na3 site to the Na1 site. In the opposite direction, the Na will experience a barrier of 0.37eV followed by a very small barrier of less than 0.10 eV.

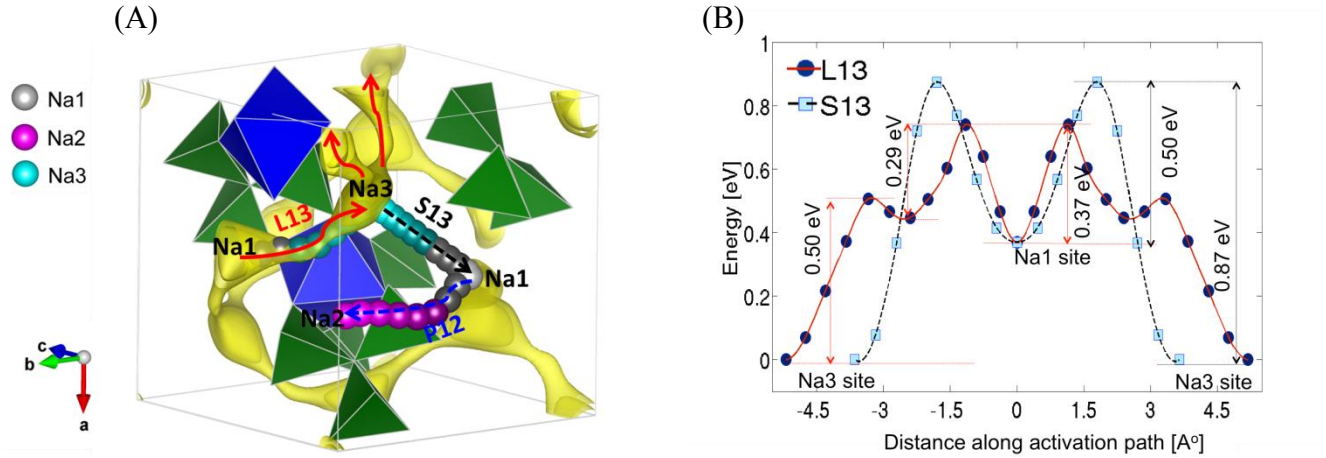

Figure 2.20 (A) Visualization of the three potential diffusion paths evaluated using DFT+U calculations, superimposed on the BVS map ((| Δ V|=0.05, yellow). The favoured L13 path (red, 0.50 / 0.37 eV) is marked with a solid red arrow, while dashed lines indicate the high barrier pathways S13 (black, 0.87 / 0.50 eV) and P12 (blue, 0.98 / 0.75 eV). (B) DFT+U energies for points along the short (S13) and long (L13) Na1-Na3 pathways, with energies evaluated at positions marked by spheres in the left panel.

Although the net energy barrier of 0.75 eV for moving from Na3 to Na1 is higher than the experimentally measured activation energy of 0.54 eV, the possibility of a stable intermediate would lower the theoretical barrier to only 0.50 eV, a value in good agreement with experiment. The simple GGA energy profile obtained without include the inclusion of a Hubbard U shows a similar total energy barrier (0.62 eV) but does not exhibit a well-resolved intermediate site (Figure 2.21). The complexity of the energy landscape connecting Na1 and Na3 sites makes it uncertain that the total migration barrier from Na1 to Na3 can simply be equated to an average activation barrier obtained experimentally. Further Kinetic Monte Carlo simulations will be needed to better determine the equivalent average migration barrier for a complex energy landscape with many distinct hop types having a spectrum of migration barriers. Intriguingly, the potential energy landscape suggests that the overall diffusional barrier could potentially be further lowered if the Na3 site is destabilized through chemical substitutions (at the sites of non-mobile ions), as a major contributor L13 diffusional barrier is the difference in Na potential energy between the Na1 and Na3 sites.

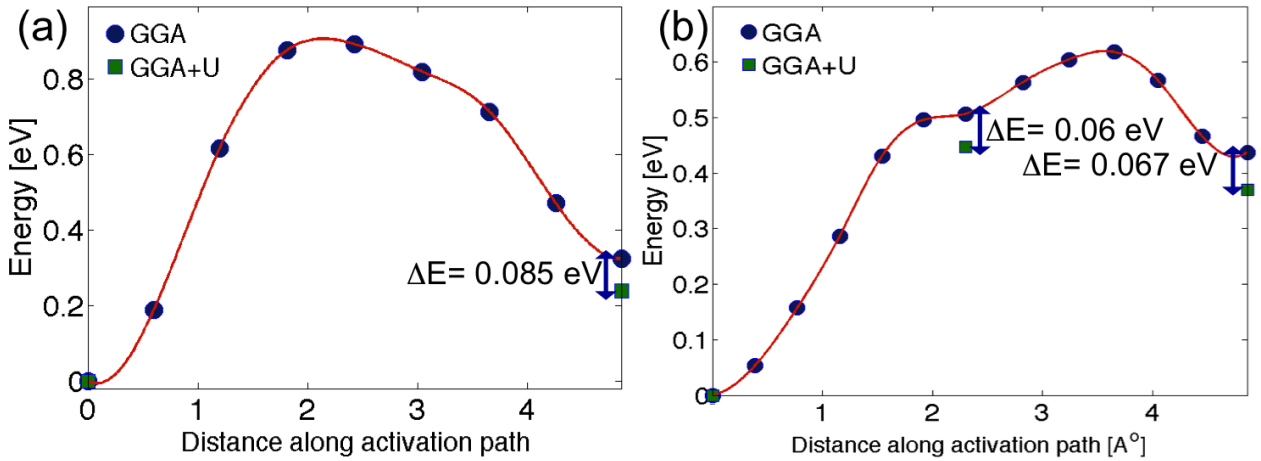

Figure 2.21 (a) DFT-calculated energies for points along the Na1-Na2 type pathway (P12). Distances are given in Å. Green squares correspond to DFT+U energies for selected points. (b) DFT calculated energies along the L13 path connecting Na1 and Na3. The green squares are DFT+U energies and suggest that the reported DFT migration barriers are slightly overestimated (by ~0.06 eV).

Although a shorter S13 diffusion path between the Na1 and Na3 sites is nominally available, the limiting barrier for this pathway is calculated to be 0.87 eV for Na3→Na1 hops. Due to the difference in the Na1 and Na3 site energies, a lower barrier of 0.47 is predicted for Na3→Na1 hops, though this lower barrier is not the limiting one for diffusion through the network of Na1 and Na3 sites. In contrast to the L13 hop, the S13 barrier shows no evidence of an intermediate resting site and clearly must be overcome in a single hop. The high barrier of 0.87 eV for the S13 path suggests that this pathway is unlikely to be important to ion diffusion in $Na_3TiP_3O_9N$. A similar energy barrier (0.89/0.57 eV) is found for the lowest energy path for Na migration between the Na1 and Na2 sites, denoted P12. While this barrier is too large for the Na2 site to significantly contribute to the overall ionic mobility of $Na_3TiP_3O_9N$ at room temperature, it is not expected to be large enough to prevent site exchange at the Na2 site at elevated temperatures. This is experimentally confirmed by our Li ion-exchange studies, which will be described elsewhere.[57]

2.3.4 Thermal stability of $Na_3TiP_3O_9N$ framework

The safety of battery systems is of significant concern for portable electronics applications, and may become even more important in applications which utilize larger battery systems (electric vehicles, grid-scale storage). The thermal stability of cathode materials has been shown to be a good predictor of

stability against overcharge.[58] Although nitride and oxynitride systems can be susceptible to decomposition by oxygen attack, some systems like GaN or SIALONs have very good temperature stability to ~900 °C[59,60]. Furthermore, nitridophosphate systems have the potential for the loss of inert N_2 rather than reactive O_2 loss, potentially mitigating their reactivity with organic electrolytes. Finally, the fully charged state of $Na_3TiP_3O_9N$ contains Ti^{4+}, an oxidation state which is very resistant to oxygen loss (in sharp contrast to tetravalent *3d* transition metals such as Mn, Fe, or Co, which are typically susceptible to oxygen loss). Thermogravimetric analyses (TGA) was used to assess the thermal stability of $Na_3TiP_3O_9N$ by following the mass changes that occurred on heating in an O_2 atmosphere (Figure 2.22). Full decomposition did not occur until temperatures in excess of 550 °C. The onset of mass gain begins above 400 °C, although it is not clear if initial mass loss is due to framework decomposition (1.5 O^{2-} ions replace each N^{3-}) or Ti oxidation (Ti^{3+} oxidized to Ti^{4+} charge balanced by the gain of 0.5 O^{2-}) as both of these processes involve mass gains. In either case, this mixed anion compound can be considered to have good oxidative stability in a manner analogous to $LiFePO_4$, which thermally decomposes around 550 °C.[61] When$Na_3TiP_3O_9N$ is fully desodiated to produce $Na_2TiP_3O_9N$ using a chemical oxidant, this framework still remains stable against oxidation in O_2 up to at least 400 °C.

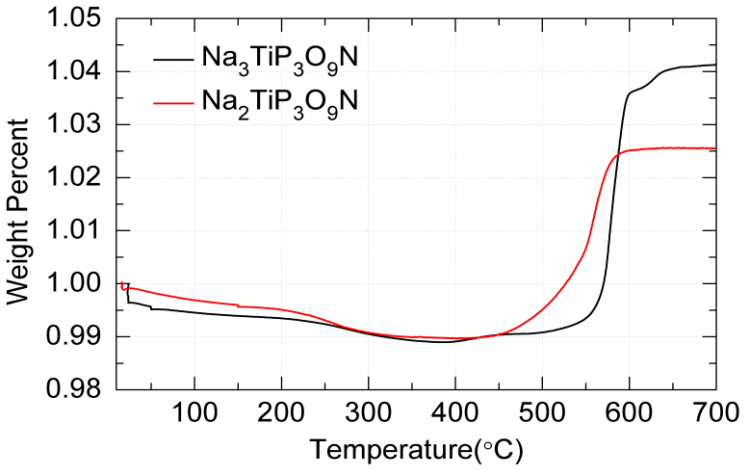

Figure 2.22 Thermogravimetric response of pristine $Na_3TiP_3O_9N$ (black) and chemically desodiated $Na_2TiP_3O_9N$ (red) on heating (2 °C/min, flowing O_2).

In order to get a more direct measure of the framework stability and the decomposition processes, *in situ* X-ray diffraction data were collected at the X7B beamline of the NSLS synchrotron (Figure 2.23). Up to 550 °C, the only crystalline phase is $Na_3TiP_3O_9N$. At 575°C, peaks appear for a second crystalline

phase which can be indexed based on the NASICON-type phase $NaTi_2(PO_4)_3$. Rietveld refinement of the last diffraction pattern collected at 200 °C (Figure 2.24) showed this phase crystalized in space group of *R-3c* with lattice parameters of a = 8.4736(3) and b = 21.9502(10). These result are in consistent with our synthetic studies, which also show this NASICON phase as a common impurity which cannot be converted to $Na_3TiP_3O_9N$ by any amount of annealing under NH_3, suggesting that this is an irreversible transformation driven by nitrogen loss. The transformation of $Na_3TiP_3O_9N$ to $NaTi_2(PO_4)_3$ was observed to be complete by 725 °C, suggesting that this reaction occurs quickly in the present of oxygen.

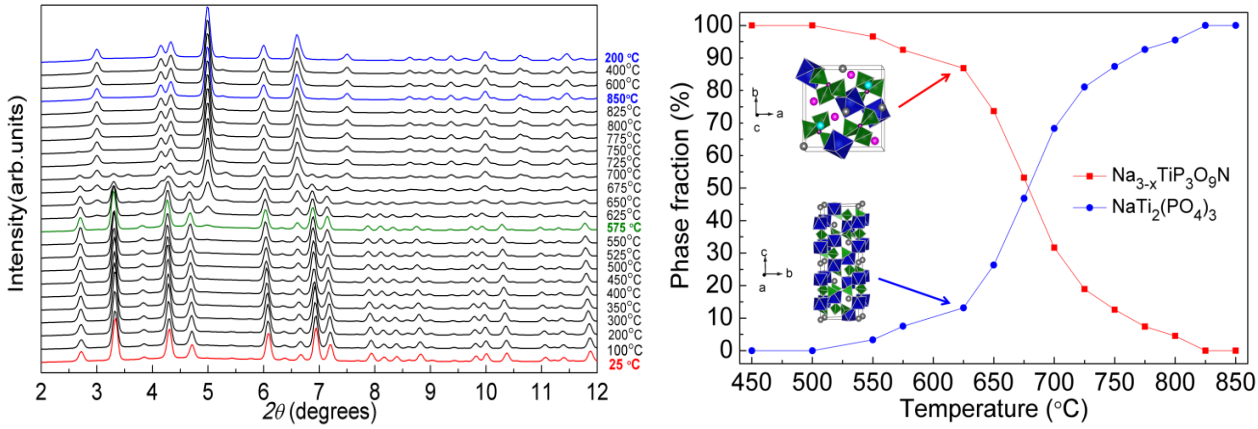

Figure 2.23 Left, *in situ* XRD data (λ = 0.3196 Å) following the transformation of CUBICON $Na_3TiP_3O_9N$ heated under flowing air. Thermal decomposition was first observed at 575 ℃, and the only decomposed product giving diffraction peaks could be indexed as NASICON-type $NaTi_2(PO_4)_3$. Right, refined phase fractions of CUBICON and NASICON components.

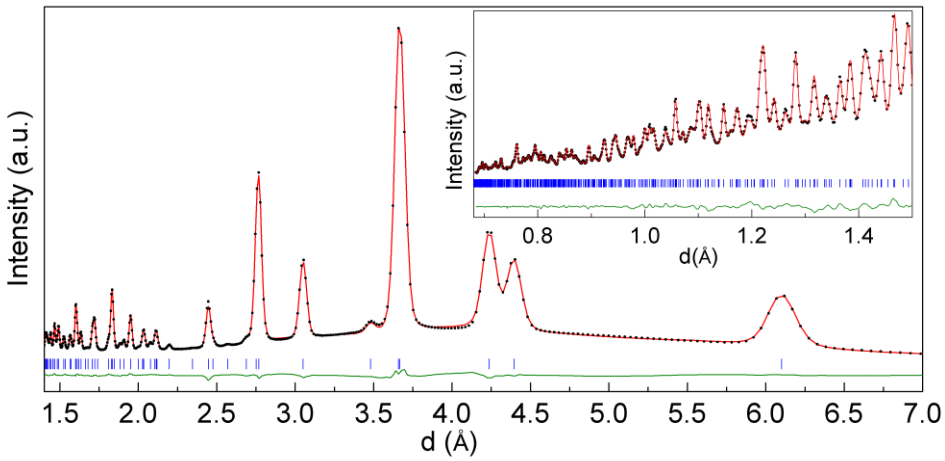

Figure 2.24 Rietveld refinement of final diffraction pattern (scan number 168, λ = 0.3196 Å) containing $NaTi_2(PO_4)_3$ at the conclusion of the *in situ* heating experiment for $Na_3TiP_3O_9N$.

Table 2.11 Crystallographic data of $NaTi_2(PO_4)_3$ from the Rietveld refinement of 200 ℃ data.

Formula $\mathbf{NaTi_2(PO_4)_3}$		**Space group** ***R-3c* (# 167)**		**Lattice parameters (Å)** **a = 8.4736(3) b = 21.9502(10)**		
Atom	Wyckoff symbol	*x*	*y*	*z*	Occ.	B_{iso} (Å^2)
Na	6b	0	0	0	1	4.35(14)
Ti	12c	0	0	0.1459 (1)	1	0.91(4)
P	18e	0.2857 (2)	0	0.25	1	1.15(5)
O1	36f	0.0307 (4)	0.2000 (4)	0.1926 (1)	1	1.62(8)
O2	36f	0.1934 (3)	0.1653 (3)	0.0900(1)	1	1.08 (7)

2.4. Conclusion

In conclusion, $Na_3TiP_3O_9N$ is shown to be the first member of the CUBICON family of nitridophosphate compounds that can effectively cycle Na ions reversibly at room temperature. The 3D Na-ion conduction pathways, good sodium ionic conductivity, extremely small volume changes and good thermal stability make this structure type particularly attractive for rechargeable Na-ion battery applications. Although the capacity of $Na_3TiP_3O_9N$ is somewhat limited (74 mAh/g) for practical cathode applications, this CUBICON framework contains at two readily mobile Na-ions (and three Na ions in total) per transition metal site, so the theoretical capacity of this framework could be doubled if transition metals such as V^{3+} (V^{4+}, V^{5+}) or Cr^{3+} (Cr^{4+}, Cr^{5+}, Cr^{6+}) that can access more than two oxidation states are substituted for Ti^{3+}. In general, the Li-ion variants of the CUBICON framework appear to have substantially higher ionic conductivities than their Na-ion analogues, and appropriate chemical substitutions may offer the possibility of discovering superionic conductivity within this isotropic cubic framework ideal behavior for a solid state electrolyte.

Reference

(1) Liu, J.; Chang, D. H.; Whitfield, P.; Janssen, Y.; Yu, X. Q.; Zhou, Y. N.; Bai, J. M.; Ko, J.; Nam, K. W.; Wu, L. J.; Zhu, Y. M.; Feygenson, M.; Amatucci, G.; Van der Ven, A.; Yang, X. Q.; Khalifah, P. *Chem. Mater.* **2014**, *26*, 3295.
(2) Pan, H. L.; Hu, Y. S.; Chen, L. Q. *Energy & Environmental Science* **2013**, *6*, 2338.
(3) Palomares, V.; Serras, P.; Villaluenga, I.; Hueso, K. B.; Carretero-Gonzalez, J.; Rojo, T. *Energy & Environmental Science* **2012**, *5*, 5884.
(4) Kim, S. W.; Seo, D. H.; Ma, X. H.; Ceder, G.; Kang, K. *Advanced Energy Materials* **2012**, *2*, 710.
(5) Braconnier, J. J.; Delmas, C.; Fouassier, C.; Hagenmuller, P. *Mater. Res. Bull.* **1980**, *15*, 1797.
(6) Delmas, C.; Fouassier, C.; Hagenmuller, P. *Physica B & C* **1980**, *99*, 81.
(7) Braconnier, J. J.; Delmas, C.; Hagenmuller, P. *Mater. Res. Bull.* **1982**, *17*, 993.
(8) Didier, C.; Guignard, M.; Denage, C.; Szajwaj, O.; Ito, S.; Saadoune, I.; Darriet, J.; Delmas, C. *Electrochemical and Solid State Letters* **2011**, *14*, A75.
(9) Komaba, S.; Takei, C.; Nakayama, T.; Ogata, A.; Yabuuchi, N. *Electrochem. Commun.* **2010**, *12*, 355.
(10) Zhou, Y. N.; Ding, J. J.; Nam, K. W.; Yu, X. Q.; Bak, S. M.; Hu, E. Y.; Liu, J.; Bai, J. M.; Li, H.; Fu, Z. W.; Yang, X. Q. *Journal of Materials Chemistry A* **2013**, *1*, 11130.
(11) Caballero, A.; Hernan, L.; Morales, J.; Sanchez, L.; Pena, J. S.; Aranda, M. A. G. *J. Mater. Chem.* **2002**, *12*, 1142.
(12) Berthelot, R.; Carlier, D.; Delmas, C. *Nat. Mater.* **2011**, *10*, 74.
(13) Yabuuchi, N.; Kajiyama, M.; Iwatate, J.; Nishikawa, H.; Hitomi, S.; Okuyama, R.; Usui, R.; Yamada, Y.; Komaba, S. *Nat. Mater.* **2012**, *11*, 512.
(14) Moreau, P.; Guyomard, D.; Gaubicher, J.; Boucher, F. *Chem. Mater.* **2010**, *22*, 4126.
(15) Lee, K. T.; Ramesh, T. N.; Nan, F.; Botton, G.; Nazar, L. F. *Chem. Mater.* **2011**, *23*, 3593.
(16) Goodenough, J. B.; Hong, H. Y. P.; Kafalas, J. A. *Mater. Res. Bull.* **1976**, *11*, 203.
(17) Delmas, C.; Cherkaoui, F.; Nadiri, A.; Hagenmuller, P. *Mater. Res. Bull.* **1987**, *22*, 631.
(18) Plashnitsa, L. S.; Kobayashi, E.; Noguchi, Y.; Okada, S.; Yamaki, J. *J. Electrochem. Soc.* **2010**, *157*, A536.
(19) Jian, Z. L.; Zhao, L.; Pan, H. L.; Hu, Y. S.; Li, H.; Chen, W.; Chen, L. Q. *Electrochem. Commun.* **2012**, *14*, 86.
(20) Barker, J.; Saidi, M. Y.; Swoyer, J. L. *Electrochem. Solid-State Lett.* **2003**, *6*, A1.

(21) Gover, R.; Bryan, A.; Burns, P.; Barker, J. *Solid State Ionics* **2006**, *177*, 1495.
(22) Chihara, K.; Kitajou, A.; Gocheva, I. D.; Okada, S.; Yamaki, J. *J. Power Sources* **2013**, *227*, 80.
(23) Ellis, B. L.; Makahnouk, W. R. M.; Makimura, Y.; Toghill, K.; Nazar, L. F. *Nat. Mater.* **2007**, *6*, 749.
(24) Recham, N.; Chotard, J. N.; Dupont, L.; Djellab, K.; Armand, M.; Tarascon, J. M. *J. Electrochem. Soc.* **2009**, *156*, A993.
(25) Chen, H. L.; Hao, Q.; Zivkovic, O.; Hautier, G.; Du, L. S.; Tang, Y. Z.; Hu, Y. Y.; Ma, X. H.; Grey, C. P.; Ceder, G. *Chem. Mater.* **2013**, *25*, 2777.
(26) Barpanda, P.; Oyama, G.; Ling, C. D.; Yamada, A. *Chem. Mater.* **2014**, *26*, 1297.
(27) Liu, J.; Yu, X. Q.; Hu, E. Y.; Nam, K. W.; Yang, X. Q.; Khalifah, P. G. *Chem. Mater.* **2013**, *25*, 3929.
(28) Conanec, R.; Feldmann, W.; Marchand, R.; Laurent, Y. *J. Solid State Chem.* **1996**, *121*, 418.
(29) Feldmann, W. *Zeitschrift Fur Chemie* **1987**, *27*, 182.
(30) Feldmann, W. *Zeitschrift Fur Chemie* **1987**, *27*, 100.
(31) Zatovsky, I. V.; Vorobjova, T. V.; Domasevitch, K. V.; Ogorodnyk, I. V.; Slobodyanik, N. S. *Acta Crystallogr., Sect. E: Struct. Rep. Online* **2006**, *62*, 32.
(32) Liu, J. unpublished results
(33) Lee, M. S.; Kang, J. K.; Kim, S. J. *Bull. Korean Chem. Soc.* **2012**, *33*, 2083.
(34) Yao, Y. F. Y.; Kummer, J. T. *Journal of Inorganic & Nuclear Chemistry* **1967**, *29*, 2453.
(35) Hammersley, A. P.; Svensson, S. O.; Hanfland, M.; Fitch, A. N.; Hausermann, D. *High Pressure Research* **1996**, *14*, 235.
(36) Hu, E.; Bak, S.-M.; Liu, J.; Yu, X.; Zhou, Y.; Ehrlich, S. N.; Yang, X.-Q.; Nam, K.-W. *Chem. Mater.* **2014**, *26*, 1108.
(37) Neuefeind, J.; Feygenson, M.; Carruth, J.; Hoffmann, R.; Chipley, K. K. *Nuclear Instruments & Methods in Physics Research Section B-Beam Interactions with Materials and Atoms* **2012**, *287*, 68.
(38) Ravel, B.; Newville, M. *J Synchrotron Radiat* **2005**, *12*, 537.
(39) Rodriguez-carvajal, J.; Gonzalez-Platas, J. *Acta Crystallographica Section A* **2002**, *A58*, C87.
(40) Adams, S. *Acta Crystallographica Section B-Structural Science* **2001**, *57*, 278.
(41) Momma, K.; Izumi, F. *J. Appl. Crystallogr.* **2008**, *41*, 653.
(42) Thangadurai, V.; Adams, S.; Weppner, W. *Chem. Mater.* **2004**, *16*, 2998.
(43) Adams, S. *J. Solid State Electrochem.* **2010**, *14*, 1787.
(44) Adams, S.; Rao, R. P. *Physica Status Solidi a-Applications and Materials Science* **2011**, *208*, 1746.
(45) Janssen, Y.; Middlemiss, D. S.; Bo, S. H.; Grey, C. P.; Khalifah, P. G. *J. Am. Chem. Soc.* **2012**, *134*, 12516.
(46) Kresse, G.; Furthmuller, J. *Physical Review B* **1996**, *54*, 11169.
(47) Blochl, P. E. *Physical Review B* **1994**, *50*, 17953.
(48) Dudarev, S. L.; Botton, G. A.; Savrasov, S. Y.; Humphreys, C. J.; Sutton, A. P. *Physical Review B* **1998**, *57*, 1505.
(49) Sanchez, J. M.; Ducastelle, F.; Gratias, D. *Physica A* **1984**, *128*, 334.
(50) Van der Ven, A.; Thomas, J. C.; Xu, Q. C.; Swoboda, B.; Morgan, D. *Physical Review B* **2008**, *78*.
(51) Wood, R. M.; Palenik, G. J. *Inorg. Chem.* **1999**, *38*, 3926.
(52) Ohzuku, T.; Ueda, A.; Yamamoto, N. *J. Electrochem. Soc.* **1995**, *142*, 1431.
(53) Neudecker, B. J.; Weppner, W. *J. Electrochem. Soc.* **1996**, *143*, 2198.
(54) Aono, H.; Sugimoto, E. *J. Am. Ceram. Soc.* **1996**, *79*, 2786.

(55) Brown, I. D. *Chem. Rev. (Washington, DC, U. S.)* **2009**, *109*, 6858.
(56) Van der Ven, A.; Bhattacharya, J.; Belak, A. A. *Acc. Chem. Res.* **2013**, *46*, 1216.
(57) Liu, J. unpublished results
(58) Ong, S. P.; Jain, A.; Hautier, G.; Kang, B.; Ceder, G. *Electrochem. Commun.* **2010**, *12*, 427.
(59) Reinert, A. A.; Payne, C.; Wang, L. M.; Ciston, J.; Zhu, Y. M.; Khalifah, P. G. *Inorg. Chem.* **2013**, *52*, 8389.
(60) Hewett, C. L.; Cheng, Y. B.; Muddle, B. C.; Trigg, M. B. *J. Eur. Ceram. Soc.* **1998**, *18*, 417.
(61) Delacourt, C.; Poizot, P.; Tarascon, J.-M.; Masquelier, C. *Nat. Mater.* **2005**, *4*, 254.

Chapter 3 $Na_3VP_3O_9N$ as high voltage and multi-electron transfer cathode material for rechargeable Na-ion and Li-ion batteries

3.1 Introduction

Exploring cathode materials with multi-electron transfer redox couples for rechargeable Li/Na-ion batteries has attracted tremendous attentions in recent years[1,2], because these materials can deliver higher theoretical capacity and higher voltage than analogue materials with a single electron transfer redox couple. However, until today, this concept has only been achieved in a few oxides, mainly by uitlizing Ni^{2+}/Ni^{4+}, such as layered $LiNi_{0.5}Mn_{0.5}O_2$[3,4] and spinel $LiNi_{0.5}Mn_{1.5}O_2$[5,6]. Utilizing multi-electron transfer redox couples in polyanion compounds has been found to be more challenge due to the high voltage, sluggish kinetics and structure decomposition associated with oxidizing transition metal ions to very high oxidation states, such as. V^{4+}/V^{5+} [7,8], $Fe^{3+/}Fe^{4+}$ [9], $Mn^{3+/}Mn^{4+}$ [10] and Cu^{2+}/Cu^{3+} [11]. Nevertheless, few exceptions existed, such as monoclinic $Li_3V_2(PO_4)_3$[12,13], $VOPO_4$[14-16], sidorenkite $Na_3Mn(PO_4)(CO_3)_3$[17] and molybdenum oxy-pyrophosphate $(MoO_2)_2P_2O_7$[18]. This motivates us to further explore other novel polyanion compounds with potential multi-electron transfer redox couples for rechargeable Li^+/Na^+ batteries.

Recently, we have demonstrated that $Na_3TiP_3O_9N$ can work as a zero volume change cathode material for rechargeable Na-ion batteries with very high $Ti^{3+/}Ti^{4+}$ redox potential (2.7 V v.s. Na^+/Na)[19]. However, only one (Na1) out of two potential mobile sodium ions (Na1 and Na3) has been used in this Ti-based compound due to the single Ti^{3+}/Ti^{4+} redox couple. Therefore, theoretical capacity of $Na_3M(III)P_3O_9N$ (*M* = Ti, V and Cr) could be doubled (to 145 mAh/g) if multi-electron transfer redox couple can be utilized. In this chapter, we will demonstrate the plausibility of utilizing $V^{3+}/V^{4+/}V^{5+}$

multi-electron transfer redox couples in $Na_3VP_3O_9N$ to design high voltage cathode materials for rechargeable Na^+/Li^+ batteries.

3.2 Experimental

3.2.1 Synthesis of $Na_3VP_3O_9N$ and $Na_3V_{1-x}Al_xP_3O_9N$

Stoichiometric amount of $NaPO_3$ (Fisher Scientific, n ~ 6), V_2O_3 (Aldrich, >99%) or V_2O_5 (Alfa Aesar, 99.6%) were first mixed and ground for 10 min using mortar and pestle. The mixture was vibrated ball milled for another 2 hours. It is necessary to add small amount (molar ratio V_2O_5 to ascorbic acid is 10:1) of ascorbic acid in the starting material to synthesize samples without NASICON-type $Na_3V_2(PO_4)_3$ impurity. The well mixed starting materials were then transferred to a Mo (99.985%, Alfa Aesar, 0.025 mm thick, 5 × 1.5 × 1.5 cm after fold) boat (quartz boat was reacting with the starting materials at temperatures higher than 650 ℃). The boat was then transferred into an 1 inch diameter quartz tube, the tube was first purged with anhydrous argon or nitrogen gas for about 1 hour and then flowed anhydrous NH_3 gas with a flowing rate of 50 mL/min. The mixture was heated up to 650 ℃ to 750 ℃ at a temperature ramp rate of 200 ℃/h and was further held at this temperature for 20 hours before cooling down to room temperature at furnace cooling rate. Unlike $Na_3TiP_3O_9N$ and $Na_2Fe_2P_3O_9N$ [19,20], which can be synthesized as fine powders, the as-prepared $Na_3VP_3O_9N$ was found to be dense crack even at synthetic temperature as low as 650 ℃. To synthesize well crystalline and highly purified $Na_3VP_3O_9N$, the optimized synthetic temperature is around 700 ℃ to 730 ℃. Rock salt type VO_xN_y impurity (black color) will form at higher synthetic temperature, while lower temperature will lead to incomplete reaction. $Na_3V_{0.9}Al_{0.1}P_3O_9N$ was synthesized at similar condition but with V_2O_3 partially replaced by Al_2O_3 (Alfa Aesar, 99.9%). The as-prepared sample was then ground with mortar and pestle for about 40 min. For samples that were used for electrochemical test, the hand grounded samples were further vibrantly ball milled for 1 hour or high energy ball mill for 30 min.

3.2.2 Scanning electron microscopy

Scanning electron microscopy (SEM) images of $Na_3VP_3O_9N$ powder synthesized at 720 ℃ were collected on a JEOL 7600 SEM operating at 5 kV. Elemental-dispersive X-ray analysis (EDX) spectra of the as-prepared samples were collected on a JEOL 7600 SEM operating at 15 kV with Oxford EDX spectrometer.

3.2.3 Chemical desodiation

Chemical desodiation of $Na_3VP_3O_9N$ was carried out in an argon filled glove box. About 0.4 g well ground $Na_3VP_3O_9N$ powder was added to excess 1.0 M NO_2BF_4 in acetonitrile solution. The mixture was stirred for 24 hours in the glove box and sit for 1 hour for precipitation before the up level liquid in the glass vial was pulled out and another 20 mL fresh 1.0 M NO_2BF_4 solution was added. The mixture was further stirred for another 24 hours, it was then filtered and washed with acetonitrile for 4 times, the final black powder was recovered from the filter paper and dried in the glove box.

3.2.4 Powder X-ray and neutron diffraction

Room temperature XRD data of the as-prepared $Na_3VP_3O_9N$, $Na_3V_{0.9}Al_{0.1}P_3O_9N$ and chemically desodiated $Na_{3-x}VP_3O_9N$ were collected on a Bruker D8 Advance diffractometer with Cu Kα radiation, a working distance of 300 mm working distance and 1D position sensitive LynxEye Si detector with 192 channels. Synchrotron XRD data of powder samples were collected at beamline X-14A of the National Synchrotron Light Source (NSLS) with 1D linear position sensitive detector at a distance of 1433 mm and a wavelength of about 0.77 Å. Time-of-flight neutron diffraction data of $Na_3V_{0.9}Al_{0.1}P_3O_9N$ was collected at Nanoscale Ordered Materials Diffractometer (NOMAD) at the Spallation Neutron Source, Oak Ridge National Laboratory, this neutron beamline has a total flight path of 21.5 m and the neutron beam is collimated into a diameter of 6 mm, about 0.3 g powder sample was packed into a 3 mm quartz capillary and a data acquisition time of 90 min was used. Neutron diffraction pair distribution function (PDF) data were generated from software developed for NOMAD instrument. Further Rietveld refinement[21] or Le Bail fitting[22] was carried out by using TOPAS software (version 4.2).

3.2.5 *Ex situ* X-ray absorption

Ex situ XAS of pristine $Na_3VP_3O_9N$, chemical desodiated $Na_{3-x}VP_3O_9N$ and recovered electrodes were collected at beamline X-19A at NSLS, BNL using a Si (111) double crystal monochromator in transmission model, the beam intensity was detuned to 50% to minimize the high-order harmonics. Reference spectrum of V foil was collected simultaneous as energy calibrant. XANES and EXAFS spectra were processed using the Athena software package. AUTOBK code was implemented to normalize corresponded absorption coefficient. The obtained EXAFS signal $\chi(k)$ was weighted by k^3 and then Fourier transferred into real space.

3.2.6 Electrochemistry test

For Na-ion batteries, the electrochemical performances were evaluated within a 2013-type coin cell using Na metal as anode, and saturated $NaClO_4$ in EC/DMC as electrolyte. The cathode electrode was made of well mixed $Na_3VP_3O_9N$, which was either vibrated ball milled for 3 hours or high energy ball milled for 10 min, carbon black (acetylene black), and polyvinylidene difluoride (PVDF) in a weight ratio of 7:2:1. An appropriate amount of 1-methyl-2-pyrrolidinone (NMP) was added to the mixed powder to form thick slurry. This slurry was then manually painted onto Al foil with doctor blade, the whole foil was then dried at a vacuum oven at 100 ℃ for 12 hours. The dried foil was then cut into disc shaped electrodes with a diameter of 9/16 inch with a typical active materials loading of 2-3 mg/each disc. The galvanostatic cycling of Na-ion batteries were carried out on either Biological VSP or Land cycler at 20 ℃ or 40 ℃. A typical rate of C/30 was used based on theoretical capacity of 144 mAh/g (corresponding to 2 Na^+).

For hybrid-ion type batteries, the cathode electrode preparation procedure is exactly the same as that for Na-ion batteries. The hybrid-ion batteries were also tested in 2013-type coin cell but with Li metal as anode, 1M $LiPF_6$ in EC/DMC with high voltage additives, and this electrolyte was previously used for high voltage cycling of high voltage spinel, which can well cycled up to 5.2 V[23]. The batteries are tested at 23 ℃ with highest charge/discharge potential varies from 4.7 V to 5.2 V. We also noticed the possibility of PF^{6-} intercalation into graphite at high voltage[24], hence, a contrast cell using acetylene black as cathode was carried out in a similar configuration as the hybrid-ion cell.

For hybrid-ion coin cell used for *in situ* XAS and XRD. The battery configuration is the same as that for regular hybrid-ion type cells, the only difference is the small holes (~2 mm) on the coin cell cap, can and spacer that allows the X-ray beam to pass through the whole cell. For *in situ* XRD, the battery was cycled between 2.00 V and 4.95 V at C/18 rate (based on fully extract/insert 2 Na^+/Li^+); for in situ XAS, coin cell was cycled between 4.95 V and 1.00 V at C/15 rate. For coin cells used for in situ battery test, a larger polarization between charge/discharge curve were usually observed compared to the normal cell testing, this is mainly due to the pressure inhomogeneity in this type *in situ* coin cell configuration, which will be more obvious at high voltage.

3.2.7 Ac impedance measurement

The well ground $Na_3VP_3O_9N$ powder was pressed into a ¼'' diameter pellet in an isostatic press generating a pressure of ~ 1 GPa. The density of this pellet was measured to be ~91%. This pellet was further polished and coated with a thin layer of silver epoxy on each side and then mounted into a spring loaded Teflon cell and placed into a steel tank. Shielded copper wire was used to connect the Teflon cell to coaxial cable interface with a Biologic VMP3 spectrometer (100 mHz – 1 MHz, 100 mV ac potential). Detailed instrument information can be found in our $Li_2Mg_2P_3O_9N$ paper[25] and chapter 4.

3.2.8 *In situ* XAS

In situ V K-edge XAS was carried out at beamline X-11A at NSLS. XAS data was collected in transmission model with metallic vanadium foil as simultaneous energy calibratant, due to the relative thin electrode film and low vanadium concentration in the sample, EXAFS data was found to be too noise to carry out robust refinements, hence, only the X-ray near edge spectroscopy (XANES) data was used to evaluate the vanadium oxidation changes. Data reduction and analysis was carried out in a similar manner as that for *ex situ* XAS data. *In situ* cell for was cycled between 1.0 V and 4.95 V at C/15 rate.

3.2.9 *In situ* XRD

In situ XRD was carried out at beamline X-14A at NSLS, BNL. The as-assembled *in situ* coin cell was tested between 2.0 V and 4.95 V at C/18 rate. XRD pattern was collected between 6.4 °and 34.4 °at a step size of 2 ℅step with scan speed of 40 seconds/step. Le Bail fittings of the collected patterns were carried using TOPAS software (version 4.2).

3.3 Results and discussion

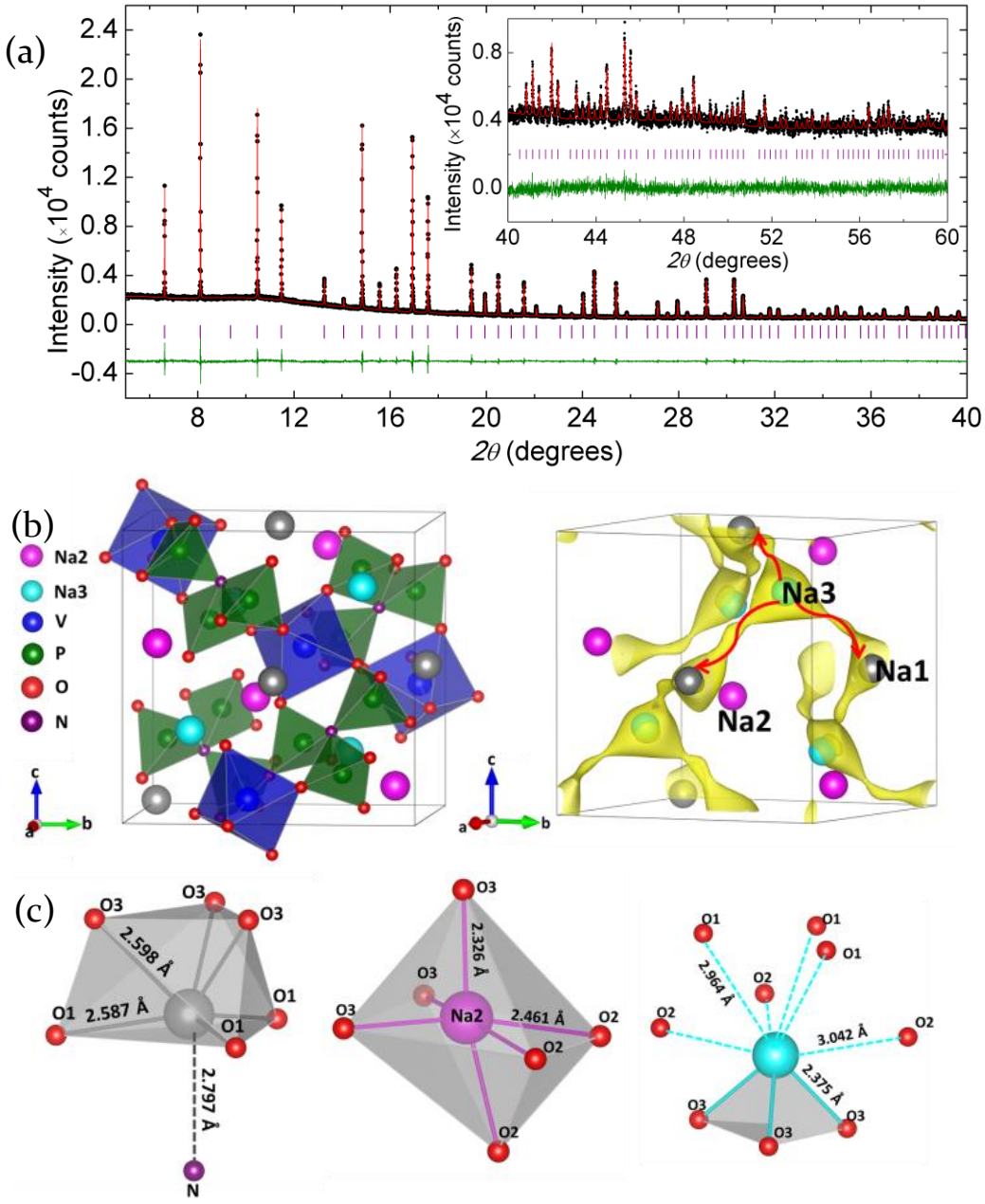

Figure 3.1 (a) Rietveld refinement of $Na_3VP_3O_9N$ structure using synchrotron XRD (λ = 0.771718 Å) data, with data points shown in black, the calculated intensities in red, and the difference curve in olive. (b) Local environments of the three different Na sites in $Na_3VP_3O_9N$ (c) Structure of $Na_3VP_3O_9N$ refined from synchrotron diffraction data (left) and the BVS difference map calculated for this structure with a threshold of $|\Delta V| \leq 0.12$ valence units. The Na1 and Na3 sites are part of the low-energy diffusion network identified in this manner, while the Na2 site is much more difficult to access.

$Na_3VP_3O_9N$ can be synthesized from either V_2O_3 or V_2O_5 by using thermal ammonolysis at synthetic temperatures between 650 ℃ and 800 ℃, the as-prepared powder was found to be partially melted at temperature higher than 700 ℃. The color of the as-prepared powder sample varies from light green to dark green as the synthetic temperature is increased. Small amount of NASICON-type $Na_3V_2(PO_4)_3$ impurity (< 5%) was often found in the products. The formation of NASICON impurity can be decreased or even diminished by adding small amount of carbon sources (e.g. ascorbic acid or citric acid) into the starting material. From SEM images, shown in Figure 3.2, the as-prepared sample has a particle size distribution between 5 μm and 20 μm, thus, for samples that were used for electrochemistry test, vibrated ball mill or high energy ball mill was carried out to break down the large particles into micron or sub-micron meter sized particles.

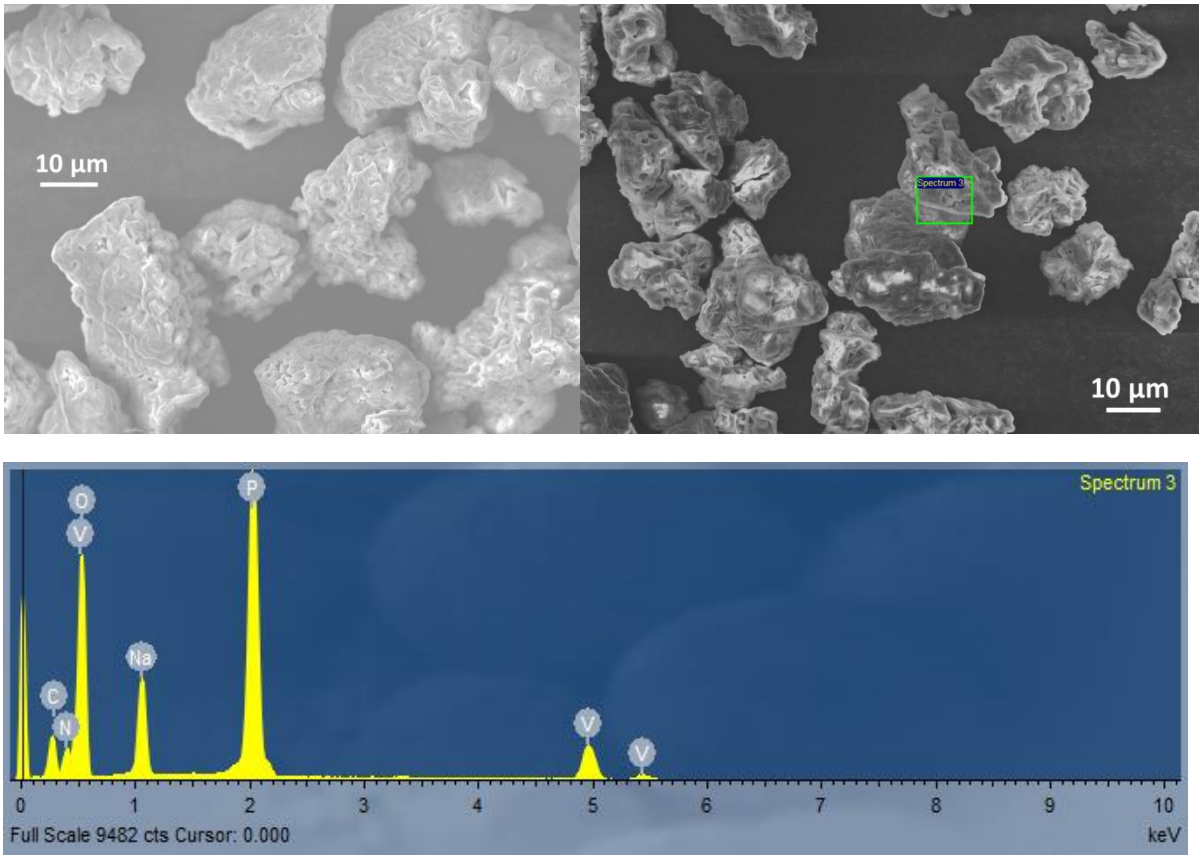

Figure 3.2 Top, SEM images of $Na_3VP_3O_9N$ synthesized at 720 ℃ with V_2O_5 as starting material. Bottom, SEM-EDX pattern of corresponded region shown in the green box.

Rietveld refinement of synchrotron XRD data of powder sample synthesized at 720 ℃ reveals that $Na_3VP_3O_9N$ has very similar crystal structure as previous reported $Na_3MP_3O_9N$ (M =Al, Ti) [19,26-31]. It also crystallizes in cubic $P2_13$ space group but with slightly different lattice parameter of 9.4507(3) Å. Three different sodium ion sites have been identified, Na1 was found to sit in a distorted octahedron formed by three O3 and three O1, a very long Na1-N cap (2.98 Å) was found to go through the center of the triangle formed by three O1, which overlaps with the 3-fold axis in the structure; Na2 sits in the center of a highly distorted octahedron formed by three O2 and three O3 with Na2-O1 and Na2-O2 distance equal to 2.461(7) Å and 2.326(6) Å separately; while Na3 can be best described by three coordinated with three Na3-O3 bonds of 2.375(7) Å, although it is also connected to three O1 and three O2 with very long Na3-O1 and Na3-O2 distances of 2.964(7) Å and 3.042(5) Å. Na bond valence sums (BVS) calculated for Na1, Na2 and Na3 are 0.71, 1.09 and 0.77 separately (R_{Na-O} = 1.756 Å, R_{Na-N} = 2.01 Å, b = 0.37)[32], indicating Na1 and Na3 are weakly bonded while Na2 is well bonded. Vanadium was found to sit in the center of a slightly distorted octahedron with two different types of vanadium oxygen bond distances, this VO_6 octahedron was further connected to six PO_3N tetrahedra via corner sharing oxygen ions (three O2 and three O3). Detailed structure information can be found in Tables 3.1 and 3.2. BVS calculation (R_V^{3+} =1.743 Å, b=0.37)[33] indicates vanadium is at the oxidation state of 3+ in $Na_3VP_3O_9N$, this is in consistent with V K-edge X-ray absorption near edge spectroscopy (XANES) data, which clearly showed vanadium is near 3+ and sit in an octahedron environment as indicated by the very weak pre-edge absorption peak, as can be seen in Figure 3.5.

Table 3.1 Atomic parameters for $Na_3VP_3O_9N$ (synchrotron XRD, X14A)

Atom	Wyck.	x	y	z	Occ.	B_{eq} (Å^2)
Na1	4a	0.0127(3)	0.0127(3))	0.0127(3))	1	2.53 (14)
Na2	4a	0.3920(4)	0.3920(4)	0.3920(4)	1	1.07 (14)
Na3	4a	0.7991(4)	0.7991(4)	0.7991(4)	1	2.63 (15)
V1	4a	0.5802(2)	0.5802(2)	0.5802(2)	1	1.11 (5)
P1	12b	0.0843(2)	0.0843(2)	0.0843(2)	1	0.68 (3)
O1	12b	0.0248(5)	0.8504(5)	0.2326(5)	1	1.12 (12)
O2	12b	0.0017(5)	0.1114(5)	0.3719(5)	1	0.56 (12)
O3	12b	0.1681(5)	0.3089(5)	0.4524(5)	1	1.15 (14)
N1	4a	0.1946(7)	0.1946(7)	0.1946(7)	1	0.91 (25)

Table 3.2 Selected bond lengths and bond valence sum values for $Na_3VP_3O_9N$

Bond type	**Distance (Å)**	**Atom**	**BVS**
Na1-O1 (×3)	2.586(5)	Na1	+0.71
Na1-O3 (×3)	2.596(6)	Na2	+1.08
Na1-N1	2.977(12)	Na3	+0.78
Na2-O2 (×3)	2.461(7)	V1	+3.14
Na2-O3 (×3)	2.328(6)	P1	+4.69
Na3-O1 (×3)	2.967(8)	O1	-1.88
Na3-O2 (×3)	3.045(5)	O2	-1.96
Na3-O3 (×3)	2.371(7)	O3	- 1.80
V1-O1 (×3)	1.957(5)	N1	-2.94
V1-O2 (×3)	2.009(5)	Gii	0.08
P1-O1	1.565(5)		
P1-O2	1.522(5)		
P1-O3	1.524(6)		
P1-N1	1.722(3)		

To estimate Na^+ conductivity of the as-prepared $Na_3VP_3O_9N$, sodium difference bond valence sum map was carried out in similar way as that of $Na_3TiP_3O_9N$[19]. The obtained difference BVS map is shown on the right side of Figure 3.1b, a much higher threshold value of 0.12 is needed to connect the potential mobile Na1 and Na3 sites, indicating more sluggish Na^+ ionic mobility in $Na_3VP_3O_9N$ than that in $Na_3TiP_3O_9N$. This was indeed confirmed by our temperature dependent ac impedance measurement of $Na_3VP_3O_9N$ pellet (density > 90 %), the room temperature resistance of this pellet falls out of the range of the impedance spectroscopy, as can be seen in Figure 3.4, we can easily assign a conductivity of $< 10^{-9}$ S/cm, the ionic conductivity was found to be about 3×10^{-8} S/cm at 60 ℃ with an activation energy of 0.84 eV, as shown in Figure 3.4. Although this material is not an excellent sodium ionic conductor as that of $Na_3TiP_3O_9N$[19], this conductivity value is reasonable for designing battery cathode, as exemplified by $LiFePO_4$[34,35].

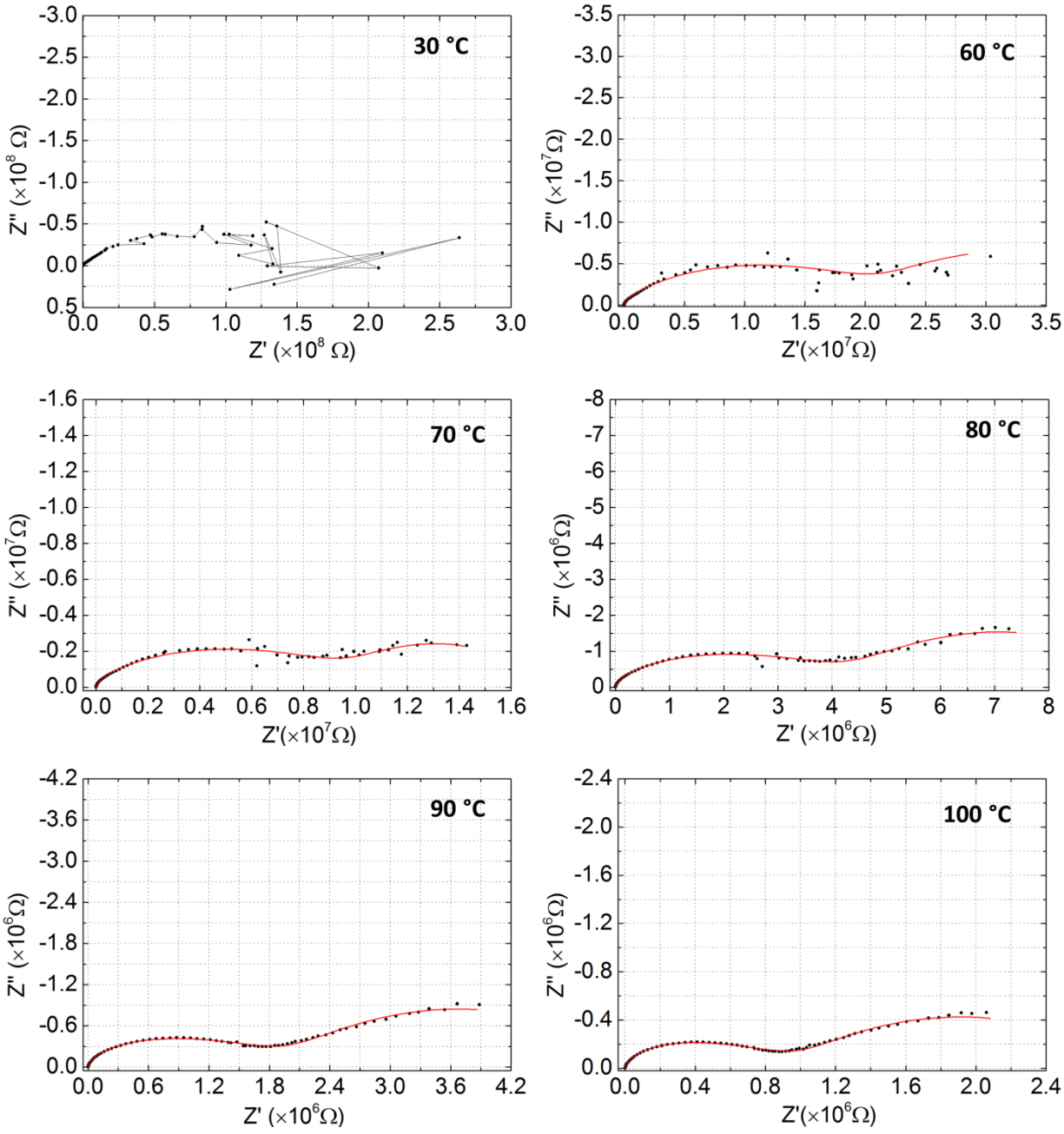
30 °C
Z'' (×10^8 Ω)
Z' (×10^8 Ω)
60 °C
Z'' (×10^7Ω)
Z'(×10^7Ω)
70 °C
Z'' (×10^7Ω)
Z'(×10^7Ω)
80 °C
Z'' (×10^6Ω)
Z' (×10^6Ω)
90 °C
Z'' (×10^6Ω)
Z' (×10^6Ω)
100 °C
Z'' (×10^6Ω)
Z'(×10^6Ω)

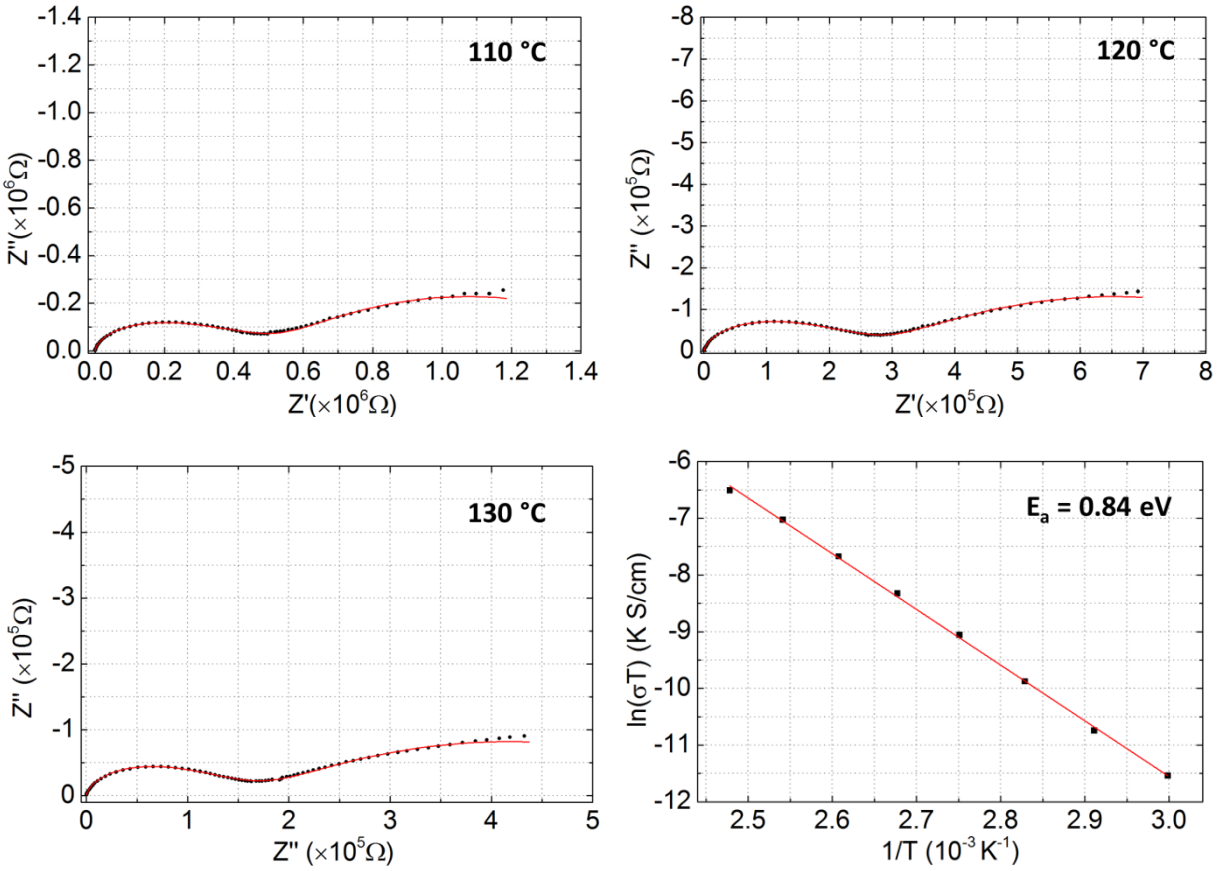

Figure 3.3 Temperature dependent a.c. impedance data of $Na_3VP_3O_9N$ pellet. Data was collected between 1MHz and 100 mHz with an polarization voltage of 100 mV.

To confirm that it is possible to remove Na^+ in the as-prepared $Na_3VP_3O_9N$, chemical desodiation was carried out, detailed information can be found in experimental parts. After desodiation for 48 hours, the color of the recovered powder was found to change from green to greenish black, as can be seen in Figure 3.5, indicating the oxidation of V^{3+} to V^{4+}. This was further confirmed by the shifting of V K-edge absorption edge to higher energy and the decrease of corresponded V-O distance. From X-ray diffraction pattern, shown in Figure 3.6, two different phases with distinct lattice parameters can be identified, and further whole pattern fitting reveals the lattice parameter was 9.3276(7) Å and 9.4333(5) Å for these two different phases separately, indicating a phase separation after desodiation. Although Rietveld refinement cannot be realized due to the serious peak overlapping at the high diffraction angles, the decreasing peak intensity of (002) peak while increasing intensity of (022) peak of the desodiated

phase indicates that Na1 site could be the potential sodium vacancy site, as proved in our previous report on desodiation of $Na_3TiP_3O_9N$[19]

.

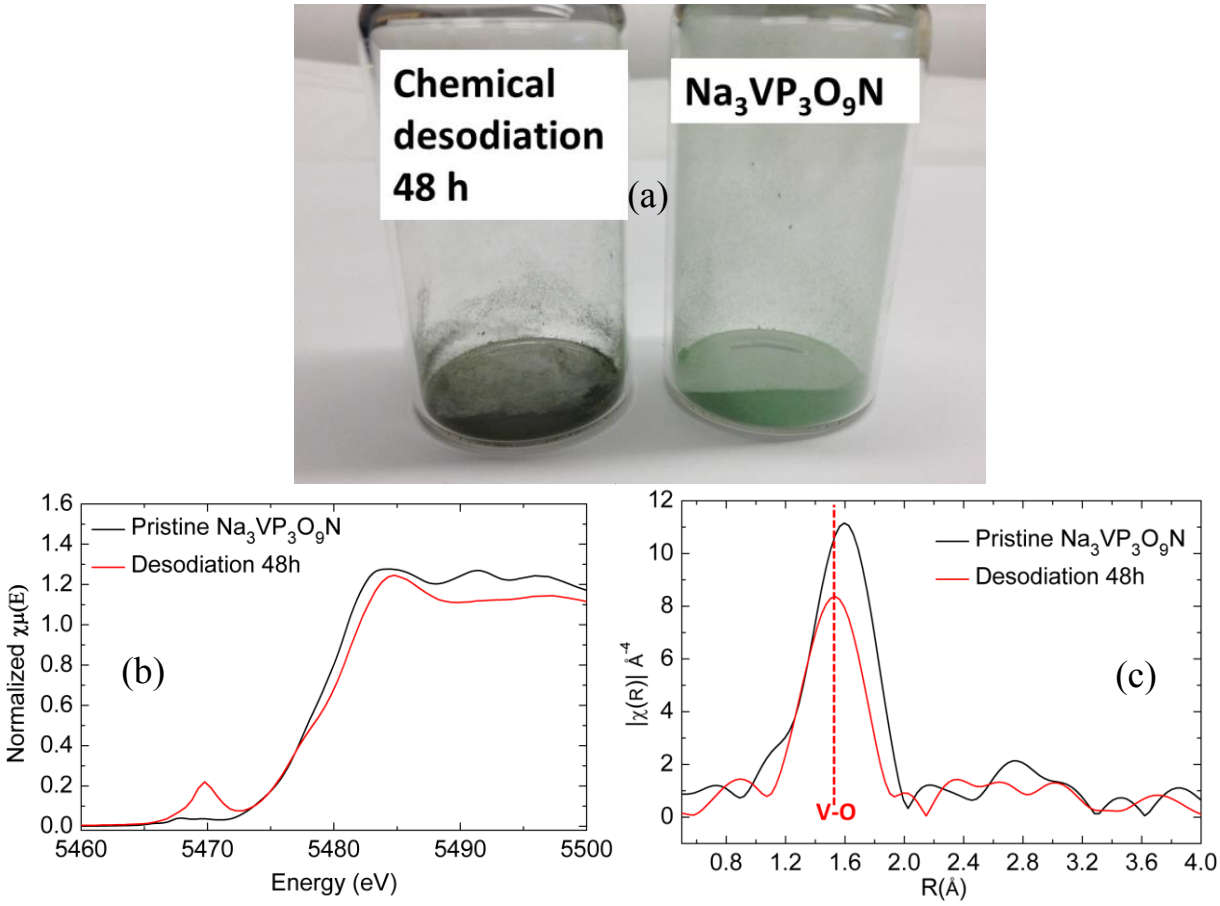

Figure 3.4 (a) Comparison of powders of pristine $Na_3VP_3O_9N$ and the reaction product after chemical desodiation (NO_2BF_4, 48 h treatment). (b) V K-edge XANES spectra for $Na_3VP_3O_9N$ before (black) and after (red) desodiation. (c) EXAFS spectra (k^3-weighted) obtained at the V K-edge is principally sensitive to the V-O interactions, and reflects the reduction in V-O bond lengths after chemical desodiation.

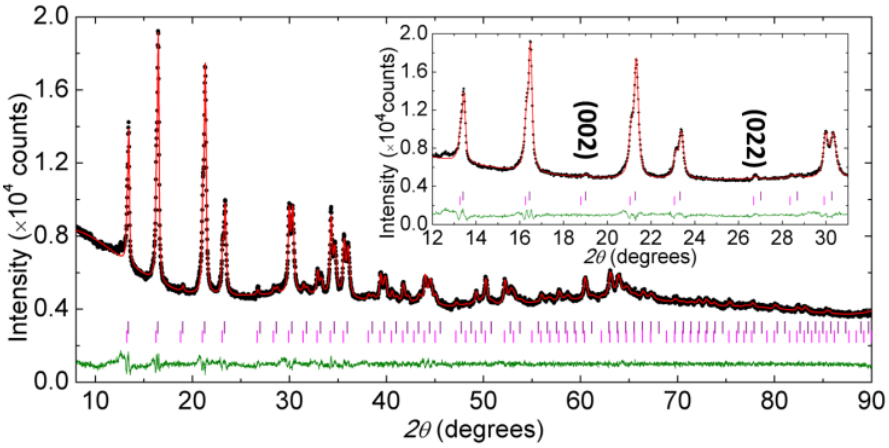

Figure 3.5 Le Bail fit to laboratory (Cu Kα) XRD data for chemically desodiated $Na_3VP_3O_9N$. Data are shown as black dots, the calculated intensity curve in red, and the difference curve in olive. The positions of Bragg peaks are marked in purple (smaller cubic phase) and magenta (larger cubic phase). The zoom region shows the intensity of the (002) and (022) diffraction peaks for the desodiated phase, whose pattern of intensity changes is characteristic of removal of Na from the Na1 site.

All of the above results indicate that $Na_3VP_3O_9N$ can work as potential cathode material for rechargeable Na-ion batteries. Indeed, this material can effectively cycle against Na^+/Na at at 20 °C, a reversible specific capacity of about 35 mAh/g, corresponding to about 0.5 Na^+, can be achieved, as can be seen in Figure 3.6 and 3.7b. Interestingly, the average charge/discharge plateau was found to be as high as 4.0 V, which is 0.6 V higher than the well-known NASICON-type $Na_3V_2(PO_4)_3$[36]. To achieve higher capacity, further battery test was carried out at 40 °C to improve both electronic and ionic conductivity. A reversible discharge capacity of 60 mAh/g, corresponding to 0.83 Na^+, was obtained between 2.5 V and 4.4 V at C/30 rate, as shown in Figure 3.8a. Further attempts to increase the charge voltage were unsuccessful, which may due to the electrolyte decomposition at voltages higher than 4.5 V. Thus, the development of high voltage sodium-ion electrolyte will be critical for further optimization of this high voltage sodium-ion cathode material.

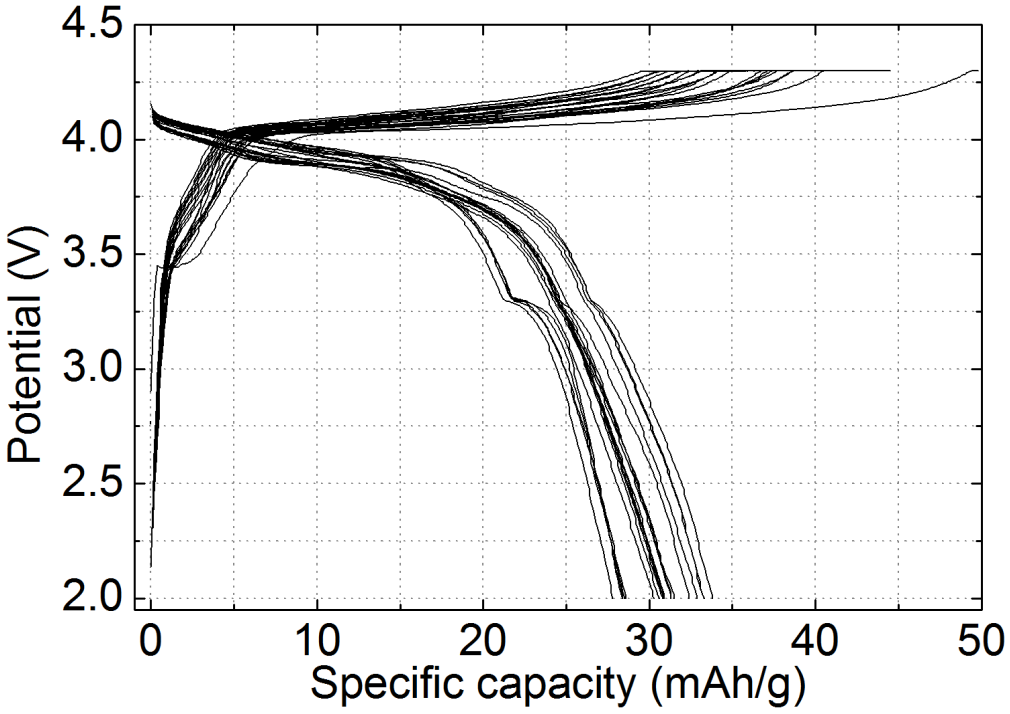

Figure 3.6 Galvanostatic cycling of $Na_3VP_3O_9N$ against Na^+/Na at a rate of C/30 and temperature of 20 ℃ over a voltage window of 2.0 V to 4.4 V.

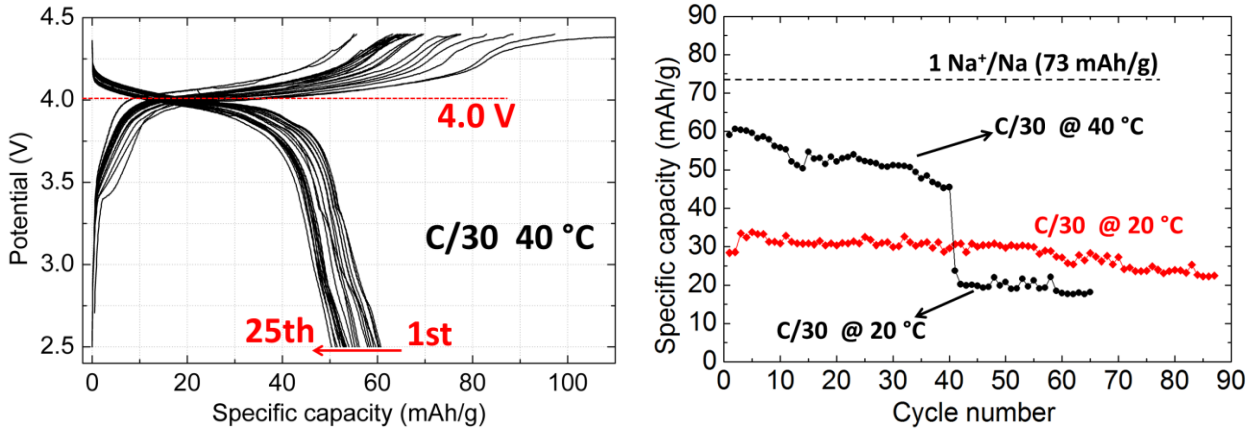

Figure 3.7 Left, Galvanostatic cycling of $Na_3VP_3O_9N$ against Na^+/Na at a rate of C/30 and temperature of 40 ℃ between 2.5 V and 4.4 V. Right, cycling performance of $Na_3VP_3O_9N$ against Na^+/Na at C/30 rate and temperature of 20 ℃ and 40 ℃.

Based on the structure study, we have noticed the existence of at least two potential mobile Na^+ (Na1 and Na3) within this structure type, therefore, if the $V^{3+}/V^{4+}/V^{5+}$ multi-electron redox couples can be utilized, a theoretical capacity of 145 mAh/g can be achieved. What's more, the redox potential associated with V^{3+}/V^{4+} in this compound was found to be averaged at 4.0 V for the Na-ion battery, thus it is expected that the redox potential of V^{4+}/V^{5+} could be even higher. Hence, a minimum theoretical energy density of 580 W/kg (based on 4.0 V redox potential) could be potentially realized. Utilizing high potential V^{4+}/V^{5+} redox couple is found to be difficult in a sodium-ion battery due to the decomposition of electrolyte and relative poor sodium ion mobility in the highly desodiated state. However, it may be realized in Li-ion batteries for two reasons: first, lithium-ion electrolyte is well optimized after many years' development. Various additives, such as fluoroethylene carbonate (FEC)[37,38], have been demonstrated to be effective to inhibit the decomposition of electrolyte at high voltages. Second, these cubic nitridophosphate compounds showed much higher Li^+ conductivity than Na^+ conductivity, which has been demonstrated in our study of $Li_xFe_2P_3O_9N$ and $Li_2Mg_2P_3O_9N$[19,25]. Therefore, to further explore the plausibility of utilizing V^{4+}/V^{5+} in $Na_3VP_3O_9N$, hybrid-ion type batteries ($Na_3VP_3O_9N$ against Li^+/Li), were constructed. This hybrid-ion system has been previously used to evaluate electrochemical performance of Na_2FePO_4F and $NaVPO_4F$[39,40].

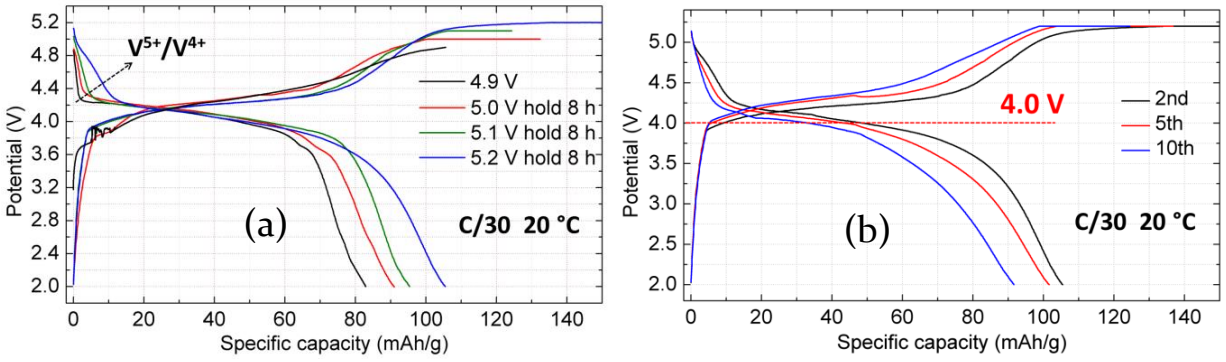

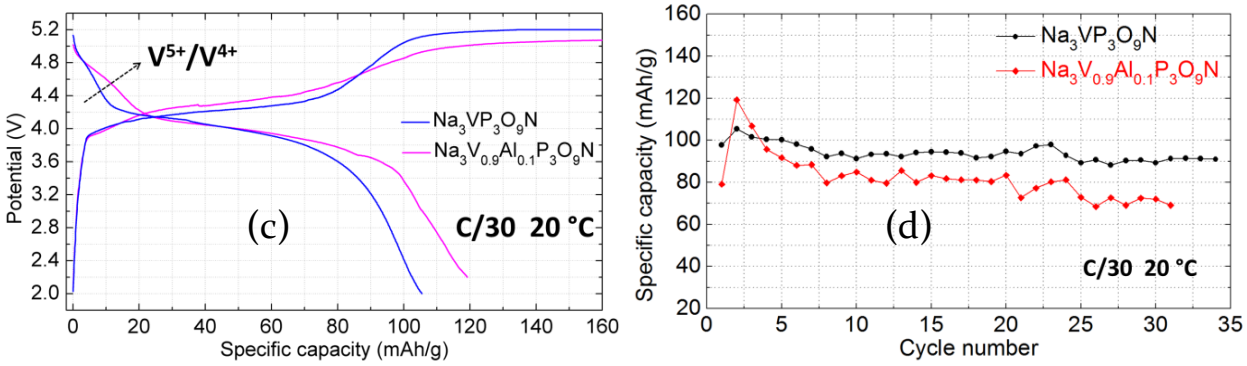

Figure 3.8 (a) Charge/discharge curves of $Na_3VP_3O_9N$ against Li^+/Li with different charge voltage cut offs, it clearly shows the increase of discharge capacity contributed from V^{5+}/V^{4+}. (b) 2nd, 5th, and 10th charge/discharge curve of $Na_3VP_3O_9N$ against Li^+/Li between 2.0 V and 5.2 V (hold for 8 hours). The increased polarizatoin may due to the electrolyte decomposition at high voltages associated with strong catalytic effect of V^{4+}/V^{5+} (c) 2nd charge/discharge curves of $Na_3VP_3O_9N$ and $Na_3V_{0.9}Al_{0.1}P_3O_9N$ in hybrid-ion cell at C/30 rate, $Na_3V_{0.9}Al_{0.1}P_3O_9N$ shows higher discharge capacity contributed from V^{5+}/V^{4+} (d) Cylability of the $Na_3VP_3O_9N$ and $Na_3V_{0.9}Al_{0.1}P_3O_9N$ hybrid-ion cells between 2.0 V and 5.2 V at C/30 rate.

Different cut off voltages (4.9 V, 5.0 V, 5.1 V and 5.2 V) were tested for $Na_3VP_3O_9N$ against Li^+/Li, as can be seen in Figure 3.9a. When the cell was charged to 4.9 V, a discharge capacity of 80 mAh/g was obtained, corresponding to the insertion of 1.10 Li^+/Na^+ ion in $Na_{3-x}Li_xVP_3O_9N$. When the cell was charged to 5.0 V and hold at his potential for 8 hours, a higher discharge capacity of 90 mAh/g can be achieved, corresponding to the insertion of 1.25 $Li^{+/}Na^+$. The discharge capacity can be further increased to 95 mAh/g and 105 mAh/g, corresponding to about 1.30 and 1.50 $Li^{+/}Na^+$ separately, when the hybrid-ion cell was charged to 5.1 V and 5.2 V and held at these voltages for 8 hours. Interestingly, the increased capacity contribution from V^{4+}/V^{5+} can be clearly seen on the discharge curve, which is associated with the high voltage plateau centered at about 4.70 V. The accessibility of V^{5+} has been further confirmed by V *K*-edge XANES spectrum, which clearly showed the *K*-edge absorption energy of recovered electrode (after charging to 5.2 V) is much higher than that of V^{4+} (VO_2) and is near that of V_2O_5 (V^{5+}). Extensively cycling of the battery between 2.0 V and 5.2 V would result in increasing polarization of charge and discharge curves, as can be seen in Figure 3.9b, which is likely due to the decomposition of the electrolyte, this assumption was further confirmed by the cycling of samples after high energy ball mill with much smaller particle sizes, which showed much worse capacity retention

and higher polarization, as can be seen in Figure 3.10. Nevertheless, a reversible discharge capacity of 90 mAh/g can be maintained after 30 cycles.

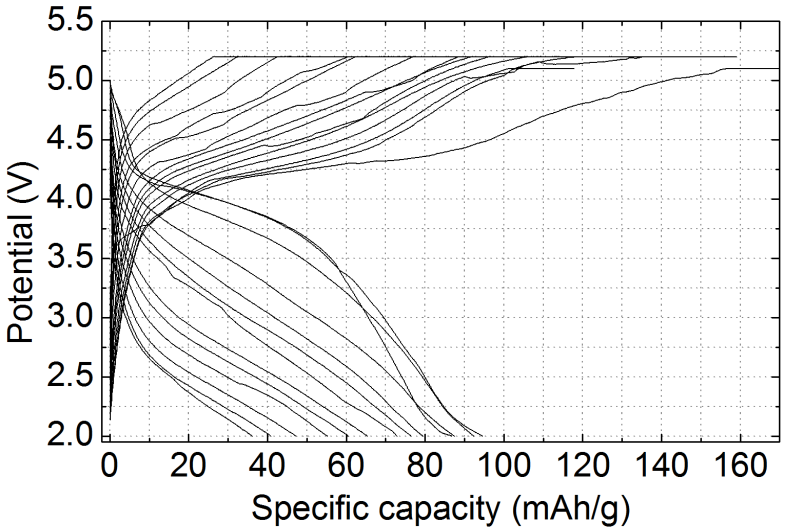

Figure 3.9 Galvanostatic cycling of high energy ball milled $Na_3VP_3O_9N$ against Li^+/Li at a rate of C/30 rate and temperature of 20 ℃ with voltage window of 2.0 V to 5.2 V.

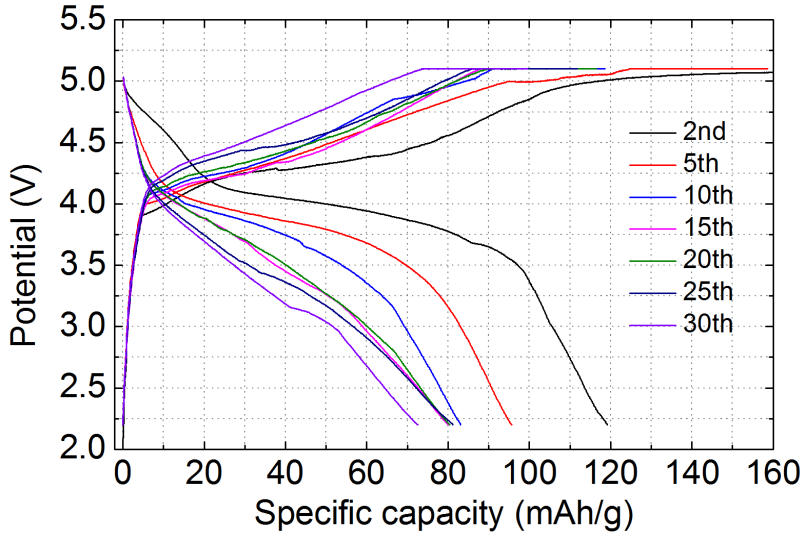

Figure 3.10 $Na_3V_{0.9}Al_{0.1}P_3O_9N$ cycled against Li^+/Li at a rate of C/30 and temperature of 20 ℃ between 2.2V and 5.2 V.

For $Na_3VP_3O_9N$, a discharge capacity of 105 mAh/g can be achieved between 2.0 V and 5.2 V, which means only 50 % V^{3+} has been fully oxidized to V^{5+}, the other half has only been oxidized to V^{4+}. Therefore, the discharge capacity can be further increased if more V^{3+} can be oxidized to V^{5+}. It has been reported previously that Al^{3+}/V^{3+} substitution can be used to increase high voltage capacity (associated with V^{5+}/V^{4+}) for monoclinic $Li_3V_2(PO_4)_3$[41]. Thus, we used similar strategy and synthesized the 10% aluminum substituted $Na_3V_{0.9}Al_{0.1}P_3O_9N$, the galvanostatic charge/discharge curve of this material between 2.2V and 5.15 V is shown in Figure 3.9c and 3.9d. A much higher discharge capacity of 120 mA/g, corresponding to 1.8 Li^+/Na^+, was achieved for this 10% aluminum substituted sample. It is also worth to notice that the increased capacity is mainly due to the utilization of high voltage V^{5+}/V^{4+}. Unfortunately, the cyclability is worsening when large amount of V^{5+} is utilized, as can be seen in Figure 3.11. However, it is expected that surface coating may help to reduce this type of capacity fading[42].

Ex situ synchrotron XRD pattern of electrode materials recovered after 10 cycles (discharge to 2.0 V) is shown in Figure 3.11, it can be seen that the sample is still well crystallized with all major diffraction peaks that can be indexed to the non-centersymmetrical cubic space group $P2_13$. Rietveld refinement of this data showed that Na^+ at Na2 site has been fully replaced by Li^+, and Na^+ at Na3 site has been mostly exchanged by Li^+ while Na^+ at Na1 site is only slightly exchanged. The local Na^+/Li^+ environment change is shown in Figure 3.11c, it was found that the average Na1(Li1)-O3 bond distances increased while Na1(Li1)-O1 and Na1(Li1)-N distances declined compared to pure sodium analogue, Li2 sit in a rather distorted LiO_6 octahedron, Na3(Li3) still sit on the top of triangle formed by three O3 but with much shorter average Na3(Li3)-O3 bond lengths of 2.10 Å, this result is consistent with our Li^+/Na^+ ion exchange study of $Na_3MP_3O_9N$ (M = Al, Ga or V), details can be found in chapter 4 and chapter. The 10^{th} cycled material has the chemical formula of $(Li1)_{\sim 0.2}(Na1)_{\sim 0.8}(Li2)_1(Li3)_{\sim 0.7}(Na3)_{\sim 0.3}VP_3O_9N$. Interestingly, from the calculated lithium difference BVS map, it can be seen that all three Na1, Li2 and Na3 sites are located within an potential three dimensional Li^+ diffusion channel with minimum threshold value ($|\Delta V|$) of 0.05 valence unit, indicating this hybrid Li^+/Na^+ compound has facile Li^+ conductivity, which may also be the reason for much better performance of hybrid-ion batteries than that of pure Na-ion batteries.

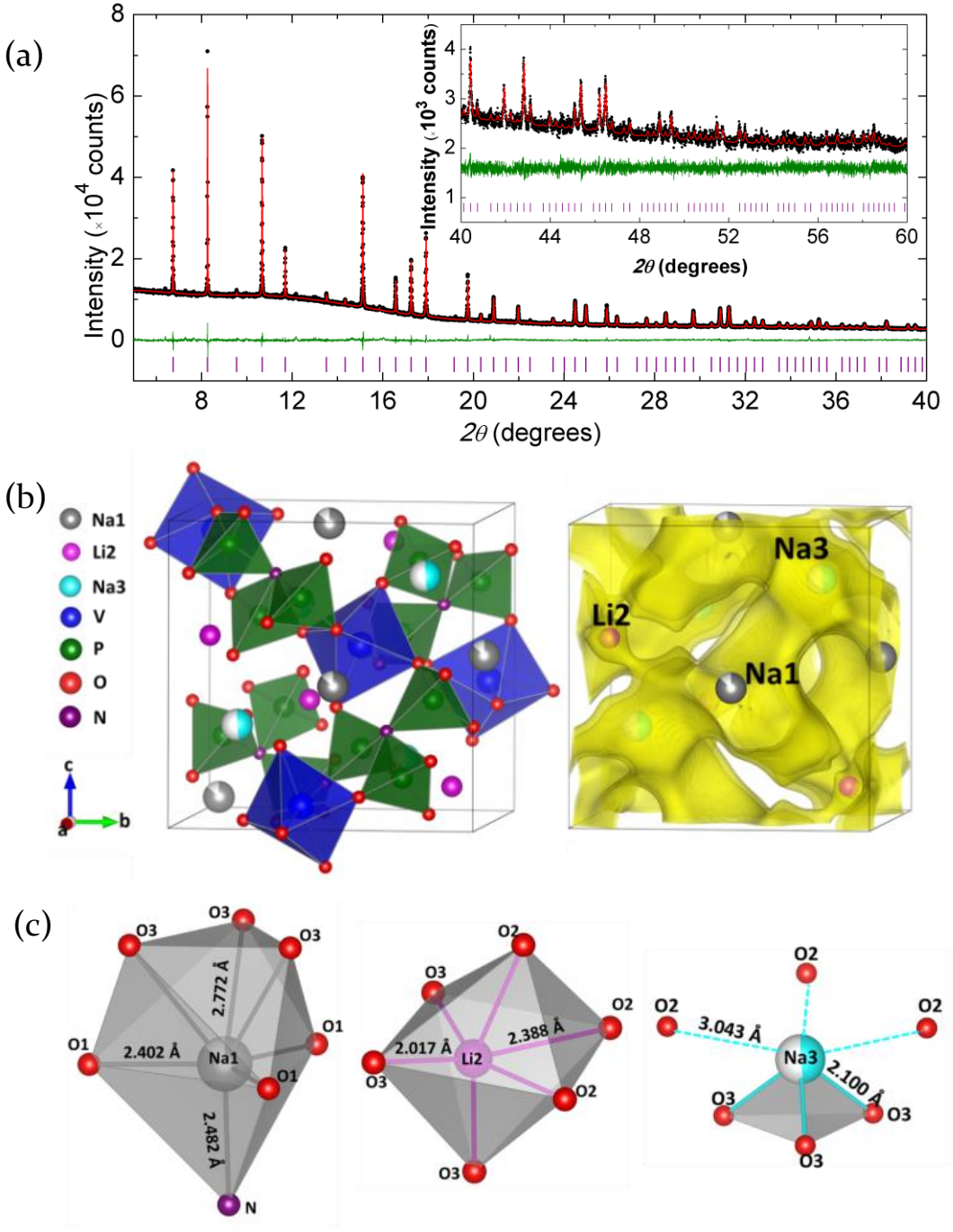

Figure 3.11 (a) Rietveld refinement of $Na_3VP_3O_9N$ structure using synchrotron XRD (λ=0.7714 Å) data, with data points shown in black, calculated curve in red and difference curve in olive. (b) Left, crystal structure of the compound after 10 cycles; right, Li^+ difference BVS map of the compound after 10 cycles with threshold value of 0.05 valence unit. (c) Local environments of Na1(Li1), Li2 and Na3(Li3).

Table 3.3 Atomic parameters for $Na_{3-x}Li_xVP_3O_9N$ (synchrotron XRD, X14A)

Atom	Wyck.	*x*	*y*	*z*	Occ.	B_{eq} (Å^2)
Na1	4a	0.0358(4)	0.0358(4)	0.0358(4)	0.86(1)*	2
Li2	4a	0.3797(17)	0.3797(17)	0.3797(17)	1	2
Na3	4a	0.8170(9)	0.8170(9)	0.8170(9)	0.48(1)*	2
V1	4a	0.5725(1)	0.5725(1)	0.5725(1)	1	0.44(5)
P1	12b	0.0894(3)	0.0894(3)	0.0894(3)	1	0.58(4)
O1	12b	0.0194(6)	0.0194(6)	0.0194(6)	1	1.32(7)
O2	12b	-0.0023(6)	-0.0023(6)	-0.0023(6)	1	1.32(7)
O3	12b	0.1822(5)	0.1822(5)	0.1822(5)	1	1.32(7)
N1	4a	0.1904(7)	0.1904(7)	0.1904(7)	1	1.76(30)

* X-ray scattering factor ratio of $f_{Na}/f_{Li} \approx 3$, hence Na1 site is occupied by 80% Na^+ and 20% Li^+, Na3 site is occupied by 30 % Na^+ and 70% Li^+.

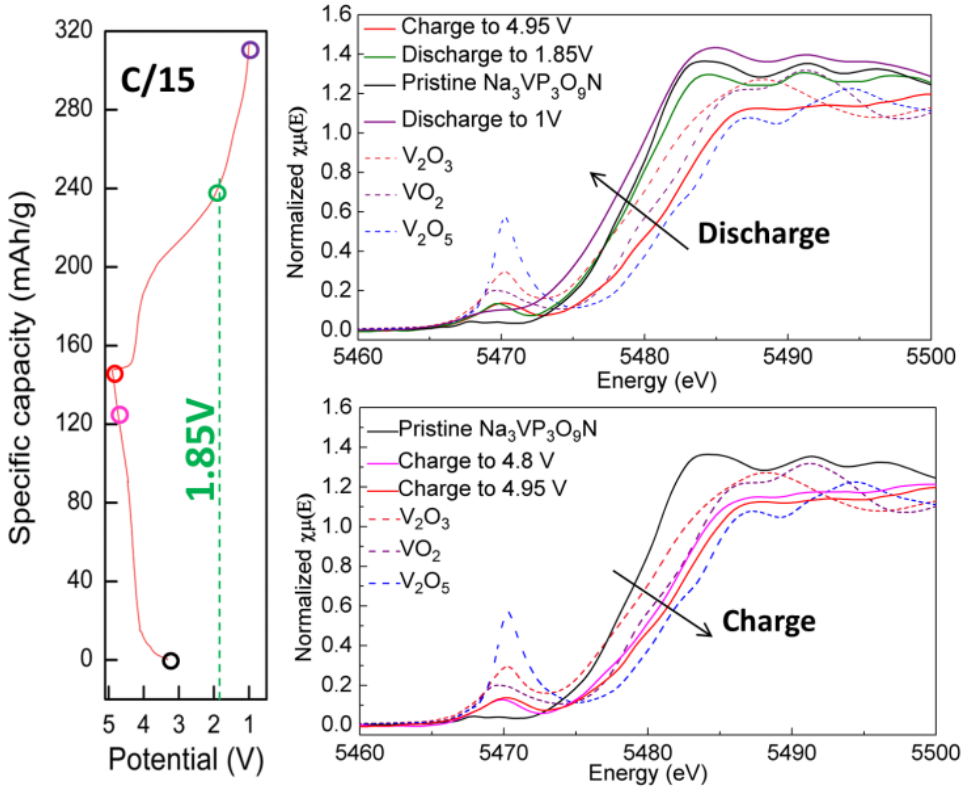

Figure 3.12 *In situ* V K-edge XANES spectra of $Na_3VP_3O_9N$ collected during initial charge and discharge cycle against Li^+/Li between 1.0 V and 4.95 V at C/15 rate. It clearly shows vanadium was oxidized to V^{5+} at voltage higher than 4.8 V during charge, and it was fully reduced back to V^{3+} at around 1.85 V, further discharge of the cell led to the formation of V^{2+}.

To further confirm that vanadium multi-electron redox couples has been successfully utilized during charge and discharge, *in situ* XANES spectra were collected for $Na_3VP_3O_9N$ hybrid-ion cell cycled between 1.0 V and 4.95 V. Results are shown in Figure 3.12. During initial charge process, V^{3+} was first oxidized to V^{4+} at voltage around 4.0 V, and further oxidizing of V^{4+} to V^{5+} happened at voltages higher than 4.8 V; during initio discharge, V^{5+} was first reduced to V^{4+} at voltages above 4.15 V, and it was then fully reduced back to V^{3+} at about 1.85 V. However, it is worth to note that it is difficult to figure out the exact charge compensation mechanism between 4.3 V and 4.15 V during discharge, since both V^{5+}/V^{4+} and V^{4+}/V^{3+} may contribute to the capacity within this voltage window. Interestingly, it was found that V^{3+} can be further reduced to V^{2+} when the *in situ* cell was discharged to lower voltages, indicating the possibility of incorporating more than three Li^+ into this compound, this was further confirmed by large discharge capacity (~ 160 mAh/g) obtained for hybrid-ion batteries cycled between 1.0 V and 4.95 V, as can be seen in Figure 3.13.

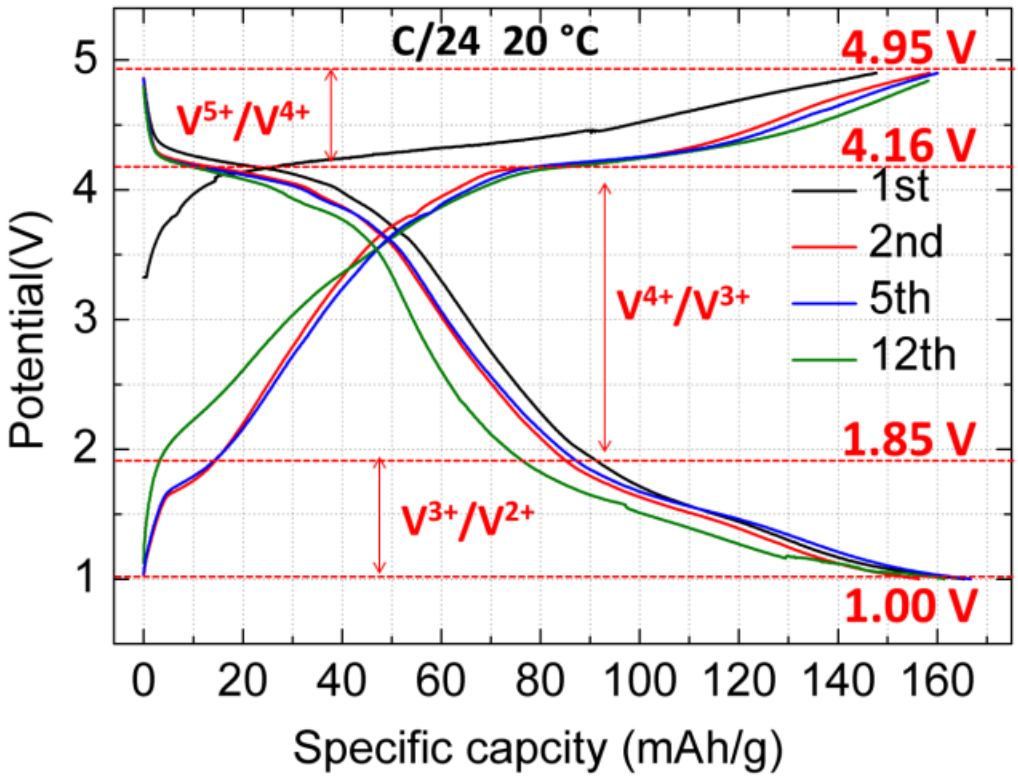

Figure 3.13 $Na_3VP_3O_9N$ cycled against Li^+/Li at C/24 rate at 20 ℃ between 1.0 V and 4.95 V.

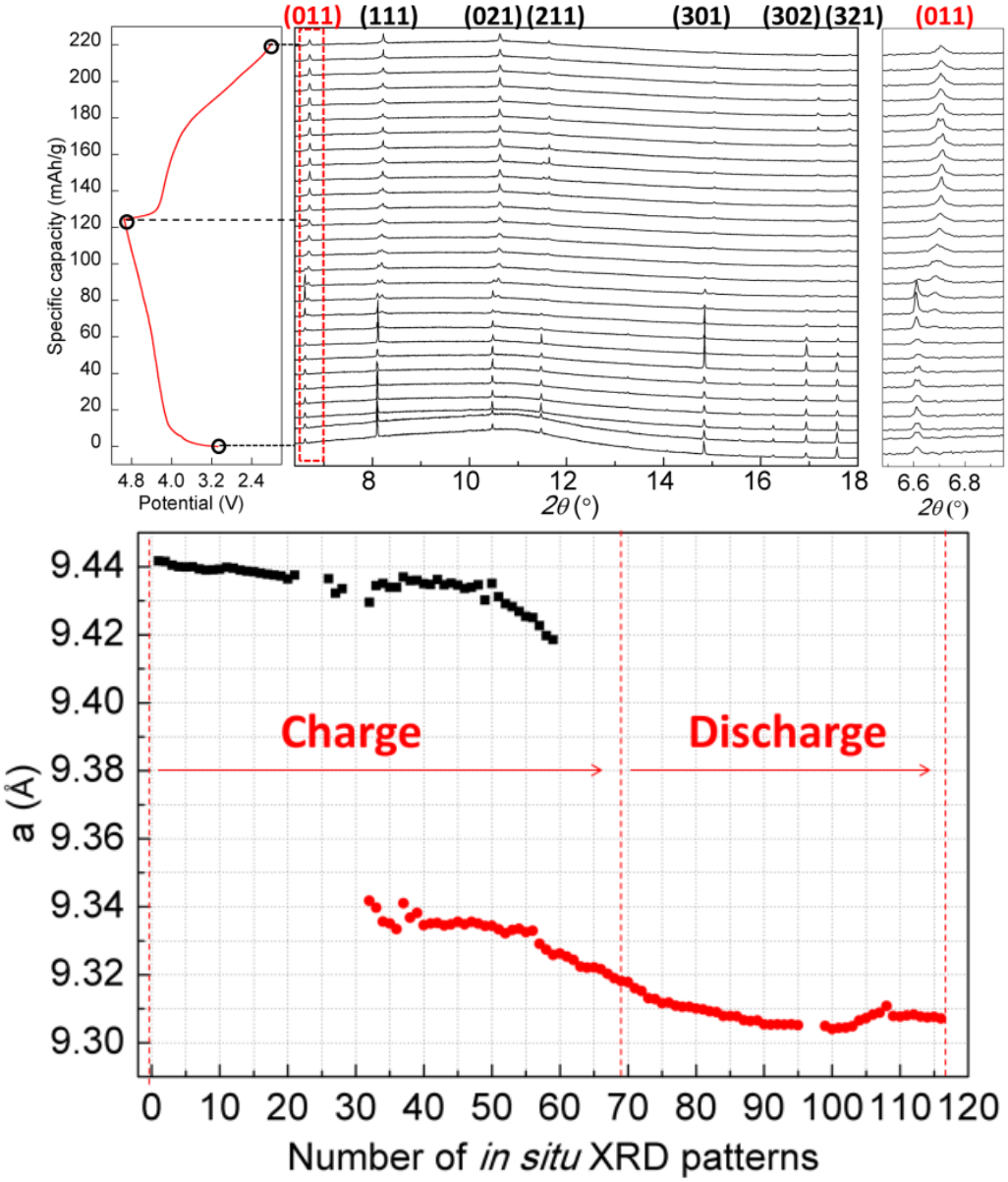

Figure 3.14 Top, *in situ* XRD patterns collected during charge and discharge of $Na_3VP_3O_9N$ against Li^+/Li between 2.0 V and 4.95 V at C/18 rate, only one out of every four patterns are shown here for clarity. Bottom, lattice parameter evolution of two distinct phases during charge/discharge.

While XANES proves the feasibility of using multi-electron redox couple in this compound, XRD can further reveal the structure evolution during charge/discharge process. *In situ* XRD patterns collected during initial charge/discharge cycle between 2.0 V and 4.95 V are shown in Figure 3.14.

During charge, the structure was found to first follow a solid solution reaction, the second phase was not formed until the voltage reached 4.3 V, this biphasic region continues until about 4.7 V, further charge process was found to follow another solid solution with lattice parameter decreased monotonically. Surprisingly, only one phase was found during the initial discharge with lattice parameter decreasing as Li^+/Na^+ intercalating. this phenomenon may due to two reasons: first, aside from Li^+/Na^+ reinsertion into the structure during discharge (contributes to discharge capacity), simultaneously, there is Li^+/Na^+ ion exchange carrying on between Na^+ in the cation deficient $Na(Li)_{3-x}VP_3O_9N$ and Li^+ in the Li-containing electrolyte, this ion exchange will result in the shrinkage of volume since Li^+ has much smaller ion radii (0.74 Å) than that of Na^+ (1.02 Å)[43]; second, Li^+ reinsertion into specific vacant sites may result into volume shrinkage instead of volume expansion, although this is rare for most battery cathode but not entirely impossible, this has also been observed in our *in situ* XRD study of charge/discharge of pure lithium variant $Li_3VP_3O_9N$, which showed volume expansion during lithium extraction and shrinkage during lithium reinsertion, which can be found in Chapter 5. As been mentioned above, and also been proved in our previous reports on $Li_xFe_2P_3O_9N$[20] and $Li_2Mg_2P_3O_9N$[25]. Li variants of CUBICON nitridophosphates usually showed way much higher Li^+ conductivity than Na^+ conductivity of corresponded sodium analogues, thus, it is expected that higher rate and better cycle performance could be achieved for $Li_3VP_3O_9N$, which we are planning to discuss in another paper.

3.4 Conclusion

In summary, $Na_3VP_3O_9N$ has been first time demonstrated to be a promising 4.0 V cathode material for rechargeable Na/Li-ion batteries. The $V^{3+}/V^{4+}/V^{5+}$ multi-electron redox couples can be utilized when $Na_3VP_3O_9N$ is cycled against Li^+/Li between 2.0 V and 5.2 V, a specific discharge capacity of 105 mAh/g can be delivered. Redox potential of V^{4+}/V^{5+} was found to be as high as 4.7 V in this system. To the best of our knowledge, this is the highest redox potential that has ever been observed for vanadium-based polyanion compounds. These results proved the feasibility of utilizing multi-electron transfer redox couples in the CUBICON nitridosphophates. Further improvements can be achieved by synthesizing carbon coated materials or improving high voltage electrolyte additives.

Reference

(1) Whittingham, M. S. *Chem. Rev.* **2014**, *114*, 11414.
(2)Hautier, G.; Jain, A.; Ong, S. P.; Kang, B.; Moore, C.; Doe, R.; Ceder, G. *Chem. Mater.* **2011**, *23*, 3495.
(3) Ohzuku, T.; Makimura, Y. *Chem. Lett.* **2001**, 744.
(4)Lu, Z. H.; MacNeil, D. D.; Dahn, J. R. *Electrochemical and Solid State Letters* **2001**, *4*, A191.
(5)Zhong, Q. M.; Bonakdarpour, A.; Zhang, M. J.; Gao, Y.; Dahn, J. R. *J. Electrochem. Soc.* **1997**, *144*, 205.
(6) Amine, K.; Tukamoto, H.; Yasuda, H.; Fujita, Y. *J. Electrochem. Soc.* **1996**, *143*, 1607.
(7) Cushing, B. L.; Goodenough, J. B. *J. Solid State Chem.* **2001**, *162*, 176.
(8) Gaubicher, J.; Wurm, C.; Goward, G.; Masquelier, C.; Nazar, L. *Chem. Mater.* **2000**, *12*, 3240.
(9) Nishimura, S.; Nakamura, M.; Natsui, R.; Yamada, A. *J. Am. Chem. Soc.* **2010**, *132*, 13596.
(10) Tamaru, M.; Barpanda, P.; Yamada, Y.; Nishimura, S.; Yamada, A. *J. Mater. Chem.* **2012**, *22*, 24526.
(11) Sun, M. L.; Rousse, G.; Abakumov, A. M.; Saubanere, M.; Doublet, M. L.; Rodriguez-Carvajal, J.; Van Tendeloo, G.; Tarascon, J. M. *Chem. Mater.* **2015**, *27*, 3077.
(12) Saidi, M. Y.; Barker, J.; Huang, H.; Swoyer, J. L.; Adamson, G. *Electrochemical and Solid State Letters* **2002**, *5*, A149.
(13) Huang, H.; Yin, S. C.; Kerr, T.; Taylor, N.; Nazar, L. F. *Adv. Mater.* **2002**, *14*, 1525.
(14) Gaubicher, J.; Le Mercier, T.; Chabre, Y.; Angenault, J.; Quarton, M. *J. Electrochem. Soc.* **1999**, *146*, 4375.
(15) Kerr, T. A.; Gaubicher, J.; Nazar, L. F. *Electrochemical and Solid State Letters* **2000**, *3*, 460.
(16) Dupre, N.; Gaubicher, J.; Le Mercier, T.; Wallez, G.; Angenault, J.; Quarton, M. *Solid State Ionics* **2001**, *140*, 209.
(17) Chen, H. L.; Hao, Q.; Zivkovic, O.; Hautier, G.; Du, L. S.; Tang, Y. Z.; Hu, Y. Y.; Ma, X. H.; Grey, C. P.; Ceder, G. *Chem. Mater.* **2013**, *25*, 2777.
(18) Wen, B. H.; Chernova, N. A.; Zhang, R. B.; Wang, Q.; Omenya, F.; Fang, J.; Whittingham, M. S. *Chem. Mater.* **2013**, *25*, 3513.
(19) Liu, J.; Chang, D. H.; Whitfield, P.; Janssen, Y.; Yu, X. Q.; Zhou, Y. N.; Bai, J. M.; Ko, J.; Nam, K. W.; Wu, L. J.; Zhu, Y. M.; Feygenson, M.; Amatucci, G.; Van der Ven, A.; Yang, X. Q.; Khalifah, P. *Chem. Mater.* **2014**, *26*, 3295.
(20) Liu, J.; Yu, X. Q.; Hu, E. Y.; Nam, K. W.; Yang, X. Q.; Khalifah, P. G. *Chem. Mater.* **2013**, *25*, 3929.
(21) Rietveld, H. M. *J. Appl. Crystallogr.* **1969**, *2*, 65.
(22) Lebail, A.; Duroy, H.; Fourquet, J. L. *Mater. Res. Bull.* **1988**, *23*, 447.
(23) Hu, E.; Bak, S.-M.; Liu, J.; Yu, X.; Zhou, Y.; Ehrlich, S. N.; Yang, X.-Q.; Nam, K.-W. *Chem. Mater.* **2014**, *26*, 1108.
(24) Seel, J. A.; Dahn, J. R. *J. Electrochem. Soc.* **2000**, *147*, 892.
(25) Liu, J.; Whitfield, P.; Saccomanno, M.; Bo, S.-H.; Hu, E.; Yu, X.; Bai, J.; Grey, C.; Yang, X.-Q.; Khalifah, P.
(26) Zatovsky, I. V.; Vorobjova, T. V.; Domasevitch, K. V.; Ogorodnyk, I. V.; Slobodyanik, N. S. *Acta Crystallogr., Sect. E: Struct. Rep. Online* **2006**, *62*, 32.
(27) Massiot, D.; Conanec, R.; Feldmann, W.; Marchand, R.; Laurent, Y. *Inorg. Chem.* **1996**, *35*, 4957.
(28) Conanec, R.; Feldmann, W.; Marchand, R.; Laurent, Y. *J. Solid State Chem.* **1996**, *121*, 418.

(29) Conanec, R.; Lharidon, P.; Feldmann, W.; Marchand, R.; Laurent, Y. *Eur. J. Solid State Inorg. Chem.* **1994**, *31*, 13.
(30) Feldmann, W. *Zeitschrift Fur Chemie* **1987**, *27*, 100.
(31) Feldmann, W. *Zeitschrift Fur Chemie* **1987**, *27*, 182.
(32) Wood, R. M.; Palenik, G. J. *Inorg. Chem.* **1999**, *38*, 3926.
(33) Brown, I. D.; Altermatt, D. *Acta Crystallographica Section B-Structural Science* **1985**, *41*, 244.
(34) Li, J. Y.; Yao, W. L.; Martin, S.; Vaknin, D. *Solid State Ionics* **2008**, *179*, 2016.
(35) Padhi, A. K.; Nanjundaswamy, K. S.; Goodenough, J. B. *J. Electrochem. Soc.* **1997**, *144*, 1188.
(36) Jian, Z. L.; Zhao, L.; Pan, H. L.; Hu, Y. S.; Li, H.; Chen, W.; Chen, L. Q. *Electrochem. Commun.* **2012**, *14*, 86.
(37) Hu, L. B.; Zhang, Z. C.; Amine, K. *Electrochem. Commun.* **2013**, *35*, 76.
(38) Zhang, Z. C.; Hu, L. B.; Wu, H. M.; Weng, W.; Koh, M.; Redfern, P. C.; Curtiss, L. A.; Amine, K. *Energy & Environmental Science* **2013**, *6*, 1806.
(39) Ellis, B. L.; Makahnouk, W. R. M.; Makimura, Y.; Toghill, K.; Nazar, L. F. *Nat. Mater.* **2007**, *6*, 749.
(40) Barker, J.; Saidi, M. Y.; Swoyer, J. L. *J. Electrochem. Soc.* **2004**, *151*, A1670.
(41) Barker, J.; Gover, R. K. B.; Burns, P.; Bryan, A. *J. Electrochem. Soc.* **2007**, *154*, A307.
(42) Rui, X. H.; Li, C.; Chen, C. H. *Electrochim. Acta* **2009**, *54*, 3374.
(43) Shannon, R. D.; Prewitt, C. T. *Acta Crystallographica Section B-Structural Crystallography and Crystal Chemistry* **1969**, *B 25*, 925.

Chapter 4 Metastable Li-ion CUBICONs as potential cathode materials for rechargeable Li-ion batteries

4.1 Introduction

During the early years of exploration for practical cathode materials for rechargeable Li-ion batteries, lithium transition metal oxides such as $LiCoO_2$[2] and $LiNiO_2$[3] had attracted tremendous attention due to their high energy density and ease of synthesis. Later on, more complex oxides such as $LiNi_{1/3}Co_{1/3}Mn_{1/3}O_2$[4] and $LiNi_{0.80}Al_{0.15}Al_{0.05}O_2$[5] were considered to be competitive to $LiCoO_2$ due to their higher energy density and improved safety. However, the peculiar crystallographic structure of these two dimensional oxides often lead to the irreversible structure change (i.e. oxygen release or cation migration) after particular amount of Li^+ extraction. It is for this reason that lithium transition metal oxides with three dimensional structures such as spinel $LiMn_2O_4$[6] and $LiNi_{0.5}Mn_{1.5}O_4$[7] were later investigated. Although these spinel structures showed improved structure stability compared to layered oxides, they suffer from other issues such as manganese dissolution and limited capacity etc. Besides lithium transition metal oxides, another type of three dimensional framework build upon polyanion $(XO_4)^{m-}$ (X = S, P, Si, As, Mo and W etc.) based skeletons were also widely investigated due to their higher structure stability and higher redox potential, which was later explained by using inductive effects[8,9]. Among these polyanion based cathode materials, olivine $LiFePO_4$ became the most widely investigated since it can safely deliver a good energy density utilizing only earth-abundant materials[10]. However, the olivine materials have limitations which include a poor electrical conductivity[10,11] and one-dimensional (1D) Li-ion diffusion pathways that can be easily blocked[12], and as a result only achieve optimal performance with nanoscale particles whose low tap density limits the energy density that can be realized in commercial devices. The search for next-generation phosphate materials has broadened to include transition metal fluorophosphates which incorporate a second anion moiety of F^-, and which have good electro-chemical performance and favorable intrinsic properties such as 2D ion diffusion channels and small volume changes during ion removal and insertion[13,14]. However, these modifications are often done with the expense of specific capacity of related materials by introducing anions such as F^-. Therefore, exploring new types of polyanion-based cathode materials with high specific capacity and energy density is of great importance. As mentioned in the previous chapters, our strategies to incorporate N^{3-} into $[PO_4]^{3-}$ has been proven to be able to increase the theoretical capacity

and redox potentials of specific Na-based nitridophosphates. Although Na^+ and Li^+ have showed a variety of similarities as charge carries, Li^+ is much lighter than Na^+ and thus often lead to higher energy density for Li-ion batteries. In this chapter, we will demonstrate the feasibility of utilizing $Li_2MP_2O_9N$ (*M* = Mn, Fe) and $Li_3MP_3O_9N$ (*M* = Ti, V) as promising cathode materials for rechargeable Li-ion batteries.

4.2 Experimental parts

4.2.1 Synthesis of $Na_2MP_2O_9N$ (*M* = Mn, Fe) and $Na_3MP_3O_9N$ (*M* = Ti, V)

$Na_2Fe_2P_3O_9$: $NaPO_3$ (Fisher Scientific, $n \sim 6$), Fe_2O_3 (< 5μm, Alfa Aesar, 99.9%) and $(NH_4)_2HPO_4$ (AMRESCO) were combined in a molar ratio of 2.01:1:1 and ball milled for 6 h in a vibratory ball mill. The mixture was then heated at a temperature of 600 ℃ to 675 ℃ for 20 h in a 1 inch diameter quartz tube in a Lindberg/Blue M Mini-Mite furnace under flowing NH_3 with a flow rate of 50 mL/min. The resulting powder was ground for 30 min and then reheated at the same conditions. The final product was a light yellow powder that was identified to be single-phase cubic $Na_2Fe_2P_3O_9N$ by powder X-ray diffraction.

$Na_2Fe_{2-x}Mn_xP_3O_9$: Similar to that of $Na_2Fe_2P_3O_9$, it should be noticed that we can only synthesize pure $Na_2Fe_{2-x}Mn_xP_3O_9$ for x up to 1.6. Pure $Na_2Mn_2P_3O_9$ has not been synthesized using thermal ammonolysis. Synthesis of $Na_3TiP_3O_9$ and $Na_3VP_3O_9$ can be found in chapters 2 and 3.

4.2.2 Synthesis of $Li_{2-x}M_2P_3O_9N$ (*M* = Mn, Fe) and $Li_{3-x}MP_3O_9N$ (*M* = Ti, V)

$Li_{2-x}M_2P_3O_9N$ (*M* = Mn, Fe) and $Li_3VP_3O_9N$ were synthesized using a similar solid-solid Li^+/Na^+ ion exchange method as that used to synthesize $Li_2Mg_2P_3O_9N$ and $Li_3AlP_3O_9N$. $Li_{2+x}TiP_3O_9N$ can be synthesized from either the solid-solid ion exchange method or the traditional liquid ion exchange method. Solid-solid Li^+/Na^+ ion exchange method is explicitly described in chapter 4. Here, only the liquid ion exchange of $Na_3TiP_3O_9N$ will be described. For the ion exchange of $Na_3TiP_3O_9N$, saturated LiBr in acetonitrile solution was used as the lithium exchange source. About 0.5 g of $Na_3TiP_3O_9N$ was added into 50 mL saturated LiBr solution, the ion exchange was carried out at 80 ℃ for 24 hours, the exchanged products were filtered and washed by acetonitrile for twice and acetone for three times. The obtained greyish powder was dried at 100 ℃ for overnight. It should be noticed that both $Li_2Fe_2P_3O_9N$ and $Li_3TiP_3O_9N$ were oxidized during ion exchange process due to the relative low redox potential of

Fe^{2+}/Fe^{3+} and Ti^{3+}/Ti^{4+}. *In situ* X-ray diffraction study of Li^{+}/Na^{+} ion exchange of $Na_3VP_3O_9N$ was carried out in similar manner as that for $Na_3AlP_3O_9N$, details can be found in chapter 4.

4.2.3 X-ray and time-of-flight (TOF) neutron diffraction

Room temperature X-ray diffraction data of powder samples were collected on a Bruker D8 Advance diffractometer utilizing Cu K_α radiation from a fine focus X-ray tube ($K_{\lambda1}$ = 1.54053 Å, $K_{\lambda2}$ = 1.54431 Å) at a 300 mm working radius and with a 1D position-sensitive LynxEye Si detector with 192 channels. The data were collected at 0.02 °/step with a count time of 2 seconds/step (384 seconds/point). Slit settings were 12 mm for variable divergence slits and 2.5 mm for both Soller slits. Synchrotron X-ray diffraction data for powder samples were collected at beamline X-14A of the National Synchrotron Light Source (NSLS) with a 1D linear position sensitive silicon strip detector with 640 channels at a distance of 1433 mm and a wavelength of approximately 0.77 Å. Time-of-flight neutron diffraction measurements were carried out on the nanoscale-ordered materials diffractometer (NOMAD) of the Spallation Neutron Source (SNS) at Oak Ridge National Laboratory, which has a total flight path of 21.5 m, utilizing a neutron beam collimated down to a diameter of ~6 mm. Sample powders (~200 mg) were loaded into a 2 mm diameter capillary which was held in the beam using a linear automated sample changer. A typical data acquisition time of 100 min were used for each sample. Neutron powder diffraction data were generated using a software package developed for NOMAD instrument. Structures were refined using the Rietveld method as implemented in the TOPAS software package (Bruker-AXS, version 4.2). Additional refinements were carried out in Jana 2006[15].

4.2.4 X-ray absorption

Ex situ V and Ti K-edge XAS data were collected at beamline X-19A at NSLS, BNL using a Si (111) double crystal monochromator in transmission model, the beam intensity was detuned to 50% to minimize the high-order harmonics. Reference spectrum of V foil was collected simultaneous as energy calibrant. XANES and EXAFS spectra were processed using the Athena software package[16]. AUTOBK code was implemented to normalize corresponded absorption coefficient. The obtained EXAFS signal $\chi(k)$ was weighted by k^3 and then Fourier transferred into real space. *Ex situ* Fe K-edge XAS data were collected at beamline X-18A at NSLS, BNL using similar configuration as X-19A. *In situ* V K-edge XAS of $Li_3VP_3O_9N$ was carried out at beamline X-19A at NSLS. XAS data was collected in transmission model with metallic vanadium foil as simultaneous energy calibratant, due to the relative

thin electrode film and low vanadium concentration in the sample, EXAFS data was found to be too noise to carry out robust refinements. Thus, only the X-ray near edge spectroscopy (XANES) data was used to evaluate the vanadium oxidation changes. Data reduction and analysis was carried out in a similar manner as that for *ex situ* XAS data. *In situ* cell for was cycled between 2.0 V and 4.8 V at C/20 rate.

4.2.5 Electrochemistry performance

The cathode electrodes of sodium variants were prepared by mixing powder sample, carbon (acetylene black), and polyvinylidene difluoride (PVDF) in a 6:3:1 weight ratio. An appropriate amount of 1-methyl-2-pyrrolidinone (NMP) was added as a solvent to the well-mixed powders to form thick slurry. The slurry was then manually painted on an Al foil with a thickness of about 50 μm, and the whole foil was dried in a vacuum oven at 80 ℃ for about 8 hours. After that, the dried foil was cut into several disc shape electrodes with the area of about 0.8 cm^2 /each, and a typical active material loading of 2-5 mg. Similar conditions were used to prepare Li variants electrodes, with only the modification being the active material to carbon to PVDF ratio (7:2:1). Galvanostatic cycling of hybrid-ion batteries was carried out on a Land battery station at C/20 to C/30 rate. The extended galvanostatic cycling of Li variants/Li batteries was done with a current density at C/15 to C/30 rate, though different C rates were also examined. Cyclic voltammetry (CV) data were collected on a Biologic cycler at a scan rate of 0.05 mV/ second (0.18 V / h). Galvanostatic Intermittent Titration Technique (GITT) data of $Li_3VP_3O_9N$ and $Li_2TiP_3O_9N$ were collected on a Land battery station.

4.2.6 Electron microscopy

Scanning electron microscopy (SEM) images were collected on a JEOL 7600 SEM operating at 5 kV in a low vacuum condition to minimize charging effects. Elemental-dispersive X-ray analysis (EDX) spectra were collected on the same instrument at 15 kV, utilizing an Oxford EDX spectrometer.

4.3 Results and discussion

4.3.1 Synthesis and structure study of $Na_2M_2P_3O_9N$ (M = Mn, Fe)

The compound $Na_2Fe_2P_3O_9N$ and $Na_2Mn_2P_3O_9N$ belongs to a class of known compounds with general formula $A^I{}_2M^{II}{}_2P_3O_9N$ which are known to exist for A^I = Na and for M^{II} = Mg, Fe, Mn, and Co.

Although our attempts to synthesize pure $Na_2Mn_2P_3O_9N$ and $Na_2Co_2P_3O_9N$ failed, it has been found that phase pure $Na_2Mg_2P_3O_9N$, $Na_2Fe_2P_3O_9N$ and $Na_2Fe_{2-x}Mn_xP_3O_9N$ ($0 < x < 1.6$) can be synthesized. Although the crystal crystal structure of $Na_2Mg_2P_3O_9N$ has been previously reported. To the best of our knowledge, no other structure reports can be found in the literature about the other $Na_2M_2P_3O_9N$. Therefore, it is worthwhile to carry out a detailed structure study of these series of compounds to gain more insights about the atomic environments, especially the Na-ion environments.

Lab X-ray diffraction data of the as-prepared $Na_2Fe_2P_3O_9N$ and $Na_2Fe_{2-x}Mn_xP_3O_9N$ are shown in Figure 4.1, clearly peak shifts can be observed for the $Na_2Fe_{2-x}Mn_xP_3O_9N$ solid solution phase, indicating the successfully substitution of Fe^{2+} by Mn^{2+}. Le Bail fits[17] were carried out for all these diffraction patterns, the obtained lattice parameters are shown in Table 4.1. To further reveal the accurate crystal structure of these compounds, synchrotron XRD (λ = Å) and TOF neutron data was collected, detailed data collection information can be found in the experimental parts. Rietveld refinements were carried out for the as-collected XRD and TOF neutron diffraction data with refinement results shown in Figures 4.2 and 4.3. The final refined structure of $Na_2Fe_2P_3O_9N$ is shown in Figure 4.4, it shares the same frame-work of tetrahedral trimeric $P_3O_9N^{6-}$ anionic blocks as 3:1 $Na_3MP_3O_9N$ analogues (M = Ti, V, etc.). Although these two structural variants both maintain charge balance for the anionic groups using four cations that are found at the same crystallographic sites, they differ in their ratio of monovalent to multivalent cations (2:2 or 3:1). The additional divalent Fe cation in $Na_2Fe_2P_3O_9N$ occupies an octahedral site that corresponds to the Na2 position in the 3:1 structure type. As a result, the two FeO_6 octahedra in $Na_2Fe_2P_3O_9N$ share a face, as illustrated in Figure 4.3. This close proximity of the two Fe ions (~3.0 Å) is expected to strongly influence redox potentials both through electrostatic repulsions and through potentially contradictory bond length preferences for the three shared oxygen ligands if two Fe ions of different valence are found in a single dimer. Detailed refinement result and crystal structure information are listed in Tables 4.2 to 4.4 with important bond lengths shown in Table 4.5.

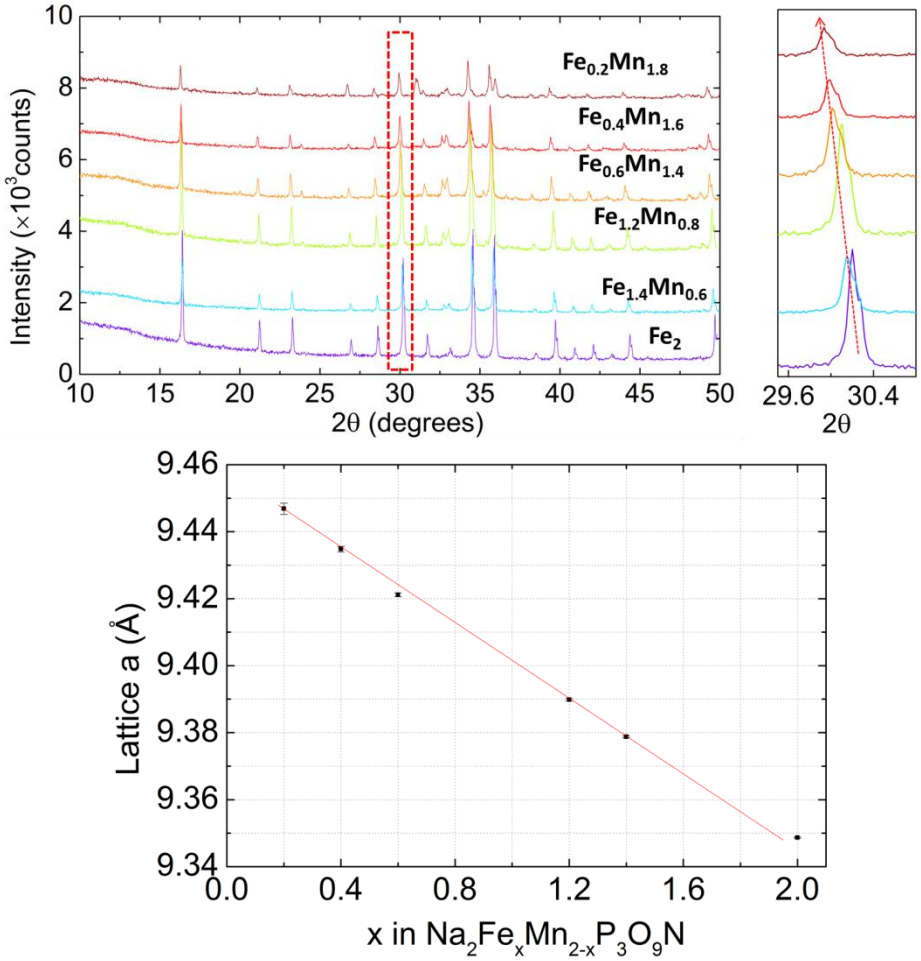

Figure 4.1 Top, Lab X-ray diffraction data (CuKα radiation) of the as-synthesized $Na_2Fe_{2-x}Mn_xP_3O_9N$ solid solution. Bottom, refined lattice parameters of corresponded compounds plotted as a function of Fe content.

Table 4.1 Refined Lattice parameters of $Na_2Fe_xMn_{2-x}P_3O_9N$.

x in $Na_2Fe_xMn_{2-x}P_3O_9N$	**Lattice parameter a (Å)**
2	9.3486(1)
1.4	9.3788(1)
1.2	9.3898(1)
0.6	9.4212(1)
0.4	9.4348(1)
0.2	9.4469(2)

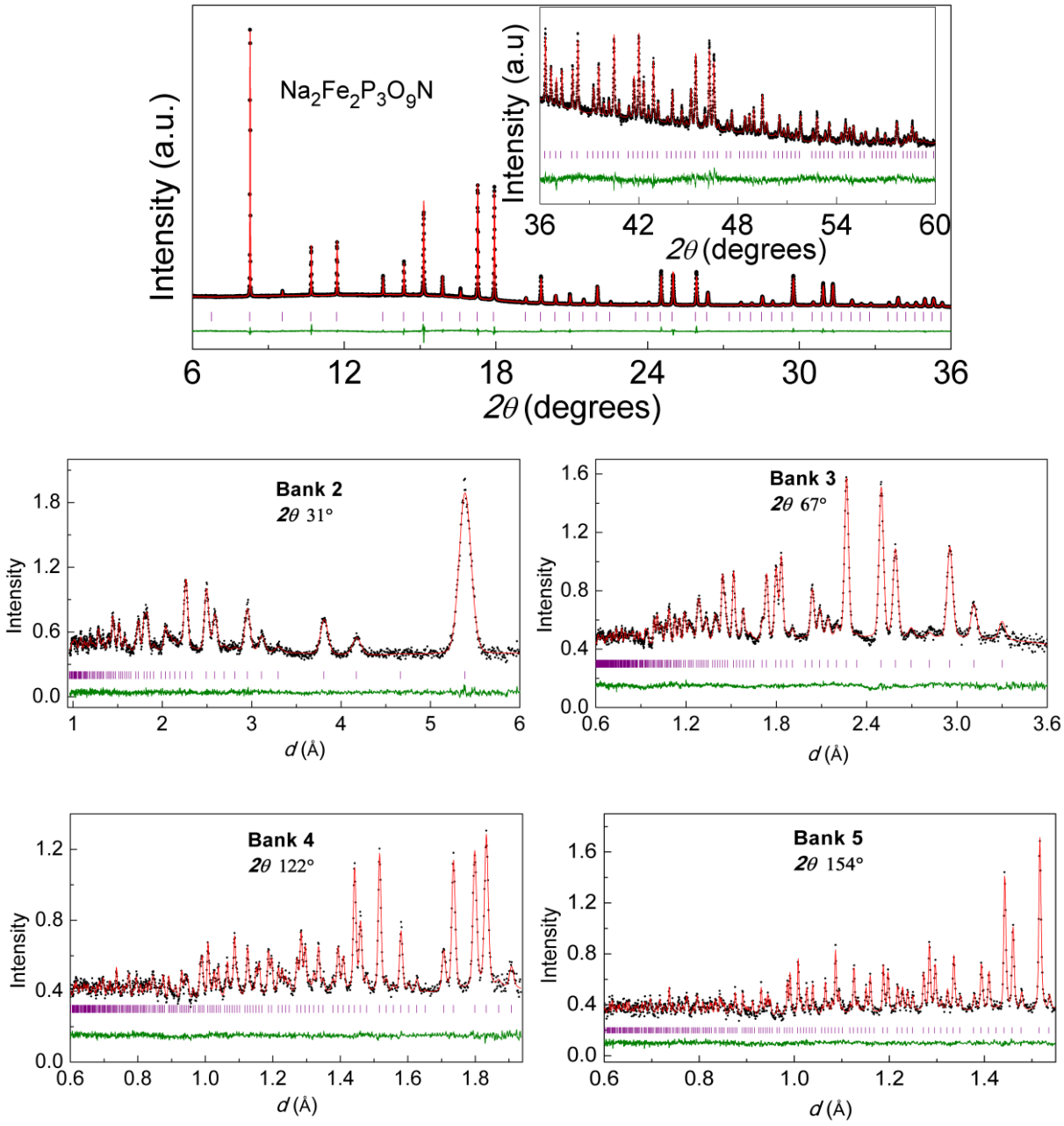

Figure 4.2 (Top panel) Rietveld refinement of $Na_2Fe_2P_3O_9N$ with synchrotron diffraction data (λ=0.7787Å) with experimental data (black dots), calculated intensities (red line) and different curve (green line), and positions of Bragg diffraction peaks are marked in purple. (Bottom panels) Rietveld refinement of $Na_2Fe_2P_3O_9N$ with TOF neutron diffraction data.

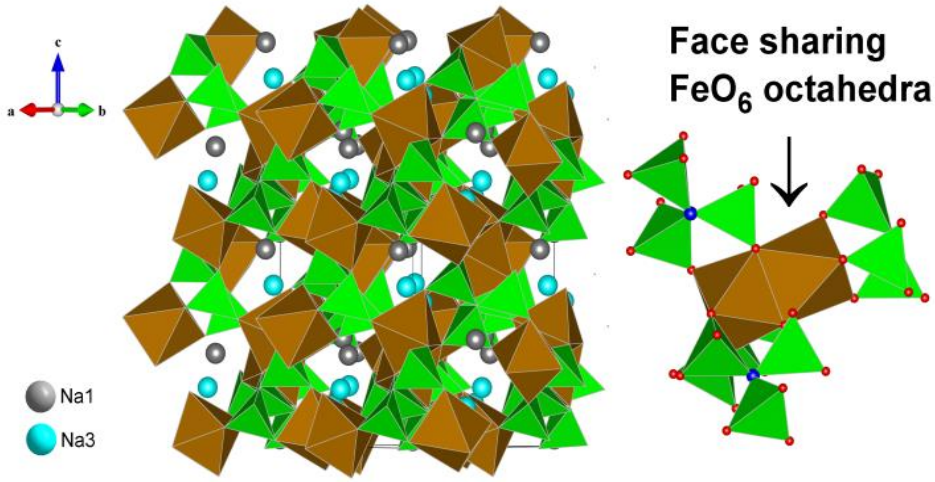

Figure 4.3 Structure of $Na_2Fe_2P_3O_9N$, with zoom showing face-sharing Fe_2O_9 octahedra (brown) and trimeric $P_3O_9N^{6-}$ tetrahedral units (green), with O shown in red and N in dark blue.

Table 4.2 Atomic coordinates and thermal parameters of $Na_2Fe_2P_3O_9N$ (synchrotron, λ=0.7787Å)

Atom	Wyck.	x	y	z	Occ.	B_{iso}(Å^2)
Na1	4a	0.0402(2)	0.0402(2)	0.0402(2)	1	1.39(12)
Na3	4a	0.7918(3)	0.7918(3)	0.7918(3)	1	1.52(12)
Fe1	4a	0.5788(1)	0.5788(1)	0.5788(1)	1	0.70(5)
Fe2	4a	0.3983(2)	0.3983(2)	0.3983(2)	1	0.55(4)
P1	12b	0.0946(3)	0.2604(3)	0.3419(3)	1	0.62(4)
O1	12b	0.0095(4)	0.8717(5)	0.2210(5)	1	0.97(6)
O2	12b	0.0044(4)	0.1372(4)	0.3964(6)	1	0.97(6)
O3	12b	0.1952(5)	0.3193(5)	0.4572(5)	1	0.97(6)
N1	4a	0.2014(5)	0.2014(5)	0.2014(5)	1	0.96(3)

Table 4.3 Atomic coordinates and thermal parameters of $Na_2Fe_2P_3O_9N$ (TOF neutron)

Atom	Wyck.	x	y	z	Occ.	$B_{iso}(Å^2)$
Na1	4a	0.0446(7)	0.0446(7)	0.0446(7)	1	1.80(1.20)
Na3	4a	0.7924(10)	0.7924(10)	0.7924(10)	1	2.30(60)
Fe1	4a	0.5793(3)	0.5793(3)	0.5793(3)	1	0.22(12)
Fe2	4a	0.3998(4)	0.3998(4)	0.3998(4)	1	0.68(18)
P1	12b	0.0959(9)	0.2693(10)	0.3358(20)	1	0.78(40)
O1	12b	0.0107(10)	0.8713(20)	0.2236 (20)	1	0.82(8)
O2	12b	0.0065(9)	0.1322(10)	0.3895(10)	1	0.82(8)
O3	12b	0.1953(20)	0.3212(10)	0.4527(16)	1	0.82(8)
N1	4a	0.2030(4)	0.2030(4)	0.2030(4)	1	0.37(12)

Table 4.4 Crystallographic data for $Na_2Fe_2P_3O_9N$ at room temperature

Ridiation	XRD	TOF neutron
Formula	$Na_2Fe_2P_3O_9N$	$Na_2Fe_2P_3O_9N$
Crystal system	Cubic	Cubic
Space group	*$P2_13(198)$*	*$P2_13(198)$*
Lattice parameter	9.3459(1) Å	9.3453(5) Å
Cell volume	816.33(1) $Å^3$	816.17(3) $Å^3$
Density (calculated)	3.324 g/cm^3	3.325 g/cm^3
λ	0.7788 Å	0.1Å-3Å
$\mathbf{R_{Bragg}}$	0.89%	N/A
$\mathbf{R_{wp}}$	2.41%	4.88%
$\mathbf{R_p}$	1.71%	3.99%
χ^2	2.96	N/A

Table 4.5 Selected bond distances (Å) for $Na_2Fe_2P_3O_9N$

	$Na_2Fe_2P_3O_9N$ (XRD)	$Na_2Fe_2P_3O_9N$ (TOF neutron)
Fe1 – O1(×3)	2.033(5)	2.080(9)
Fe1– O2 (×3)	2.149(4)	2.105(9)
Fe2 – O2(×3)	2.185(5)	2.173(10)
Fe2 – O3(×3)	2.110(5)	2.130(11)
P – O1	1.541(5)	1.526(13)
P – O2	1.515(5)	1.540(13)
P – O3	1.533(6)	1.493(13)
P – N	1.739(3)	1.719(9)
Na1 – O1 (×3)	2.327(4)	2.298(9)
Na1 – O3 (×3)	3.016(6)	3.044(14)
Na1 – N	2.611(8)	2.565(13)
Na3 – O1(×3)	3.053(6)	3.064(11)
Na3 – O2(×3)	3.011(4)	3.040(10)
Na3/Li3 – O3(×3)	2.362(6)	2.401(11)

For $Na_2Fe_{2-x}Mn_xP_3O_9N$, a selected structure study was carried out for x = 0.6. Rietveld refinement of corresponded TOF neutron diffraction was shown in Figure 4.4. Detailed refinement result and structure information can be found in Table 4.6. Interestingly, we found Mn^{2+} on both Fe1 and Fe2 site, indicating that there is no obvious site preference for Mn^{2+} within this solid solution phase. Our attempts to synthesize pure $Na_2Mn_2P_3O_9N$ were failed, and further study is required to fully understand the structure stability of these two phases.

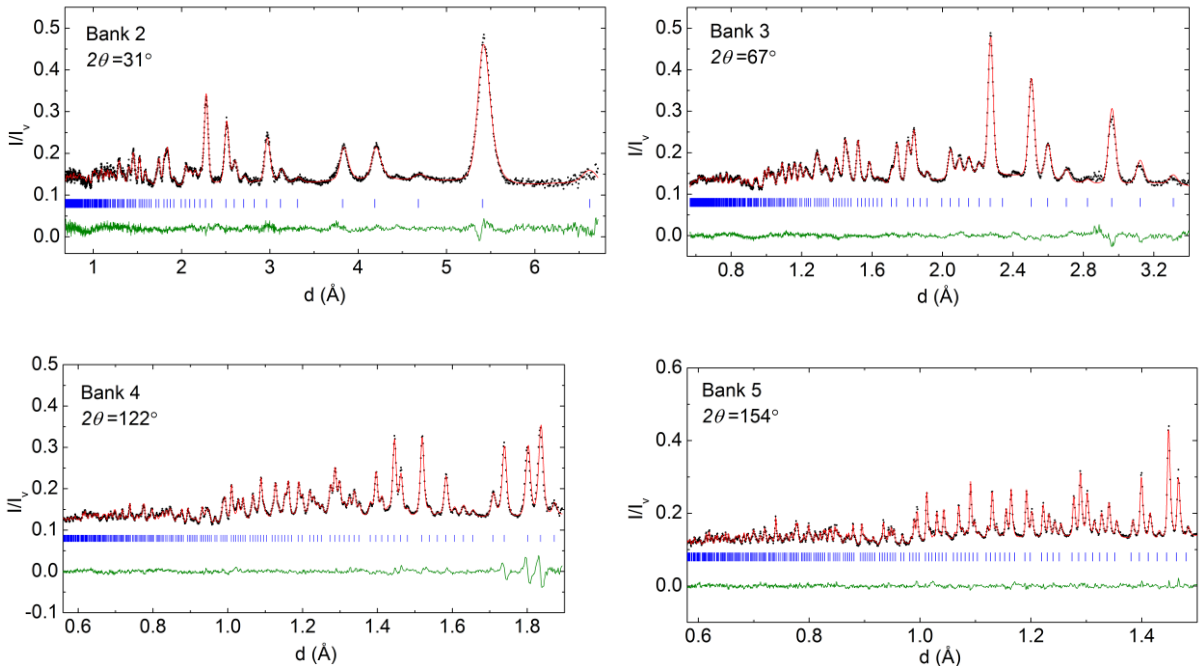

Figure 4.4 Rietveld refinement of $Na_2Fe_{1.4}Mn_{0.6}P_3O_9N$ using TOF neutron diffraction data with experimental data (black dots), calculated intensities (red line) and different curve (green line), and positions of Bragg diffraction peaks are marked in blue.

Table 4.6 Refinement results, atomic coordinates and thermal parameters of $Na_2Fe_{1.4}Mn_{0.6}P_3O_9N$ (TOF neutron)

R_{wp} = 2.77% χ^2 =1.3 S.G. *P2₁3* a = 9.3629(3) Å						
Atom	Wyck.	x	y	z	Occ.	B_{iso}(Å^2)
Na1	4a	0.0431(4)	0.0431(4)	0.0431(4)	1	1.77(16)
Na3	4a	0.7913(6)	0.7913(6)	0.7913(6)	1	2.32(19)
Fe1	4a	0.5797(2)	0.5797(2)	0.5797(2)	0.802(6)	0.54(9)
Mn1	4a	0.5797(2)	0.5797(2)	0.5797(2)	0.198(6)	0.54(9)
Fe2	4a	0.4038(6)	0.4038(6)	0.4038(6)	0.490(5)	0.13(2)
Mn2	4a	0.4038(6)	0.4038(6)	0.4038(6)	0.510(5)	0.13(2)
P1	12b	0.0946(3)	0.26167(3)	0.3427(3)	1	0.36(6)
O1	12b	0.0082(3)	0.8678(3)	0.2184(3)	1	1.34(7)
O2	12b	0.0063(3)	0.1312(2)	0.3942(3)	1	0.66(6)
O3	12b	0.1902(3)	0.3193(4)	0.4523(3)	1	1.42(7)
N1	4a	0.2041(2)	0.2041(2)	0.2041(2)	1	0.29(6)

4.3.2 $Na_2Fe_2P_3O_9N$ and $Na_2Fe_{1.4}Mn_{0.6}P_3O_9N$ as cathode materials for hybrid-ion batteries

Two different sodium ions have been identified within this type of structure, and Fe^{2+} or Mn^{2+} can work as potential redox active center. Thus, these materials can potentially work as cathode materials for rechargeable Li^+/Na^+ batteries. Electrochemistry performances of these two materials were evaluated in 2032-type coin cells in a hybrid-ion configuration. In this configuration, sodium-ion containing cathode materials, $Na_2Fe_2P_3O_9N$ and $Na_2Fe_{1.4}Mn_{0.6}P_3O_9N$, were cycled against Li^+/Li, detailed information can be found in the experimental section. Galvanostatic charge and discharge curves (1.5 V to 4.6 V, C/20) of $Na_2Fe_2P_3O_9N$ indicated that less than one half of its theoretical capacity of 131 mAh/g could be realized, and that large polarization is present (Figure 4.5). These features are both likely the result of low Na^+ mobility within the $Na_2Fe_2P_3O_9N$ lattice. An analysis of bond valence sum difference (ΔV) maps calculated for Na^+ ions within the $Na_2Fe_2P_3O_9N$ lattice (Figure 4.6) shows that a very large ΔV threshold of 0.5 valence units need to be overcome before a viable Na diffusion pathway is established, suggesting that the removal of Na ions is difficult at room temperature, and that low ionic conductivity may be limiting cell performance. This ΔV threshold is much higher than is found for the 3:1 stoichiometry compounds $Na_3VP_3O_9N$ ($\Delta V \sim 0.12$) and $Na_3TiP_3O_9N$ ($\Delta V \sim 0.05$), and likely indicates that Na-ion mobility in this structure family is closely correlated with unit cell dimensions (a = 9.35 Å for M= Fe, 9.45 Å for M = V, and 9.52 Å for M = Ti). When Mn^{2+} was substituted into the $Na_2Fe_2P_3O_9N$ structure, the as-formed solid solution showed a lattice parameter increase due to the relative larger ionic radii of Mn^{2+} (0.82 Å) compared to Fe^{2+} (0.77 Å)[18]. Curiously, although with larger unit cell volume, these Mn^{2+} substituted samples showed even lesser charge/discharge capacity, as can be seen in Figure 4.7. This is presumably due to the decrease of electronic conductivity that results from Mn^{2+} substitution, which is has also been observed in olivine type $LiMnPO_4$ and $LiFePO_4$. It is expected that electrochemical performance of these materials can be improved by synthesizing nanoparticles.

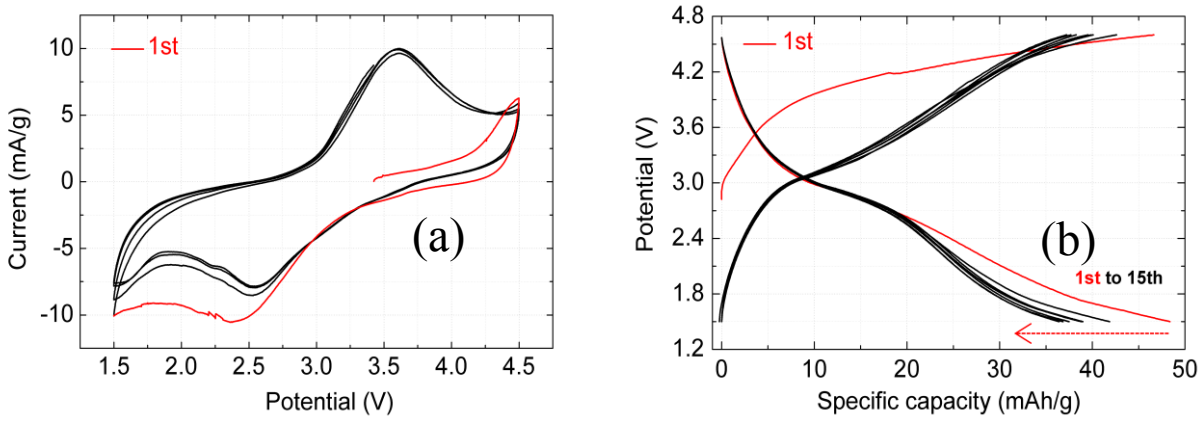

Figure 4.5 (a) Cyclic voltammetry (CV) curves of $Na_2Fe_2P_3O_9N$ cycled against Li metal, with a scan rate of 0.05 mV/second. (b) Charge-discharge profiles of $Na_2Fe_2P_3O_9N$ cycled against Li metal at a C/20 rate.

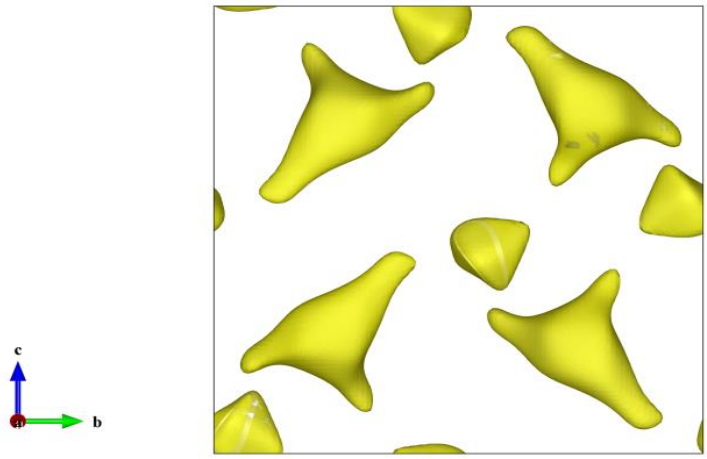

Figure 4.6 Na^+ difference bond valence sum (BVS) map of $Na_2Fe_2P_3O_9N$ with valence difference (ΔV) of 0.4. The Na1 and Na3 sites are isolated, indicating a high energy barrier for Na^+ to hop between these sites.

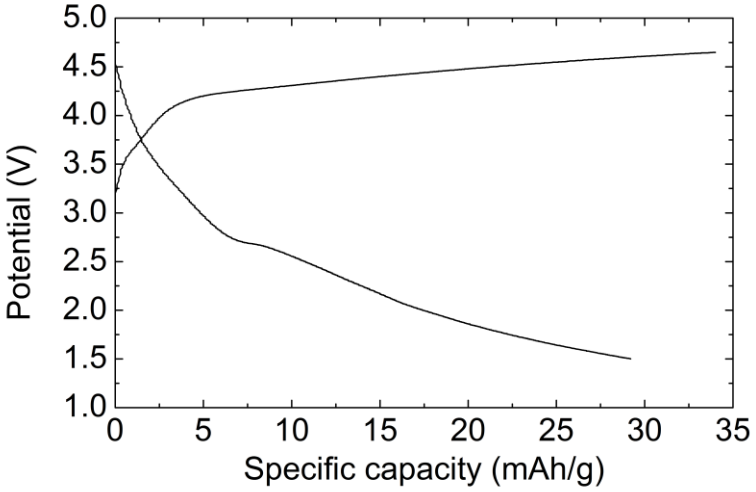

Figure 4.7 Charge-discharge profiles of $Na_2Mn_2P_3O_9N$ cycled against Li^+/Li at a C/20 rate.

4.3.3 Synthesis and structure study of $Li_xFe_2P_3O_9N$

As mentioned in the previous section, the poor electrochemical performance of $Na_2Fe_2P_3O_9N$ is very likely to be due to the poor sodium ionic mobility within the structure. In contrast to the large Na^+ (0.92 Å)[18], Li^+ has much smaller ion radii (0.74 Å)[18], suggesting that far better Li-ion kinetics may be observed if all of the Na-ions can be chemically removed or replaced by Li^+ prior to electrochemical cell fabrication. Ion exchange of Li^+ for Na^+ was therefore carried out by heating well ground LiBr and $Na_2Fe_2P_3O_9N$ powders at 280 ℃ for 20 hours under flowing N_2 gas. The resulting mixture was washed with methanol and filtered. This process was repeated (3 times) until the starting phase disappeared (as judged by XRD), giving a final product of a reddish black $Li_{2-x}Fe_2P_3O_9N$ powder. The removal of Na^+ ions was confirmed by a comparison of SEM-EDX spectra before and after ion exchange, as can be seen in Figure 4.8, which found that the Na signal was reduced to less than 1% of its original value. Diffraction studies showed that the simple cubic lattice is maintained throughout the exchange process, and that the *a*-lattice parameter shrinks to 9.2565(1) Å. The Rietveld refinement of high resolution synchrotron XRD data confirmed the removal of Na^+ ions from both sites (Na1 and Na3), with the crystallographic parameters and relevant bond lengths provided in the Tables 4.7 to 4.10. Electron density corresponding to Li ions was only observed near the Na3 site and not near the Na1 site, indicating that the final product was oxidized during the ion exchange process, resulting in a

composition of $Li_{2-x}Fe_2P_3O_9N$ with $x \sim 1.7$. The new Li3 site is located close to three oxygen ions with a refined bond distance of 1.89(1) Å, a result which is consistent with the bond preferences[19] of Li (BVS value 0f 0.96) and which is in clear contrast to the original Na3-O bond lengths (2.36 Å). Confirmation of this site was obtained through the Rietveld refinement of time-of-flight neutron diffraction data (Figure 4.9), though with less precision due to the poorer counting statistics of the experiment. Fe *K*-edge XANES spectra of $Li_{2-x}Fe_2P_3O_9N$, shown in Figure 4.10, clearly indicates very substantial oxidation during ion exchange, in agreement with the Rietveld results. The sample oxidation during ion exchange is reflected in ~0.05 Å shorter Fe-O bond lengths at both Fe sites. Curiously, the Fe1 bond lengths are about 0.05 Å shorter than those of Fe2 both before and after oxidation, perhaps reflecting substantial differences in ligand bonding at these two sites.

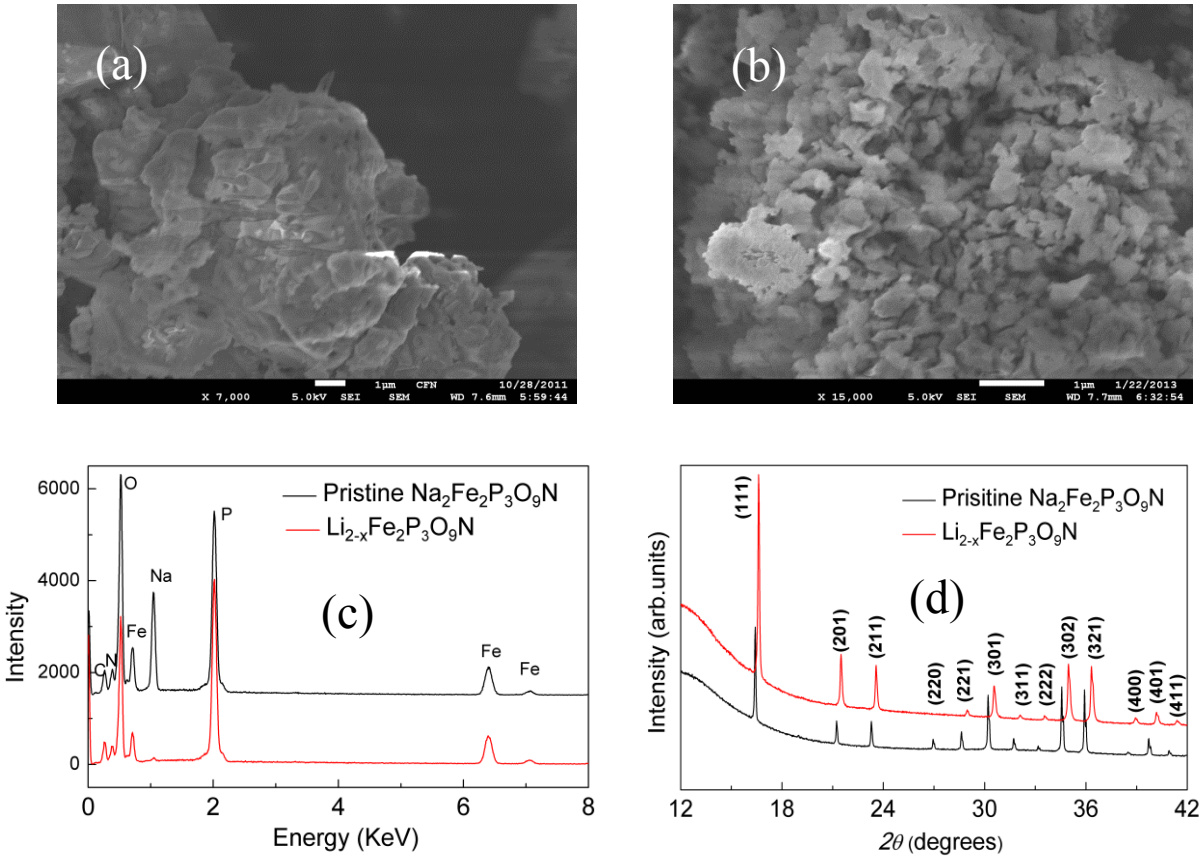

Figure 4.8 (a) SEM image of $Na_2Fe_2P_3O_9N$ syntheiszed by solid state methods. (b) SEM image of $Li_{0.3}Fe_2P_3O_9N$. (c) EDS spectra of pristine $Na_2Fe_2P_3O_9N$ and ion-exchanged $Li_{0.3}Fe_2P_3O_9N$. (d) Overlayed XRD patterns of pristine $Na_2Fe_2P_3O_9N$ and ion-exchanged $Li_{2-x}Fe_2P_3O_9N$ (Cu K_α).

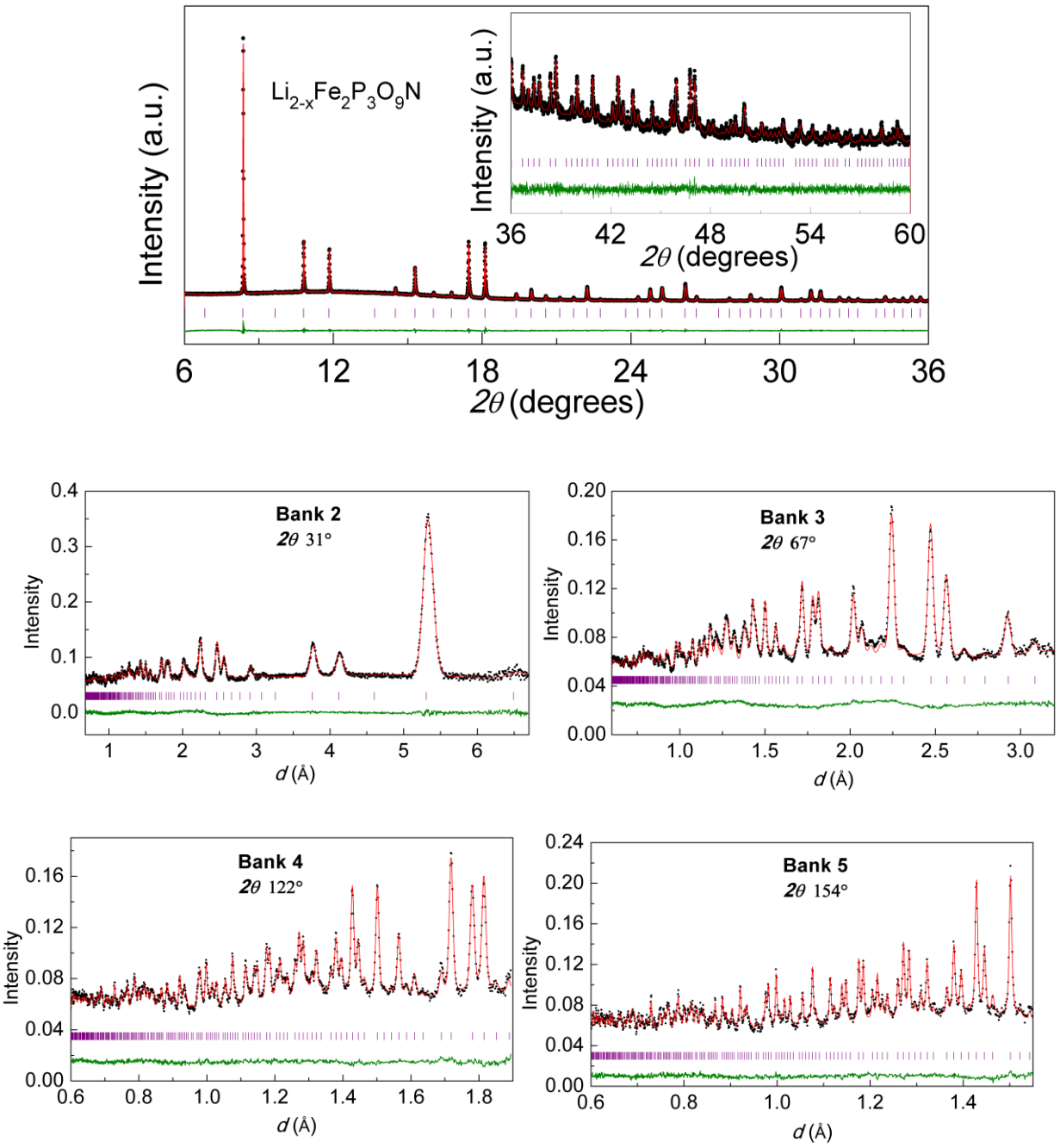

Figure 4.9 Rietveld refinement of ion-exchanged $Li_{0.3}Fe_2P_3O_9N$ using synchrotron XRD data (top panel) and TOF neutron diffraction data (bottom panel), with experimental data (black dots), calculated intensities (red line) and different curve (green line), and positions of Bragg diffraction peaks are marked in purple.

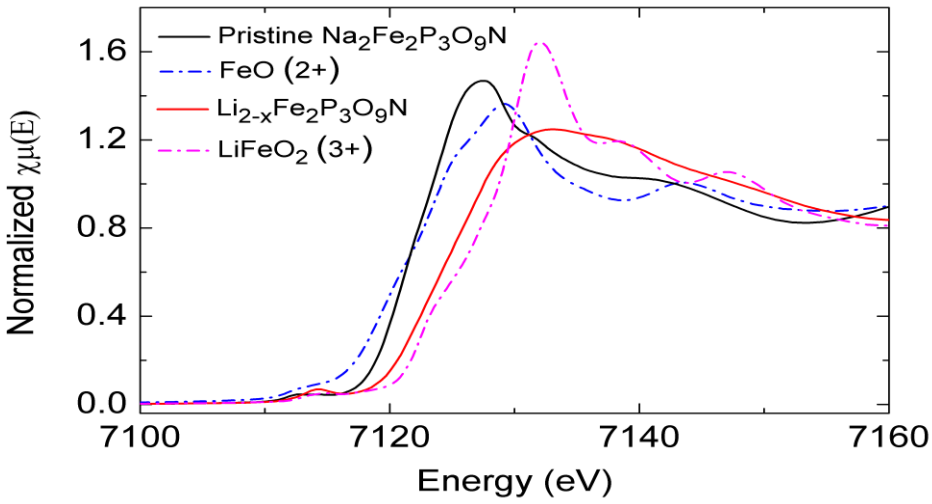

Figure 4.10 Fe K-edge XANES spectra of $Na_2Fe_2P_3O_9N$ and $Li_{2-x}Fe_2P_3O_9N$.

Table 4.7 Crystallographic data for $Li_{0.3}Fe_2P_3O_9N$ at room temperature

Ridiation	XRD	TOF neutron
Formula	$Li_{0.3}Fe_2P_3O_9N$	$Li_{0.3}Fe_2P_3O_9N$
Crystal system	Cubic	Cubic
Space group	*$P2_13(198)$*	*$P2_13(198)$*
Lattice parameter	9.2565(1) Å	9.2566(6) Å
Cell volume	793.12(1) $Å^3$	793.15(4) $Å^3$
Density (calculated)	3.054 g/cm^3	3.054 g/cm^3
λ	0.7787 Å	0.1 Å-3 Å
R_{Bragg}	0.80%	N/A
R_{wp}	2.68%	4.32%
R_p	2.01%	3.55%
χ^2	2.05	N/A

Table 4.8 Atomic coordinates and thermal parameters of $Li_{0.3}Fe_2P_3O_9N$ (synchrotron)

Atom	Wyck.	x	y	z	Occ.	$B_{iso}(Å^2)$
Li3	4a	0.8448(46)	0.8448(46)	0.8448(46)	0.3	2
Fe1	4a	0.5793(1)	0.5793(1)	0.5793(1)	1	0.21(5)
Fe2	4a	0.3940(2)	0.3940(2)	0.3940(2)	1	0.62(6)
P1	12b	0.0899(3)	0.2585(3)	0.3364(3)	1	0.30 (4)
O1	12b	0.0123(5)	0.8679(5)	0.2265(7)	1	0.65(7)
O2	12b	0.0083(6)	0.1263(6)	0.3941(7)	1	0.65(7)
O3	12b	0.1903(7)	0.3248(6)	0.4542(6)	1	0.65(7)
N1	4a	0.1984(7)	0.1984(7)	0.1984(7)	1	0.43(6)

Table 4.9 Atomic coordinates and thermal parameters of $Li_{0.3}Fe_2P_3O_9N$ (TOF neutron)

Atom	Wyck.	x	y	z	Occ.	$B_{iso}(Å^2)$
Li3	4a	0.8506(43)	0.8506(43)	0.8506(43)	0.3	0.21(1.20)
Fe1	4a	0.5806(3)	0.5806(3)	0.5806(3)	1	0.65(14)
Fe2	4a	0.3971(4)	0.3971(4)	0.3971(4)	1	0.91(14)
P1	12b	0.0898(8)	0.2614(9)	0.3370(9)	1	0.25 (9)
O1	12b	0.0157(7)	0.8662(7)	0.2373(8)	1	0.51(11)
O2	12b	0.0083(6)	0.1263(6)	0.3941(7)	1	0.31(10)
O3	12b	0.1682(5)	0.3087(15)	0.4522(4)	1	0.79(13)
N1	4a	0.2026(4)	0.2026(4)	0.2026(4)	1	0.45(13)

Table 4.10 Selected bond distances (Å) for $Li_{0.3}Fe_2P_3O_9N$

	$Li_{0.3}Fe_2P_3O_9N$ (XRD)	$Li_{0.3}Fe_2P_3O_9N$ (TOF neutron)
Fe1 – O1(×3)	1.963(6)	1.894(7)
Fe1– O2 (×3)	2.124(4)	2.041(7)
Fe2 – O2(×3)	2.145(7)	2.179(8)
Fe2 – O3(×3)	2.068(6)	2.068(9)
P – O1	1.505(6)	1.559(10)
P – O2	1.513(6)	1.558(10)
P – O3	1.559(7)	1.534(11)
P – N	1.717(4)	1.686(8)
Li3 – O3(×3)	1.897(3)	1.879(24)

4.3.4 $Li_2Fe_2P_3O_9N$ as cathode material for rechargeable Li-ion batteries

The calculated bond valence sum difference map for Li-ions suggests the existence of isotropic three dimensional Li-ion diffusion channels within $Li_{2-x}Fe_2P_3O_9N$ structure which are accessible at a very small observed ΔV threshold of 0.03 valence units. Based on the BVS analysis, much better battery performance is expected for Na-free compounds $Li_{2-x}Fe_2P_3O_9N$, which were therefore prepared by ion exchange. The voltage charge-discharge profiles of $Li_{2-x}Fe_2P_3O_9N$ cathodes cycled against Li^+/Li at C/10 are shown in Figure 4.11, and indeed show greatly improved performance relative to $Na_2Fe_2P_3O_9N$ cathodes. Since $Li_{2-x}Fe_2P_3O_9N$ is mostly oxidized during the ion-exchange process, it was first discharged to intercalate Li^+ into the structure with a measured initial discharge capacity of 100 mAh/g that corresponds to about 1.4 Li^+ inserted into the structure. In subsequent cycles, specific discharge capacities of 125 mAh/g are achieved, corresponding to 85% of the theoretical capacity of 145 mAh/g (1.7 Li^+ per f.u.) of $Li_{0.3}Fe_2P_3O_9N$. A capacity of about 110 mAh/g remains after 20 cycles. In cyclic voltammetry studies (Figure 4.12), two separate redox potentials are observed at 3.55V/3.5V and 3.1V/2.95V. The higher potential occurs at about 3.5V, indicating that the PO_3N groups in the structure generate a strong inductive effect, which is comparable that produced by PO_4 groups in $LiFePO_4$. The lower potential of the second couple is attributed to antagonistic effects between the two distinct Fe sites mediated by the three face-shared O anions. The small shifts in potential between anodic and cathodic cycles are indicative of reasonable kinetics for these processes, something that can be seen in more explicit rate performance tests (Figure 4.12). This performance was achieved with relative large particles (~1 μm size, Figure 4.8), so it is expected that this system has good intrinsic properties and that nanoscale particles will exhibit better rate performance.

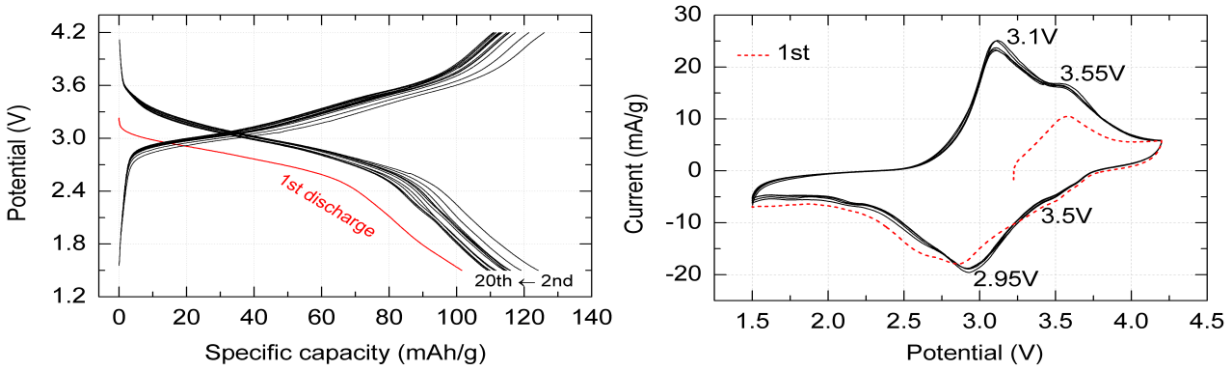

Figure 4.11 Left, charge-discharge profiles of $Li_{2-x}Fe_2P_3O_9N$ cycled against a Li anode at a rate of C/10. The theoretical capacity of $Li_2Fe_2P_3O_9N$ is 142 mAh/g. Right, CV curves of $Li_{2-x}Fe_2P_3O_9N$ coin cell (sweep rate: 0.18 V/ h).

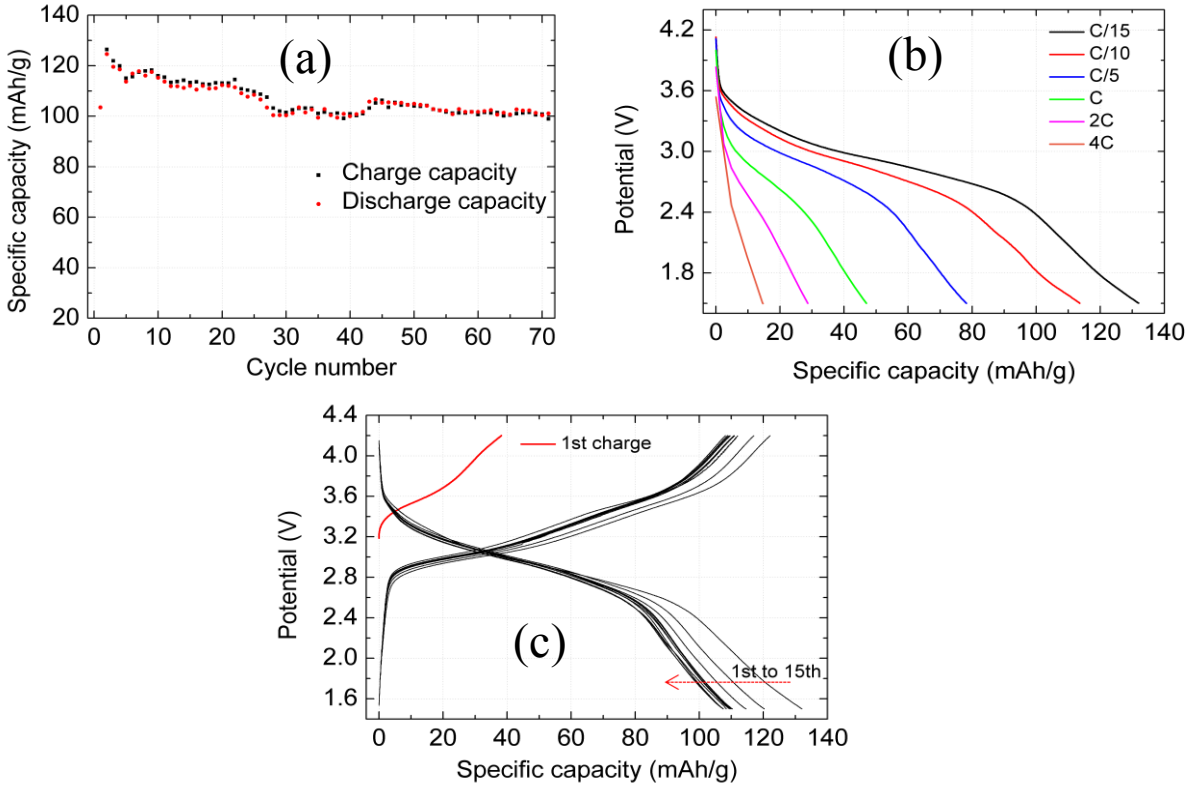

Figure 4.12 (a) Capacity retention of $Li_{2-x}Fe_2P_3O_9N$ cycled against a Li anode at a rate of C/10, discharge first (as in Fig. 3a). (b) Discharge profile of $Li_{2-x}Fe_2P_3O_9N$ cycled against a Li anode at different C rates. (c) Charge-discharge profiles of $Li_{0.3}Fe_2P_3O_9N$ cycled between 1.5 V and 4.2 V (vs. Li^+/Li) at a C/15 rate. The theoretical capacity of this specific non-stoichiometric composition is 146 mAh/g.

4.3.5 Synthesis and structure study $Li_3VP_3O_9N$

$Na_3TiP_3O_9N$ and $Na_3VP_3O_9N$ can be synthesized using high temperature thermal ammonolysis, details can be found in Chapters 2 and 3. However, our attempts to synthesize the corresponded lithium variants using similar methods failed, indicating that $Li_3TiP_3O_9N$ and $Li_3VP_3O_9N$ are very likely to be metastable phases. Therefore, Li^+/Na^+ ion exchange was utilized to synthesize these lithium variants. A thorough introduction about Li^+/Na^+ ion exchange technique can be found in chapter 4. Based on the state of Li source, these ion exchange methods can be divided into two categories: one with Li containing source in liquid state such as molten salts or highly concentrated Li^+ solutions, the other is the newly developed solid-solid ion exchange method with solid state LiCl or LiBr as ion exchange source. It has been found that both ion exchange methods can be used to synthesize $Li_2TiP_3O_9N$ (Ti^{3+} will be oxidized to Ti^{4+}during ion exchange due to the relatively low Ti^{3+}/Ti^{4+} redox potential, this process is associated with Li^+ removal). Whereas the solid-solid ion exchange method has been found to be more effective for the synthesis of $Li_3VP_3O_9N$, presumably due to the lower Na^+ ionic conductivity in $Na_3VP_3O_9N$ related to that in $Na_3TiP_3O_9N$ (see conductivity measurements in chapters 2 and 3), thus requires higher temperature to achieve fully Li^+/Na^+ ion exchange.

As mentioned in chapter 3, $Na_3VP_3O_9N$ can work as promising cathode materials with multi-electron transfer redox couple $V^{3+}/V^{4+}/V^{5+}$. However, it has been found that Na^+ ionic mobility may be the limiting factor for achieving theoretical capacity of this compound (144 mAh/g). We have demonstrated that Li variants of nitridophosphate compounds have higher ionic conductivity than their Na analogues in chapter 4. Thus, it may be possible to fully utilize the $V^{3+}/V^{4+}/V^{5+}$ multi-electron redox couple in $Li_3VP_3O_9N$. This motivates us to carry out a thorough synthesis and structure study of this novel phase. Solid-solid Li^+/Na^+ ion exchange method was used to synthesize $Li_3VP_3O_9N$ from its sodium analogue $Na_3VP_3O_9N$. It has been found that three repeated ion exchanges were required to obtain the phase pure $Li_3VP_3O_9N$ sample. Corresponded laboratory XRD data of the products after each ion exchange process are shown in Figure 4.13. It can be seen that three different phases co-existed after the initial ion exchange process (XRD pattern in red), similar to what has been observed during the ion exchange of $Na_3AlP_3O_9N$. These three phases will be named phase A (with largest lattice parameter), phase B (with intermediate lattice parameter) and phase C (with the smallest lattice parameter) separately.

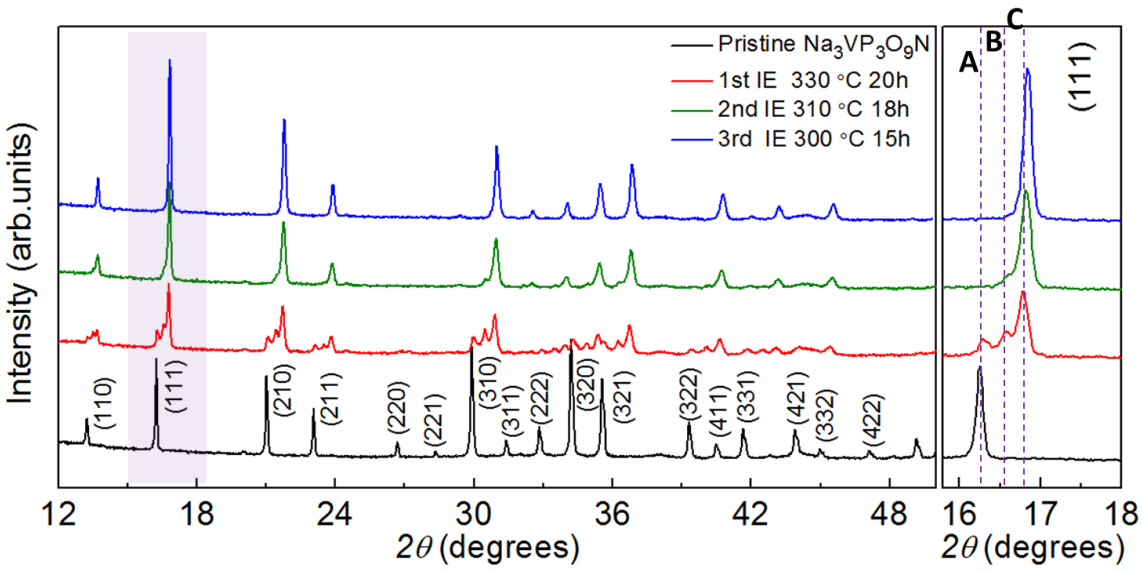

Figure 4.13 X-ray diffraction patterns of $Na_{3-x}Li_xVP_3O_9N$ products collected after each ion exchange process.

To confirm the effective sodium removal after ion exchange, SEM-EDX data of the sample after the third ion exchange was collected, as can be seen in Figure 4.14. It can be clearly seen that sodium signal has diminished after three ion exchanges, indicating that Na^+ in $Na_3VP_3O_9N$ has been effectively replaced. The existence of Li^+ in this sample has been confirmed by using TEM EELS spectra, shown in Figure 4.15. This combined information confirms the effectively Li^+/Na^+ ion exchange of $Na_3VP_3O_9N$.

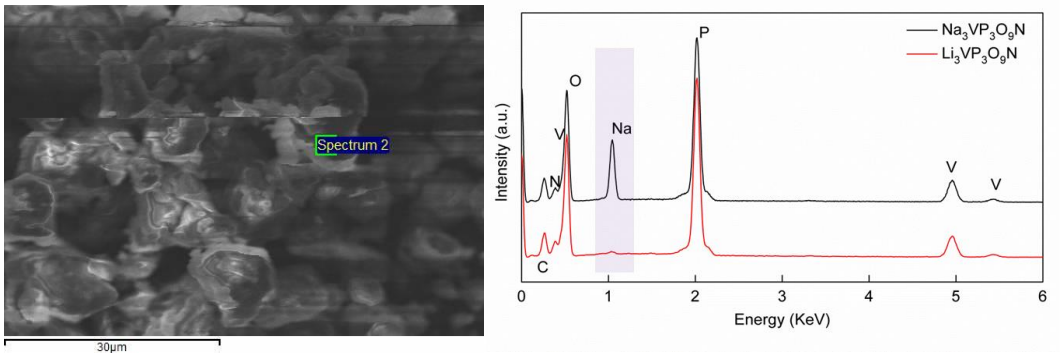

Figure 4.14 SEM-EDX of pristine $Na_3VP_3O_9N$ and ion-exchanged $Li_3VP_3O_9N$. No obvious sodium signal can be observed after three cycles of ion exchange.

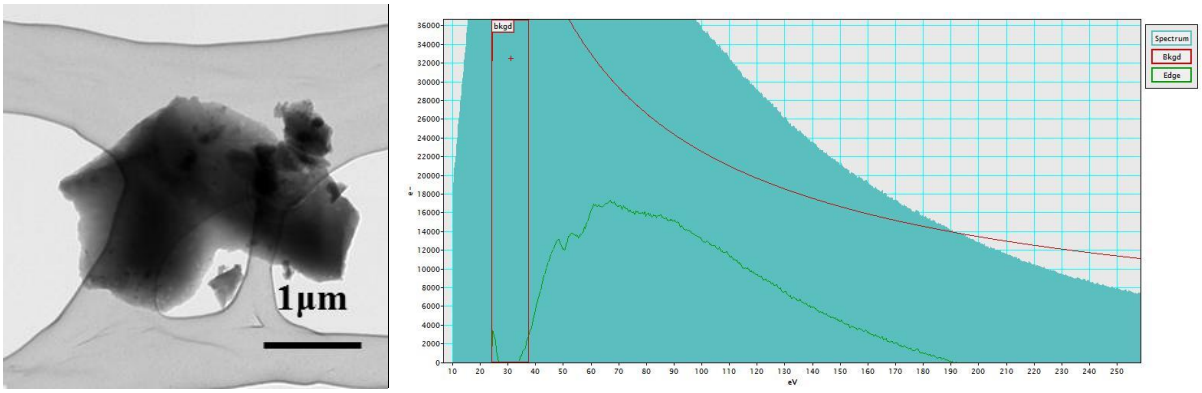

Figure 4.15 TEM image (left) and electron energy loss spectroscopy (eels) spectra (right) of ion exchanged $Li_3VP_3O_9N$.

Since no report of $Li_3VP_3O_9N$ can be found in the literature, it is therefore worthwhile to first solve and refine the crystal structure of this compound. Similar to the structure study of $Li_2Mg_2P_3O_9N$ and $Li_3AlP_3O_9N$, both biased and unbiased method can used to refine the structure of newly synthesized $Li_3VP_3O_9N$: for the ubaised method, Le Bail fitting was first carried out for the as collected high resolution synchrotron XRD data, the obtained intensity files were used to locate the atomic postions of heavy atoms (e.g. V, P, O and N) using charge flipping algorithm[20]. The obatined VP_3O_9N framework was then used as initial structure model for Rietveld refinement of corresponded X-ray or neutron diffraction data, Fourier difference maps were then calculated to locate the residual electron or nuclear scattering length densities, as can be seen in Figure 4.16. It can be seen that similar residual electron density and nuclear scattering length density can be identified in the structure, indicating those positions are the potential Li-ion positions. After incorporating Li ions into the structure, final Rietveld refinemetn was carried out for both synchrotron X-ray and neutron diffraction data. The refinement results are shown in Figures 4.17 and 4.18. Detailed refinement and structure information can be found in Tables 4.11- 4.13. For biased method, the crystal structure $Li_3AlP_3O_9N$ was used as the initial structure model for Rietveld refinement, it was found that similar refined crystal structure was obtained from both methods, confirming the accuracy of the prosposed $Li_3VP_3O_9N$ structure which is plotted in Figure 4.20. It was found that VO_6 octahedra and PO_3N tetrahedra are very similar in both $Na_3VP_3O_9N$ and $Li_3VP_3O_9N$. However, the environments for Li varies substantially in these two samples. Na1 can

be best described as sitting in a highly distorted trigonal prism with a very long Na1-N distance of 2.797 Å, Na2 sits in the center of a distorted NaO_6 octahedron, whereas Na3 sits on the top of a triangle plane formed by three O3 atoms (see chapter 3 for more inforamtion). As can be seen in Figure 4.19, Li1 is found to occupy a highly disorted $Li(O1)_3N$ tetrahedron. Li2 still sits in a distorted LiO_6 octahedron but with substantially shorter Li-O bond distances, Li3 is also found to sit at the top of the equalateral triangle formed by three O3 but with much shorter Li3-O3 distance of 1.87 Å (from neutron diffraction) relative to that of ~2.375 Å for Na3-O3.

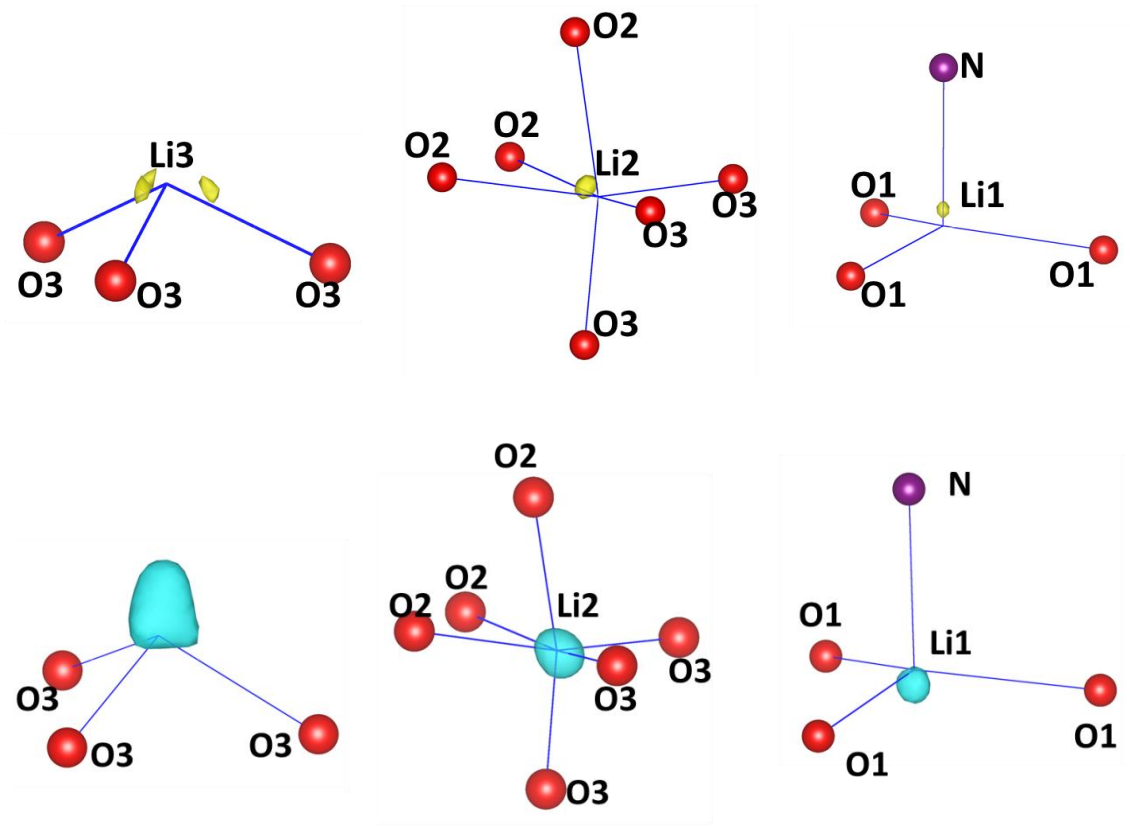

Figure 4.16 Top panel, calculated Fourier difference map from XRD data with yellow isosurface showing the residual electron density (threshold 0.75 e/Å^3). I should be noted that the splitting of electron density at Li3 site is presumably an artificial effect due to the symmetry constraint, detailed information can be found in the refinement part. Bottom panel, calculated Fourier difference map from neutron data (bank 2) with cyan isosurfac showing the residual nuclear scattering length density (threshold 0.45 fm/Å^3). The blue colored bonds are drawn to the final refined Li^+ positions.

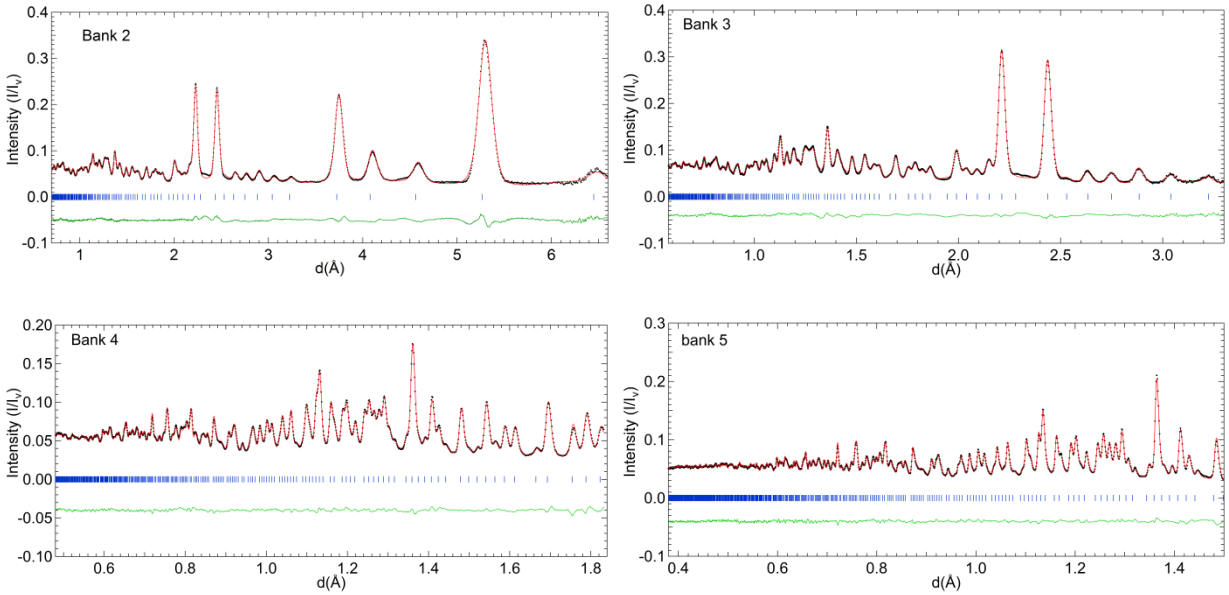

Figure 4.17 Rietveld refinement of $Li_3VP_3O_9N$ using TOF neutron diffraction data with experimental data (black dots), calculated intensities (red line) and different curve (green line), and positions of Bragg diffraction peaks are marked in blue.

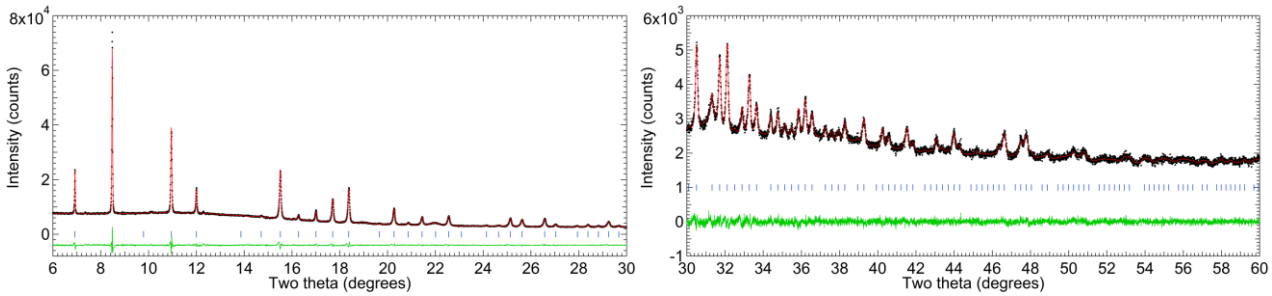

Figure 4.18 Rietveld refinement of $Li_3VP_3O_9N$ using synchrotron XRD data (λ = 0.77878 Å) with experimental data (black dots), calculated intensities (red line) and different curve (green line), and positions of Bragg diffraction peaks are marked in blue.

Table 4.11 Summary of Rietveld refinement results of $Li_3VP_3O_9N$.

Radiation	XRD	TOF neutron
λ	0.77878 Å	0.1-3 Å
Formula	$Li_3VP_3O_9N$	$Li_3VP_3O_9N$
Crystal system	Cubic	Cubic
Space group	*$P2_13$(198)*	*$P2_13$(198)*
Lattice a	9.1237(1)Å	9.1214(3)Å
Cell volume	759.48(2)$Å^3$	758.91(8) $Å^3$
R_{wp}	2.76%	2.88%
R_p	2.03%	2.48%
χ^2	1.68	2.79

Table 4.12 Rietveld refinement results for $Li_3VP_3O_9N$ using TOF neutron diffraction data measured at 300 K. (NOMAD, SNS).

Atom	Wyck.	*x*	*y*	*z*	Occ.	B_{eq} ($Å^2$)
Li1	4a	0.0573(6)	0.0573(6)	0.0573(6)	1	2.3(2)
Li2	4a	0.3915(5)	0.3915(5)	0.3915(5)	1	0.97(14)
Li3	4a	0.8396(5)	0.8396(5)	0.8396(5)	1	1.06(14)
V	4a	0.575(2)	0.575(2)	0.575(2)	1	0.4*
P1	12b	0.08845(17)	0.25995(19)	0.34134(18)	1	0.40(2)
O1	12b	0.01528(15)	0.87597(17)	0.22303(16)	1	0.75(3)
O2	12b	-0.00099(15)	0.12845(14)	0.38858(16)	1	0.50(2)
O3	12b	0.18897(17)	0.3239(2)	0.45612(14)	1	0.78(3)
N1	4a	0.20025(10)	0.20025(10)	0.20025(10)	1	0.25(2)

***** Fixed

Table 4.13 Rietveld refinement results for $Li_3VP_3O_9N$ using synchrotron diffraction data measured at 300 K. (X14A, NSLS)

Atom	Wyck.	*x*	*y*	*z*	Occ.	B_{eq} ($Å^2$)
Li1	4a	0.0574(17)	0.0574(17)	0.0574(17)	1	2.81*
Li2	4a	0.390(2)	0.390(2)	0.390(2)	1	2.56*
Li3	4a	0.8448(17)	0.8448(17)	0.8448(17)	1	3.24*
V	4a	0.57285(17)	0.57285(17)	0.57285(17)	1	0.66(6)
P1	12b	0.0902(3)	0.2620(3)	0.3399(3)	1	0.56(4)
O1	12b	0.0149(8)	0.8795(6)	0.2228(5)	1	1.65(16)
O2	12b	-0.0033(6)	0.1331(5)	0.3917(5)	1	0.74(13)
O3	12b	0.1890(5)	0.3266(6)	0.4595(6)	1	0.73(13)
N1	4a	0.1994(8)	0.1994(8)	0.1994(8)	1	1.4(3)

* Fixed when refining atomic positions.

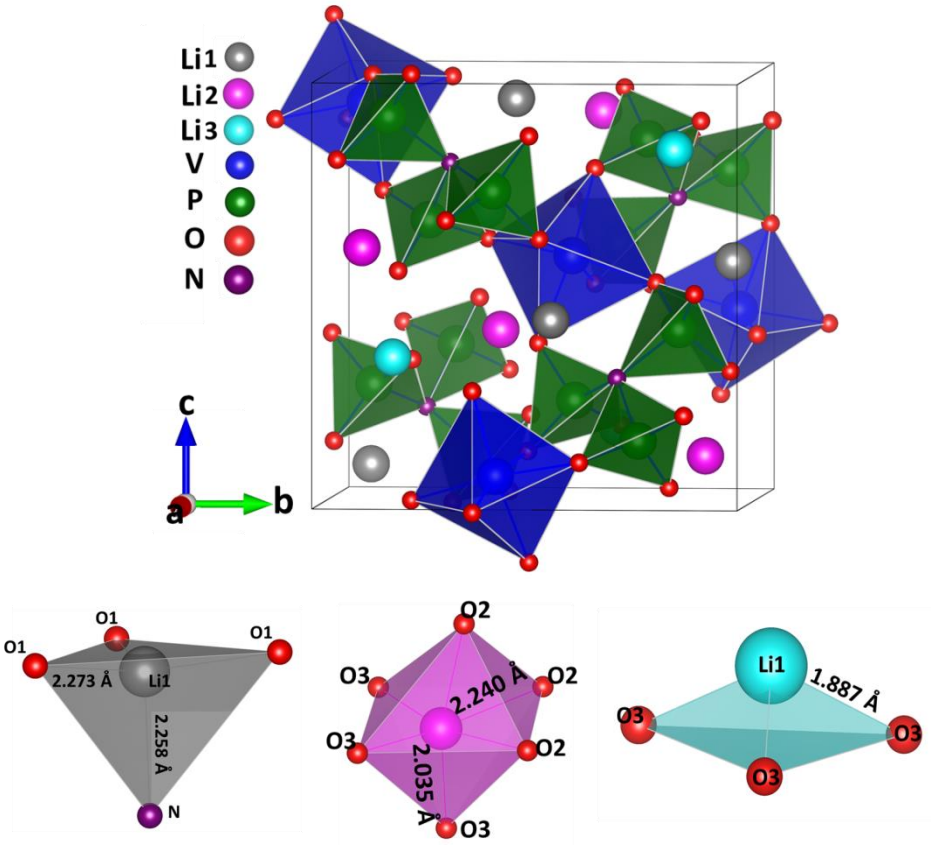

Figure 4.19 Top, Crystal structure of $Li_3VP_3O_9N$ (from neutron diffraction). Bottom, environments for three different Li-ion sites.

4.3.6 *In situ* XRD study of Li^+/Na^+ ion exchange of $Na_3VP_3O_9N$

Similar to the *in situ* XRD study of Li^+/Na^+ ion exchange of $Na_3AlP_3O_9N$, ion exchange of $Na_3VP_3O_9N$ was also collected at X-14A beamline at NSLS. The as-collected diffraction data as a function of temperature evolution were shown in Figure 4.20. It can be seen that no obvious second phase can be observed until the temperature reached 200 ℃. However, the diffraction peaks associated with NaCl (one of the product of ion exchange of $Na_3VP_3O_9N$ and LiCl) were observed at amuch lower temperature of 180 ℃, indicating the onset temperature for ion exchange is much lower than that of the appearance of second ion exchanged phase (phase B). This also indicates the existence of solid solution region between pristine phase A and ion exchanged phase B, which has been further confirmed by the formation of asymmetrical diffraction peaks of these two phases with peak tail to opposite direction, as

can be seen in the bottom panel of Figure 4.20. Detailed structure evolution studies are undergoing and will be presented in follow up papers.

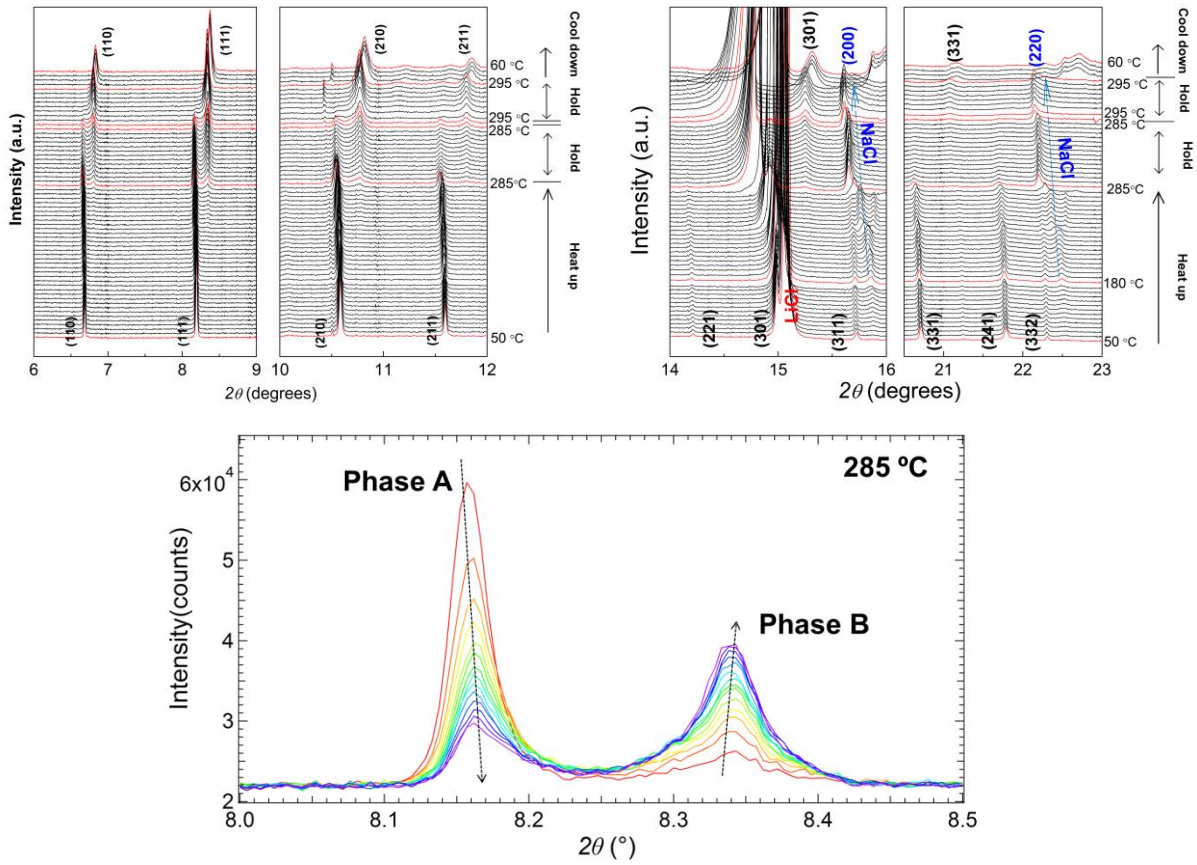

Figure 4.20 (Top panels) selected regions of synchrotron XRD patterns collected during *in situ* Li^+/Na^+ ion exchange. Temperature profiles are shown on the right side. It can be seen that the second phase formed at 180 ℃ degrees, whereas NaCl phase formed at much lower temperature of 125 ℃. (Bottom panel) evolution of $Na_3VP_3O_9N$ (111) diffraction peak during isothermal hold at 285 ℃.

4.3.7 Synthesis and structure study of $Li_2TiP_3O_9N$

Both the traditional ion exchange methods (liquid or molten salt) and newly developed solid-solid ion exchange method can be used to synthesize $Li_{3-x}TiP_3O_9N$. Only the latter method will be addressed here. Unlike the ion exchange of $Na_3AlP_3O_9N$ and $Na_3VP_3O_9N$, which took three to four repeated ion exchanges to synthesize pure lithium variants, it only took two repeated solid-solid ion exchange

process to fully ion exchange $Na_3TiP_3O_9N$, as can be seen in Figure 4.21. Interestingly, only two distinct phases were observed during the whole exchange process, in contrast to three phases in the case of $Na_3AlP_3O_9N$ and $Na_3VP_3O_9N$. This is very likely to be caused by the oxidation of Ti^{3+} to Ti^{4+} during ion exchange due to the relative low redox potential of Ti^{3+}/Ti^{4+}. This oxidation process is associated with simultaneous Na^+/Li^+ removal, leaving an empty Li/Na site (Li1 or Na1 site, see Rietveld refinement result). Thus, only two potential ion exchange sites exist in the structure (Na2 and Na3). The oxidation of Ti^{3+} has been confirmed by corresponded Ti K-edge absorption spectra shown in Figure 4.22. It can be seen that the absorption edge of ion exchanged products almost fully overlaps with that of reference TiO_2, indicating that Ti^{3+} has been essentially oxidized to Ti^{4+}. The effective sodium removal after ion exchange has been confirmed by the SEM-EDX pattern (Figure 4.22).

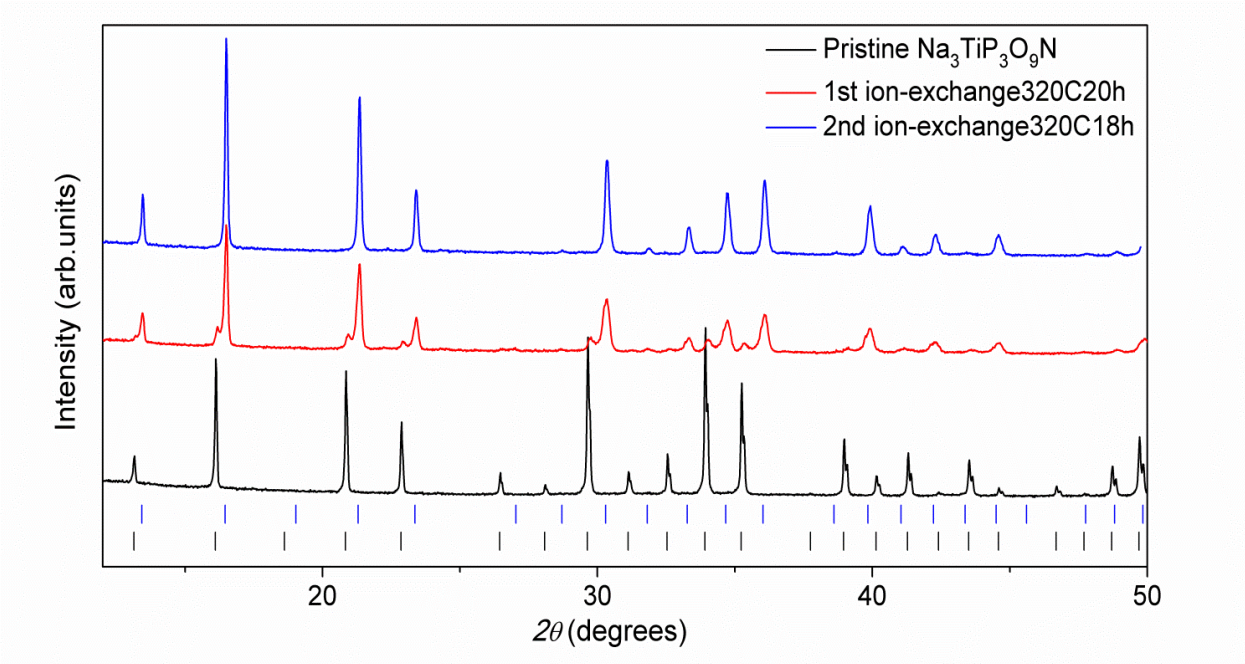

Figure 4.21 Evolution of $Na_{3-x}Li_yTiP_3O_9N$ phases after each ion exchange process.

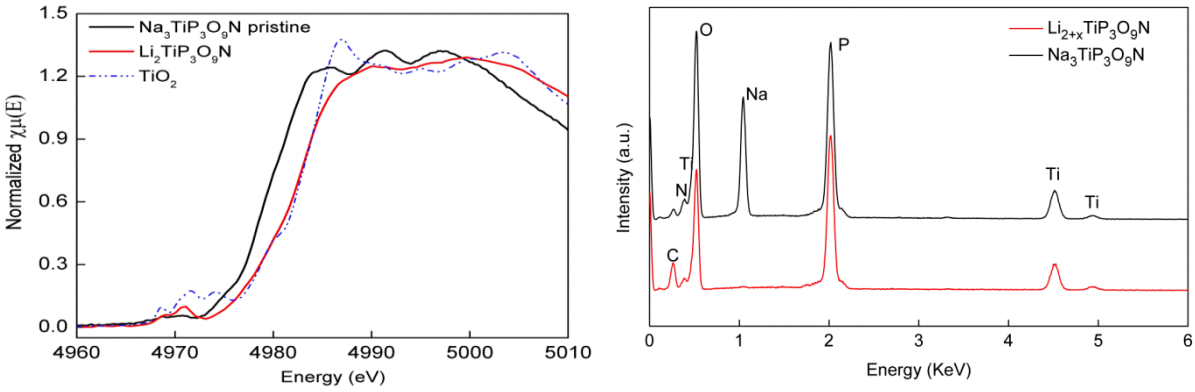

Figure 4.22 Left, Ti K-edge XANES spectra of pristine $Na_3TiP_3O_9N$ and ion exchanged $Li_2TiP_3O_9N$, it can be seen that Ti^{3+} was fully oxidized to Ti^{4+} after Li^+/Na^+ ion exchange, forming $Li_2TiP_3O_9N$ instead of $Li_3TiP_3O_9N$. Right, SEM-DEX of pristine $Na_3TiP_3O_9N$ and ion exchanged $Li_2TiP_3O_9N$. No obvious Na signal can be observed in the ion exchanged products.

Detailed structure information, especially about the atomic environments of different lithium ions, can be obtained by carrying out Rietveld refinement of the structure using high quality synchrotron XRD data. The crystal structure of $Li_3VP_3O_9N$ was used as initial structure model for the Rietveld refinement (Figure 4.23). It was found that Li1 site is the actual vacant lithium site in $Li_2TiP_3O_9N$. After the refinement converged, a reasonably good fit can be achieved with R_{wp} of 4.08% and χ^2 of 3.44. It should be noted that the lattice parameter of $Li_2TiP_3O_9N$ is 9.3074(1) Å, substantially larger than that of $Li_3VP_3O_9N$ (9.1237(1) Å). This difference is associated with the abnormal volume expansion of $Li_3MP_3O_9N$ after Li^+ extraction at Li1 site, which will be discussed in the electrochemistry part.

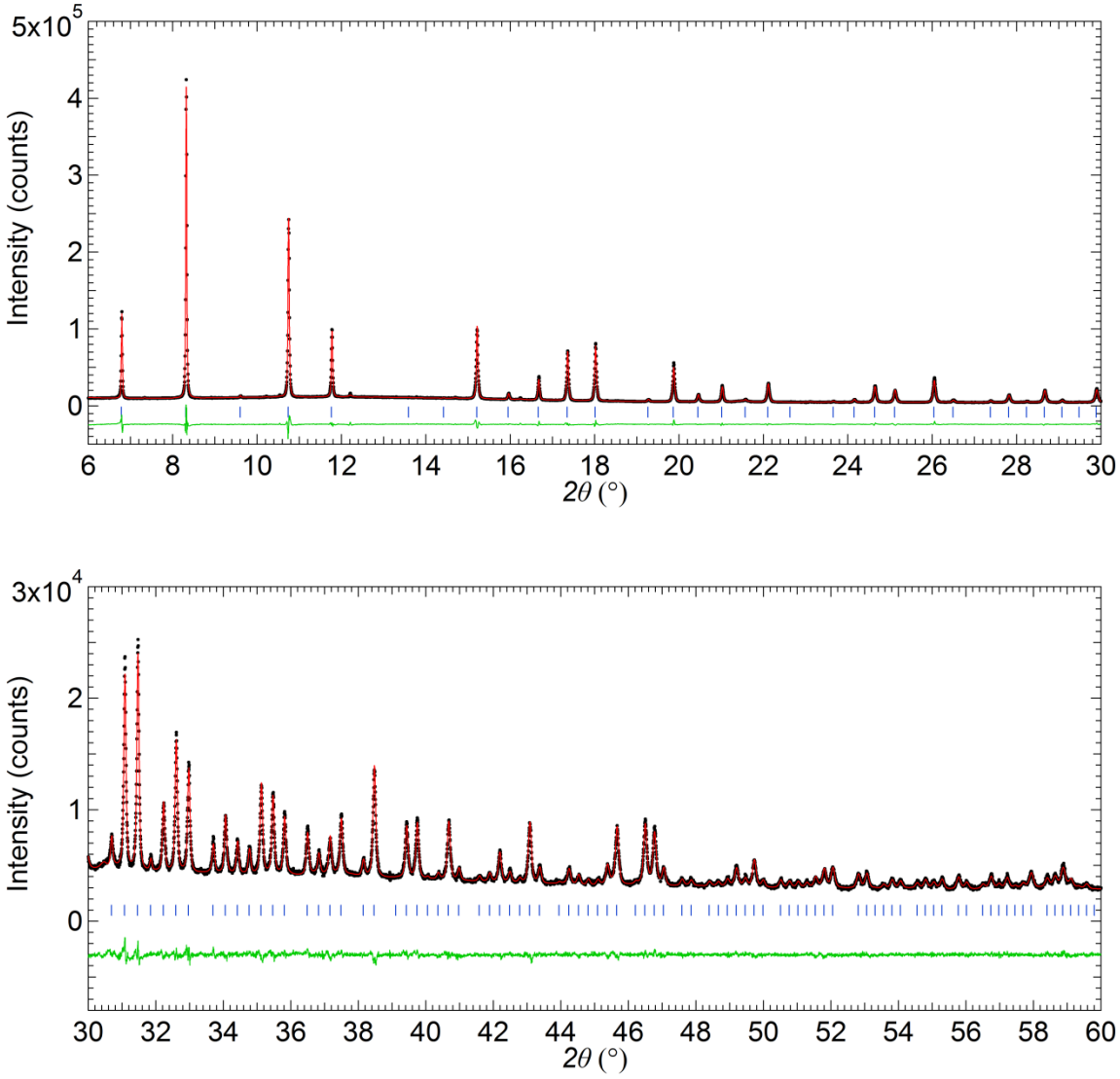

Figure 4.23 Rietveld refinement of $Li_2TiP_3O_9N$ using synchrotron XRD data (λ = 0.77878 Å) of with experimental data (black dots), calculated intensities (red line) and difference curve (green line), and positions of Bragg diffraction peaks are marked in blue.

Table 4.14 Rietveld refinement results for $Li_2TiP_3O_9N$ using synchrotron diffraction data measured at 300 K. (X14A, NSLS)

S.G. *P2₁3*	**a = 9.3074(1) Å**				
Atom	Wyck.	*x*	*y*	*z*	Occ.	B_{eq} (Å^2)
Li2	4a	0.3826(10	0.3826(10	0.3826(10	1	1.93(41)
Li3	4a	0.8605(8)	0.8605(8)	0.8605(8)	1	1.29(34)
V	4a	0.57682(8)	0.57682(8)	0.57682(8)	1	0.47(3)
P1	12b	0.0886(2)	0.2551(2)	0.3337(1)	1	0.52(2)
O1	12b	0.0178(3)	0.8560(3)	0.2406(3)	1	0.30(3)
O2	12b	0.0062(3)	0.1242(2)	0.3916(3)	1	0.30(3)
O3	12b	0.1799(3)	0.3301(3)	0.4477(3)	1	0.30(3)
N1	4a	0.1992(4)	0.1992(4)	0.1992(4)	1	0.30(3)

4.3.8 Electrochemistry of $Li_3VP_3O_9N$

$Na_3VP_3O_9N$ and $Na_3TiP_3O_9N$ can work as promising cathode materials for rechargeable Na^+/Li^+ batteries. However, the relatively heavy Na^+ limits the theoretical capacity of these compounds. Also, we have demonstrated that Li^+ variants of these CUBICON compounds showed substantially higher Li^+ conductivity than the Na^+ ionic conductivity of corresponded sodium analogues. This motivates us to explore the electrochemical performance of $Li_3VP_3O_9N$ and $Li_2TiP_3O_9N$ as cathode materials for rechargeable lithium ion batteries.

The as-prepared $Li_3VP_3O_9N$ electrode was cycled against Li^+/Li at C/20 rate between 2.0 V and 4.2 V. The first two galvanostatic charge/discharge curves are shown in Figure 4.24. It can be seen that the average redox potential is around 3.8 V. The cyclability of this compound at C/20 rate is shown on the right side of Figure 4.24. An average discharge capacity of 70 mAh/g was achieved with good capacity retention. As noticed in chapter 3, potential multi-electron redox couple $V^{3+}/V^{4+}/V^{5+}$ can be for $Na_3VP_3O_9N$ as a cathode in hybrid ion battery. Therefore, it is also expected that multi-electron redox couples may also be accessible for $Li_3VP_3O_9N$. To explore this possibility, cyclic voltammetry (CV) data of $Li_3VP_3O_9N$ electrode against lithium metal anode were collected for different voltage windows. The data are shown in Figure 4.25. When the battery was charged to 5.1 V, it clearly showed the existence of two distinct charge plateaus, one at 3.9 V and the other at 4.9 V. However, no obvious discharge plateaus were observed and a broad redox peak instead appeared on the CV curve, indicating

a structure change or even collapsing after charging to this high voltage. For the CV curve collected between 1.2 V and 4.5 V, two clear reversible redox peaks were observed, one at 3.9 V and the other at 1.6 V, the first peaks is associated with the $V^{3+/}V^{4+}$ couple while the latter is due to the V^{2+}/V^{3+} couple. These results indicate that 2.0 V to 4.5 V is the optimized charge/discharge voltage window for $Li_3V_3P_3O_9N$ cathode.

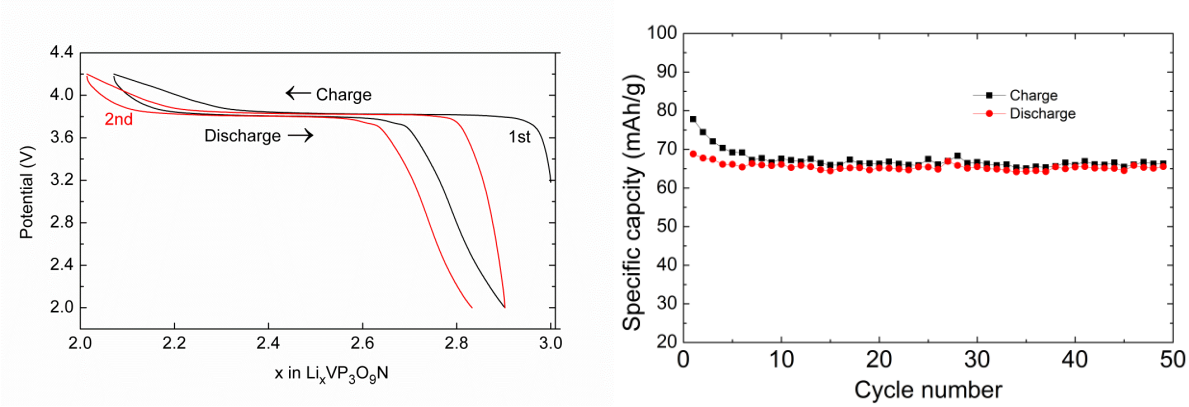

Figure 4.24 Left, the first two charge/discharge curves of $Li_3VP_3O_9N$ against Li^+/Li at C/20 rate. Right, cyclability of $Li_3VP_3O_9N$ at C/20 rate.

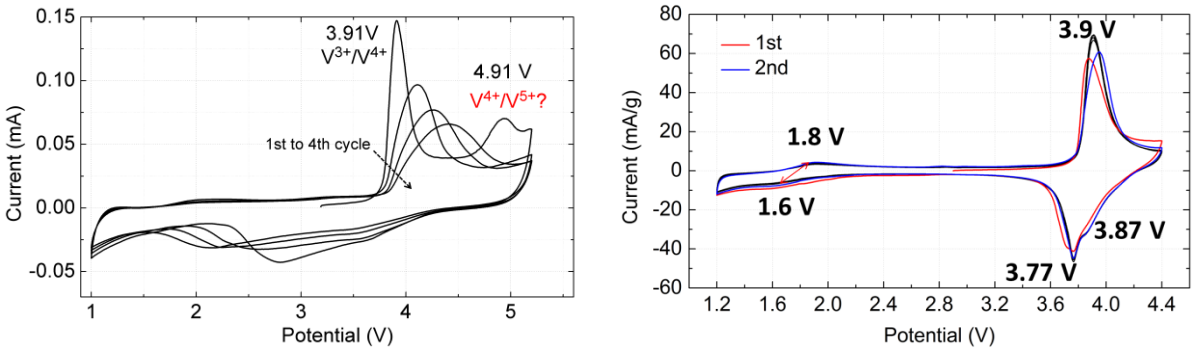

Figure 4.25 Left, CV curves of $Li_3VP_3O_9N$ against Li^+/Li at 0.05mV/s scan rate between 1.0 V and 4.9 V. Right, CV curves of $Li_3VP_3O_9N$ against Li^+/Li at 0.05mV/s scan rate between 1.2 V and 4.5 V.

Further insights into the structure evolution during electrochemical Li^+ intercalation/deintercalation can be obtained by carrying out *in situ* X-ray diffraction studies. The *in situ* diffraction patterns as a function of charge/discharge state are shown in Figure 4.26. A clear phase transition can be observed

after the cell is charged to voltages higher than 3.8 V, indicating the delithiation process follows a two phase reaction. The most intriguing feature is the lattice parameter increase during lithium removal, as can be seen from the shift of diffraction peaks to the lower two theta angle direction during charge. A detailed Rietveld refinement of synchrotron XRD data of chemical delithiated sample indicates that the Li1 site is the actual vacant lithium site, which is consistent with our observation for $Li_2TiP_3O_9N$. Further work is required to understand the exact reason for this abnormal volume expansion, results will be reported elsewhere soon.

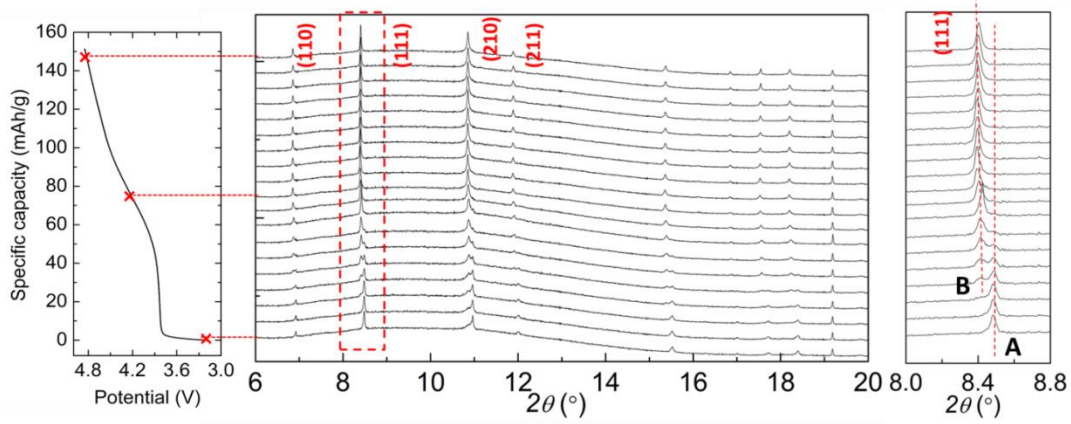

Figure 4.26 *In situ* XRD patterns collected of $Li_3VP_3O_9N$ cycled against Li^+/Li at C/20 rate. Data were collected at X-14A beamline (λ = 0.7787 Å). Phase A is the pristine phase and Phase B is the Li deficient phase.

4.3.9 Electrochemistry study of $Li_2TiP_3O_9N$

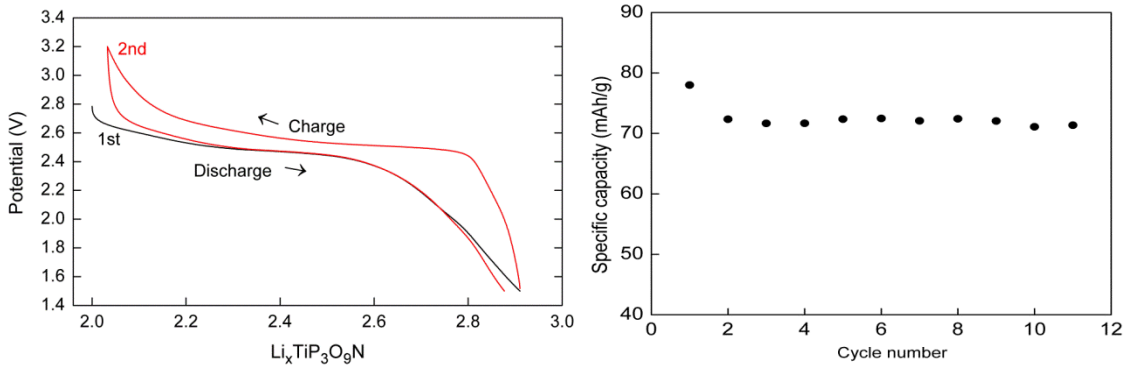

Figure 4.27 Left, first and second charge/discharge curve of $Li_2TiP_3O_9N$ against Li^+/Li at C/20. Right, specific discharge capacity of $Li_2TiP_3O_9N$ at C/20 rate.

Since $Li_3TiP_3O_9N$ was oxidized to $Li_2TiP_3O_9N$ after ion exchange, the as-prepared electrode was discharged first, as can be seen in Figure 4.27. Curiously, the average redox potential of $Li_2TiP_3O_9N$ against Li^+/Li (~2.5 V) is about 0.2 V lower than that of $Na_3TiP_3O_9N$ against Na^+/Na (~2.7 V), indicating that local alkali ion environments played a very important role in determining the actual redox potential. A reversible discharge capacity of about 70 mAh/g was obtained after 10 cycles, as can be seen on the right side of Figure 4.27.

4.4 Conclusion

$Li_xFe_2P_3O_9N$, $Li_2TiP_3O_9N$ and $Li_3VP_3O_9N$ have been successfully synthesized from their sodium analogues by a newly developed solid-solid ion exchange method. These compounds have similar crystal structure as their sodium analogues but with much smaller lattice parameters, lithium ion positions are successfully identified. All of these compounds have been proven to work as promising cathode materials for rechargeable Li-ion batteries. An unusual volume expansion was observed for $Li_3VP_3O_9N$ after lithium removal, future structural and theoretical work is needed to fully unravel the origin of this behavior.

References

(1) Liu, J.; Yu, X. Q.; Hu, E. Y.; Nam, K. W.; Yang, X. Q.; Khalifah, P. G. *Chem. Mater.* **2013**, *25*, 3929.
(2) Mizushima, K.; Jones, P. C.; Wiseman, P. J.; Goodenough, J. B. *Mater. Res. Bull.* **1980**, *15*, 783.
(3) Ohzuku, T.; Ueda, A.; Nagayama, M. *J. Electrochem. Soc.* **1993**, *140*, 1862.
(4) Ohzuku, T.; Makimura, Y. *Chem. Lett.* **2001**, 642.
(5) Guilmard, M.; Pouillerie, C.; Croguennec, L.; Delmas, C. *Solid State Ionics* **2003**, *160*, 39.
(6) Thackeray, M.; David, W.; Bruce, P.; Goodenough, J. *Mater. Res. Bull.* **1983**, *18*, 461.
(7) Lu, Z.; MacNeil, D.; Dahn, J. *Electrochem. Solid-State Lett.* **2001**, *4*, A191.
(8) Manthiram, A.; Goodenough, J. B. *J. Power Sources* **1989**, *26*, 403.
(9) Manthiram, A.; Goodenough, J. B. *J. Solid State Chem.* **1987**, *71*, 349.
(10) Padhi, A. K.; Nanjundaswamy, K. S.; Goodenough, J. B. *J. Electrochem. Soc.* **1997**, *144*, 1188.
(11) Masquelier, C.; Croguennec, L. *Chem. Rev.* **2013**, *113*, 6552.
(12) Islam, M. S.; Driscoll, D. J.; Fisher, C. A.; Slater, P. R. *Chem. Mater.* **2005**, *17*, 5085.
(13) Ellis, B. L.; Makahnouk, W. R. M.; Makimura, Y.; Toghill, K.; Nazar, L. F. *Nat. Mater.* **2007**, *6*, 749.
(14) Barker, J.; Gover, R. K. B.; Burns, P.; Bryan, A.; Saidi, M. Y.; Swoyer, J. L. *J. Power Sources* **2005**, *146*, 516.
(15) Petricek, V.; Dusek, M.; Palatinus, L. *Z. Kristallogr.* **2014**, *229*, 345.

(16) Ravel, B.; Newville, M. *J Synchrotron Radiat* **2005**, *12*, 537.
(17) Lebail, A.; Duroy, H.; Fourquet, J. L. *Mater. Res. Bull.* **1988**, *23*, 447.
(18) Shannon, R. D.; Prewitt, C. T. *Acta Crystallographica Section B-Structural Crystallography and Crystal Chemistry* **1969**, *B 25*, 925.
(19) Brese, N. E.; Okeeffe, M. *Acta Crystallographica Section B-Structural Science* **1991**, *47*, 192.
(20) Oszlanyi, G.; Suto, A. *Acta Crystallographica Section A* **2004**, *60*, 134.

Chapter 5 Redox-inactive $Li_2Mg_2P_3O_9N$ and $Li_3AlP_3O_9N$ as promising solid state electrolytes for rechargeable Li-ion batteries

5.1 Introduction

Ionic exchange property of open framework solid state inorganic compounds had been recognized for a long time[1], however, it was not until the early 20th century that this property was utilized for designing functional materials for water softening, nuclear waste recover or catalysis.[2-4] Later on, the significant mobility of specific monovalent cations, such as H_3O^+, Li^+, Na^+, K^+. Cs^+, Tl^+, Cu^+ and Ag^+, within more compacted solid state inorganic frameworks attracted broad interest.[5-9] They have been widely investigated for electrochemical applications, such as batteries and ionic conductors[10]. It was during this era, several important fast ionic conductors such as β''-alumina and NASICON[5,8] were discovered. Among these studies, ionic exchange was not only used to evaluate the ionic conductivity of a specific structure framework but was also used to synthesize metastable phases that cannot be directly obtained from high temperature solid state synthesis, as exemplified by $NaSbO_3$[8] and $Li_2Ti_6O_{13}$[11].

Among different types of ionic exchange, Na^+/Li^+ ionic exchange is of great importance. It can be used to synthesize a variety of Li-based cathode materials, such as layered $LiMnO_2$[12], O2-type $LiCoO_2$[13], rhombohedral $Li_3V_2(PO_4)_3$[14] and $Li_xFe_2P_3O_9N$[15], for rechargeable Li-ion batteries. Although Na^+/Li^+ ion exchange has been widely used to synthesize many new electrode/solid state electrolyte materials, most of these studies only focused on the structures of ion exchanged products and their electrochemical performance. Very few reports have investigated the mechanism of Na^+/Li^+ ion exchange. The lack of this type of study is mainly due to the limitation of utilizing *in situ* characterization techniques for this system. The difficulties can be explained in two ways. First, molten salts or highly concentrated liquid solutions create very strong amorphous scattering background which will be difficult to model and thus prevent quantitative phase analysis. Second, molten salts may attack holders used for *in situ* experiments. Hydrogen containing (organic solvents or aqueous) liquids may be problematic for *in situ* neutron diffraction due to the strong incoherent nuclear scattering of hydrogen (H), which can only be partially resolved using expensive deuterium (D). Exploring new types of ion exchange methods is critical for designing effective *in situ* diffraction techniques to monitor Na^+/Li^+ ion exchange.

The CUBICON compounds $Na_2Mg_2P_3O_9N$[16-19] and $Na_3AlP_3O_9N$[17-19] have been reported by several groups. The structure of $Na_3AlP_3O_9N$ and $Na_2Mg_2P_3O_9N$ were studied by single crystal X-ray

diffraction, powder synchrotron X-ray and neutron diffraction by our group and other groups. Prior electrochemical impedance spectroscopy studies of the performance of $Na_2Mg_2P_3O_9N$ as a Na-ion conductor found that the sodium ionic mobility at 440 ℃ was about 1.0 $\times 10^{-5}$ S/cm with an activation energy of E_a = 0.75 eV[16], suggesting that the room temperature Na-ion conductivity is very poor. Similar limitations have been found for Na-ion conductivity in $Na_2Fe_2P_3O_9N$, in which only a limited degree of Na-ion removal (~1/3 of ions) was achievable during electrochemical de-intercalation or chemical desodiation[20]. Although the room temperature removal of Na-ions from $Na_2Fe_2P_3O_9N$ was difficult, it was demonstrated that Na-ions could be effectively removed at elevated temperatures, and $Li_{2-x}Fe_2P_3O_9N$ works as an effective Li-ion battery cathode which can essentially achieve its theoretical capacity. The excellent battery performance indicates that the Li-ion mobility is substantially higher than the Na-ion mobility in corresponded $Na_2Mg_2P_3O_9N$. The other member of the Na-based cubic nitridophoshpates $Na_3TiP_3O_9N$ showed much higher Na-ion conductivity of 4×10^{-7} S/cm at room temperature. A thorough structure and density function theory (DFT) investigation revealed that this higher conductivity is probably due to the larger unit cell volume of $Na_3TiP_3O_9N$ and the oxidation of Ti^{3+} to introduce sodium vacancies into the structure. Nevertheless, if Li-ion conductivities are significantly higher for these cubic nitridophosphates, it is plausible that fast Li-ion conductivity may be found for Li-containing CUBICON compounds. This motivates us to investigate the Li^+ mobility of $Li_3AlP_3O_9N$ and $Li_2Mg_2P_3O_9N$, which has not previously been reported. It should be noted that these Li variants cannot be directly synthesized from high temperature solid state reactions, presumably due to the metastable nature of these compounds. Therefore, Li^+/Na^+ ion exchange methods were utilized to synthesize phase pure Li variants of cubic nitridophosphates.

In this chapter, we will first focus on the synthesis, structure and ionic conductivity study of $Li_2Mg_2P_3O_9N$ and $Li_3AlP_3O_9N$. Then the combined *in situ* neutron and X-ray diffraction study of Li^+/Na^+ ion exchange of $Na_2Mg_2P_3O_9N$ and $Na_3AlP_3O_9N$ will be addressed.

5.2 Experimental section

5.2.1 Synthesis of $Na_3AlP_3O_9N$ and $Na_2Mg_2P_3O_9N$

Phase pure $Na_3AlP_3O_9N$ was synthesized by using thermal ammonolysis. Stoichiometric amounts of $NaPO_3$ (Fisher Scientific, n ~ 6) and Al_2O_3 (Alfa Aesar, 99.9%) were mixed together, hand ground, and then ball milled for 120 min in an agate vibratory ball mill (Fischer). The mixture was then transferred

to a boat constructed from thin Mo foil (Alfa Aesar, 0.025 mm thick, purity > 99.985%), which was then loaded into a 1 inch diameter quartz tube inside a horizontal Minimite tube furnace. The whole tube was first purged with a high flow rate of N_2 gas, and then adjusted to a lower flow rate of NH_3 gas at 50 mL/min for the synthesis reaction. The sample was heated directly to 700 ℃ to 780 ℃ at a ramping rate of 150 ℃/h and held there for 20-24 hours, and then cooled down to room temperature inside the furnace at furnace cooling rate. $Na_2Mg_2P_3O_9N$ was synthesized from stoichiometric amounts of $NaPO_3$ (Fisher Scientific, n ~ 6), MgO and $(NH_4)_2HPO_4$ at similar synthetic condition as that of $Na_3AlP_3O_9N$. The as-prepared white $Na_3AlP_3O_9N$ and $Na_2Mg_2P_3O_9N$ powder was then ground and stored in a desiccator for further characterization.

5.2.2 Synthesis of $Li_3AlP_3O_9N$ and $Li_2Mg_2P_3O_9N$

About 0.6 g $Na_3AlP_3O_9N$ or $Na_2Mg_2P_3O_9N$ were mixed with anhydrous LiBr (SPECTRUM, > 99%) in a molar ratio of 1:8 (Na to Li) in an argon-filled glove box. The mixture was ground in an agate mortar and pestle for 30 min before filling into a 50 mL graphite crucible, and transferred into a home-made desiccator prior to reaction. For the ion exchange reaction, the powder mixture was quickly loaded into a mullite tube inside a horizontal tube furnace (Mellen, SV Series), which was then purged with Ar gas for about 40 min. Ion exchange was carried out at 340 ℃ for 20 hours under the flowing of Ar. The reaction product was first washed by methanol 5 times, and then washed twice by acetone and placed in an oven at 80 ℃ for ~ 4 hours. It was found four cycles of repeated ion-exchange were needed to obtain pure $Li_3AlP_3O_9N$ and $Li_2Mg_2P_3O_9N$. About 0.2 g – 0.4 g final product could be recovered at the end of the exchange process.

5.2.3 XRD and neutron diffraction

Laboratory X-ray diffraction (XRD) data of the as-prepared $Li_xNa_{3-x}AlP_3O_9N$ ($0 \leq x \leq 3$) and $Li_xNa_{2-x}Mg_2P_3O_9N$ ($0 \leq x \leq 2$) were collected on a Bruker D8 Advance diffractometer utilizing Cu Kα radiation from a fine focus X-ray tube (Kα1 = 1.54053 Å, Kα2 = 1.54431 Å). The system was operating at a 217.5 mm working radius with a 1D position-sensitive LynxEye Si detector with 192 channels. A step size of 0.02 ° and count time of 2s/step were used for data collection. Synchrotron XRD data were collected at the X 14A beam line of the National Synchrotron Light Source (NSLS) at Brookhaven National Laboratory (λ ~ 0.778 Å). Data were collected using a 1D linear position sensitive silicon strip detector with 640 channels at a distance of 1433 mm, and the final patterns for refinement was obtained

by merging data sets collected at a number of different fixed angles. Data was collected between 6 ° and 60 ° with a step size of 2 ° and count time of 40 s/step were used for data collection.

Time-of-flight powder neutron diffraction data of $Na_3AlP_3O_9N$, $Na_2Mg_2P_3O_9N$, $Li_3AlP_3O_9N$ and $Li_2Mg_2P_3O_9N$ were collected on the NOMAD beamline at the Spallation Neutron Source (SNS) of Oak Ridge National Laboratory (ORNL). About 200 mg of powder was loaded into a 3 mm diameter quartz capillary. Typical data collection times were 100 – 120 min. The NOMAD data were reduced using custom beamline software[21] which allowed both the analysis of Bragg diffraction data through Rietveld refinement and pair distribution function (PDF) data.

5.2.4 *In situ* x-ray diffraction studies of ion exchange of $Na_3AlP_3O_9N$

Anhydrous LiCl was used as lithium source. $Na_3AlP_3O_9N$ was ground with LiCl in a molar ratio of 6: 1 (Li:Na moalr ratio) in an argon filled glove box. The mixture was then loaded into a 7 mm (diameter) quartz capillary, the capillary was then sealed with clay before transfer to the beamline X14A, NSLS for mounting. For data collection, the sample was heated up at a ramp rate of 2 ℃/min up to 330 ℃ with interval holdings at 150 ℃, 240 ℃ and 280 ℃ separately. The mixture was held at 330 ℃ for 10 hours and then cooled down naturally to 40 ℃. Diffraction scans were collected continuously through the whole ion exchange process with scan speed of 15 min/scan between 6 ° and 40 °. Data were collected using a 1D linear position sensitive silicon strip detector with 640 channels at a distance of 1433 mm, and the final patterns for refinement was obtained by merging data sets collected at a number of different fixed angles.

5.2.5 *In situ* neutron diffraction studies of ion exchange of $Na_3AlP_3O_9N$ and $Na_2Mg_2P_3O_9N$

For *in situ* neutron diffraction study, ^{7}LiCl was used as lithium source. To synthesize dehydrated ^{7}LiCl, 5 grams $^7Li^2CO_3$ (Sigma Aldrich, > 99% atom) was dissolved into 500 ml 0.5 M HCl solution, (~1:4 molar ratio of $^7Li_2CO_3$ to HCl). The mixture were magnetic stirred for about 30 min until a transparent solution was formed, and then heated to 150 ℃ to evaporate residual water and excess HCl. The white powder of hydrated ^{7}LiCl was then collected and transferred to a 50 ml alumina crucible and further dried at 400 ℃ for 12 hours in box furnace, and the crucible was immediately transferred while hot into a home-made desiccator and then into an argon filled glove box in which the sample was fully cooled down to room temperature. About 1.2 grams of $Na_3AlP_3O_9N$ were ground with 4 g ^{7}LiCl in an argon filled glove box, the mixture was then transferred into a 6 mm thin walled vanadium can which

was sealed and then attached to the end of the cryofurnace sample stick, more details can be found in reference[22].The temperature of the system was calibrated using diffraction data from a corundum standard and the previously determined thermal expansion properties of this phase. In situ neutron diffraction patterns were collected at 8 different temperatures during the initial ramp from 27 ℃ to 332 ℃ during the ion exchange process. The sample was equilibrated at each temperature for 15 min before a 1 h data collection. After the temperature reached 332 ℃, the sample was then held at this temperature for another 24 hours, data was collected in consecutive 30 min scans during this holding. Then the furnace was allowed to cool down to 27 ℃ naturally. Finally, a 4 hours scan was collected at 27 ℃. Neutron diffraction data from POWGEN were reduced using the MANTID software package. In all cases, data were normalized to the scattering of a V rod (after stripping Bragg peaks and smoothing), and were corrected for absorption effects during refinement.

5.2.6 Refinements and fittings

Le Bail fitting of *ex situ* laboratory X-ray diffraction (XRD) data of $Li_xNa_{3-x}AlP_3O_9N$ ($0<x<3$) and $Li_xNa_{2-x}Mg_2P_3O_9N$ ($0\leq x\leq 2$) was carried out using the TOPAS software package (Bruker-AXS, v4.2) with a fundamental parameters approach. Rietveld refinement of crystal structures from *ex situ* synchrotron XRD data was carried out with similar conditions, with additional refinements of $Li_3AlP_3O_9N$ data carried out in Jana 2006[23] to generate Fourier difference maps. The conversion from time-of-flight to *d*-spacing was done using 2nd degree polynomial parameters (d0, dfa, dfc) refined from a LaB_6 standard sample. The peak shapes were primarily modeled using a pseudo-Voigt function, with an additional exponential convolution used to model the extended peak tails on the high *d*-spacing side of the peaks. No absorption correction was applied to the NOMAD data, since the absorption by the sample and the capillary were both small. PDF data were fit using the PDFgui software package[24] using the average structure obtained from Rietveld refinement as the starting model. For POWGEN data, an estimated absorption coefficient of $\varepsilon = 0.4\ cm^{-1}$ was used to model the absorption from both the sample and the V can.

Le Bail fittings of *in situ* x-ray diffraction patterns was carried out in the TOPAS software package (version 4.2) in a parametric manner. Sample displacement, background and instrumental broadening related parameters were fixed for all patterns collected at the same temperature, and the only variables to be refined are lattice parameters and the isotropic strain/size broadening term. Similar refinement

conditions were used for *in situ* neutron diffraction patterns to gain insights into lattice parameter evolution. Rietveld refinements of selected *in situ* x-ray diffraction patterns were also carried out in parameteric manner, lattice parameters were fixed to the value obtained from Le Bail fitting of specific diffraction patterns. However, since LiCl diffraction peaks are too strong to be simultaneously refined with ion exchanged $Li_xNa_{3-x}AlP_3O_9N$ phases, LiCl related diffraction peaks were excluded during Rietveld refinement. For Rietveld refinements of *in situ* neutron diffraction patterns, all phases are quantitatively refined in a parametric manner, LiCl and the as-formed NaCl were also included into the refinement.

5.2.7 Scanning electron microscopy

Scanning electron microscopy images and energy dispersive X-ray (EDX) spectra were collected on JEOL 7600 instrument. Powder samples were loaded onto carbon tape for measurements. The data collection and analysis of EDX was carried out using the INCA software. The SEM was operated at 5 kV in low vacuum condition during imaging to minimize charging effects. For EDX data collection, the operation voltage was set to 15 kV.

5.2.8 Solid state ^{7}Li NMR

^{7}Li NMR measurement of $Li_3AlP_3O_9N$ and $Li_2Mg_2P_3O_9N$ powder was performed on an 8.46 T Wide-bore Varian Chemagnetics Infinity Plus 360 MHz spectrometer equipped with a 1.8 mm HX probe (Argo Samoson). $Li_3AlP_3O_9N$ powder was packed into a 1.8 mm silicon nitride rotor and spun at 36 kHz. A rotor-synchronized spin echo sequence ($\pi/2$-$\tau1$-π-$\tau2$-acquisition) was utilized with a pulse width of 1.85 μs and a recycle delay of 1 s. ^{7}Li chemical shift was externally referenced to 1 M LiCl solution at 0 ppm.

5.2.9 Impedance measurement

Ac impedance spectra were utilized to evaluate lithium ionic conductivity in the as-prepared $Na_3AlP_3O_9N$, $Na_2Mg_2P_3O_9N$, $Li_3AlP_3O_9N$ and $Li_2Mg_2P_3O_9N$. For the measurement of Na^+ conductivity, the as-prepared $Na_3AlP_3O_9N$ and $Na_2Mg_2P_3O_9N$ powder was pressed into ½ inch diameter pellet with hydraulic press. Silver paste was coated on each side of the pellet and was cured at 300 ℃. For lithium variants, the well ground $Li_3AlP_3O_9N$ and $Li_2Mg_2P_3O_9N$ powder was pressed into ¼ inch diameter) pellets in an isostatic press with ~ 1 GPa pressure. The density of these pellet was found to be over 90%

and no obvious structure change was observed after applying high pressure to these materials. The pellets were further polished and coated with a thin layer of Pt on each side. For impedance measurements, the pellets were first loaded into a spring loaded Teflon cell and the whole cell was then sealed in a layer of aluminum foil and placed into a steel tank. Shielded copper wire was used to connect Teflon cell with coaxial cable and then connected to a BIOLOGIC VMP3 electrochemical station. Data was collected between 0.1 Hz and 1 MHz with amplitude of 100 mV to 200 mV. Data analysis was carried out in the Zview software.

5.3. Results and discussions

5.3.1 $Li_2Mg_2P_3O_9N$

5.3.1.1 Synthesis and structure study of $Na_2Mg_2P_3O_9N$

$Na_2Mg_2P_3O_9N$ was first synthesized in bulk quantities using solid state reaction procedures in order to have sufficient sample to explore the structural and ion exchange properties of this phase. Laboratory X-ray diffraction patterns of the white powders resulting from this ammonolysis reaction showed no evidence of impurity phases, and indicated that the cubic nitridophosphate had good crystallinity. Structural data was obtained by the Rietveld refinement of both synchrotron (X14A, NSLS) and neutron diffraction data (NOMAD, SNS), and confirmed the expected space group of $P2_13$ (#198), with a cubic lattice parameter of a = 9.2439(1) Å refined from the synchrotron data. The details of the method and the refined crystallographic parameters are presented in the Figure 5.1, 5.2 and Tables 5.4, with the structure obtained from this refinement shown in Figure 5.3. The neutron data was particularly sensitive to the light atoms (O, N) due to the large nuclear scattering length of these atoms, and enabled the refinement of anisotropic displacement parameters for all sites as well as the precise determination of bond lengths.

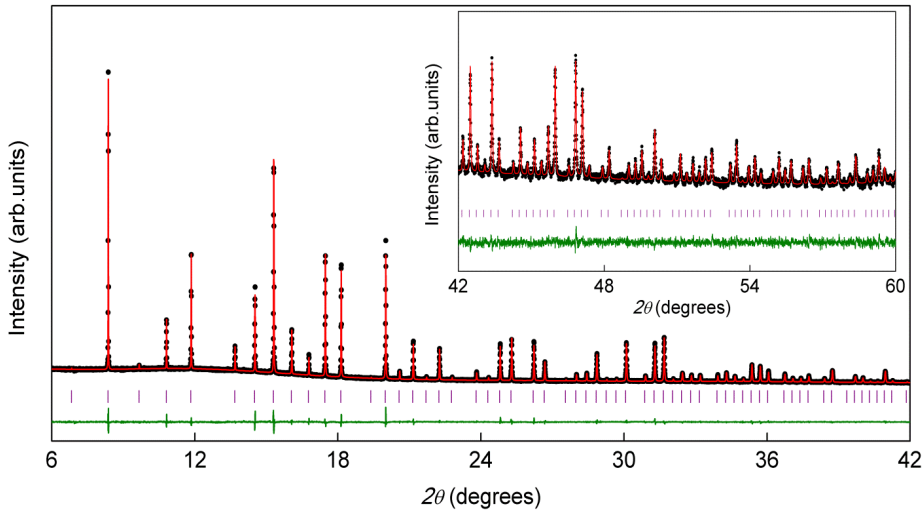

Figure 5.1 Rietveld refinement of $Na_2Mg_2P_3O_9N$ using synchrotron XRD data ($\lambda = 0.77878$ Å) collected at 298 K, with experimental data shown in black (dots), calculated pattern in red, difference curve in green, and Bragg diffraction positions marked in purple.

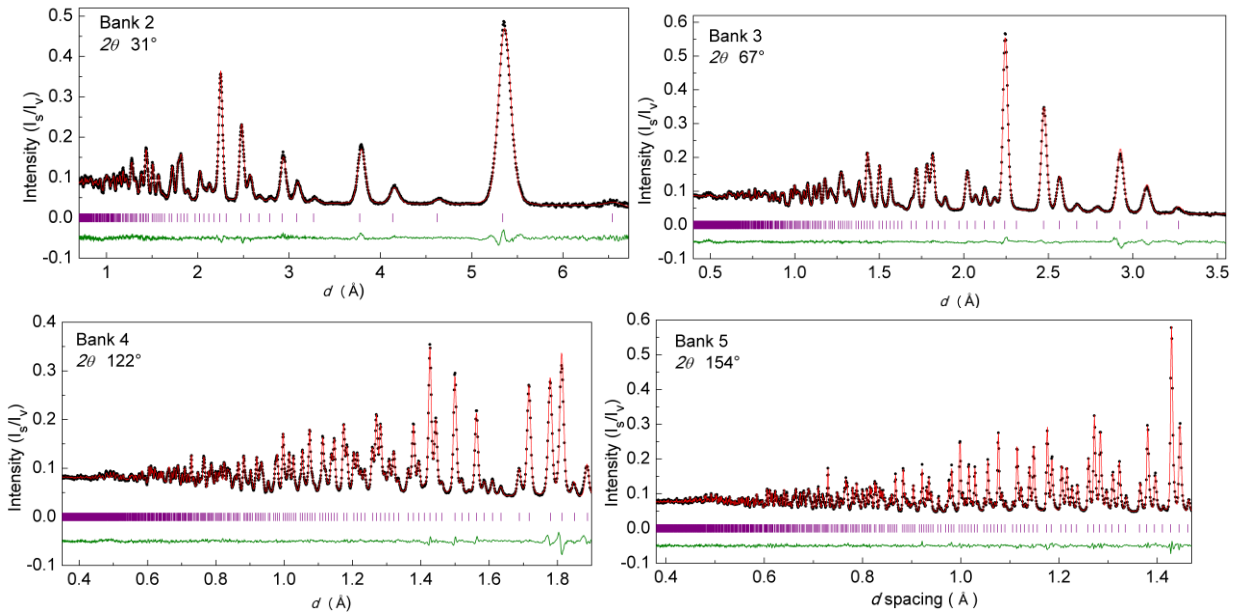

Figure 5.2 Rietveld refinement of $Na_2Mg_2P_3O_9N$ using time-of-flight (TOF) neutron diffraction data collected at 300 K, with experimental data shown in black (dots), calculated pattern in red, difference curve in green, and Bragg diffraction positions marked in purple.

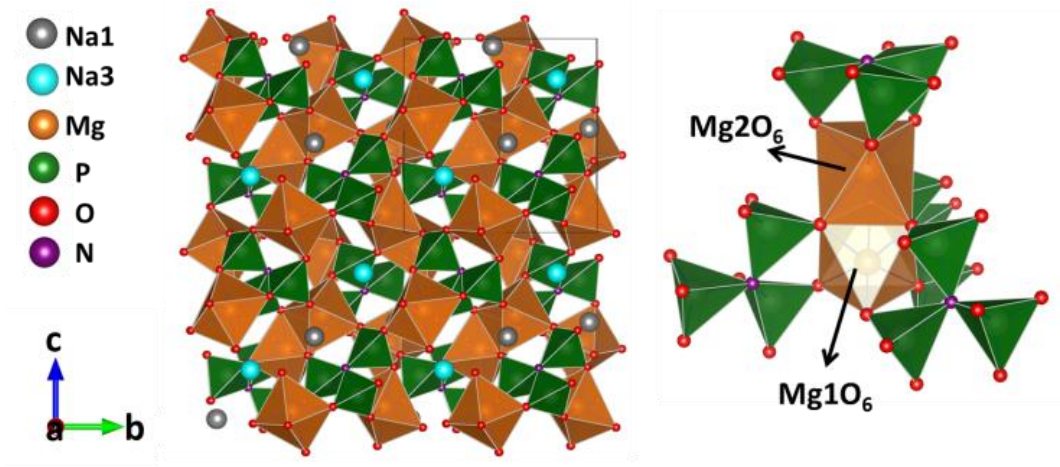

Figure 5.3 $Na_2Mg_2P_3O_9N$ crystal structure with MgO_6 octahedra shown in brown and trimeric PO_3N tetrahedral are shown in green.

Table 5.1 Crystallographic parameters for $Na_2Mg_2P_3O_9N$ obtained by Rietveld refinement

Radiation	X-ray	TOF neutron
Beamline	X14A, NSLS	NOMAD, SNS
wavelength	0.77878 Å	0.1 – 3 Å
Formula	$Na_2Mg_2P_3O_9N$	$Na_2Mg_2P_3O_9N$
Crystal system	Cubic	Cubic
Space group	*$P2_13$ (198)*	*$P2_13$ (198)*
Lattice *a*	9.2439(1) Å	9.2484(1) Å
Cell volume	789.87(1) Å^3	791.05(2) Å^3
R_{wp}	3.53%	2.57%
R_p	2.48%	2.28%
χ^2	2.40	1.36

Table 5.2 Atomic parameters for $Na_2Mg_2P_3O_9N$ (synchrotron XRD, X14A, 298 K)

Atom	Wyck.	*x*	*y*	*z*	Occ.	B_{eq} (Å^2)
Na1	4a	0.03859(19)	0.03859(19)	0.03859(19)	1	1.33(8)
Na3	4a	0.79207(23)	0.79207(23)	0.79207(23)	1	1.54(9)
Mg1	4a	0.57808(18)	0.57808(18)	0.57808(18)	1	0.87(7)
Mg2	4a	0.39824(27)	0.39824(27)	0.39824(27)	1	0.61(7)
P1	12b	0.09072(19)	0.26122(19)	0.34138(18)	1	0.51(2)
O1	12b	0.01349(34)	0.86877(34)	0.22530(38)	1	0.83(7)
O2	12b	0.00146(38)	0.13215(28)	0.39914(34)	1	0.74(8)
O3	12b	0.19248(33)	0.32911(36)	0.45207(35)	1	0.65 (8)
N1	4a	0.19924(37)	0.19924(37)	0.19924(37)	1	0.49(16)

Table 5.3 Atomic parameters for $Na_2Mg_2P_3O_9N$ (TOF neutron, NOMAD, 300 K)

Atom	Wyck.	*x*	*y*	*z*	Occ.	B_{eq} (Å^2)
Na1	4a	0.03785(20)	0.03785(20)	0.03785(20)	1	1.50
Na3	4a	0.79197(23)	0.79197(23)	0.79197(23)	1	2.06
Mg1	4a	0.57742(12)	0.57742(12)	0.57742(12)	1	0.56
Mg2	4a	0.39877(14)	0.39877(14)	0.39877(14)	1	0.80
P1	12b	0.09104(15)	0.26109(14)	0.34149(15)	1	0.57
O1	12b	0.01397(12)	0.86908(13)	0.22297(13)	1	0.88
O2	12b	0.00529(13)	0.13300(11)	0.39951(13)	1	0.66
O3	12b	0.19280(12)	0.32725(13)	0.45090(10)	1	0.89
N1	4a	0.19994(8)	0.19994(8)	0.19994(8)	1	0.59

Atom	U_{11}(Å^2)	U_{22}(Å^2)	U_{33}(Å^2)	U_{12}(Å^2)	U_{13}(Å^2)	U_{23}(Å^2)
Na1	0.0191(7)	0.0191(7)	0.0191(7)	0.0015(6)	0.0015(6)	0.0015(6)
Na3	0.0262(10)	0.0262(10)	0.0262(10)	-0.0007(10)	-0.0007(10)	-0.0007(10)
Mg1	0.0072(4)	0.0072(4)	0.0072(4)	0.0005(4)	0.0005(4)	0.0005(4)
Mg2	0.0103(5)	0.0103(5)	0.0103(5)	-0.0027(5)	-0.0027(5)	-0.0027(5)
P1	0.0084(6)	0.0064(6)	0.0070(5)	0.0013(5)	0.0002(5)	0.0024(4)
O1	0.0130(6)	0.0113(6)	0.0091(6)	-0.0068(5)	-0.0025(4)	-0.0010(4)
O2	0.0079(6)	0.0082(5)	0.0090(5)	-0.0019(4)	0.0020(4)	0.0021(4)
O3	0.0121(14)	0.0157(7)	0.0062(6)	-0.0034(5)	-0.0023(4)	-0.0027(4)
N1	0.0075(3)	0.0075(3)	0.0075(3)	-0.0003(3)	-0.0003(3)	-0.0003(3)

Table 5.4 Selected $Na_2Mg_2P_3O_9N$ bond distances, BVS-calculated valences, and bond angles

Bond	Distance (Å)	Atom	BVS	Angle type	Angle (°)
Na1-O1 (×3)	2.3273(12)	Na1	+0.98	O1-Na1-O1 (×3)	119.970(15)
Na1-N	2.5965(35)	Na3	+0.83	O1-Na1-N (×3)	90.990(84)
Na1-O3 (×3)	2.8905(28)	Mg1	+2.39	O3-Na3-O3 (×3)	78.46(11)
Na3-O3 (×3)	2.4045(27)	Mg2	+2.14	O1-Mg1-O1 (×3)	96.612(75)
Na3-O1 (×3)	2.9745(33)	P	+4.69	O2-Mg1-O2 (×3)	80.029(75)
Na3-O2 (×3)	3.0048(15)	O1	-1.90	O1-Mg1-O2 (×3)	89.778(49)
Mg1-O1 (×3)	1.9993(15)	O2	-1.91	O2-Mg2-O2 (×3)	77.264(80)
Mg1-O2 (×3)	2.0682(16)	O3	- 1.91	O3-Mg2-O3 (×3)	89.697(79)
Mg2-O2 (×3)	2.1301(19)	N	-2.95	O2-Mg2-O3(×3)	92.587(43)
Mg2-O3 (×3)	2.0733(17)	Gii*	0.18	O1-P-O2	108.51(10)
P-O1	1.5153(18)			O1-P-O3	113.31(10)
P-O2	1.5232(17)			O2-P-O3	113.78(11)
P-O3	1.5113(17)			N-P-O1	106.75(9)
P-N	1.7458(14)			N-P-O2	108.21(9)
				N-P-O3	105.90(10)

*Gii: global instability index

While single crystals of the 3:1 CUBICON phases $Na_3TiP_3O_9N$ and $Na_3AlP_3O_9N$ have previously been prepared and structurally characterized[25,26], single crystals have not yet been grown for 2:2 CUBICON phases such as $Na_2Mg_2P_3O_9N$, making the present neutron diffraction data particularly valuable. From the present neutron diffraction data, it can be clearly determined that one Mg^{2+} ion in $Na_2Mg_2P_3O_9N$ replaces the Na^+ ion on the large octahedral Na2 site of $Na_3AlP_3O_9N$, while the other Mg^{2+} ion replaces an Al^{3+} ion at a smaller octahedral site, allowing overall charge balance to be maintained. The two octahedral Mg^{2+} ions in $Na_2Mg_2P_3O_9N$ share a common face, and have similar sizes, as was also seen in our neutron diffraction studies of the closely related compound $Na_2Fe_2P_3O_9N$[15]. In order to be consistent with the nomenclature of the 3:1 CUBICON phases, the two different Na sites in $Na_2Mg_2P_3O_9N$ are labelled as Na1 and Na3. Both of these Na ion sites have low coordination numbers, as was also observed for $Na_3AlP_3O_9N$. Na3 sits above an equilateral triangle formed by three O3 oxygen with Na3-O3 bond distances of about 2.40 Å, while Na1 is found near the center of an equilateral triangle formed by three O1 anions (Na-O bond distances of 2.33 Å), with a single capping Na1-N bond (2.60 Å) that is much shorter than in the 3:1 compound $Na_3AlP_3O_9N$ (2.89 Å).

5.3.1.2 Synthesis and structure study of $Li_2Mg_2P_3O_9N$

$Na_2Mg_2P_3O_9N$ is a thermodynamically stable phase which can be directly synthesized by the methods described here and in the prior literature[16,18]. However, there were no previous reports of the existence of $Li_2Mg_2P_3O_9N$, and our efforts to synthesize this novel phase at a variety of temperatures using methods analogous to those used to prepare the Na-analogue were unsuccessful, suggesting that this phase is at best a metastable compound. Low temperature non-molten salt ion-exchange methods which we originally developed to produce $Li_{2-x}Fe_2P_3O_9N$ cathodes[15] were therefore also investigated as a method of replacing the Na^+ cations in $Na_2Mg_2P_3O_9N$ with Li^+. Although solid-solid Li-ion exchange reactions might be expected to be much slower than analogous liquid-solid reactions due to both the reduced surface area and the reduced mobility of Li^+, *ex situ* X-ray diffraction studies clearly indicated that Li^+ ions could be introduced into $Na_2Mg_2P_3O_9N$ at 330 °C using LiBr as the Li source, as can be seen in Figure 5.4. SEM-EDX spectra confirmed that the removal of Na^+ ions was essentially complete after the fourth exchange cycle (Figure 5.5), resulting in the production of the novel phase $Li_2Mg_2P_3O_9N$.

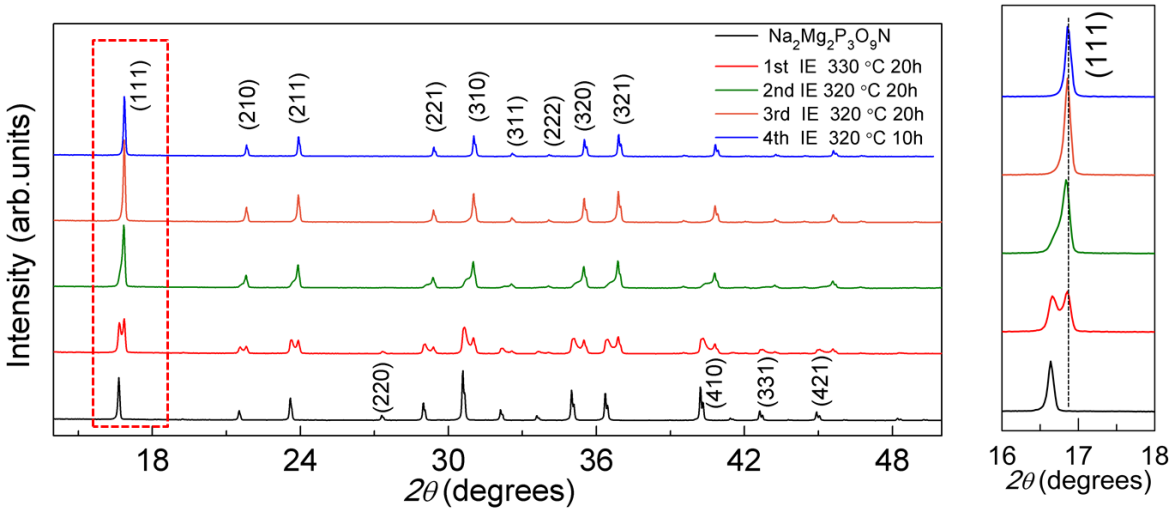

Figure 5.4 Evolution of $Li_xNa_{2-x}Mg_2P_3O_9N$ phases after four successive ion-exchange (IE) steps probed by XRD.

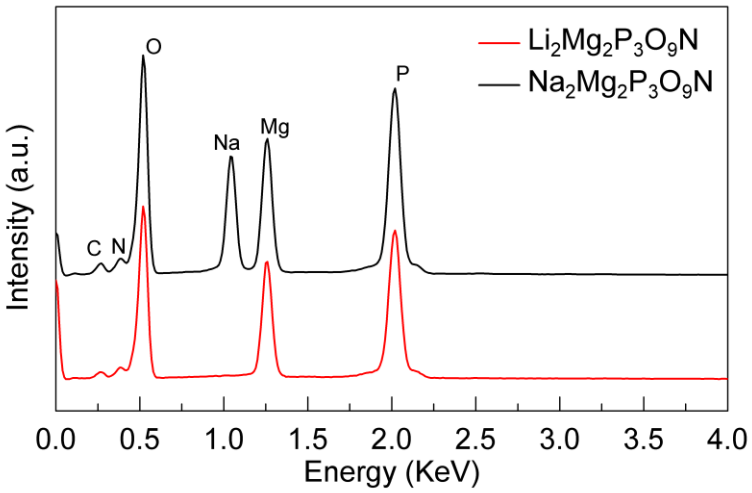

Figure 5.5 Comparison of SEM-EDS spectra of pristine $Na_2Mg_2P_3O_9N$ and ion exchanged $Li_2Mg_2P_3O_9N$.

The non-molten salt ion exchange temperature of 330 °C is well below the 552 °C melting point of LiBr, and suggests that there is extensive surface mobility of both Li^+ and Na^+ ions in both the salt and the oxynitride at these conditions. When ion exchange was attempted at similar temperatures using a low melting (~280 °C) eutectic melt of LiCl and $LiNO_3$, undesired decomposition products such as Li_3PO_4 formed during the ion exchange process. A liquid state ion exchange also proved ineffective for preparing $Li_2Mg_2P_3O_9N$, as there was no significant reaction of $Na_2Mg_2P_3O_9N$ with 1M LiBr in acetonitrile during the course of a 48 h reaction at the boiling point of acetonitrile (~82 °C). Thus the advantages of the non-molten salt ion exchange technique for producing $Li_2Mg_2P_3O_9N$ are clear.

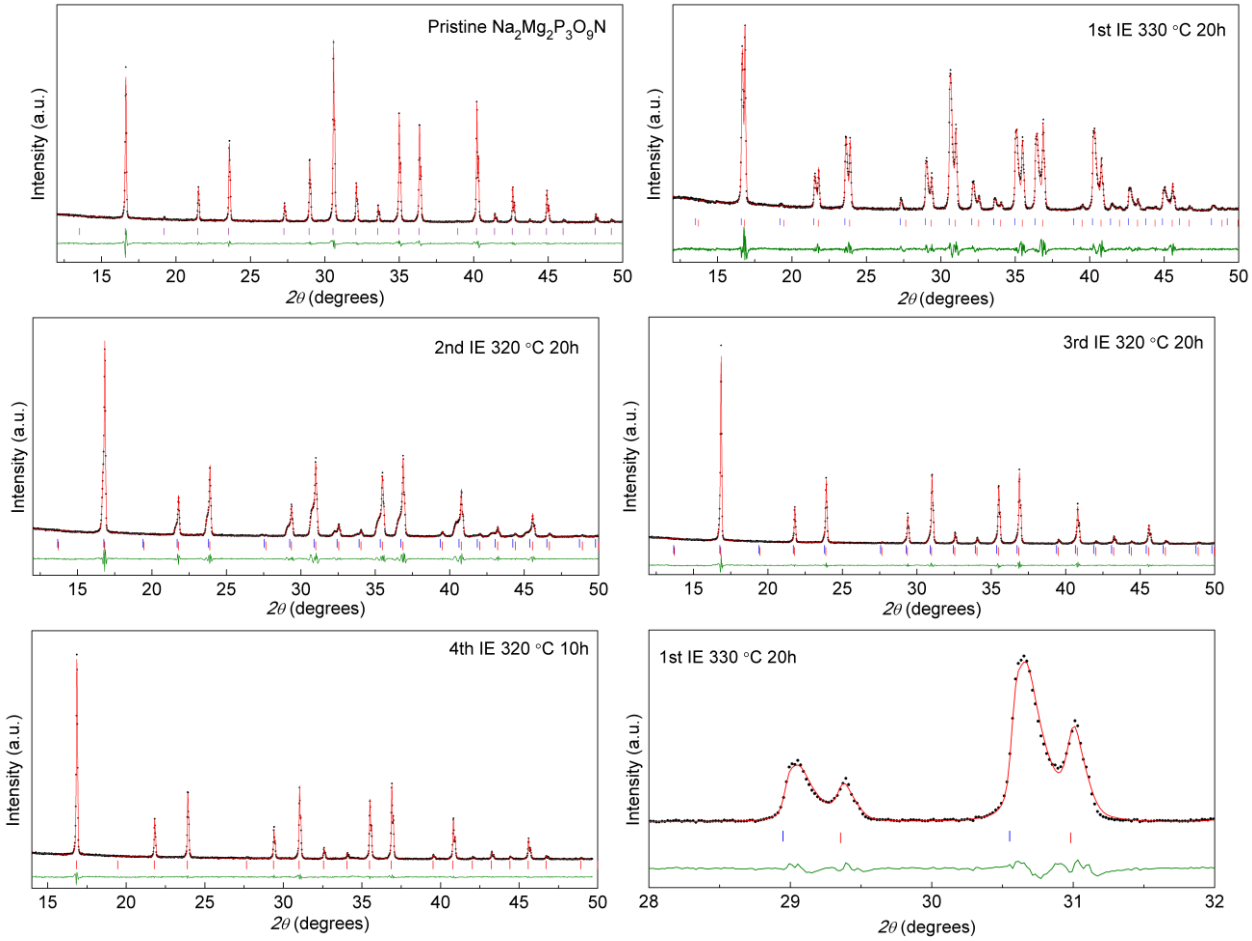

Figure 5.6 Le Bail fitting of *ex situ* laboratory XRD data (Cu K_α) for $Li_xNa_{2-x}Mg_2P_3O_9N$ collected at five different stages during the ion exchange process (pristine, and after 1 – 4 exchange reactions). The sixth pattern shows a zoom of the XRD pattern of $Li_xNa_{2-x}Mg_2P_3O_9N$ after one ion exchange reaction, allowing the asymmetry of the diffraction peaks of sodium-rich phase A to be clearly seen. Experimental data are shown in black (dots), calculated patterns in red, difference curves in green, and Bragg diffraction positions in blue (sodium-rich phase A) or red (lithium-rich phase B).

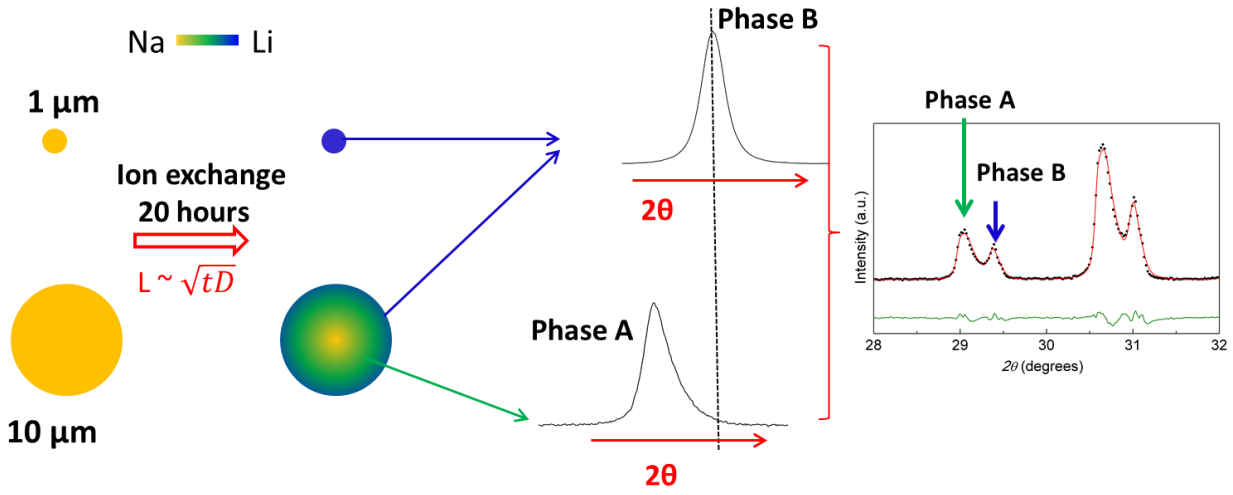

Figure 5.7 Schematic illustration of spatial distribution of phases during Li^+ exchange into host particles of $Na_2Mg_2P_3O_9N$. Within the $Na_2Mg_2P_3O_9N$ ceramic particles which are ~10 microns in size, the diffusion of ions is slow relative to the time scale of diffraction experiments, where the length (L) that ions will diffuse into a material is approximately proportional to the square root of reaction time (t) and diffusion coefficient (D). This leads to a concentration gradient in samples which are partially ion-exchanged. In the midst of the ion exchange process, the core of particles will still contain pure $Na_2Mg_2P_3O_9N$ (yellow) surrounded by a contiguous region of the $Li_xNa_{2-x}Mg_2P_3O_9N$ ($0 < x < t$) solid solution (green) with the Li content increasing at distances further from the core until the solubility limit of Li is reached ($x = t$). Outside this region, the particles consist of pure $Li_2Mg_2P_3O_9N$ (blue). Thus the $Li_2Mg_2P_3O_9N$ at the exterior of particles is responsible for the symmetric "Phase B" diffraction peaks, while interior regions are responsible for the asymmetric "Phase A" diffraction peaks. This asymmetry of the peaks is due to the composition distribution of the $Li_xNa_{2-x}Mg_2P_3O_9N$ phase, for which the Na-rich regions (*e.g.* pure $Na_2Mg_2P_3O_9N$ core) are more abundant than the Li-rich regions. To model the asymmetrical diffraction peaks of $Li_xNa_{2-x}Mg_2P_3O_9N$ (Phase A), the sample profile was convoluted with three terms in a fundamental parameters approach. These three terms included Gaussian strain broadening, Lorentzian size broadening, and a third compositional broadening term. This last term consisted of a pseudo-exponential tail for one side of the peak that represents compositional broadening (*e.g.* a tail on the low *d*-spacing side of the $Na_{1-x}Li_xCl$ solid solution resulting from the partial substitution of Li into NaCl) and which was therefore given the same 2θ-dependence as the conventional strain broadening term ($\propto \tan\theta$) . In the TOPAS software package, the functional form of the pseudo-exponential term was $f(x) = \exp[\ \ln(0.001)/x]$.

Table 5.5 Lattice parameter evolution during IE.

	Na-rich phase	*Li-rich phase*
Pristine	9.2467(1)	N/A
1st IE	9.2348(2)	9.1191 (5)
2nd IE	9.1487(9)	9.1154(2)
3rd IE	9.1425(4)	9.1156(1)
4th IE	N/A	9.1129(1)

Some initial insights into the mechanism of the ion exchange reaction which produces $Li_2Mg_2P_3O_9N$ were obtained from *ex situ* X-ray diffraction studies (Figure 5.6). It can be seen that two distinct phases are present in the intermediate stages of ion exchange, indicating that there is not a complete solid solution between $Li_2Mg_2P_3O_9N$ and $Na_2Mg_2P_3O_9N$ under these conditions. Whole-pattern Le Bail fitting (Figure 5.6) indicated that no more than two phases were present at each step, and the refined lattice parameters of these two phases are presented in Table 5.5. The phase with larger lattice parameter was assumed to be Na-rich (and the smaller phase Li-rich) based on the larger ionic radius of Na^+ relative to Li^+. The Li-rich phase is found to have essentially constant lattice parameters, while the cubic *a*-lattice parameter of the Na-rich phase decreases from its initial value of 9.25 Å (for pristine $Na_2Mg_2P_3O_9N$) to a minimum value of 9.14 Å during the ion exchange process. While the peaks for the Li-rich phase could be described in a fundamental parameters treatment using a standard symmetrical pseudo-Voigt peak shape with appropriate size and strain broadening, this was not the case for the Na-rich phase which had a more pronounced tail on the lower *d*-spacing side of the peaks (Figure 5.7). This was attributed to an asymmetrical lattice parameter distribution for the Na-rich phase that results from a compositional gradient within this phase, as can often be seen solid solution phases that are not fully equilibrated. It is therefore concluded that ion exchange begins through an initial solid solution pathway forming $Li_xNa_{2-x}Mg_2P_3O_9N$ ($0 < x < t$), beyond which there is no further Li solubility and the additional Li exchange occurs through two-phase reaction mechanism in which the two phases are $Li_tNa_{2-t}Mg_2P_3O_9N$ and $Li_2Mg_2P_3O_9N$.

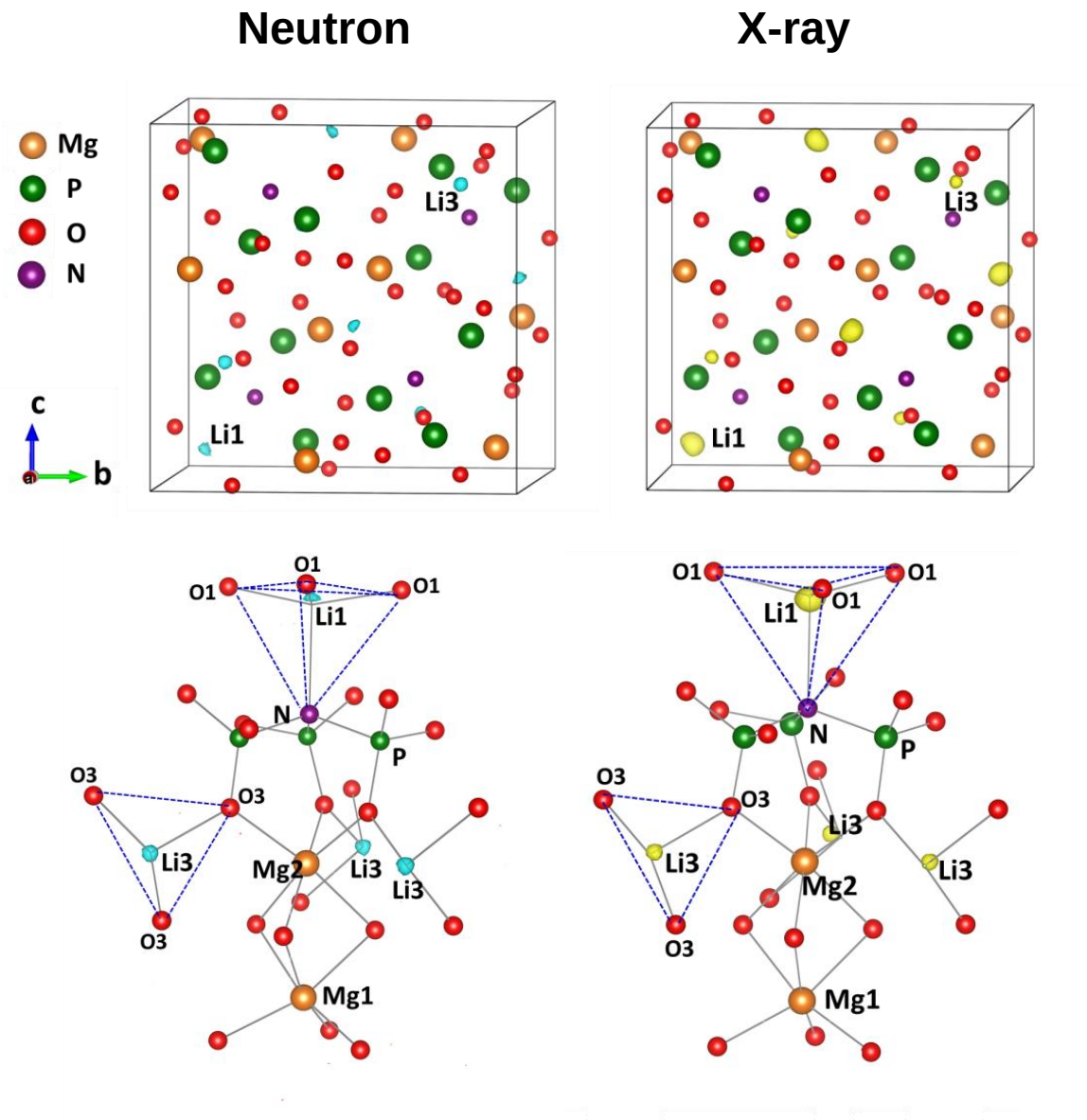

Figure 5.8 Difference Fourier maps used to identify Li sites based on neutron diffraction data (left, where blue regions indicate negative peaks associated with the Li nuclear density) or X-ray diffraction data (right, where yellow regions indicate positive difference peaks associated with the Li electron density). The peaks are shown both in the context of the full unit cell (top) and the local coordination environment of the Li1 and Li3 sites (bottom). The map thresholds are -0.70 fm/Å^3 for the neutron data and 0.95 e/Å^3 for the X-ray data.

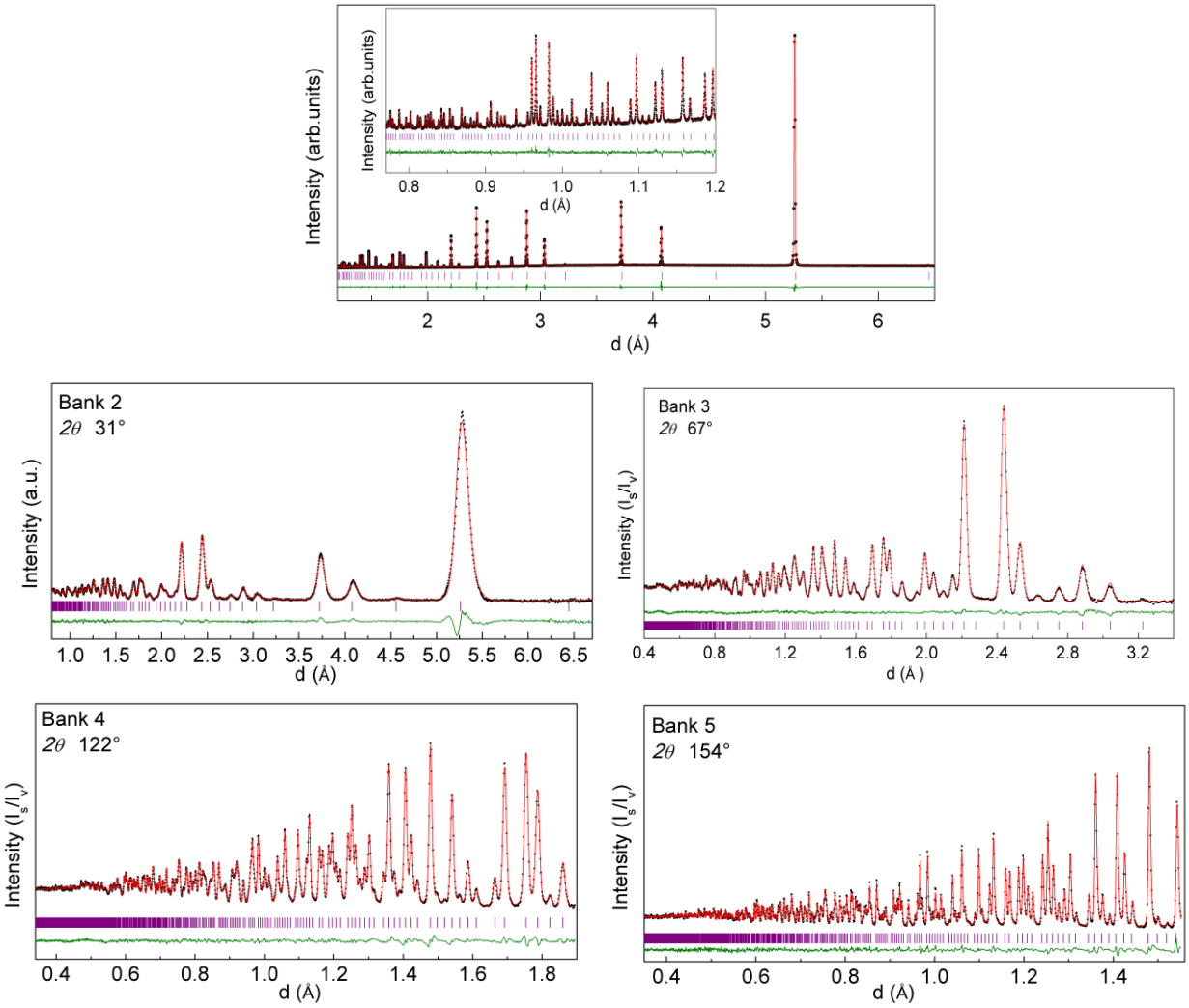

Figure 5.9 Combined Rietveld refinement of $Li_2Mg_2P_3O_9N$ prepared by non-molten salt ion exchange using synchrotron XRD data (left, λ = 0.7788 Å) and TOF neutron diffraction data (right). Experimental data are shown as black dots, the refined model as a red line, the difference curve in green, and the positions of Bragg diffraction peaks as purple tick marks.

The phase $Li_2Mg_2P_3O_9N$ has not previously been reported, and it is therefore important to solve the structure of this phase to both gain insights into the atom site positions and into the potential mobility of the Li^+ ions through an analysis of atomic displacement parameters. The Na^+ and Li^+ ions are sufficiently different in size for Li^+ ions to potentially have a different preferred coordination geometries and/or atomic sites relative those present in $Na_2Mg_2P_3O_9N$. Both synchrotron X-ray (X14A, NSLS) and time-of-flight neutron diffraction (NOMAD, SNS) data were collected for $Li_2Mg_2P_3O_9N$. The

identification of Li-ion positions could be accomplished using both biased (Rietveld refinement using atoms positions of $Na_2Mg_2P_3O_9N$) and unbiased (Fourier difference maps generated after refinement of the positions of $Mg_2P_3O_9N$ framework sites) methods for finding Li sites using either the X-ray or neutron diffraction data. The peaks in the Fourier difference maps (Figure 5.8) were clearly defined for both data sets and were more tightly localized for the neutron data (nuclear density) than for the X-ray data (electron density), as is expected. These Li1 and Li3 positions could be stably refined in subsequent Rietveld refinements of the structure of $Li_2Mg_2P_3O_9N$, resulting in excellent fits to the measured diffraction data, as can be seen in Figure 5.9.

The final structural model of $Li_2Mg_2P_3O_9N$ was obtained through the Rietveld co-refinement of X-ray and neutron diffraction data (Tables 5.6 and 5.7), weighted in approximately a 1:4 ratio so that they would contribute equally to the overall χ^2. Important bond distances and angles are provided in Table 5.8, together with a bond valence sum (BVS) analysis. The isotropic displacement parameters obtained for the non-mobile ions (Mg, P) are very similar to those previously seen for $Na_2Mg_2P_3O_9N$. However, the values for Li1 and Li3 are on average about 75% larger than those determined for Na1 and Na3, suggesting that the Li-ion mobility in $Li_2Mg_2P_3O_9N$ is very likely substantially higher than the Na-ion mobility in $Na_2Mg_2P_3O_9N$.

The Li1 and Li3 cations both remain on the 4a Wykoff sites previously identified for Na1 and Na3 (Figure 5.10), though the Li sites have much shorter bond distances which reflect the very different coordination preferences of these two ions. Na1 is closely coordinated by four anions (three O1 and one N at 2.32 and 2.60 Å, respectively), though it is also coordinated at longer distances (2.89 Å) to three O3 anions. This tetrahedral core is preserved for Li1, though it is more compact (2.16 Å Li-O and 2.29 Å Li-N bond distances) with Li at its center, and the more distant O3 anions cannot be considered to be bonded to Li1. Similarly, the Na3 site has a coordination number of CN = 9 (three short Na-O bonds of 2.40 Å and six Na-O bonds of ~3.0 Å), while the Li3 site has CN = 3 with Li-O bond distances of 1.91 Å that are much shorter (~ 0.5 Å). In contrast, the changes in average bond lengths associated with framework groups (PO_3N, MgO_6) are minor between $Na_2Mg_2P_3O_9N$ and $Li_2Mg_2P_3O_9N$. The differences between these compounds can be readily rationalized based on the different ionic radii of Na^+ and Li^+, and the bonding in $Li_2Mg_2P_3O_9N$ is seen to be normal when valences are analyzed by BVS methods (Table 5.8). This is not the case for $Li_xNa_{2-x}Mg_2P_3O_9N$ solid solutions, which will be discussed in the context of *in situ* data.

Table 5.6 Atomic sites and isotropic displacement parameters for $Li_2Mg_2P_3O_9N$ in space group $P2_13$ with a = 9.11176(8)

Atom	Wyck.	x	y	z	Occ.	B_{iso} (Å^2)
Li1	4a	0.05826(29)	0.05826(29)	0.05826(29)	1	2.93(22)
Li3	4a	0.83101(34)	0.83101(34)	0.83101(34)	1	2.73(26)
Mg1	4a	0.58095(7)	0.58095(7)	0.58095(7)	1	0.51(4)
Mg2	4a	0.40120(8)	0.40120(8)	0.40120(8)	1	0.69(4)
P	12b	0.09154(8)	0.26603(8)	0.34697(7)	1	0.58(3)
O1	12b	0.00970(8)	0.88416(8)	0.21140(9)	1	0.79(3)
O2	12b	0.00460(9)	0.13455(8)	0.39868(8)	1	0.73(3)
O3	12b	0.19862(9)	0.32375(10)	0.46095(7)	1	0.83(3)
N	4a	0.20307(6)	0.20307(6)	0.20307(6)	1	0.51 (3)

Table 5.7 Data collection / refinement parameters for combined Rietveld refinement of $Li_2Mg_2P_3O_9N$

Radiation	Synchrotron: λ = 0.7788 Å (X14A, NSLS) TOF neutron λ = 0.1 Å – 3 Å (NOMAD, SNS)
Data points	XRD 11788; PND 2999
d spacing range (Å)	XRD 0.7 Å to 6.8 Å; PND 0.32 Å to 6.7 Å
Instrument peak shape model	XRD Fundamental parameters PND Split pseudo-Voigt
Refinement software	TOPAS v4.2
Atomic parameters	27
Background function and parameters	14 for XRD; 8 for each bank of NPD
Profile parameters	10 for XRD; 12 for each bank of NPD
R_{exp}	2.33%
R_p	2.35%
R_{wp}	3.39%
χ^2	1.46

Table 5.8 Selected $Li_2Mg_2P_3O_9N$ bond distances, BVS-calculated valences, and bond angles

Bond types	Distance(Å)	Atoms	BVS	Angle types	Angle (°)
Li1-O1(×3)	2.1581(12)	Li1	+0.62	O1-Li1-O1(×3)	117.226(76)
Li1-N	2.2891(45)	Li3	+0.91	O1-Li1-N(×3)	99.69(11)
Li3-O3(×3)	1.9098(20)	Mg1	+2.24	O3-Li3-O3(×3)	100.15(15)
Mg1-O1(×3)	2.0253(9)	Mg2	+2.20	O1-Mg1-O1(×3)	101.711(44)
Mg1-O2(×3)	2.0901(11)	P	+4.82	O2-Mg1-O2(×3)	78.547(47)
Mg2-O2(×3)	2.0767(12)	O1	-1.84	O1-Mg1-O2(×3)	87.576(31)
Mg2-O3(×3)	2.0495(11)	O2	-1.95	O2-Mg2-O2(×3)	79.131(52)
P-O1	1.5146(10)	O3	-1.93	O3-Mg2-O3(×3)	91.106(51)
P-O2	1.5105(10)	N	-2.77	O2-Mg2-O3(×3)	96.996(30)
P-O3	1.5211(10)	Gii*	0.17	O1-P-O2	110.846(59)
P-N	1.7551(7)			O1-P-O3	112.587(61)
				O2-P-O3	113.488(60)
				N-P-O1	108.794(48)
				N-P-O2	106.124(53)
				N-P-O3	104.494(58)

*Gii Global Instability Index

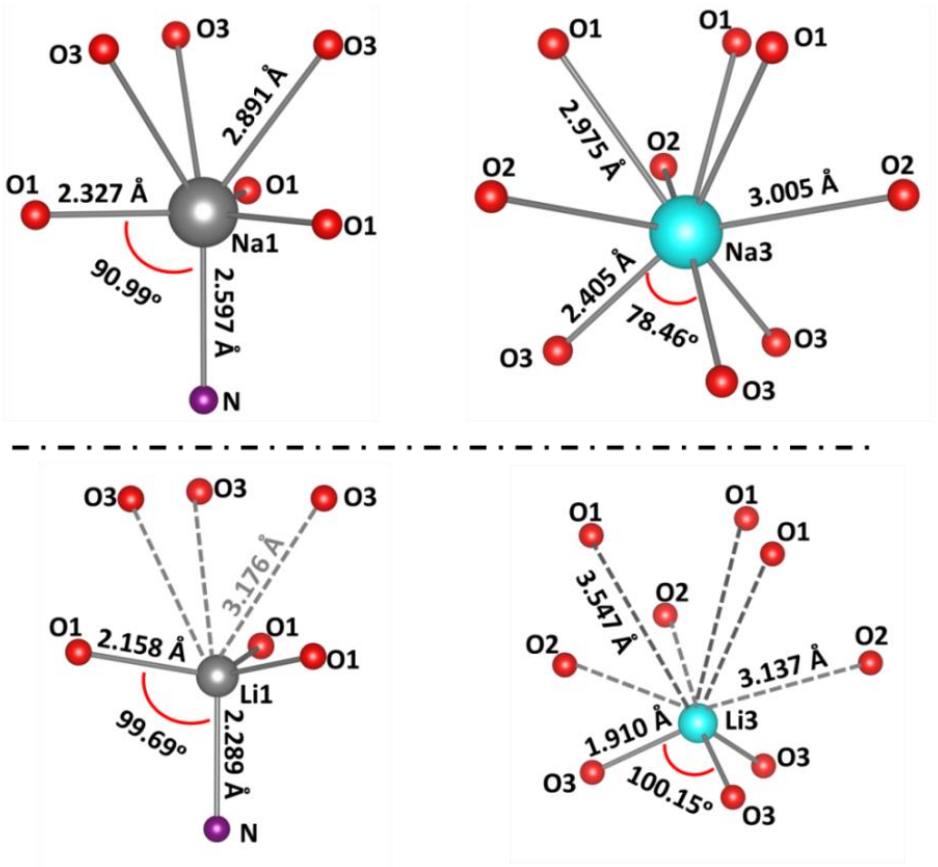

Figure 5.10 Comparison of Na1 and Na3 coordination environments in $Na_2Mg_2P_3O_9N$ (top) and Li1 and Li3 coordination environments in $Li_2Mg_2P_3O_9N$ (bottom), with three-fold symmetry axes oriented vertically. Dashed lines in the Li environments indicate long (non-bonded) Li-O distances.

The local structure of $Li_2Mg_2P_3O_9N$ was investigated by both neutron PDF and ^7Li MAS solid state NMR experiments. The PDF data for $Li_2Mg_2P_3O_9N$ could be very effectively fit (R_{wp} ~ 9%) using the average structural model from 1 – 20 Å when isotropic displacement parameters were used, as can be seen in Figure 5.10, suggesting that the local coordination environment is the same as the average coordination environment. The results of this PDF refinement are given in Table 5.9, and do not significantly differ from the Rietveld refinement results. Similarly, no evidence for split sites was seen in ^7Li MAS NMR experiments, which showed only a single peak associated with Li ions at a chemical shift of -0.8 ppm (Figure 5.12). While this could be taken as evidence for rapid site exchange between the Li1 and Li3 sites, it is also very likely that the difference in chemical shifts between the Li1 and Li3 is too small to be resolved due to the diamagnetic nature of the sample. More comprehensive

investigations will be required to determine if insights into the Li-ion mobility can be obtained from NMR experiments.

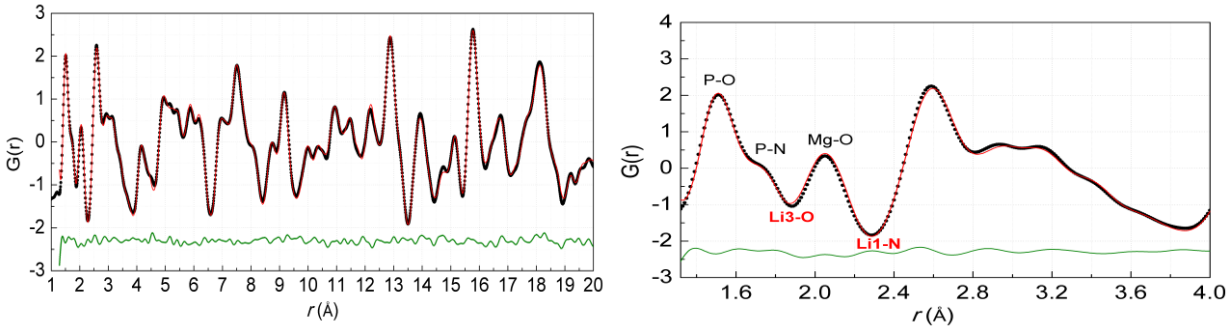

Figure 5.11 Neutron PDF data of $Li_2Mg_2P_3O_9N$ from 1 to 20 Å (left) along with a zoom from 1.4 Å and 4 Å showing peaks associated with chemical bonds (right), with experimental data in black, calculated pattern in red, and the difference curve in green.

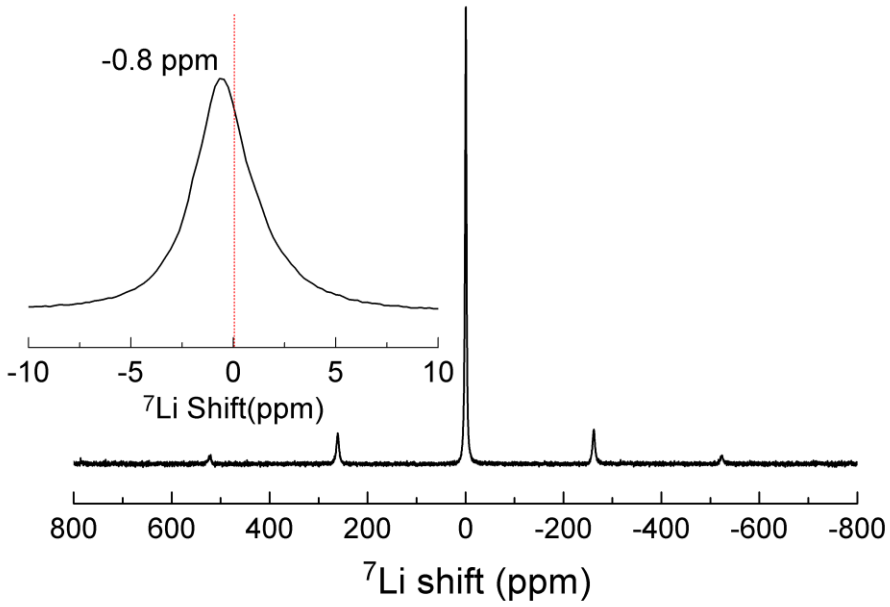

Figure 5.12 ^{7}Li solid state NMR signal from $Li_2Mg_2P_3O_9N$ collected at a spinning speed of 36 K Hz.

Table 5.9 Atomic parameters of $Li_2Mg_2P_3O_9N$ obtained from fitting neutron PDF data

Atom	Wyck.	*x*	*y*	*z*	Occ.	B_{eq} (Å^2)
Li1	4a	0.05719	0.05719	0.05719	1	1.54
Li3	4a	0.82678	0.82678	0.82678	1	2.09
Mg1	4a	0.58333	0.58333	0.58333	1	0.68
Mg2	4a	0.40054	0.40054	0.40054	1	0.48
P1	12b	0.09127	0.26436	0.34513	1	0.62
O1	12b	0.00813	0.88479	0.21108	1	0.96
O2	12b	0.00466	0.13540	0.39990	1	0.73
O3	12b	0.19795	0.32441	0.46226	1	0.85
N1	4a	0.20276	0.20276	0.20276	1	0.66

5.3.1.3 *In situ* neutron diffraction study of Li^+/Na^+ ion exchange of $Na_2Mg_2P_3O_9N$

Although *in situ* neutron diffraction studies of Li^+/Na^+ ion exchange have not previously been pursued due to the challenging nature of such experiments, our development of non-molten salt exchange methods and the construction of time-of-flight neutron diffraction beamlines with good counting statistics offer the opportunity to follow the structural changes that occur during the transformation of sodium phase to lithium phase with good sensitivity to the changes in site occupancies and bond distances that occur during this transformation. Both ^{7}LiBr and ^{7}LiCl have sufficiently low absorption cross-sections to be compatible with these experiments. However, LiCl was chosen so that comparisons with *in situ* X-ray diffraction data could more easily be made if needed, since Br is a relatively strong absorber of X-rays. Although the Na: Li molar ratio was reduced to 1:4 from the 1:10 in the *ex situ* experiments in order to increase the relative scattering from the nitridophosphate phase, this lower salt concentration does not lead to an obvious reduction in the degree of ion exchange during the experiments. The experimental configuration for the *in situ* studies is schematically illustrated in Figure 5.13. The sample resided in a 6 mm diameter V can loaded into a JANIS cryofurnace capable of controlling temperature over the modest range of temperatures required to drive the ion exchange process. Scans were collected every 0.5 h during an extended hold at 332 °C (605 K) of about 13 h, with somewhat longer collections during heating and cooling.

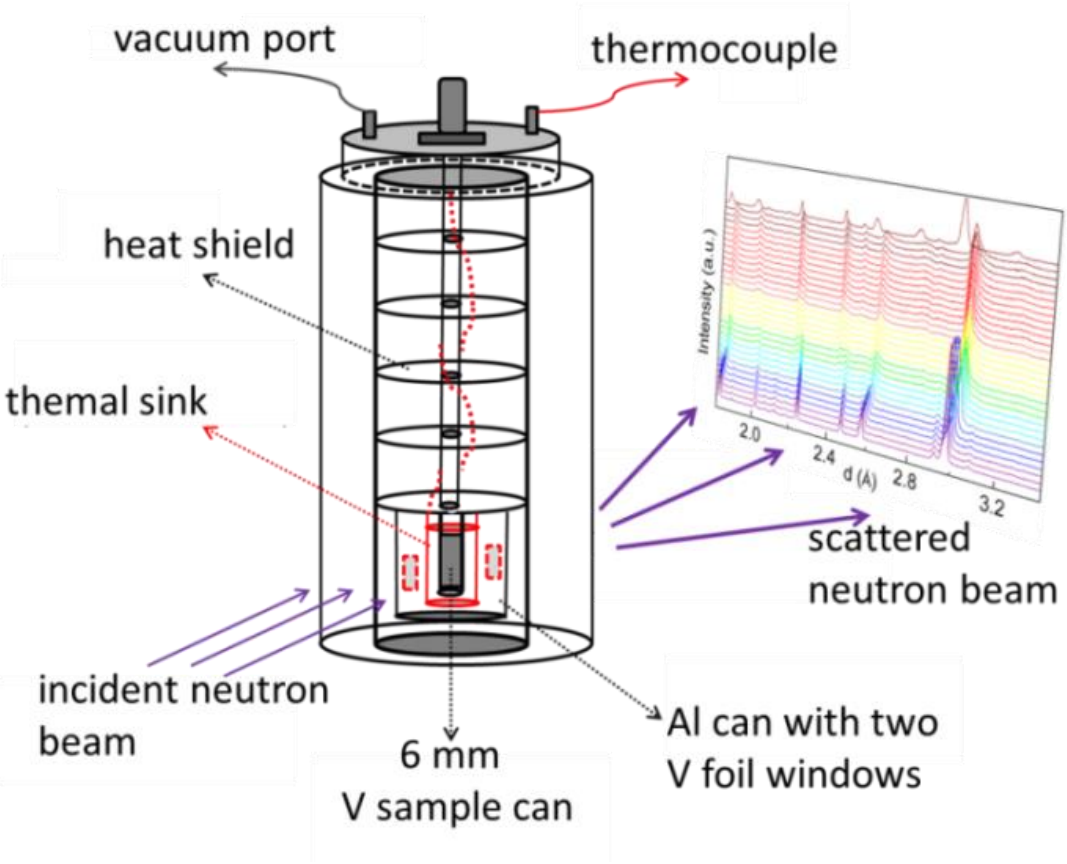

Figure 5.13 Schematic illustration of *in situ* neutron diffraction experiment.

The good quality of the *in situ* neutron diffraction patterns can be seen in Figures 5.14 and 5.15. Both sample peaks (labelled in black) and salt peaks (labelled in green for NaCl and purple for LiCl) are sharp with a sufficiently good signal/noise ratio to enable structural information to be determined through Rietveld refinement. On heating, the original $Na_2Mg_2P_3O_9N$ diffraction peaks shift to higher *d* spacing as a consequence of thermal expansion. The peaks associated with $Li_2Mg_2P_3O_9N$ are first seen at temperatures above 250 °C (524 K), indicating that the ion exchange process is quite rapid, especially since the $Li_xNa_{2-x}Mg_2P_3O_9N$ solid solution must form prior to the appearance of $Li_2Mg_2P_3O_9N$.

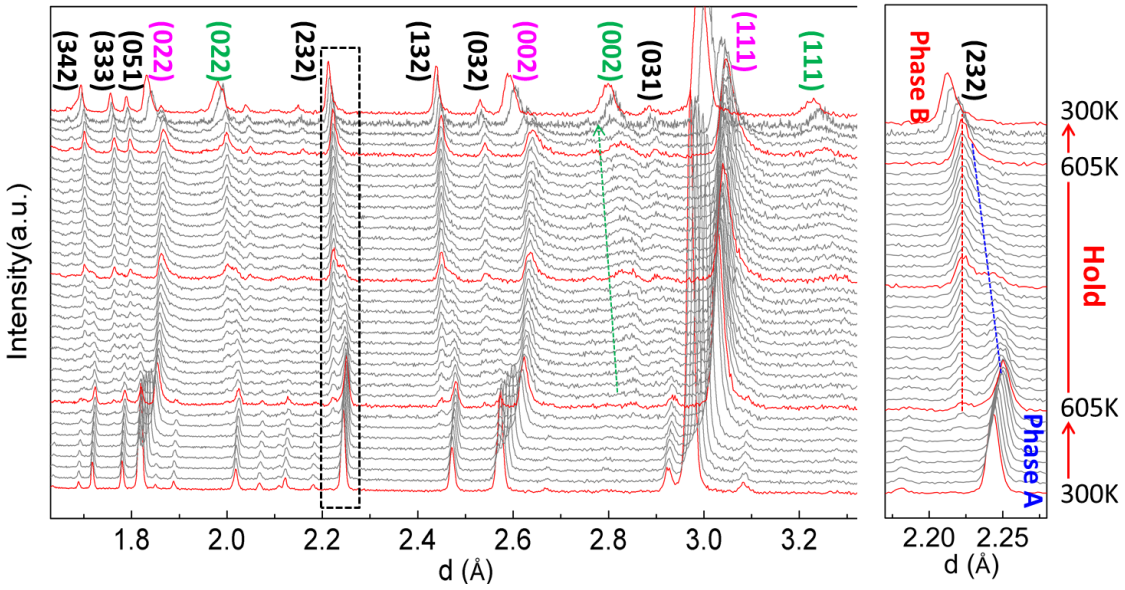

Figure 5.14 *In situ* neutron diffraction patterns collected during Li/Na ion exchange of $Na_2Mg_2P_3O_9N$ with the Miller indices of the Bragg diffraction peaks associated with CUBICON $Li_xNa_{2-x}Mg_2P_3O_9N$ ($0 < x < 2$) labeled in black, LiCl ($Li_{1-y}Na_yCl$) in pink, and NaCl ($Na_{1-z}Li_zCl$) in green. Right panel shows a zoom of the (232) diffraction peak for $Li_xNa_{2-x}Mg_2P_3O_9N$. The temperature program is labelled on the right, with diffraction patterns at the beginning/end of ramps and at the middle of the hold highlighted in red.

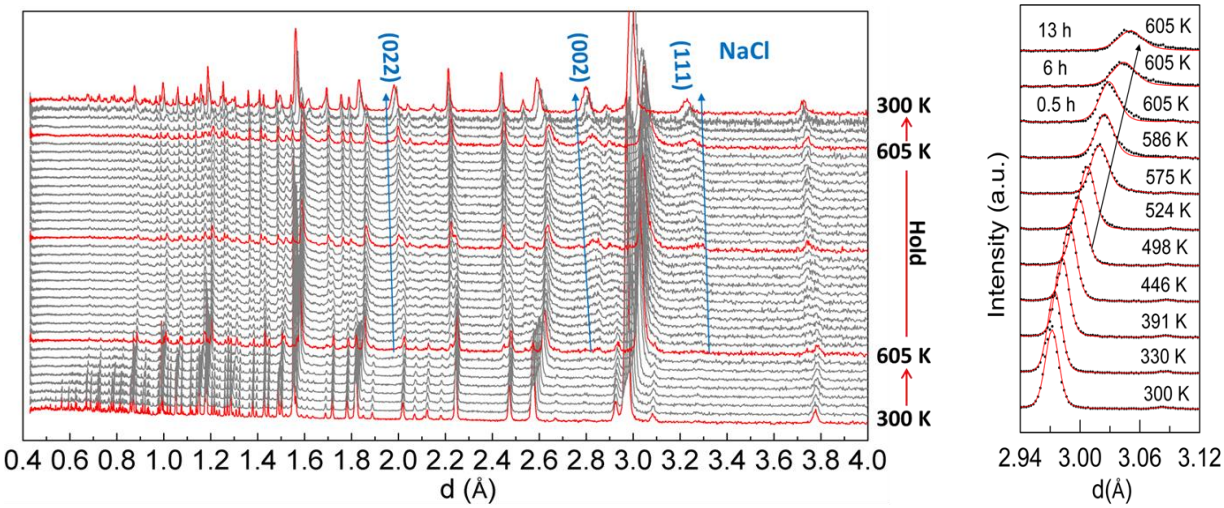

Figure 5.15 Full range of *in situ* neutron diffraction patterns collected during Li/Na ion exchange of $Na_2Mg_2P_3O_9N$. Three peaks associated with the formation of NaCl (or a slightly substituted $Na_{1-z}Li_zCl$ solid solution) are indicated with blue arrows. Right: Zoom of the 111 LiCl peak modeled by assuming a single phase with fixed instrumental broadening. Clear asymmetry can be seen at temperatures higher than 498 K, indicating the formation of a partial $Li_{1-y}Na_yCl$ solid solution.

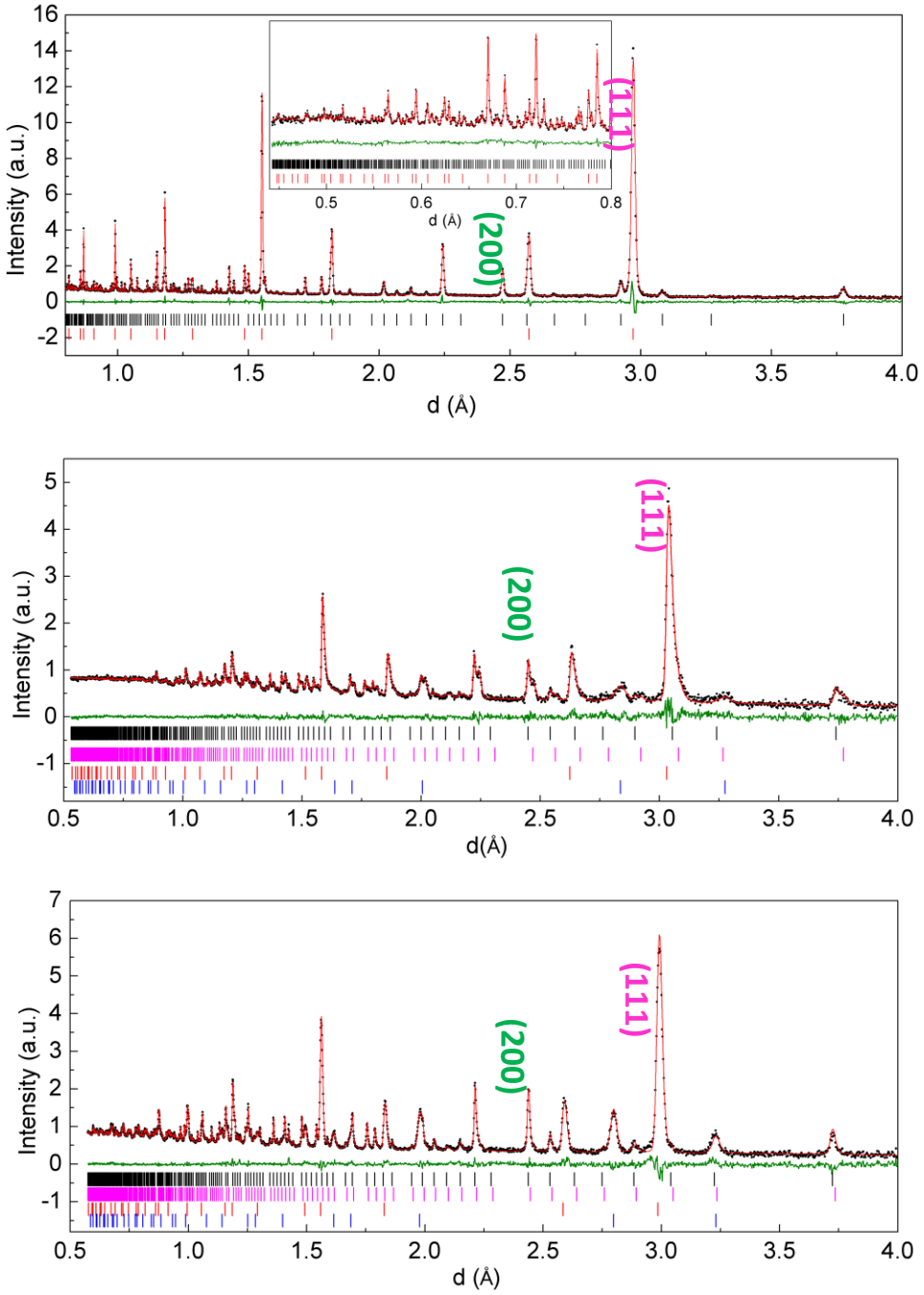

Figure 5.16 Top: Rietveld refinement of $Na_2Mg_2P_3O_9N$ and ^7LiCl collected at 300 K before heating using *in situ* neutron diffraction data for the mixture. Middle: Rietveld refinement using 605 K data (scan 18, ~ 13 h). Bottom: Rietveld refinement using 300 K data (scan 36, ~24h) after cooling back to room temperature after the 605 K hold. Experimental data are shown as black dots, the refined model as a red line, and the difference curve in green. Bragg peak positions of $Na_{2-x}Li_xMg_2P_3O_9N$ (black),

$Li_2Mg_2P_3O_9N$ (magenta), $Li_{1-y}Na_yCl$ (red), and $Na_{1-z}Li_zCl$ (blue) are indicated. Clearly asymmetrical LiCl diffraction peaks (for example, the pink labelled 111 peak of LiCl) were observed during ion exchange at 605 K, indicating the formation of a $Li_{1-y}Na_yCl$ solid solution. The $Li_{1-y}Na_yCl$ diffraction peaks became much more symmetrical when the sample was cooled down to 300 K after ion-exchange while the NaCl peak intensities (*e.g.*, green 200 peak) increased strongly, reflecting the reduced solubility limit of Li in the $Li_{1-y}Na_yCl$ solid solution at lower *T*.

Another signature of the onset of ion exchange is the asymmetry that appears in the LiCl peaks around 225 °C (498 K), indicating the formation of a partial $Li_{1-y}Na_yCl$ solid solution due to the uptake of Na originally present in $Na_2Mg_2P_3O_9N$, as can be seen in Figures 5.15 and 5.16. The formation of peaks associated with NaCl (or a slight $Na_{1-z}Li_zCl$ solid solution) is delayed until the temperature reaches 605 K relative to the observation of Na-substituted LiCl, as NaCl is not expected to form until sufficiently Na ions are exchanged out to exceed solubility limit of Na^+ in LiCl. At the end of the *in situ* ion-exchange experiment, neutron diffraction data indicate the presences of four different coexisting phases in the reaction product: $Li_{1-y}Na_yCl$, $Na_{1-z}Li_zCl$, $Li_2Mg_2P_3O_9N$ and $Li_tNa_{2-t}Mg_2P_3O_9N$, where *t* is near the solubility limit of Li^+ in this solid solution.

It is not surprising that the ion exchange reaction did not run to completion since only a limited molar excess of Li was used (4:1). The lattice parameters of the two CUBICON phases can be tracked throughout the ion exchange process. As shown in Figure 5.17a, the *a* lattice parameter of the sodium rich phase $Li_xNa_{2-x}Mg_2P_3O_9N$ ($0 < x < t$) decreases monotonically as the reaction is held at constant temperature (605 K), though the rate of change slows by scan 30 (~18 h) and it appears that equilibrium is nearly achieved at the end of the isothermal hold (scan 35, ~21 h). In contrast, the lattice parameters of $Li_2Mg_2P_3O_9N$ do not significantly vary at fixed temperature, supporting the assignment of this phase as a line compound. The relative fractions of these two phases were also followed through Rietveld refinement (Figure 5.17b), made possible by the high quality diffraction data. It can be seen that about 20% (wt%) of $Li_2Mg_2P_3O_9N$ has already formed by the time the isothermal reaction temperature of 605 K is reached. The amount of $Li_2Mg_2P_3O_9N$ continues to increase (at the expense of the decrease of $Li_xNa_{2-x}Mg_2P_3O_9N$ solid solution) until scan 20 (~14 h), after which the phase fraction remains essentially constant during the isothermal hold. Surprisingly, this equilibration in phase fraction (*i.e.*, composition) occurs well before the lattice parameters are equilibrated indicating that the reaction mechanism is more complex than apparent from the plots of phase fraction which evolve monotonically.

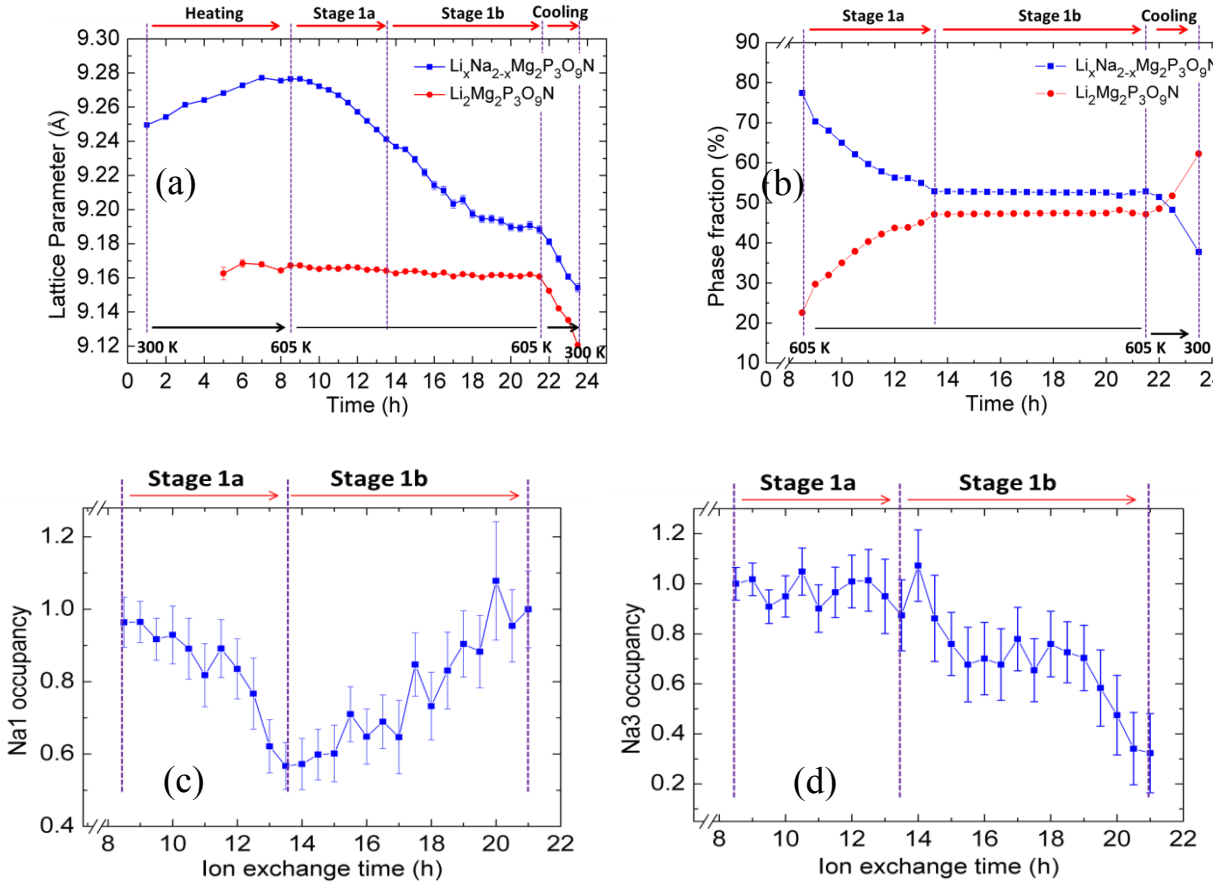

Figure 5.17 Evolution of lattice parameter (a) and phase fractions (b) for $Na_{2-x}Li_xMg_2P_3O_9N$ with $0 < x < t$ (sodium-rich phase A, blue) and $Li_2Mg_2P_3O_9N$ (phase B, red) during ion-exchange. Changes in Na-occupancy on the Na1 (c) and Na3 (d) site occupancy during the isothermal hold at 605 K. All results were obtained from Rietveld refinement of the *in situ* neutron diffraction data, with experiment time as the horizontal axis.

The refined site occupancies of the Na1 and Na3 site are shown in Figure 5.17c and 5.17d, and their behavior of these sites allows the origin of the complex reaction pathway to be understood. During the reaction, the occupancy of the Na1 site is seen to decrease from fully occupied (1.0) to about 0.6 by scan 20 (~14 h), but to then increase thereafter to a final occupancy which is essentially again fully occupied (1.0). In contrast, the Na3 site appears to remains fully occupied until scan 20 (~14 h), after which its occupancy decreases to about 0.3. While each individual data point has relatively large error bars (~0.1), the overall trend is obvious and indicates that substitution of Li for Na is initially most favorable near the Na1 site, but that as the cubic *a* lattice parameter shrinks with increasing substitution, there is a

thermodynamic crossover and it becomes more favorable for Li to substitute near the Na3 site. The refined occupancies indicate that a higher degree of Li substitution can be tolerated at the Na3 site than on the Na1 site. It therefore appears that the range of $Li_xNa_{2-x}Mg_2P_3O_9N$ compositions (Stage 1 of the phase transformation) should not be described as a single solid solution, but instead represents two thermodynamically distinct solid solutions (Stage 1a and 1b). This is further supported by the observation of very different rates of change for many individual bond lengths between Stage 1a and Stage 1b, as can be seen in Figure 5.18.

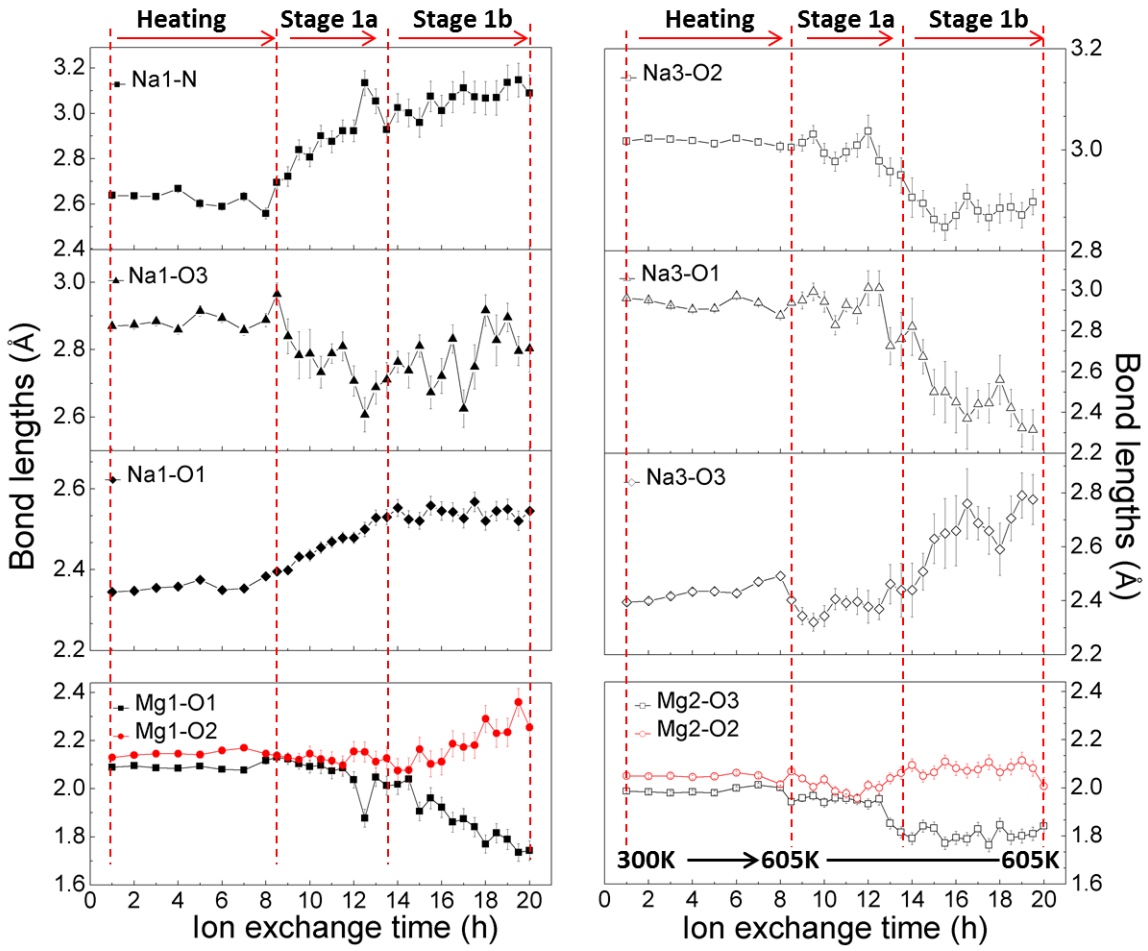

Figure 5.18 Evolution of Na-O and Mg-O bond distances within $Na_{2-x}Li_xMg_2P_3O_9N$ (sodium-rich phase A) during ion exchange.

The driving force for this complex behavior can be revealed by studying changes in the volumes of the cation coordination polyhedra during the Li-exchange process as can be seen in Figure 5.19 and

Table 5.10. Even though the overall unit cell volume shrinks during the exchange of Li^+ for Na^+, the volume of the local coordination polyhedron around Na1 increases when Li is partially substituted onto the Li1 site. In contrast, the volume of the Na3 coordination polyhedron always shrinks with Li substitution. As such, it is not surprising that it becomes more energetically favorable for Li^+ to occupy the Li3 site than the Li1 site at higher degrees of Li^+ substitution in which the cell volume is more significantly reduced from its original value due to the increasing strain associated with the volume expansion of the mixed Li1/Na1 site, thus driving the non-monotonic behavior of the Na1 site occupancy evolution. Intriguingly, this behavior of the Na1 site (increase in volume despite Na removal) is a likely reason for the extremely small volume changes (~0.5%) previously observed during the Na^+ removal at Na1 site of $Na_3TiP_3O_9N$ to form oxidized $Na_2TiP_3O_9N$[27], as the Na removal during this process was shown through both experiment and theory to occur at the Na1 (and not the Na3) site. This detailed microscopic understanding of the local forces driving the two-part phase transition would not be possible without the high quality structural data on the intermediate phases that the *in situ* neutron diffraction experiments provide.

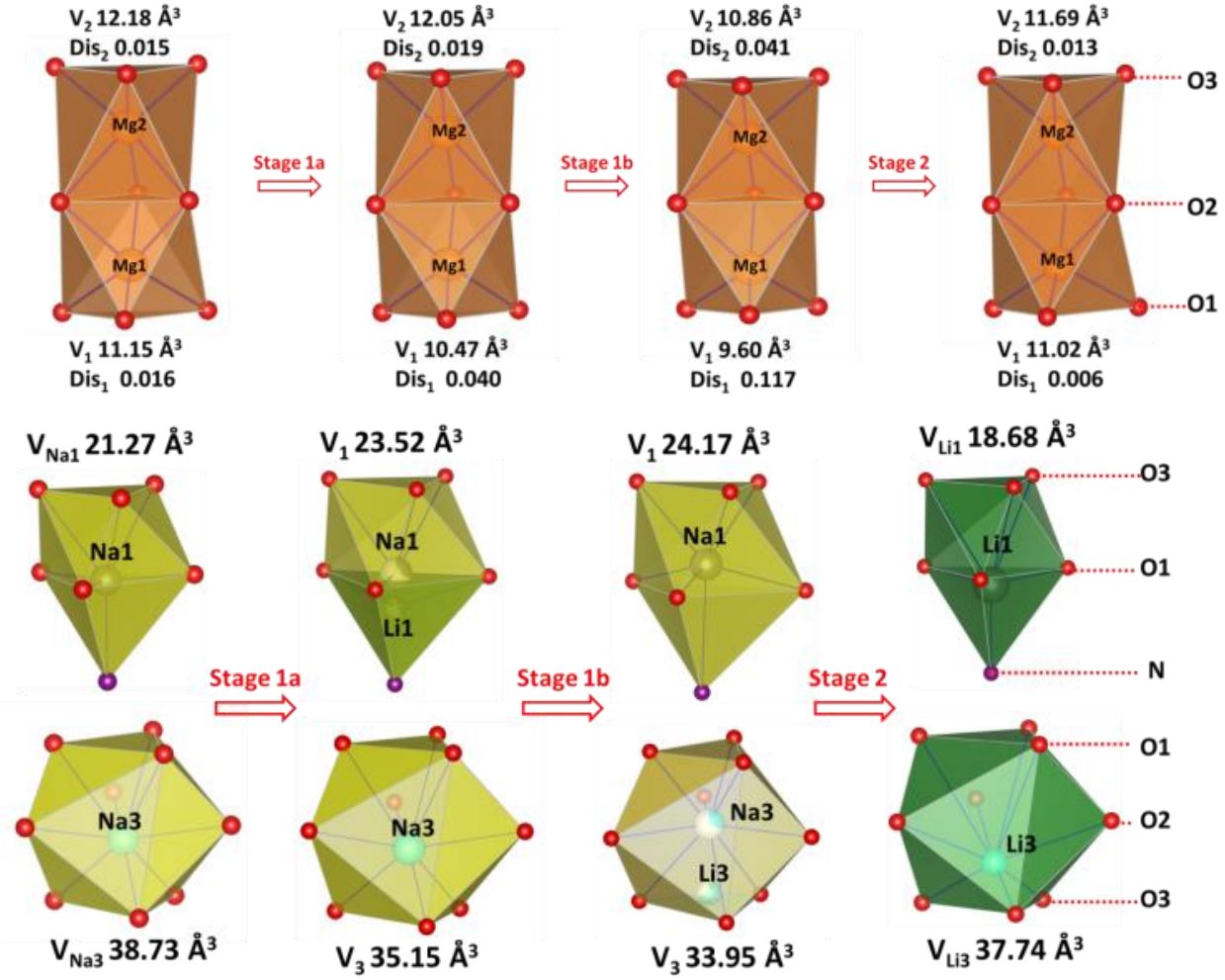

Figure 5.19 Representation (to scale) of the evolution of cation coordination polyhedral volume that occurs during ion exchange, based on the structures obtained through *in situ* neutron diffraction measurements for the initial phase ($Na_2Mg_2P_3O_9N$) and the phases at the end of Stage 1a ($Li_{0.4}Na_{1.6}Mg_2P_3O_9N$), Stage 1b ($Li_{0.7}Na_{1.3}Mg_2P_3O_9N$), and Stage 2 ($Li_2Mg_2P_3O_9N$). Polyhedral volumes ($Å^3$) are indicated, as are the distortion index of the MgO_6 octahedra. Additional comparative data are provided in Table 5.10.

Table 5.10 Volume changes for local polyhedra and over all unit cell.

	Initial state 586 K	End of stage 1a 605 K	End of stage 1 b 605 K	End of stage 2 605 K
V[$Mg1O_6$]/$Å^3$	11.15	10.47	9.6	11.02
V[$Mg2O_6$]/$Å^3$	12.18	12.05	10.86	11.69
V[$Na1O_6N$]/ $Å^3$	21.27	23.52	24.17	18.68
V[$Na3O_9$]/ $Å^3$	38.73	35.15	33.95	37.74
V[poly]/ $Å^3$	83.33	81.19	78.58	79.13
4×V[poly]/ $Å^3$	333.32	324.76	314.32	316.52
V[unit cell] / $Å^3$	797.30	788.09	776.33	768.82
4×ΔV[poly]/ $Å^3$		-8.56	-10.44	+2.2
Δ V[unit cell] / $Å^3$		-9.21	-11.76	-7.51

The limited stability range ($0 < x < 0.7$) of the $Li_xNa_{2-x}Mg_2P_3O_9N$ solid solution observed during the *in situ* ion exchange experiments suggests that it is difficult for the CUBICON framework to simultaneously satisfy the bonding preferences of Li^+ and Na^+ in the mixed sites, leading to substantial internal strains within the solid solution phases. A comparison of the local polyhedral volume changes with the volume change of the overall unit cell (Table 5.10) shows that more than 90% of the unit cell volume reduction is accounted for by the changes in the cation polyhedra for the solid solution phases, while only 60% of the volume reduction in the line compound $Li_2Mg_2P_3O_9N$ occurs in the local polyhedra. This is reflected for example in the strongly distorted MgO_6 octahedra present at the end of Stage 1a (distortion indices of 0.117/0.041; Mg-O bond lengths which differ by up to 0.60 Å) relative to the very regular MgO_6 octahedra present in both the pristine (bond length spread of 0.13 Å, distortion indices of 0.016/0.015) and fully lithiated end members (bond length spread of 0.07 Å, distortion index of 0.006/0.013). Similarly, the mixed Na1/Li1 polyhedron is larger than the Na1 polyhedron in the pristine material, while the pure Li1 polyhedron after ion exchange is smaller than the Na1 polyhedron in the pristine material. These strong local distortions highlight the energetic penalties for accommodating mixtures of Na and Li within the CUBICON framework, and it is therefore not surprising that a full solid solution does not form between the end members of $Na_2Mg_2P_3O_9N$ and $Li_2Mg_2P_3O_9N$.

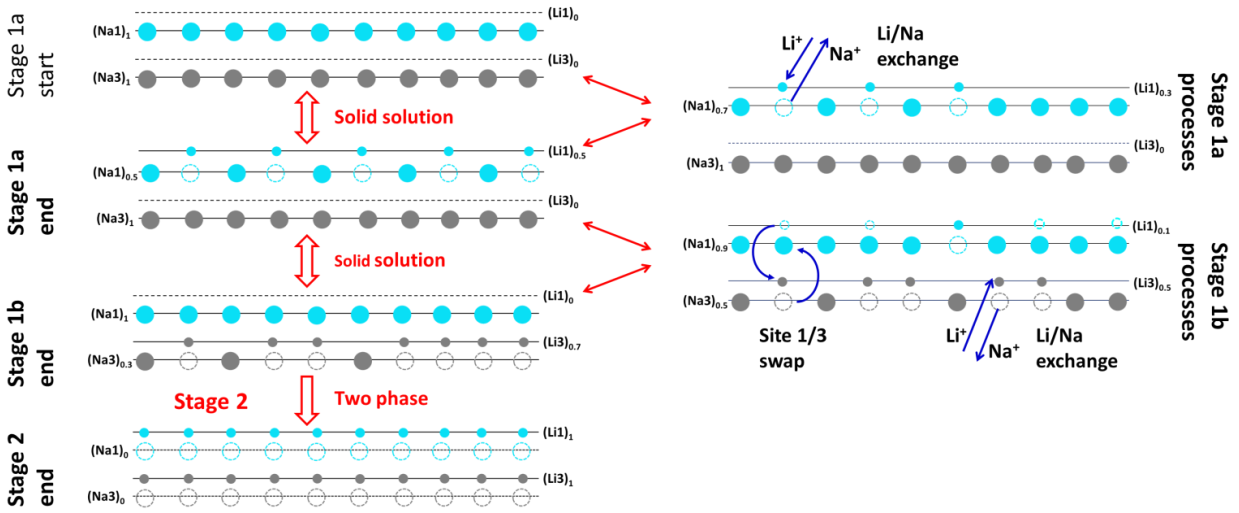

Figure 5.20 Left: Pattern of occupied sites (solid circles) during at key stages of the $Na_2Mg_2P_3O_9N$–$Li_2Mg_2P_3O_9N$ ion exchange process. The four mobile cation sites (Li1, Na1, Li3, Na3) are show in relationship to their positions within the CUBICON structure along the (111) direction. Open circles indicate the atomic sites that are depopulated to reach the endpoint of each stage (Stage 1a, Stage 1b, and Stage 2). Right: illustration of the processes that occur during the Stage 1a and Stage 1b solid solutions. During Stage 1a, Li-ion exchange results in Na1 sites being depopulated while the neighboring Li1 sites are filled. During Stage 1b, two processes are occurring during Li-ion exchange: the analogous ion exchange at the Li3/Na3 sites, and the swapping of the mobile ion site positions (Li1 → Li3, Na3 → Na1).

The reason why the variable composition $Li_xNa_{2-x}Mg_2P_3O_9N$ phases represent two thermodynamically distinct solid solutions rather than a single solid solution is schematically illustrated in Figure 5.20. The first solid solution which is accessed during Stage 1a spans structures in which the Na1 (variable), Li1 (variable), and Na3 (constant) sites are utilized. The second solid solution, accessed during Stage 1b, spans structures in which all four mobile cation sites (Na1, Li1, Na3, Li3) are utilized and have variable occupancies. Since these two solid solutions access different sets of atomic sites, they must belong to distinct thermodynamic phases. For comparison, the final reaction by which $Li_2Mg_2P_3O_9N$ is formed, Stage 2, involves a discontinuous two-phase reaction between the terminal solid solution composition of $Li_tNa_{2-t}Mg_2P_3O_9N$ (four mobile cation sites) and the simpler $Li_2Mg_2P_3O_9N$ end member, which only has two occupied mobile sites (Li1 and Li3). The $Li_xNa_{2-x}Mg_2P_3O_9N$ solid solution is different from most other solid solution in that the variable content

ions (Li and Na cations) do not occupy the same site, but instead occupy nearby sites which are clearly distinct as reflected in their different coordination numbers and very different bond lengths to the coordinating anions.

The thermodynamic (and not kinetic) origin of the Stage 1a/1b crossover is supported by prior investigations into the diffusion pathways in the CUBICON framework, which indicate that both Na1 and Na3 sites must be traversed when Na ions move along the lowest energy diffusion pathway for this system[27]. Further evidence for the thermodynamic nature of this transition is seen in behavior of the refined phase fractions. While the $Li_2Mg_2P_3O_9N$ and $Li_xNa_{2-x}Mg_2P_3O_9N$ phase fractions are constant during the last 8 h of the extended hold at 605 K, the fraction of the $Li_xNa_{2-x}Mg_2P_3O_9N$ solid solution phase decreases on cooling at the end of the hold suggesting that a different equilibrium is preferred at lower temperatures and that the time scale of equilibration is relatively fast. It is generally expected that the compositional width of solid solutions will decrease as temperature is lowered since the entropic stabilization of the mixed phase relative to its ordered alternatives will be lessened, and the present *in situ* neutron diffraction data analysis do indeed show this expected behavior. In fact, the equilibrium constants for this system could easily be studied by collecting additional *in situ* diffraction data with a different temperature program featuring holds to equilibrate the system at multiple temperatures.

The success of the Li^+/Na^+ ion exchange process indicates that both Li^+ and Na^+ ions can be mobile within this framework, though the timescale of this process is limited by the ion with the lower mobility. Rough estimates of their relative mobility can be obtained through the determination of the percolation threshold in bond valence sum difference map calculations, with the structures obtained from the present neutron diffraction investigations used as input. The 0.03 valence unit percolation threshold of Li^+ in $Li_2Mg_2P_3O_9N$ is substantially lower than the 0.20 v.u. threshold of Na^+ in $Na_2Mg_2P_3O_9N$, suggesting that the Mg CUBICON framework will have a higher Li^+ than Na^+ mobility, and that the Li ionic conductivity has a good chance of being high on an absolute scale.

5.3.1.4 Li ionic conductivity of $Li_2Mg_2P_3O_9N$

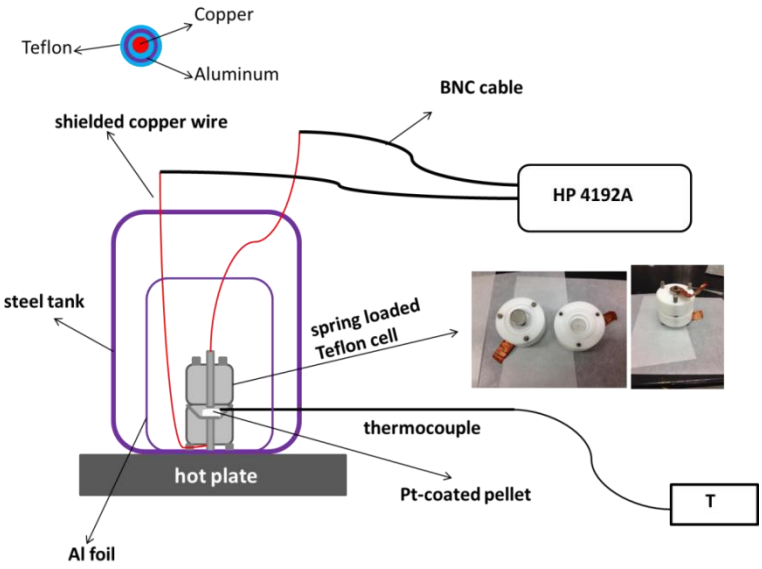

Figure 5.21 Schematic illustration of configuration utilized for room temperature electrochemical impedance spectroscopy (EIS) measurements of pellets within a fully shielded environment.

Room temperature electrochemical impedance spectroscopy data were therefore collected on dense (~92%) pellets of $Li_2Mg_2P_3O_9N$ using a custom-built measurement cell (Figure 5.21), and the data are shown in the form of a Nyquist plot in Figure 5.22. The EIS data were fit using an equivalent circuit consisting of two series elements of resistors paired with constant phase elements to model the bulk (R_b) and grain boundary (R_{gb}) resistances, with an additional constant phase element to describe the Warburg-like ionic conduction processes at low frequencies, as shown in the Figure 5.22 inset. Previous studies of CUBICON phases with redox-active transition metals (Fe, Ti)[15,27] have found the electronic conductivity to be much lower (~2 orders of magnitude) than the ionic conductivity, and the ionic conductivity is expected to be even more dominant when the octahedral cation is Mg^{2+} presumably due to the larger band gap of this compound. The electronic contributions to the measured conductivity were therefore neglected, and a room temperature bulk ionic conductivity of 9×10^{-7} S/cm was inferred from R_b, a value which was comparable to the grain boundary contributions of 4×10^{-7} S/cm. The Li^+ ionic conductivity of $Li_2Mg_2P_3O_9N$ is greatly improved relative to that of Na^+ ionic conductivity of $Na_2Mg_2P_3O_9N$ which was reported to be 8×10^{-6} S/cm at 440 ℃[16]. Additional EIS data for $Li_2Mg_2P_3O_9N$ were collected on a pellet for which moisture was more rigorously excluded, and

comparable results were obtained (Figure 5.23). Temperature dependent conductivity studies are current undergoing and will be presented elsewhere.

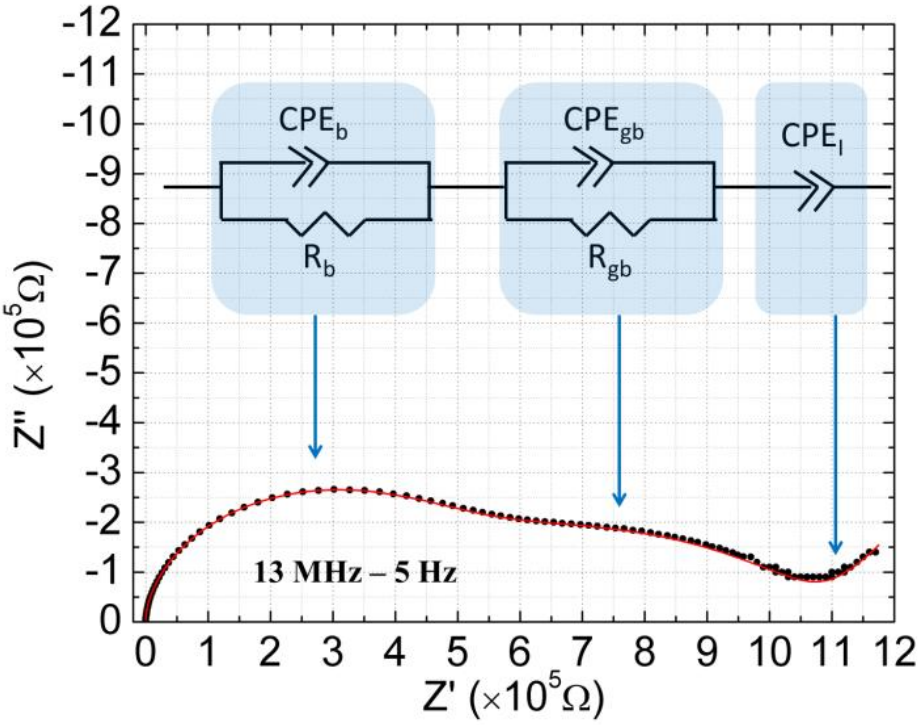

Figure 5.22 EIS data for $Li_2Mg_2P_3O_9N$ collected at 22 ℃ with frequency range of 5 Hz to 13 MHz. Since features assigned to the bulk (b) and grain boundary (gb) contribution are well-resolved in the spectrum, an equivalent circuit was used in which their resistances (R_b and R_{gb}) were separately paired with constant phase elements (CPE_b and CPE_{gb}), while a third constant phase element (CPE_I) reflects the Warburg-like ionic conductivity of Li ions being perturbed due electrolyte-electrode interface.

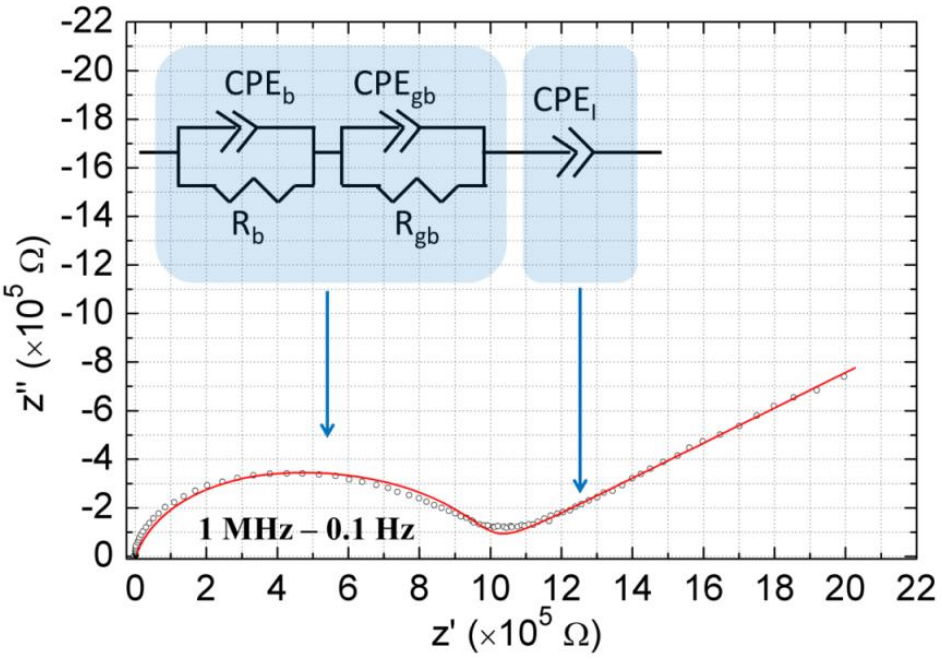

Figure 5.23 Moisture-excluded $Li_2Mg_2P_3O_9N$ ac impedance data for collected on a BIOLOGIC VMP3 instrument with 100 mV peak-to-peak polarization voltage at 24 ℃.

The room temperature Li-ion conductivity of $Li_2Mg_2P_3O_9N$ indicates promise with regard to applications as a solid state electrolyte. The measured room temperature ionic conductivity (9×10^{-7} S/cm) is presently about three orders of magnitude lower than the best room temperature solid state Li-ion conductors discovered thus far[28-31], but is comparable to the pre-optimization values of many of these known excellent Li-ion conductors. It is expected that the Li-ion conductivity of $Li_2Mg_2P_3O_9N$ can be substantially improved beyond the performance achieved in the present work by carrying out chemical substitutions that introduce persistent vacancies at the Li-ion sites, or which perturb the structural framework to make the motion of Li ions more facile. As such, this structural framework is shown to be an excellent starting point for designing fast Li^+ ionic conductors for electrochemical storage applications due to the favorable intrinsic pathways for Li-ion transport. This system has the further benefit of having fully isotropic ionic conduction (due to its cubic symmetry) and will be easier to work with in powder form than alternates with highly anisotropic conductivity.

5.3.2 $Li_3AlP_3O_9N$

5.3.2.1 Synthesis and structure study of $Na_3AlP_3O_9N$

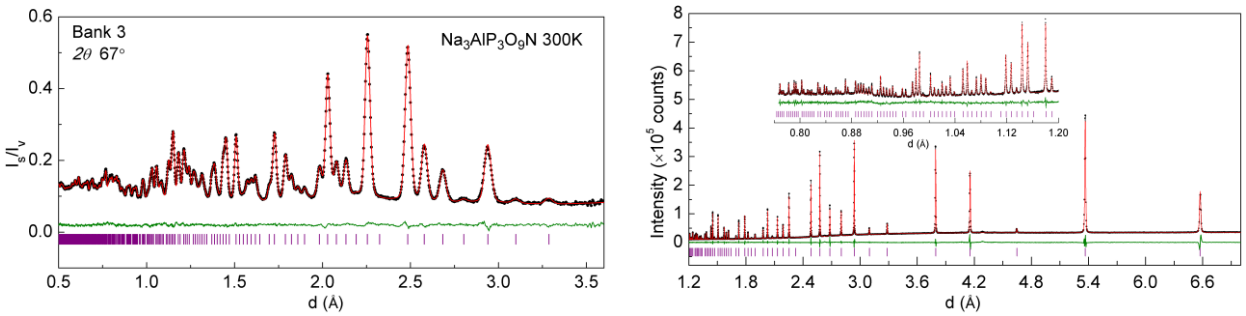

Figure 5.24 Left, Rietved refinment of $Na_3AlP_3O_9N$ using TOF (time-of-flight) neutron diffraction data, with data points shown in black dots, calculated curve in red and difference curve in olive, Bragg diffraction positions are marked with purple markers. Right, Rietved refinment using synchrotron XRD data (λ = 0.7787 Å) of $Na_3AlP_3O_9N$.

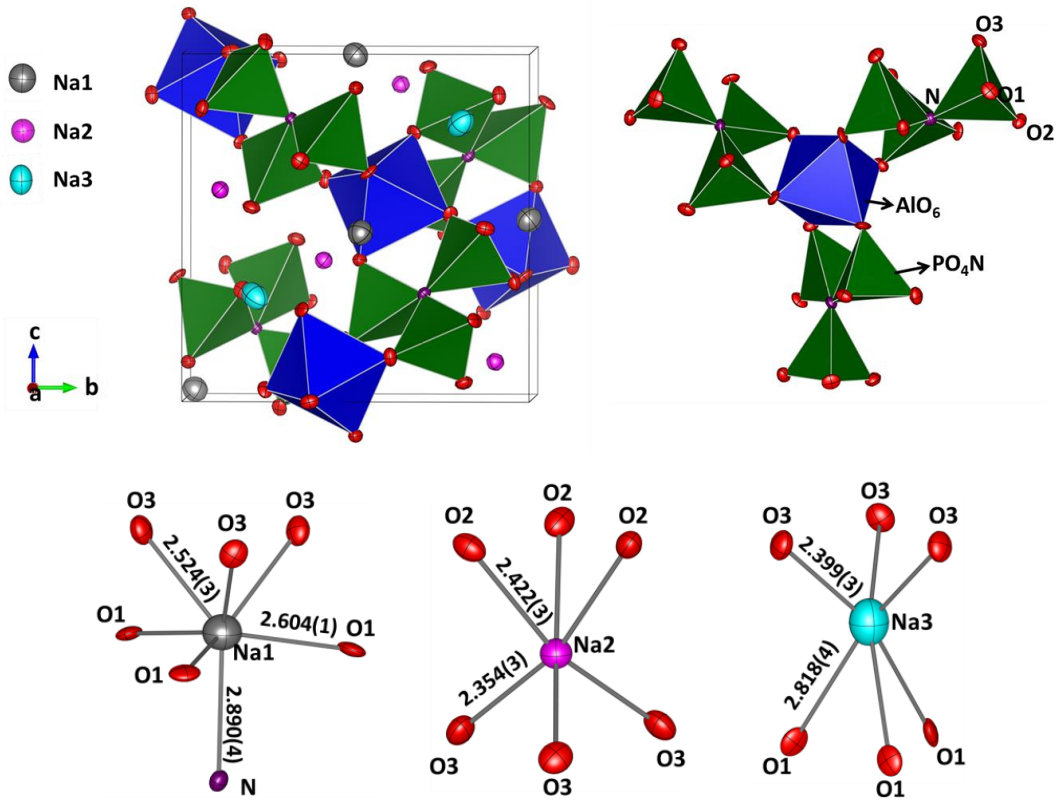

Figure 5.25 Top panel, Crystal strucutre of $Na_3AlP_3O_9N$. Bottom panel, local environements of three different sodium ions.

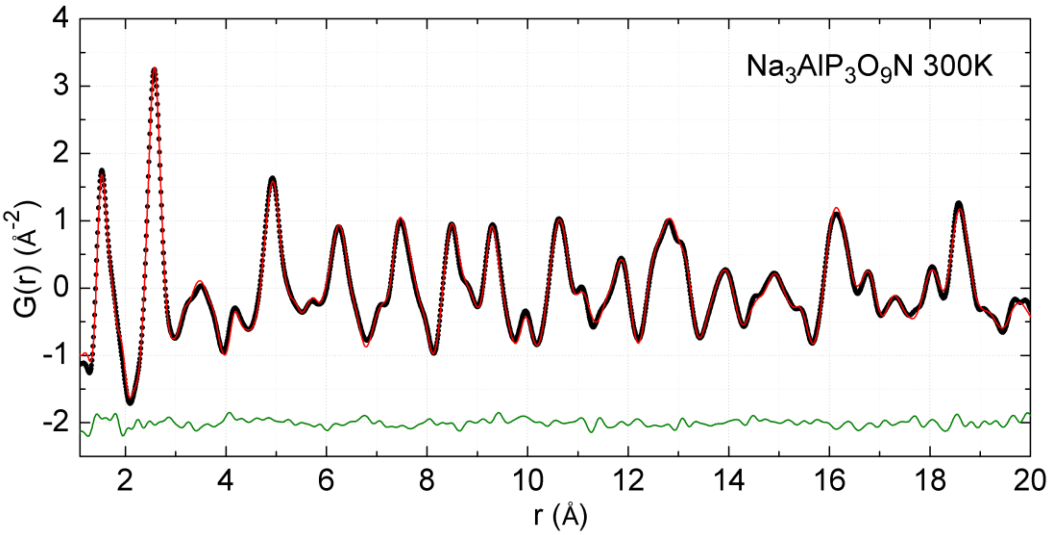

Figure 5.26 Fitting of TOF neutron PDF data of the as-prepared $Na_3AlP_3O_9N$ at 300 K, with collected data in black dots, calculated result in red and difference curve in green.

$Na_3AlP_3O_9N$ was synthesized in bulk quantities using thermal ammonolysis as previous reported[17-19,26]. No obvious impurity was found in the as-prepared sample based on the analysis of laboratory X-ray diffraction pattern. Structural information of this compound was obtained from Rietveld refinement of the structure using both synchrotron (X14A, NSLS) and neutron diffraction data (NOMAD, SNS), it has been found this compound crystallizes in cubic space group of $P2_13$ (#198) with lattice parameter of a = 9.2739(1) Å (refined from the synchrotron XRD data). The diffraction patterns are shown in Figure 5.24, with details of the refined crystallographic parameters presented in Tables 5.11 – 5.14. The neutron data is particularly sensitive to the light atoms (O, N) due to the large nuclear scattering length of these atoms, and it also provides the possibility to refine anisotropic displacement parameters for all sites as well as the precise determination of bond lengths. The structure of $Na_3AlP_3O_9N$ obtained from neutron diffraction data is shown in Figure 5.25. It has been found the crystal structure is quite similar to that of $Na_3TiP_3O_9N$[27] except that Ti^{3+} is replaced by smaller Al^{3+}. In this structure, three PO_3N tetrahedra are connected together by corner-sharing N atom, the trimer of $(PO_3)_3N$ is further connected to AlO_6 octahedral by corner shared oxygen atoms (O2 and O3). Three different sodium ions are identified to be located within large open spaces formed by O^{2-} and N^{3-}, Na1 sits in a distorted octahedron formed by three O1 and three O3, and it is further bonded to a single capping N atom with very long Na1-N bond length of 2.89 Å. Na2 is found to be at the center of a slightly distorted

octahedron formed by three O2 and three O3 with Na2-O2 and Na2-O3 bond distances of 2.42 Å and 2.36 Å separately. Na3 environment can be best described as on the top of an equilateral triangle constructed from three O3 with the Na3-O3 bond length of 2.3 Å, as can be seen in Figure 5.25. Local structure of the as-prepared sample was studied by means of neutron PDF (Figure 5.26), it has been found that the average crystal structure obtained from Rietveld refinement of neutron diffraction data can provide adequate fit for the PDF data, indicating no obvious local ordering or distortion in the as-prepared $Na_3AlP_3O_9N$.

Table 5.11 Summary of Rietveld refinement results of $Na_3AlP_3O_9N$.

Radiation	XRD	TOF neutron
λ	0.77878 Å	0.1-3 Å
Formula	$Na_3AlP_3O_9N$	$Na_3AlP_3O_9N$
Crystal system	Cubic	Cubic
Space group	*$P2_13(198)$*	*$P2_13(198)$*
Lattice a	9.2956(1)Å	9.2968(1)Å
Cell volume	803.21(2)$Å^3$	803.53(3)$Å^3$
R_{wp}	3.53%	2.57%
R_p	2.48%	2.28%
χ^2	2.40	1.36

Table 5.12 Rietveld refinement results for $Na_3AlP_3O_9N$ using synchrotron X-ray diffraction data measured at 298 K in air. (X14A, NSLS).

Atom	Wyck.	*x*	*y*	*z*	Occ.	B_{eq} ($Å^2$)
Na1	4a	0.01202(18)	0.01202(18)	0.01202(18)	1	1.80(7)
Na2	4a	0.39084(21)	0.39084(21)	0.39084(21)	1	0.59(7)
Na3	4a	0.79930(21)	0.79930(21)	0.79930(21)	1	1.34(7)
Al	4a	0.58214(15)	0.58214(15)	0.58214(15)	1	0.63(4)
P1	12b	0.07912(11)	0.23923(14)	0.32879(12)	1	0.37(2)
O1	12b	0.03179(24)	0.84346(26)	0.23640(23)	1	0.23(5)
O2	12b	-0.00263(32)	0.09990(29)	0.37107(23)	1	0.38(5)
O3	12b	0.16095(26)	0.30915(26)	0.44925(28)	1	0.51(7)
N1	4a	0.19037(40)	0.19037(40)	0.19037(40)	1	1.35(13)

Table 5.13 Rietveld refinement results for $Na_3AlP_3O_9N$ using TOF neutron diffraction data measured at 300 K (NOMAD, SNS).

Atom	Wyck.	*x*	*y*	*z*	Occ.	B_{eq} (Å^2)
Na1	4a	0.01327(28)	0.01327(28)	0.01327(28)	1	1.50
Na2	4a	0.39207(27)	0.39207(27)	0.39207(27)	1	0.58
Na3	4a	0.79751(36)	0.79751(36)	0.79751(36)	1	2.06
Al1	4a	0.58183(23)	0.58183(23)	0.58183(23)	1	0.80
P1	12b	0.07832(16)	0.23916(17)	0.34149(15)	1	0.57
O1	12b	0.01397(12)	0.86908(13)	0.22297(13)	1	0.88
O2	12b	0.00529(13)	0.13300(11)	0.39951(13)	1	0.66
O3	12b	0.19280(12)	0.32725(13)	0.45090(10)	1	0.89
N1	4a	0.19994(8)	0.19994(8)	0.19994(8)	1	0.59

Atom	U_{11}(Å^2)	U_{22}(Å^2)	U_{33}(Å^2)	U_{12}(Å^2)	U_{13}(Å^2)	U_{23}(Å^2)
Na1	0.0191(7)	0.0191(7)	0.0191(7)	0.0015(6)	0.0015(6)	0.0015(6)
Na2	0.0262(10)	0.0262(10)	0.0262(10)	-0.0007(10)	-0.0007(10)	-0.0007(10)
Na3	0.0072(4)	0.0072(4)	0.0072(4)	0.0005(4)	0.0005(4)	0.0005(4)
Al1	0.0103(5)	0.0103(5)	0.0103(5)	-0.0027(5)	-0.0027(5)	-0.0027(5)
P1	0.0084(6)	0.0064(6)	0.0070(5)	0.0013(5)	0.0002(5)	0.0024(4)
O1	0.0130(6)	0.0113(6)	0.0091(6)	-0.0068(5)	-0.0025(4)	-0.0010(4)
O2	0.0079(6)	0.0082(5)	0.0090(5)	-0.0019(4)	0.0020(4)	0.0021(4)
O3	0.0121(14)	0.0157(7)	0.0062(6)	-0.0034(5)	-0.0023(4)	-0.0027(4)
N1	0.0075(3)	0.0075(3)	0.0075(3)	-0.0003(3)	-0.0003(3)	-0.0003(3)

Table 5.14 Selected interatomic bond distances, bond valence sums (BVS) and angles for $Na_3AlP_3O_9N$

Bond types	Distance (Å)	Atoms	BVS	Angle types	Angle (degree)
Na1-O1 (×3)	2.6036(11)	Na1	+0.86	O1-Na1-O1 (×3)	117.868(33)
Na1-N	2.8899(39)	Na2	+1.22	O1-Na1-N (×3)	81.528(83)
Na1-O3 (×3)	2.5243(30)	Na3	+0.90	O3-Na1-O3 (×3)	73.469(93)
Na2-O2 (×3)	2.4221(30)	Al	+3.11	O3-Na1-N (×3)	136.319(59)
Na2-O3 (×3)	2.3539(25)	P	+4.78	O2-Na2-O2 (×3)	65.381(98)
Na3-O1 (×3)	2.8179(38)	O1	-1.93	O3-Na2-O3(×3)	89.778(49)
Na3-O2 (×3)	3.0260(17)	O2	-1.97	O2-Na2-O3 (×3)	103.631(43)
Na3-O3 (×3)	2.3996(31)	O3	-1.89	O1-Na3-O1 (×3)	56.152(83)
Al-O1 (×3)	1.8876(19)	N	-3.09	O3-Na3-O3(×3)	77.98(13)
Al-O2 (×3)	1.8988(22)	Gii*	0.13	O2-Na3-O2(×3)	115.264(64)
P-O1	1.5304(16)			O1-P-O2	109.448(94)
P-O2	1.5256(16)			O1-P-O3	110.891(97)
P-O3	1.4985(17)			O2-P-O3	114.01(11)
P-N	1.7037(13)			N-P-O1	107.009(83)
				N-P-O2	105.307(87)
				N-P-O3	109.808(94)

5.3.2.2 Synthesis and structure study of $Li_3AlP_3O_9N$

$Na_3AlP_3O_9N$, $Na_3GaP_3O_9N$, $Na_3TiP_3O_9N$, $Na_3VP_3O_9N$, $Na_2Fe_2P_3O_9N$ or $Na_2Mg_2P_3O_9N$ can all be directly synthesized by using high temperature solid state synthetic methods described here and in the prior literature reports. However, similar to the synthesis of $Li_{2-x}Fe_2P_3O_9N$ and $Li_2Mg_2P_3O_9N$, our efforts to synthesize $Li_3AlP_3O_9N$ or $Li_3GaP_3O_9N$ at various temperatures using methods analogue to those used to prepare the $Na_3AlP_3O_9N$ were unsuccessful, indicating $Li_3AlP_3O_9N$ or $Li_3GaP_3O_9N$ is very likely to be a metastable phase. So the low temperature solid-solid Li^+/Na^+ ion-exchange method that was originally developed to synthesize $Li_{2-x}Fe_2P_3O_9N$ and $Li_2Mg_2P_3O_9N$ were also utilized for synthesizing $Li_3AlP_3O_9N$.

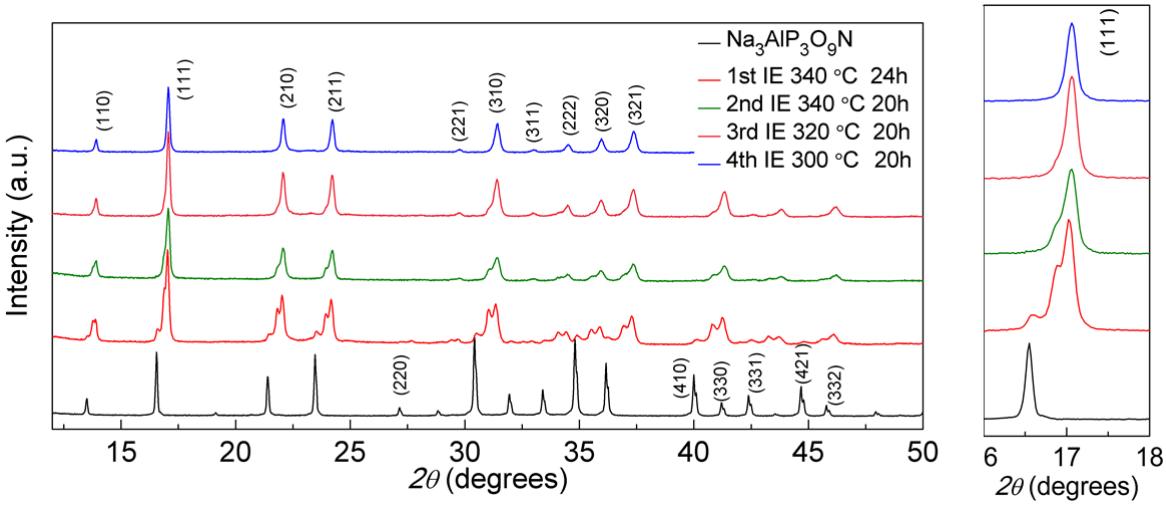

Figure 5.27 XRD patterns of $Li_xNa_{3-x}AlP_3O_9N$ collected after each ion exchange step.

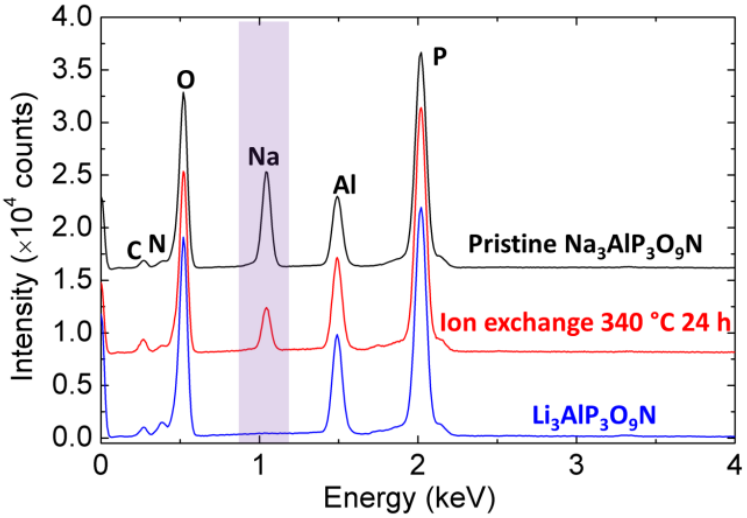

Figure 5.28 SEM-EDX patterns of $Na_3AlP_3O_9N$ and ion-exchanged "$Li_xNa_{3-x}AlP_3O_9N$". It clearly shows sodium concentration decrease as ion exchange proceeding. Carbon signal is due the carbon tape used in the experiment.

Ex situ X-ray diffraction patterns collected after each ion exchange process of $Na_3AlP_3O_9N$ are shown in Figure 5.27. It can be clearly seen that three distinct phases can be identified after initial ion exchange at 340 ℃ for 24 hours, indicating no complete solid solution between $Na_3AlP_3O_9N$ and the fully ion exchanged $Li_3AlP_3O_9N$, and these three different phases will be labeled as phase A, B and C separately. After the second repeated step of ion exchange for 20 hours, the initial phase A was found to be disappeared. Two more repeated steps were required to finish the ion exchange. To confirm the effectiveness of sodium ion removal, SEM-EDX data of the pristine $Na_3AlP_3O_9N$, sample recovered after first ion exchange and the fully ion exchanged sample were collected, as shown in Figure 5.28. A clear decrease intensity of Na signal was observed as ion exchange proceeded, and no obvious Na signal was observed in the final product. This indicates that almost all Na^+ in $Na_3AlP_3O_9N$ was replaced by Li^+ after four ion exchange steps.

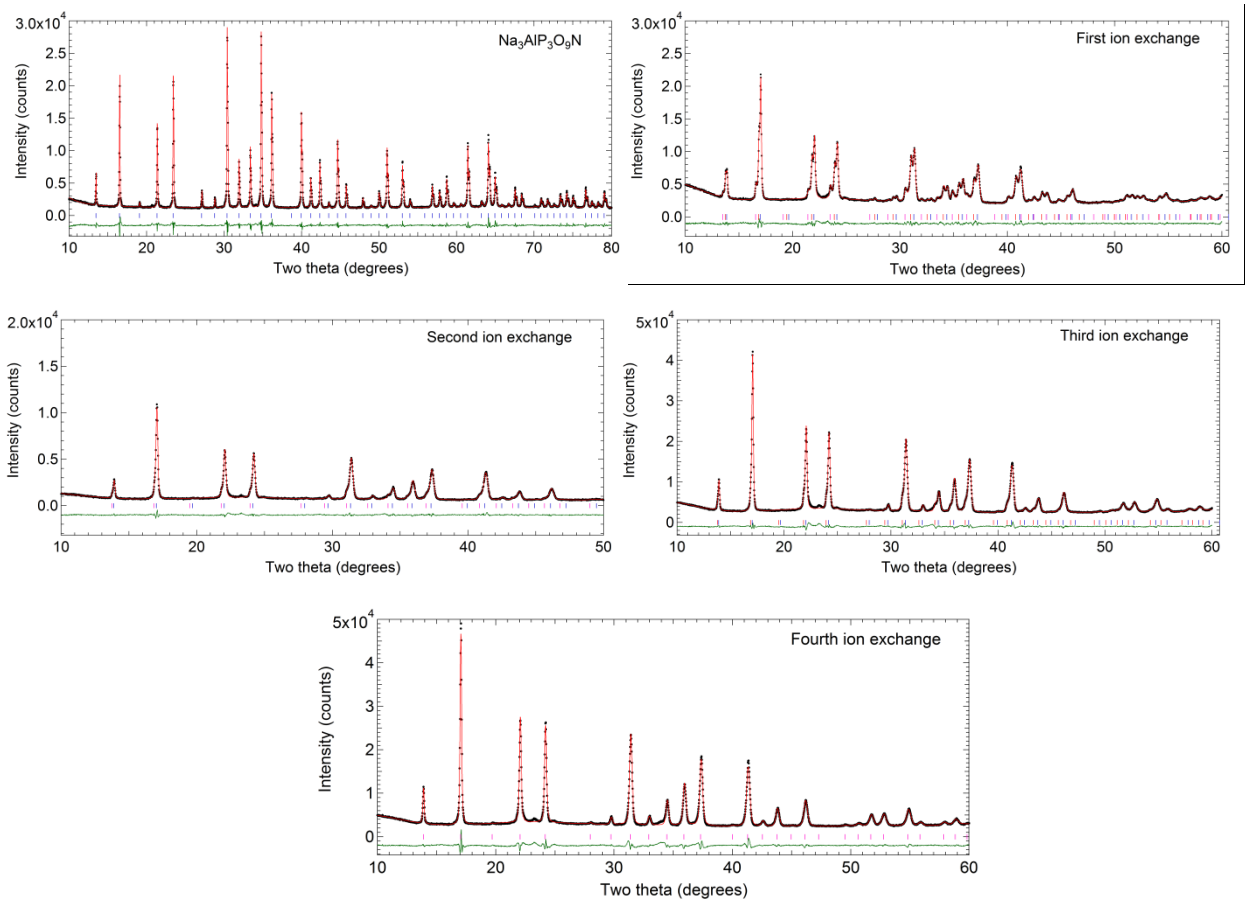

Figure 5.29 Le Bail fitting of products after different steps of ion exchange of $Na_3AlP_3O_9N$ using Lab XRD data of.

Further insights into the mechanism of the Li^+/Na^+ ion exchange reaction of $Na_3AlP_3O_9N$ can be obtained from whole pattern Le Bail fits (Figure 5.29) using *ex situ* X-ray diffraction patterns. The co-existence of three different phases indicates inhomogeneity of the ion exchange after the first ion exchange step, which is likely to be a result of an inhomogeneous particle size distribution with very large particles that have limited Li^+/Na^+ diffusion length, similar to what was found in ion exchange of $Na_2Mg_2P_3O_9N$. Considering the large ionic radii difference between Li^+ (0.74 Å) and Na^+ (1.02 Å)[32], phase A with the largest lattice parameter is assigned to be a Na-rich phase, while phase B and phase C with smaller lattice parameters are assigned to be Li-rich phases. Based on the refinement result, it was found lithium-rich phase C has essentially constant lattice parameter upon its formation, indicating this line phase is very likely to be the fully ion exchanged phase $Li_3AlP_3O_9N$. Lattice parameter of sodium-

rich phase A (initial phase) decreases slightly after one step of ion exchange, indicating the existence of small solid solution region for this phase. The lattice parameter of the intermediate Li-rich phase B decreases substantially from its initial value during the ion exchange process, indicating the existence of a wide solid solution region for this phase. These observations from *ex situ* diffraction data are consistent with our *in situ* diffraction studies which will be presented later in this chapter. Thus, it is proposed that ion exchange of $Na_3AlP_3O_9N$ starts with a solid solution reaction to form sodium-rich phase A, which is followed by a phase transition to form Li-rich intermediate phase B. Once the lithium solubility limit is reached, phase B transforms into the line phase $Li_3AlP_3O_9N$.

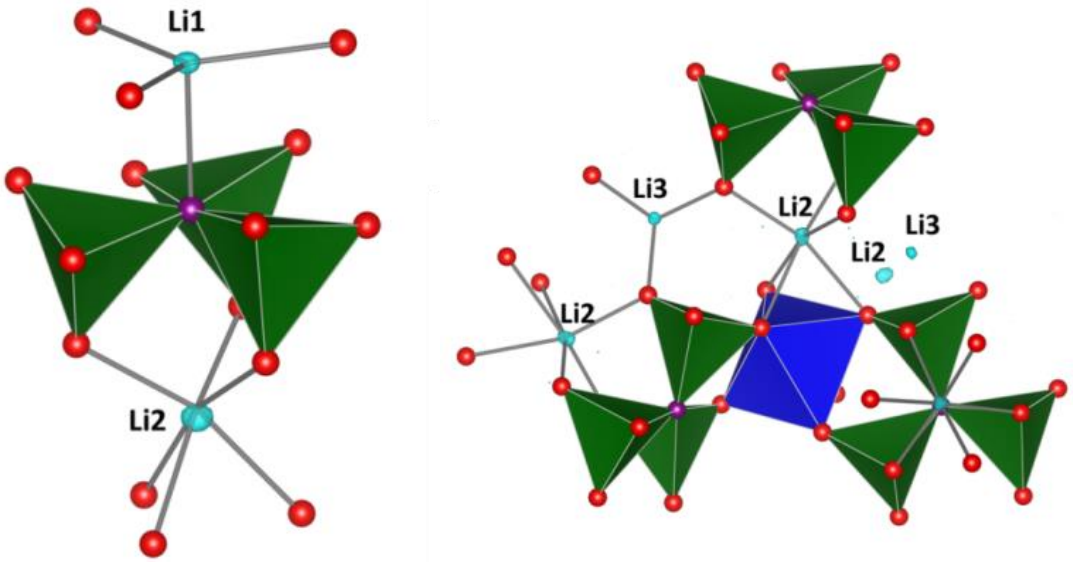

Figure 5.30 Fourier difference map calculated from TOF neutron diffraction data with initial structure model of "AlP_3O_9N". Residual nuclear scattering length densities are shown cyan isosurfaces with threshold valued of -0.95 fm/Å^3. The three Li sites are labeled.

To reveal the detailed Na/Li site exchange information, it is worthwhile to gain insights into the crystal structure of the fully ion exchanged end member $Li_3AlP_3O_9N$, especially the atomic environments of different Li ions. High quality synchrotron XRD and time-of-flight neutron diffraction data was collected for the as-prepared $Li_3AlP_3O_9N$ powder. For $Li_2Mg_2P_3O_9N$, it was previously found that Li^+ ions have very different coordination geometries relative to corresponding Na^+ sites in the analogue $Na_2Mg_2P_3O_9N$. Here, we used both the biased and unbiased method to obtain the crystal

structure of the newly discovered compound $Li_3AlP_3O_9N$. For the biased method, $Li_3AlP_3O_9N$ was treated as an analogue of $Li_2Mg_2P_3O_9$ but with one Mg^{2+} (Mg2) replaced by Li^+ (Li2) and the other Mg^{2+} (Mg1) replaced by Al^{3+}, all atomic positions, anisotropic atomic displacements (isotropic displacements for Li) were refined simultaneously until the refinement converged. For the unbiased ab initio method, the as-collected synchrotron XRD diffraction pattern was first indexed with space group $P2_13$, Le Bail fitting was then carried out to extract the integrated intensity of each diffraction peak in Jana 2006 software. Furthermore, the structure skeleton AlP_3O_9N was successfully obtained by using charge flipping [33] in Supeflip[34]. Rietveld refinements of both XRD and neutron diffraction data were carried out with the initial crystal structure of AlP_3O_9N, Fourier difference maps were calculated to locate the residual electron density or nuclear scattering length density after the refinement converged. Similar residual density positions can be observed in both maps, as can be seen in Figure 5.30, and these three most plausible atomic positions are assigned to Li1, Li2 and Li3 separately. After introducing three lithium ion positions into the structure, a final Rietveld refinement was carried out with all atomic positions and displacements refined simultaneously until the refinement converged (Figure 5.31). The final crystal structure of $Li_3AlP_3O_9N$ is shown in Tables 5.15-5.18 and Figure 5.32, with important bond lengths, angles and bond valence sum (BVS) values listed in Table 5.17. It can be seen that AlP_3O_9N skeleton is very similar to that of $Na_3AlP_3O_9N$. However, the Li^+ positions are found to be displaced substantially from the original Na^+ positions: Li1 is found to sit in a distorted tetrahedron formed by three O1 and one N with Li1-O1 and Li1-N bond lengths of 2.3356 (25) Å and 2.135 (12) Å separately; Li2 was found to be in the center of a slightly distorted $Li2O_6$ octahedron but with much shorter Li2-O bond distance relative to Na2-O. The Li3 environment can be best described as being on top of an equilateral triangle formed by three O3 anions with Li3-O3 bond distances of 1.9336 (72) Å. The bond valence sum (BVS) valences calculated for Li1, Li2 and Li3 are 0.86, 1.22 and 0.90 separately, indicating that Li2 is over bonded while Li1 and Li3 are at best weakly bonded and may be the potentially mobile lithium ions within the structure. Further Li ion mobility information can be gained from lithium atomic displacement factors obtained from Rietveld refinement. It can be seen that Li1 and Li3 have much larger displacement factors than that of Li2, indicating Li^+ on these two sites are more likely to be more mobile than that at Li2.

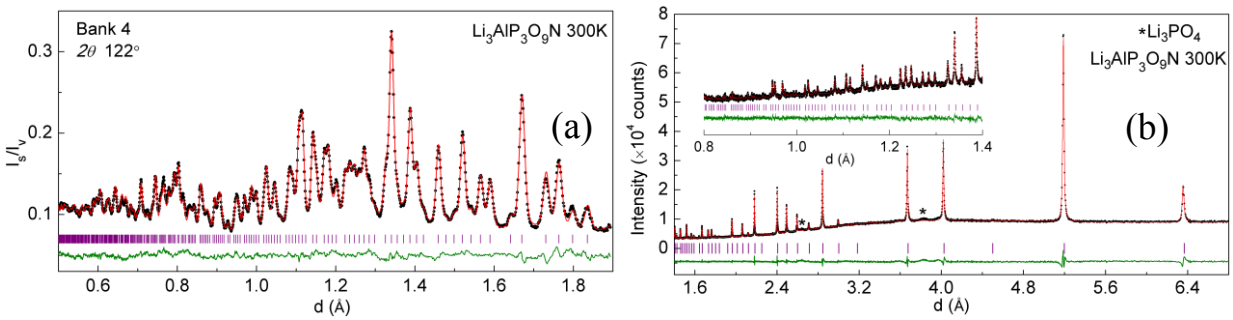

Figure 5.31 (a) Rietveld refinment $Li_3AlP_3O_9N$ structure using TOF (time-of-flight) neutron diffraction data, with data points shown in black dots, calculated curve in red and difference curve in olive, Bragg diffraction positions are marked in purple. (b) Rietved refinment using synchrotron XRD data (λ = 0.7787 Å) of $Li_3AlP_3O_9N$.

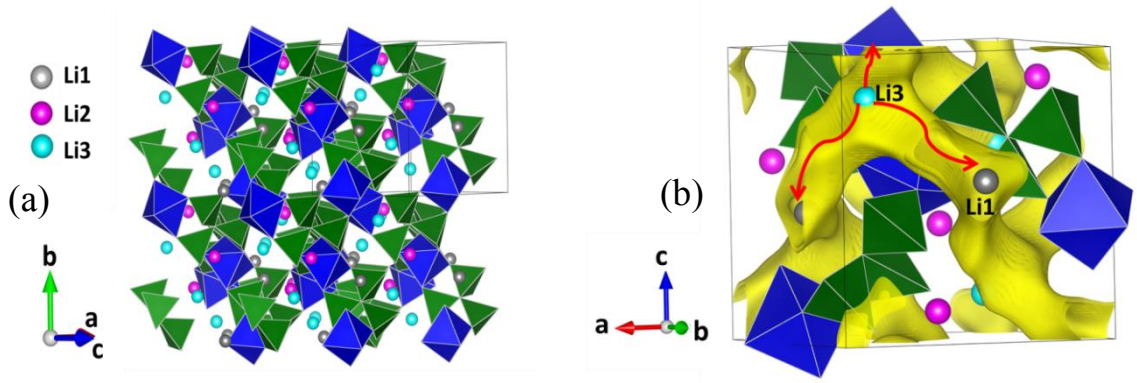

Figure 5.32 (a) Crystal structure (2 ×2 ×2) of $Li_3AlP_3O_9N$ with AlO_6 octahedron shown in blue and PO_3N tetrahedron shown in olive. (b) Lithium difference bond valence sum map (|Δ| = 0.05) calculated for $Li_3AlP_3O_9N$. The yellow isosurface represents the potential three dimensional Li^+ diffusion pathway which connects the Li1 and Li3 sites but not the Li2 site.

Table 5.15 Summary of Rietveld refinement results of $Li_3AlP_3O_9N$.

Radiation	XRD	TOF neutron
λ	0.77878 Å	0.1-3 Å
Formula	$Li_3AlP_3O_9N$	$Li_3AlP_3O_9N$
Crystal system	Cubic	Cubic
Space group	*$P2_13(198)$*	*$P2_13(198)$*
Lattice a	8.9903(1) Å	8.9922(5) Å
Cell volume	726.66(1) $Å^3$	725.76(21) $Å^3$
R_{wp}	2.60%	3.18%
R_p	1.99%	2.46%
χ^2	1.78	2.11

Table 5.16 Rietveld refinement results for $Li_3AlP_3O_9N$ using TOF neutron diffraction data measured at 300 K. (NOMAD, SNS).

Atom	Wyck.	*x*	*y*	*z*	Occ.	B_{eq} ($Å^2$)
Li1	4a	0.05817(79)	0.05817(79)	0.05817(79)	1	2.49(33)
Li2	4a	0.39302(62)	0.39302(62)	0.39302(62)	1	0.40(17)
Li3	4a	0.83257(90)	0.83257(90)	0.83257(90)	1	3.32(44)
Al	4a	0.57108(33)	0.57108(33)	0.57108(33)	1	0.67(10)
P1	12b	0.08495(22)	0.25578(23)	0.33576(25)	1	0.31(4)
O1	12b	0.02346(18)	0.86984(19)	0.23389(20)	1	0.27(4)
O2	12b	-0.00121(21)	0.12012(17)	0.38853(21)	1	0.58(6)
O3	12b	0.18046(20)	0.32927(23)	0.45268(19)	1	0.77(7)
N1	4a	0.19533(14)	0.19533(14)	0.19533(14)	1	0.41(6)

Table 5.17 Rietveld refinement results for $Li_3AlP_3O_9N$ using synchrotron diffraction data measured at 298 K. (X14A, NSLS)

Atom	Wyck.	*x*	*y*	*z*	Occ.	B_{eq} ($Å^2$)
Li1	4a	0.0440(16)	0.0440(16)	0.0440(16)	1	2.04(61)
Li2	4a	0.3978(23)	0.3978(23)	0.3978(23)	1	1.95(72)
Li3	4a	0.8424(16)	0.8424(16)	0.8424(16)	1	2.04(63)
Al	4a	0.57146(28)	0.57146(28)	0.57146(28)	1	0.59(10)
P1	12b	0.08399(26)	0.25825(28)	0.33626(29)	1	0.47(3)
O1	12b	0.02743(57)	0.87405(48)	0.23320(47)	1	0.36(7)
O2	12b	-0.00702(60)	0.12167(42)	0.38972(50)	1	0.36(7)
O3	12b	0.18557(48)	0.33098(51)	0.45555(56)	1	0.36(7)
N1	4a	0.19310(65)	0.19310(65)	0.19310(65)	1	0.36(7)

Table 5.18 Selected interatomic bond distances, bond valence sums (BVS) and angles for $Li_3AlP_3O_9N$

Bond types	Distance (Å)	Atoms	BVS	Angle types	Angle (degree)
Li1-O1 (×3)	2.3356(25)	Li1	+0.86	O1-Li1-O1 (×3)	118.91(14)
Li1-N	2.135(12)	Li2	+1.22	O1-Li1-N (×3)	96.03(30)
Li1-O2(×3)	3.0673(69)	Li3	+0.90	O3-Li1-O3 (×3)	86.60(27)
Li1-O3 (×3)	2.973(10)	Al	+3.11	O3-Li1-N (×3)	146.60(13)
Li2-O2 (×3)	2.1843(71)	P	+4.78	O2-Li2-O2 (×3)	71.40(29)
Li2-O3 (×3)	2.0651(58)	O1	-1.93	O3-Li2-O3(×3)	93.18(31)
Li3-O2 (×3)	3.0498(61)	O2	-1.97	O2-Li2-O3 (×3)	98.871(82)
Li3-O3 (×3)	1.9336(72)	O3	-1.89	O2-Li3-O2 (×3)	105.91(28)
Al-O1 (×3)	1.8806(33)	N	-3.09	O3-Li3-O3(×3)	94.30(49)
Al-O2 (×3)	1.8724(37)	Gii*	0.13	O2-Li3-O3(×3)	77.198(96)
P-O1	1.5465(27)			O1-Al-O1(×3)	90.76(20)
P-O2	1.5201(27)			O2-Al-O2(×3)	85.80(19)
P-O3	1.5089(28)			O1-Al-O2(×3)	93.429(80)
P-N	1.6946(22)			O1-P-O2	109.69(15)
				O1-P-O3	110.50(16)
				O2-P-O3	115.06(17)
				N-P-O1	106.25(14)
				N-P-O2	105.86(15)
				N-P-O3	109.02(16)

Gii: global instability index

5.3.2.3 *In situ* X-ray diffraction study of Li^+/Na^+ ion exchange of $Na_3AlP_3O_9N$

Many *in situ* XRD studies of ion exchange between monnopositive ions (Li^+/Na^+, Na^+/K^+, Cs^+/K^+ ect.) within zeolites frameworks can be found in the literature[35,36], taking advantage of the large open channels and relative stable backbone skeletons of these porous materials. One great advantage of utilizing XRD instead of neutron diffraction is the higher *d* spacing and time resolution, which means this technique can be utilized for kinetic and structure evolution study of very fast ion exchange systems, such as zeolites. However, the drawback of XRD is the relatively low sensitivity to light atoms, which is problematic for Li^+/Na^+ ion exchange. Hence, a combined *in situ* XRD and neutron diffraction was utilized for mechanistic study of Li^+/Na^+ exchange of $Na_3AlP_3O_9N$, taking advantages of both techniques.

The as-collected *in situ* XRD patterns are shown in Figure 5.33. During heating, the original diffraction peaks associated to $Na_3AlP_3O_9N$ shift to the lower two theta (higher *d* spacing) direction due to the dominant effect of thermal expansion. A clear second phase formation can be observed when ion

exchange temperature reached 240 ℃. However, it is worth to note that the formation of asymmetrical LiCl diffraction peaks due to the formation of $Li_{1-y}Na_yCl$ solid solution begins at a much lower temperature of about 150 ℃, indicating the actual onset temperature for ion exchange should be much lower than that of the appearance of the second sodium-poor phase. Moreover, this temperature gap is presumably to be caused by formation of partial solid solution of sodium-rich phase A before the phase transformation to the lithium-rich phase B. From the *ex situ* XRD study, we have noticed only a narrow solid solution region can be formed for sodium-rich phase A at room temperature. However, this solid solution region was found to be expanded dramatically at the ion exchange temperature (330 ℃), which is associated with the formation of asymmetrical diffraction peaks of phase A with tail toward higher two theta (low *d* spacing) direction, as can be seen in the zoom of the 111 diffraction peak in Figure 5.33. The diffraction peaks associated with sodium-poor phase B were also found to be asymmetrical. However, the asymmetrical shape of these peaks varies at different ion exchange stages: the more pronounced tail was found at lower two theta (higher d spacing) side at early stages of ion exchange when obvious co-existence of phase A and phase B was observed. The asymmetrical peak was found to tail more toward the higher two theta (lower d spacing) side as the decrease of sodium-rich phase A occured, indicating the solid solution phase moved toward Li-rich phase C at the later ion exchange stages. Interestingly, we also noted the existence of very weak diffraction peaks that corresponded to the third Li-rich phase C at 330 ℃. As can be seen in Figure 5.33, the intensities and positions associated with these diffraction peaks are almost constant during the hold at 330 ℃, indicating this phase is a single line phase, which is in good agreement with the *ex situ* XRD study. The co-existence of three different phases (A, B and C) at 330 ℃ can be understood by the inhomogeneity of ion exchange of $Na_3AlP_3O_9N$ with inhomogeneous particle size distribution, as the sodium-rich phase A must first transform to the Li-rich phase B before the formation of final single line phase C.

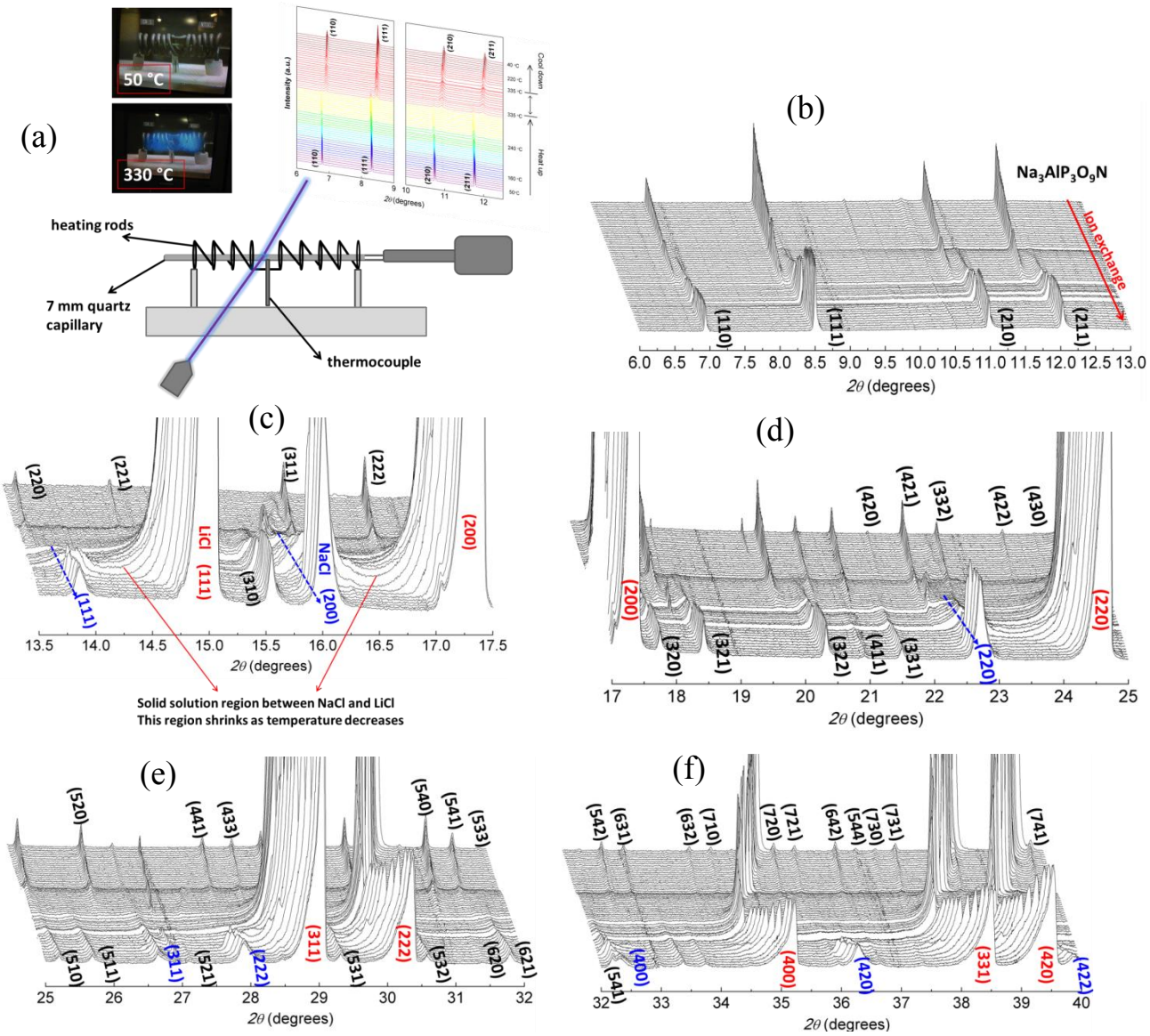

Figure 5.33 (a) Schematic illustration of *in situ* XRD study of solid-solid Li^+/Na^+ ion exchange of $Na_3AlP_3O_9N$. (b)-(f) XRD patterns collected during *in situ* ion exchange of $Na_3AlP_3O_9N$ with miller indices of $Li_xNa_{3-x}AlP_3O_9N$ phase shown in black, NaCl (or $Li_xNa_{1-x}Cl$ solid solution) miller indices in blue and LiCl (or $Na_zLi_{1-z}Cl$ solid solution) miller indices in red.

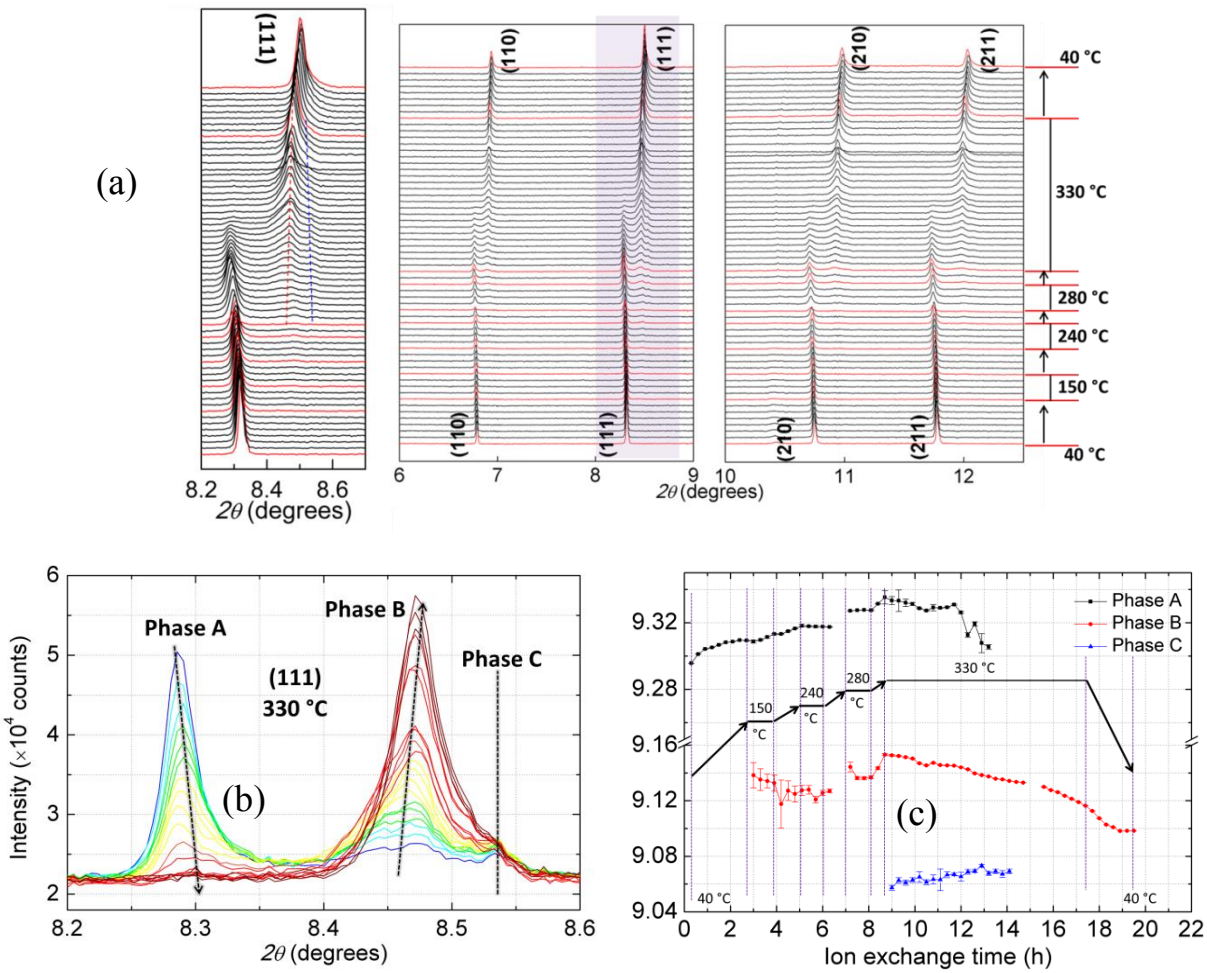

Figure 5.34 (a) Selected region of *in situ* XRD patterns collected during Li^+/Na^+ ion exchange with time profile shown on the right side. (b) Evolution of three different phases during *in situ* ion exchange. (c) Lattice parameter evolution of three different phases during ion exchange.

Further insights into the ion exchange mechanism can be obtained by tracking the lattice parameter evolution of these three phases. Whole pattern Le Bail fitting was carried out for all diffraction patterns, refinement details can be found in the experimental part. The obtained lattice parameters are plotted against ion exchange time in Figure 5.34. The sodium-rich phase A lattice parameter was found to slightly decrease while the reaction is held at constant temperatures (240 ℃, 280 ℃ and 330 ℃), indicating a limited solid solution formation of sodium-rich phase A. Further replacement of sodium ions will lead to the phase transition from the sodium-rich phase A to the Li-rich phase B with a much smaller lattice parameter. Phase B is a solid solution phase and its lattice parameter decreases

monotonically as the ion exchange proceeds. Interestingly, lattice parameter associated with the third lithium-rich phase C (single line phase at room temperature) slightly increased as ion exchange continues at 330 ℃. This may due to the slightly ion exchange reaction between the final phase, e.g. $Li_3AlP_3O_9N$, and Li-rich phase B at 330 ℃, resulting in the formation of $Na_{3-z}Li_zAlP_3O_9N$ (z is a small number). This lithium-rich phase disappeared after holding for 5 hours at 330 ℃, indicating that the lithium source does not provide enough chemical potential for full Li^+/Na^+ ion exchange.

Due to the strongly asymmetrical diffraction peaks associated with the formation of solid solution of phase A and phase B, it is difficult to utilize Rietveld refinements to extract accurate structural information of these two phases during isothermal holds at 330 ℃. Rietveld refinement was only carried out for diffraction patterns collected at first scan at 40 ℃, 150 ℃, 240 ℃, 280 ℃ and the end scan at 40 ℃. For the first four temperatures, the structure refinement was focused on the sodium-rich phase A, while the lithium-rich phase B was found to be the major phase in the end scan. Since X-rays are not sensitive to light atoms such as lithium, only sodium atomic positions and occupancies are refined. It was found Li^+ first replaced Na^+ at Na2 site in sodium-rich phase A, forming $(Na1)_1(Na2)_{1-x}(Li2)_x(Na3)_1AlP_3O_9N$, where x was found to be around 0.8 at 280 ℃. At the end of ion exchange, lithium-rich phase B was refined to have the formula of $(Na1)_1(Na2)_{\sim 0.34}(Na3)_{\sim 0.3}AlP_3O_9N$, which is close to $(Na1)_1(Li2)_1(Li3)_1AlP_3O_9N$ considering the X-ray scattering power difference between Na and Li. This is also supported by the short cation-oxygen and cation-nitrogen bond lengths formed for these two sites (Li2 and Li3).

5.3.2.4 *In situ* neutron diffraction study of Li^+/Na^+ ion exchange of $Na_3AlP_3O_9N$

As mentioned in the *in situ* XRD part, the greatest advantage of utilizing *in situ* XRD is relative higher *d* spacing resolution, while the drawback is the poor sensibility to light atoms such as lithium, oxygen or nitrogen. In contrast, neutron diffraction is quite sensitive to these atoms especially when ^7Li isotope is used. Longer data acquisition times (~hours) are usually required for collecting high quality neutron diffraction data due to much lower neutron flux, which makes it difficult to utilize this technique to study ion exchange systems associated with super ionic conductors such as that in zeolites or β''-Al_2O_3. Fortunately, ion exchange process can be slowed down to the scale of tens of hours by utilizing solid-solid ion exchange method with a proper ion exchange temperature. Also, the development of time-of-flight neutron diffraction beamlines with good counting statistics offers the

opportunity to collect high quality diffraction data within tens of minutes. ^{7}LiCl was used as lithium source in this experiment to minimize X-ray and neutron absorption, and the Na : Li molar ratio was further reduced from the 1:6 to 1: 4 in *ex situ* experiments to increase the relative scattering power of ion exchanged phase and reduce absorption associated with Li salts (e.g. LiCl). It is expected that lower lithium concentration will lead to a less complete ion exchange during experiment.

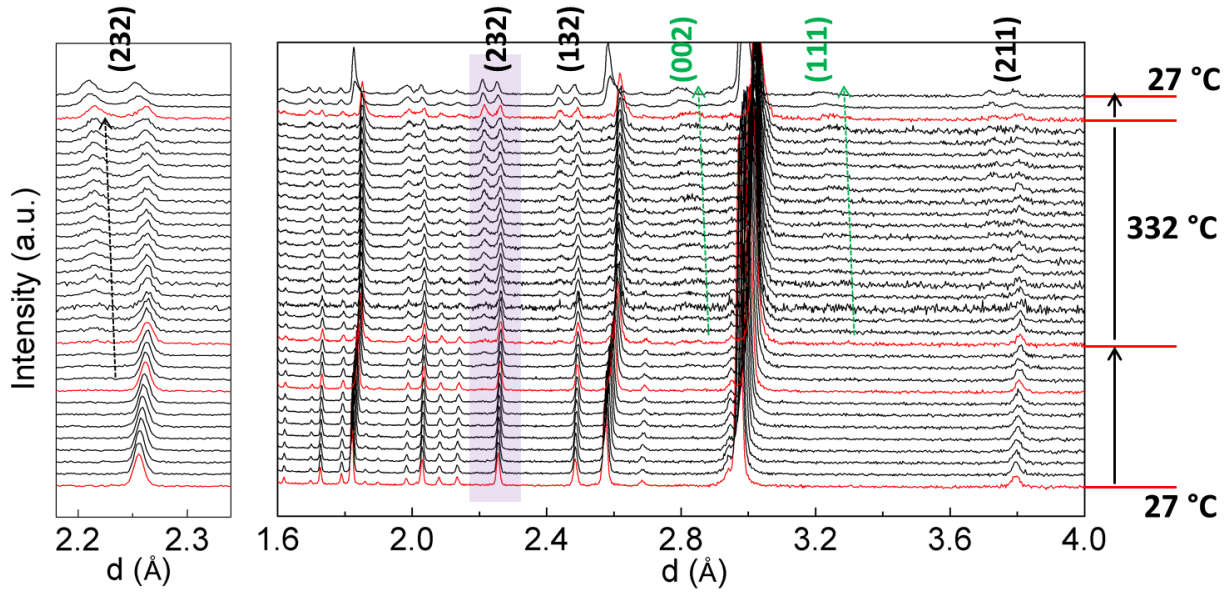

Figure 5.35 Neutron diffraction patterns collected during *in situ* ion exchange of $Na_3AlP_3O_9N$.

The as-collected *in situ* neutron diffraction patterns are shown in Figure 5.35, with sample diffraction peaks labelled in black, ^{7}LiCl salt diffraction peaks in pink and the product NaCl peaks in olive. During heating (27 ℃ to 332 ℃), the Bragg diffraction peaks associated with original $Na_3AlP_3O_9N$ were found to shift to higher *d* spacing due to thermal expansion. A second phase appeared at temperatures higher than 240 ℃, which is higher than that found in *in situ* XRD study. This may due to the lower lithium concentration or the lower d sensitivity of neutron diffraction data. The actual onset temperature for ion exchange can be judged from the formation of asymmetrical LiCl diffraction peaks which is caused by the formation of $Li_{1-y}Na_yCl$ type solid solution. As can be seen in Figure 5.35, this onset temperature was identified to be around 200 ℃. The formation of NaCl was not observed until the ion exchange temperature reached 332 ℃, indicating that the sodium concentration reached the highest limit of the $Li_{1-y}Na_yCl$ solid solution at this temperature. In contrast to *in situ* XRD study, no obvious

diffraction peaks corresponding to the third Li-rich phase C was observed, indicating a less degree of completion of ion exchange due to the lower lithium concentration. Thus, four different phases are found to co-exist in the product: $Li_{1-y}Na_yCl$, $Na_{1-z}Li_zCl$, sodium-rich phase A and Li-rich phase B.

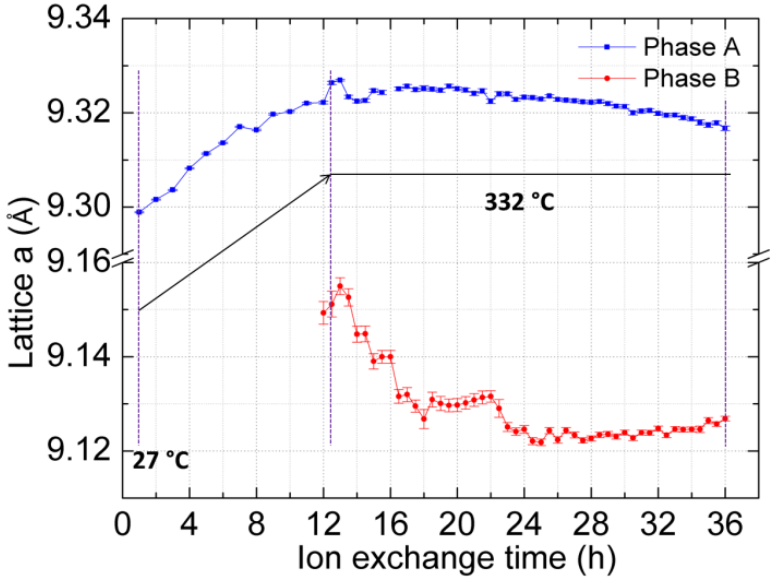

Figure 5.36 Lattice parameter evolution of sodium rich phase A and sodium poor phase B.

The lattice parameter evolution of sodium-rich phase A and sodium-poor phase B are shown in Figure 5.36, with lattice parameters obtained from Le Bail fitting of corresponded diffraction pattern. Similar to the results of the *in situ* XRD study, it was found that the lattice parameter of phase A decreased slightly during isothermal hold at 332 ℃, indicating the formation of $Na_{3-x}Li_xAlP_3O_9N$ solid solution. However, it is worth noting that the lattice parameter of this phase is still decreasing after an isothermal hold for 24 hours, indicating ion exchange is not finished at the end of *in situ* experiment. Curiously, it only took about 12 hours for lithium-rich phase B to reach the equilibrium state, which is even faster than that in *in situ* XRD study which used larger amounts of LiCl. This is presumably due to the lower molar ratio of Li to Na used in *in situ* neutron diffraction, and the lower overall degree of conversion.

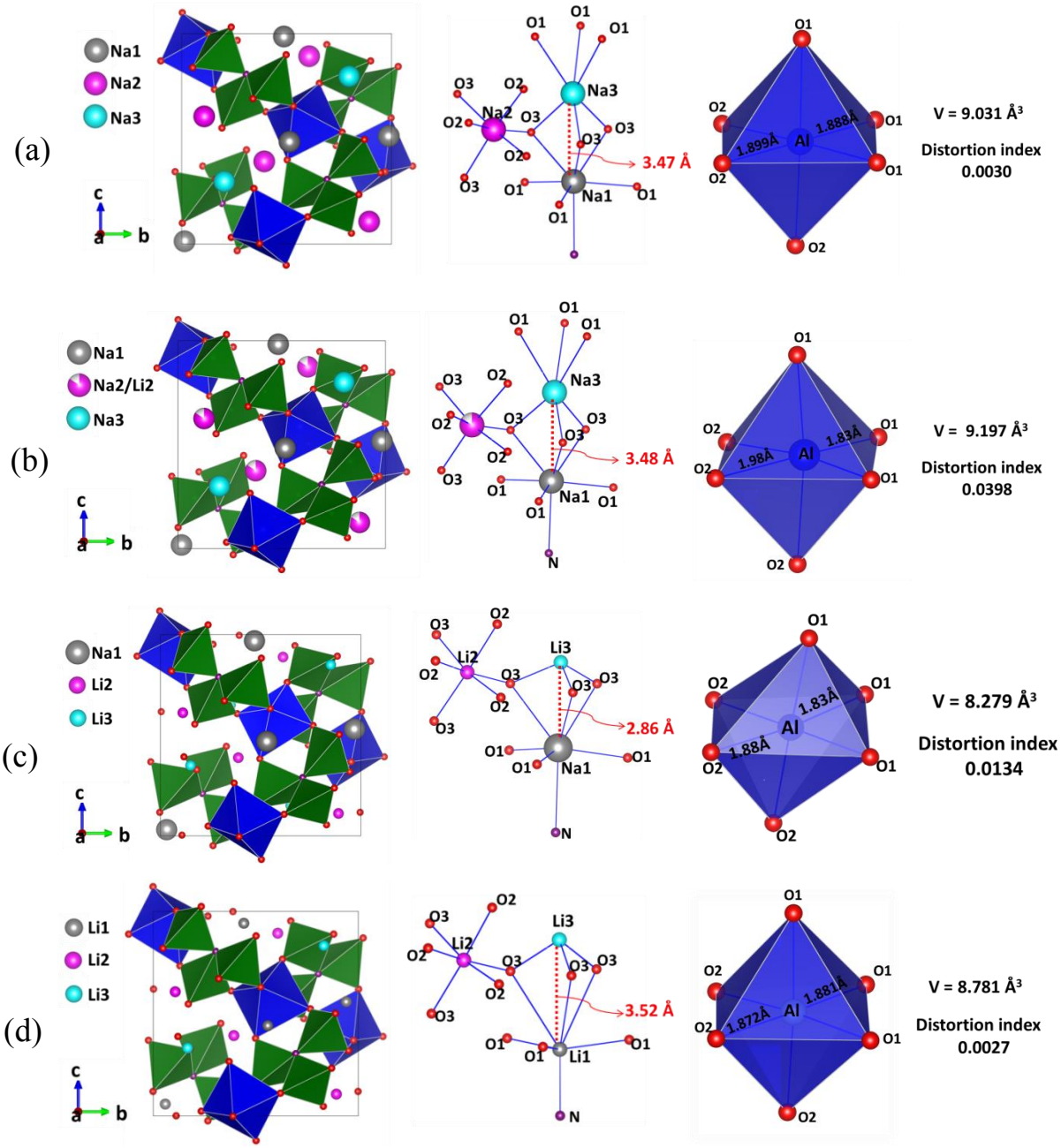

Figure 5.37 (a)-(d) Crystal structure evolution of $Na_3AlP_3O_9N$-$Na_2LiAlP_3O_9N$-$NaLi_2AlP_3O_9N$-$Li_3AlP_3O_9N$ during ion exchange.

Further insights into structural evolution can be obtained by using Rietveld refinement of selected diffraction patterns. Since the diffraction peaks associated with lithium-rich phase B are relatively weak until ion exchanging for 16 hours, this phase was only included in the refinement for patterns collected

thereafter. It was found that the Na occupancy only changed slightly at the Na2 site for the sodium-rich phase A during the whole ion exchange process. At the end of ion exchange, this phase was refined to a formula of $(Na1)_1(Na2)_{\sim 0.8}(Li2)_{\sim 0.2}(Na3)_3AlP_3O_9N$. The Li-rich phase B was found to have the formula of $(Na1)_1(Li2)_1(Na3)_1AlP_3O_9N$ upon its formation, whereas its final composition was refined to be $(Na1)_1(Li2)_1(Li3)_1AlP_3O_9N$, indicating that a full solid solution between $(Na1)_1(Li2)_1(Na3)_1AlP_3O_9N$ and $(Na1)_1(Li2)_1(Li3)_1AlP_3O_9N$ has been formed for this phase during ion exchange at 330 ℃. These results are in good agreement with the results from *in situ* XRD data.

5.3.2.5 Li^+ ionic conductivity of $Li_3AlP_3O_9N$

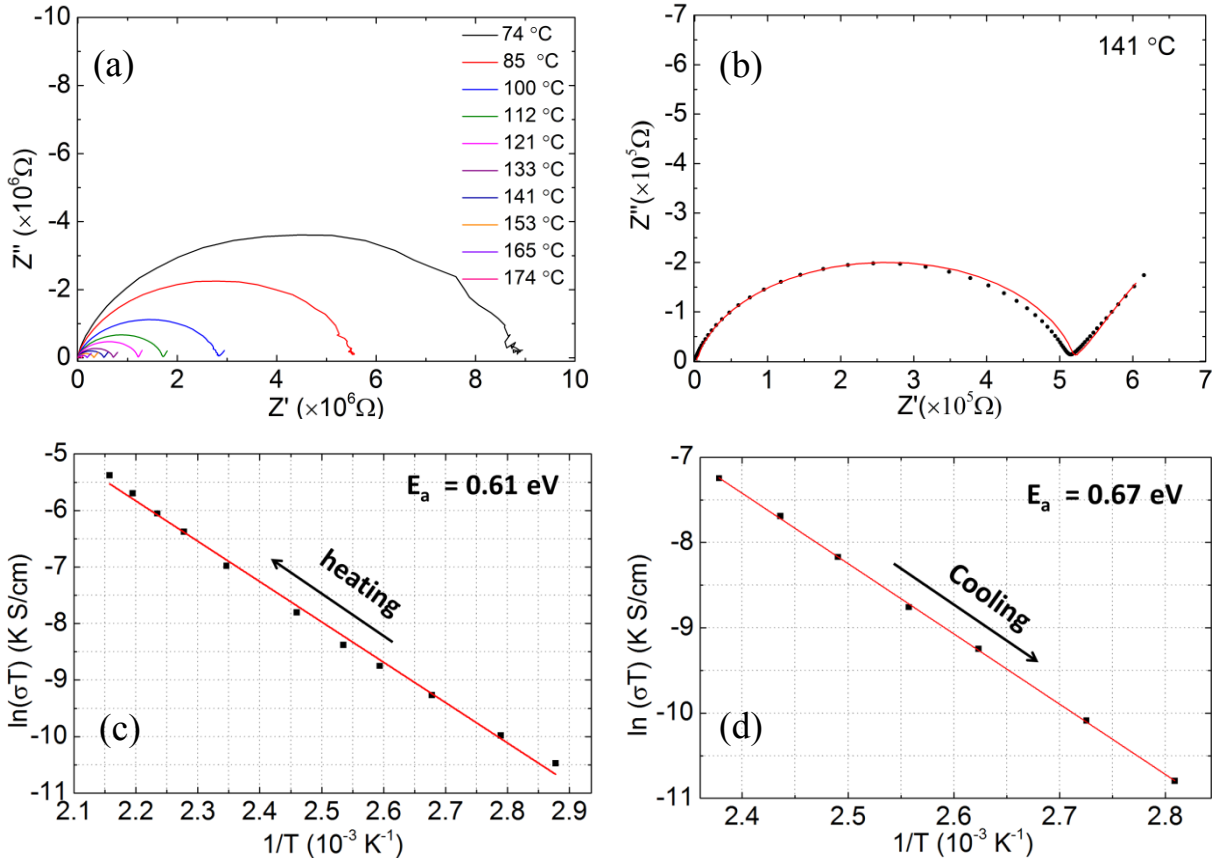

Figure 5.38 (a) Temperature dependent ac impedance data of $Li_3AlP_3O_9N$. (b) Fitting of the 141 ℃ data using equivalent circuit similar to that used for $Li_2Mg_2P_3O_9N$. (c) Arrhenius plot of the temperature dependent ionic conductivity of $Li_3AlP_3O_9N$ during heating. (d) Arrhenius plot of the temperature dependent ionic conductivity of $Li_3AlP_3O_9N$ during cooling.

In our previous report on lithium variants of CUBICONs, a reasonably high room temperature (24 ℃) Li^+ ionic conductivity of about 10^{-7} S/cm was found for $Li_2Mg_2P_3O_9N$ with potential three dimensional Li^+ ionic diffusion channels. In this report, we measured the temperature dependent Li^+ ionic conductivity of $Li_3AlP_3O_9N$ by using ac impedance spectroscopy. The total (bulk + grain boundary) Li^+ conductivity was found to be about 6×10^{-8} S/cm at room temperature, as can be seen in Figure 5.38. This conductivity value is significantly lower than that of $Li_2Mg_2P_3O_9N$, which could be attributed to the much smaller cell volume of $Li_3AlP_3O_9N$ (726.66(1) $Å^3$) relative to that of $Li_2Mg_2P_3O_9N$ (789.88(1) $Å^3$). It is expected that the $Li_3GaP_3O_9N$ or $Li_3InP_3O_9N$ variants could have higher lithium ionic conductivity due to their increased cell dimensions. Indeed, the measured room temperature Li ionic conductivity (bulk + grain boundary) of $Li_3GaP_3O_9N$ reaches 10^{-6} S/cm with activation energy of 0.5 eV, which will be described elsewhere.

5.4 Conclusion

In conclusion, $Li_2Mg_2P_3O_9N$ and $Li_3AlP_3O_9N$ were for the first time synthesized from their sodium analogues $Na_2Mg_2P_3O_9N$ and $Na_3AlP_3O_9N$ using an unconventional intermediate temperature non-molten salt ion exchange method The structures of these novel compounds were determined from synchrotron X-ray and time-of-flight neutron diffraction data, both of which clearly indicated that the Li sites are substantially displaced relative to Na site in their Na-ion analogues. The non-molten salt exchange method was demonstrated to be very well suited to *in situ* experiments, and allowed the first-ever *in situ* neutron of Li/Na ion exchange to be carried out. Both site occupancies and bond distances could be accurately determined using neutron diffraction data collected with modest counting times (~15 min steps) at elevated temperatures (~300 °C). This high quality data showed that the $Na_{2-x}Li_xMg_2P_3O_9N$ solid solution that forms during ion exchange unexpectedly spans two thermodynamically distinct phase transitions (Stage 1a and Stage 1b), resulting in the Li ions first preferentially occupying the Li1 site and then crossing over to preferentially occupy the Li3 site for higher Li contents. The room temperature Li-ion conductivity of this phase is about 10^{-7} S/cm, making this compound promising candidate for fast solid state Li-ion conductor. Both *in situ* XRD and *in situ* TOF neutron diffraction were used to study the Li^+/Na^+ ion exchange of $Na_3AlP_3O_9N$. It was found the ion exchange first happened at Na2 site, and then similar ion exchange behavior was observed for Na1 and Na3 site as that of $Na_2Mg_2P_3O_9N$. The Li-ion conductivity of $Li_3AlP_3O_9N$ was found to be one

order of magnitude lower than that of $Li_2Mg_2P_3O_9N$, presumably due to its smaller cell volume. These non-molten salt methods are generally applicable to the synthesis and *in situ* characterization of solid state compounds with mobile ions.

References

(1) Heitnerw.C; Albuyaro.A *Isr. J. Chem.* **1964**, *2*, 266.
(2) Inoue, Y.; Suzuki, S.; Goto, H. *Bull. Chem. Soc. Jpn.* **1964**, *37*, 1547.
(3) Albertss.J *Acta Chem. Scand.* **1966**, *20*, 1689.
(4) Aiello, R.; Barrer, R. M. *Journal of the Chemical Society a -Inorganic Physical Theoretical* **1970**, 1470.
(5) Yao, Y. F. Y.; Kummer, J. T. *Journal of Inorganic & Nuclear Chemistry* **1967**, *29*, 2453.
(6) Bear, I. J.; Mumme, W. G. *Chem. Commun. (Cambridge, U. K.)* **1968**, 609.
(7) Okeeffe, M. *Science* **1973**, *180*, 1276.
(8) Goodenough, J. B.; Hong, H. Y. P.; Kafalas, J. A. *Mater. Res. Bull.* **1976**, *11*, 203.
(9) Hong, H. Y. P. *Mater. Res. Bull.* **1976**, *11*, 173.
(10) England, W. A.; Goodenough, J. B.; Wiseman, P. J. *J. Solid State Chem.* **1983**, *49*, 289.
(11) Kataoka, K.; Awaka, J.; Kijima, N.; Hayakawa, H.; Ohshima, K.; Akimoto, J. *Chem. Mater.* **2011**, *23*, 2344.
(12) Armstrong, A. R.; Bruce, P. G. *Nature* **1996**, *381*, 499.
(13) Delmas, C.; Braconnier, J. J.; Hagenmuller, P. *Mater. Res. Bull.* **1982**, *17*, 117.
(14) Gaubicher, J.; Wurm, C.; Goward, G.; Masquelier, C.; Nazar, L. *Chem. Mater.* **2000**, *12*, 3240.
(15) Liu, J.; Yu, X. Q.; Hu, E. Y.; Nam, K. W.; Yang, X. Q.; Khalifah, P. G. *Chem. Mater.* **2013**, *25*, 3929.
(16) Lee, M. S.; Kang, J. K.; Kim, S. J. *Bull. Korean Chem. Soc.* **2012**, *33*, 2083.
(17) Massiot, D.; Conanec, R.; Feldmann, W.; Marchand, R.; Laurent, Y. *Inorg. Chem.* **1996**, *35*, 4957.
(18) Conanec, R.; Feldmann, W.; Marchand, R.; Laurent, Y. *J. Solid State Chem.* **1996**, *121*, 418.
(19) Feldmann, W. *Zeitschrift Fur Chemie* **1987**, *27*, 100.
(20) Liu, J.; Yu, X.; Hu, E.; Nam, K.-W.; Yang, X.-Q.; Khalifah, P. G. *Chem. Mater.* **2013**.
(21) Neuefeind, J.; Feygenson, M.; Carruth, J.; Hoffmann, R.; Chipley, K. K. *Nuclear Instruments & Methods in Physics Research Section B-Beam Interactions with Materials and Atoms* **2012**, *287*, 68.
(22) Liu, J.; Whitfield, P.; Saccomanno, M.; Bo, S.-H.; Hu, E.; Yu, X.; Bai, J.; Grey, C.; Yang, X.-Q.; Khalifah, P. In preparation.
(23) Petricek, V.; Dusek, M.; Palatinus, L. *Z. Kristallogr.* **2014**, *229*, 345.
(24) Farrow, C. L.; Juhas, P.; Liu, J. W.; Bryndin, D.; Bozin, E. S.; Bloch, J.; Proffen, T.; Billinge, S. J. L. *Journal of Physics-Condensed Matter* **2007**, *19*.
(25) Zatovsky, I. V.; Vorobjova, T. V.; Domasevitch, K. V.; Ogorodnyk, I. V.; Slobodyanik, N. S. *Acta Crystallogr., Sect. E: Struct. Rep. Online* **2006**, *62*, 32.
(26) Conanec, R.; Lharidon, P.; Feldmann, W.; Marchand, R.; Laurent, Y. *Eur. J. Solid State Inorg. Chem.* **1994**, *31*, 13.

(27) Liu, J.; Chang, D. H.; Whitfield, P.; Janssen, Y.; Yu, X. Q.; Zhou, Y. N.; Bai, J. M.; Ko, J.; Nam, K. W.; Wu, L. J.; Zhu, Y. M.; Feygenson, M.; Amatucci, G.; Van der Ven, A.; Yang, X. Q.; Khalifah, P. *Chem. Mater.* **2014**, *26*, 3295.
(28) Kamaya, N.; Homma, K.; Yamakawa, Y.; Hirayama, M.; Kanno, R.; Yonemura, M.; Kamiyama, T.; Kato, Y.; Hama, S.; Kawamoto, K.; Mitsui, A. *Nat. Mater.* **2011**, *10*, 682.
(29)Murugan, R.; Thangadurai, V.; Weppner, W. *Angewandte Chemie-International Edition* **2007**, *46*, 7778.
(30) Thangadurai, V.; Kaack, H.; Weppner, W. J. F. *J. Am. Ceram. Soc.* **2003**, *86*, 437.
(31) Zhao, Y. S.; Daemen, L. L. *J. Am. Chem. Soc.* **2012**, *134*, 15042.
(32) Shannon, R. D.; Prewitt, C. T. *Acta Crystallographica Section B-Structural Crystallography and Crystal Chemistry* **1969**, *B 25*, 925.
(33) Oszlanyi, G.; Suto, A. *Acta Crystallographica Section A* **2004**, *60*, 134.
(34) Palatinus, L.; Chapuis, G. *J. Appl. Crystallogr.* **2007**, *40*, 786.
(35) Celestian, A. J.; Parise, J. B.; Goodell, C.; Tripathi, A.; Hanson, J. *Chem. Mater.* **2004**, *16*, 2244.
(36) Celestian, A. J.; Kubicki, J. D.; Hanson, J.; Clearfield, A.; Parise, J. B. *J. Am. Chem. Soc.* **2008**, *130*, 11689.

Chapter 6 Understanding the nature of number stacking faults in honeycomb ordered $Na_3Ni_2BiO_6$

6.1 Introduction

Both Li^+ and Na^+ had been used as charge carries for electrochemical energy storage since the early 1980s[1-3], though Li-ion system has attracted much more attention due to its higher energy density[4]. It was not until recently that rechargeable sodium-ion batteries have gained broad interesting due to the lower cost and greater abundant of sodium, which is critical for grid scale electrical energy storage[5]. Although Li^+ and Na^+ showed a variety of similarities as charge carriers[1,2], the tremendous ionic radii difference between Li^+ (0.74 Å) and Na^+ (1.02 Å)[6] often leads to different electrochemical behaviors of these two ions even within similar crystal structure. One well known example is the layered AMO_2 (A= Li^+ or Na^+, M = Cr^{3+}, Fe^{3+}) with α-$NaFeO_2$ type structure, for which, sodium variants $NaCrO_2$[7,8] and $NaFeO_2$[9] can effectively cycle Na^+ in Na-ion batteries in Na-ion batteries while their lithium analogues are barely electrochemical active[8]. Another example is the honeycomb ordered $LiNi_{2/3}Sb_{1/3}O_2$ which showed serious capacity fading after initial charge due to the migration of Ni^{2+} to empty Li^+ site[10], whereas its sodium analogue $NaNi_{2/3}Sb_{1/3}O_2$ has been recently found to be able to work as promising high energy density cathode material for rechargeable sodium ion batteries[11,12]. More recently, our group reported that the electrochemical performance of $NaNi_{2/3}Sb_{1/3}O_2$ is strongly correlated with the stacking faults within the structure. These results motivate us to explore the structure and electrochemical properties of another newly synthesized honeycomb ordered analogue $NaNi_{2/3}Bi_{1/3}O_2$[13].

Honeycomb ordered layered oxides were widely investigated in the last decades due to their interesting magnetic and electrochemical properties[14-18]. These compounds can be written in the standard formula of $AM_{1/3}N_{2/3}O_2$, where A is a monovalent cation such as Li^+, Na^+, K^+, Cu^+ or Ag^+, while M/N can be the combination of monovalent/quadrivalent cation such as Li^+/Mn^{4+} [19], or the combination of divalent/pentavalent cation such as Ni^{2+}/Bi^{5+} in a molar ratio of 2:1[13,20].

To better understand the structure of these honeycomb ordered oxides, the structure relationship between the rock salt structure (e.g. FeO), the ordered O3-type[21] rock salt structure (e.g. α-$NaFeO_2$) and the honeycomb ordered structure (e.g. $NaNi_{2/3}Bi_{1/3}O_2$) is shown in Figure 6.1. Rock salt FeO has ABCABC…cubic close packed (ccp) oxygen ions stacked along [111] direction (in *Fm-3m* configuration), Fe^{2+} fully occupies octahedral interstices formed by these close packed oxygen ions,

forming FeO_6 layers. When Fe^{2+} layers were replaced by half Na^+ and half Fe^{3+} in a layer by layer manner (Figure 6.1b), ordering was then introduced into the structure along c axis direction (or (111) in original *Fm-3m* configuration). The symmetry was then reduced from the original rock salt (*Fm-3m)* to the ordered rock salt with space group *R-3m*, forming the well-known α-$NaFeO_2$ type structure. If the Fe^{3+} layer in α-$NaFeO_2$ is further replaced by 2/3 Ni^{2+} and 1/3 Bi^{5+} in a manner that every Bi^{5+} is surrounded by six Ni^{2+}, as can be seen in Figure 6.1c. A honeycomb ordered Ni^{2+}/Bi^{5+} pattern is then formed within the *ab* plane. Different stacking configurations of these honeycomb ordered layers along *c*-axis direction can result in different types of ordering. Therefore, the key to understand the structure of honeycomb ordered $NaNi_{2/3}Bi_{1/3}O_2$ lies on interpreting different stacking sequences of honeycomb-ordered Ni^{2+}/Bi^{5+} layers along staking direction.

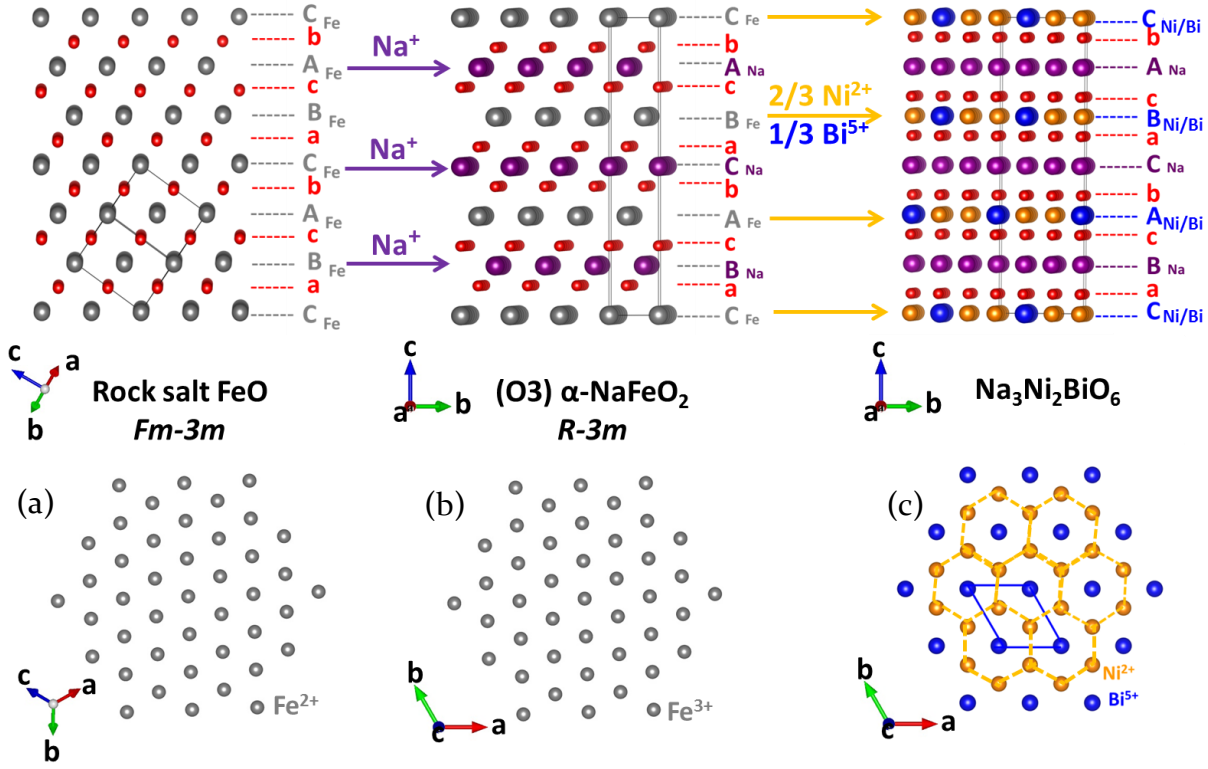

Figure 6.1 (a) Structure of rock salt type FeO. (b) Structure of O3 - type α-$NaFeO_2$ (c) Structure of honeycomb ordered $NaNi_{2/3}Bi_{1/3}O_2$ with hypothetical trigonal $P3_112$ stacking.

It is obvious that the composition and stacking sequences of sodium layers and oxygen layers are exactly the same for both α-$NaFeO_2$ and $NaNi_{2/3}Bi_{1/3}O_2$, the only difference arises from the stacking

configurations of transition metal layers, i.e. Fe^{3+} v.s. ordered Ni^{2+}/Bi^{5+} layer. To better illustrate the difference, the ABCABC… type stacked Fe^{3+} layers and honeycomb ordered Ni^{2+}/Bi^{5+} layers are shown in Figure 6.2a. For an A layer, it can be seen that Fe^{3+} has only one crystallographic distinct site, while the honeycomb ordered Ni^{2+}/Bi^{5+} have three crystallographic distinct sites, which will be labeled as 1, 2 and 3. Therefore, three different types of Ni^{2+}/Bi^{5+} configurations can be generated, which will be labeled as A_1, A_2 and A_3 with the subscripts refer to the sites that Bi^{5+} occupies. As mentioned previously, both structures (α-$NaFeO_2$ and $NaNi_{2/3}Bi_{1/3}O_2$) have cubic close packed layers, thus the three possible translation vectors that can be used to translate each two layers, e.g. A to B, B to C or C to A are (1/3,0,1/3), (0,1/3,1/3) and (1/3, 1/3, 1/3). For Fe^{3+} layers, it can be seen that all three translation vectors will translate an A layer to a unique B layer and a B layer to a unique C layer. However, for a honeycomb ordered Ni^{2+}/Bi^{5+} A_1 layer, (1/3, 0, 1/3) will translate it to a B_1 layer, while (0, 1/3, 1/3) will translate it to a B_2 layer and (2/3, 2/3, 1/3) will generate B_3 layers. Therefore, a total of three different configurations can be generated for the honeycomb B layer. Similarly, three different honeycomb-ordered C layers can be generated. Thus, there is only one ABC stacking sequence for Fe^{3+} layers in α-$NaFeO_2$, whereas a total of 27 (3×3×3) different $A_xB_yC_z$ (x=1,2,3; y=1,2,3;z=1,2,3) stacking sequences can be generated from honeycomb ordered Ni^{2+}/Bi^{5+} layers in $NaNi_{2/3}Bi_{1/3}O_2$.

The next question is how many different crystal structures can be generated from these 27 different stacking sequences of $NaNi_{2/3}Bi_{1/3}O_2$? To better illustrate this, let's set the three translation vectors as = $t_{\vec{a}}$ = (1/3,0,1/3), $t_{\vec{b}}$ = (0,1/3,1/3) and $t_{\vec{u}}$ = (-1/3,-1/3,1/3). It can be seen that the combination of identical translation vectors, such as$t_{\vec{a}}$ $t_{\vec{b}}$ $t_{\vec{u}}$, will lead to the formation of a mirror plane along the translation directions (Figure 2b). The combination of different translation vectors, such as $t_{\vec{a}}$ $t_{\vec{b}}$ $t_{\vec{u}}$, results in the formation of 31 screw axes along stacking direction (*c*-axis direction). The space groups for these two different stacking can be assigned to *C2/m* and $P3_112$ separately, as can be seen in Figure 1c. It can be seen that 1/3 (9) out of the 27 different stacking configurations belong to C2/m space group whereas the other 2/3 (18) have the $P3_112$ space group. Detailed translation vector configurations can be found in Table 6.1.

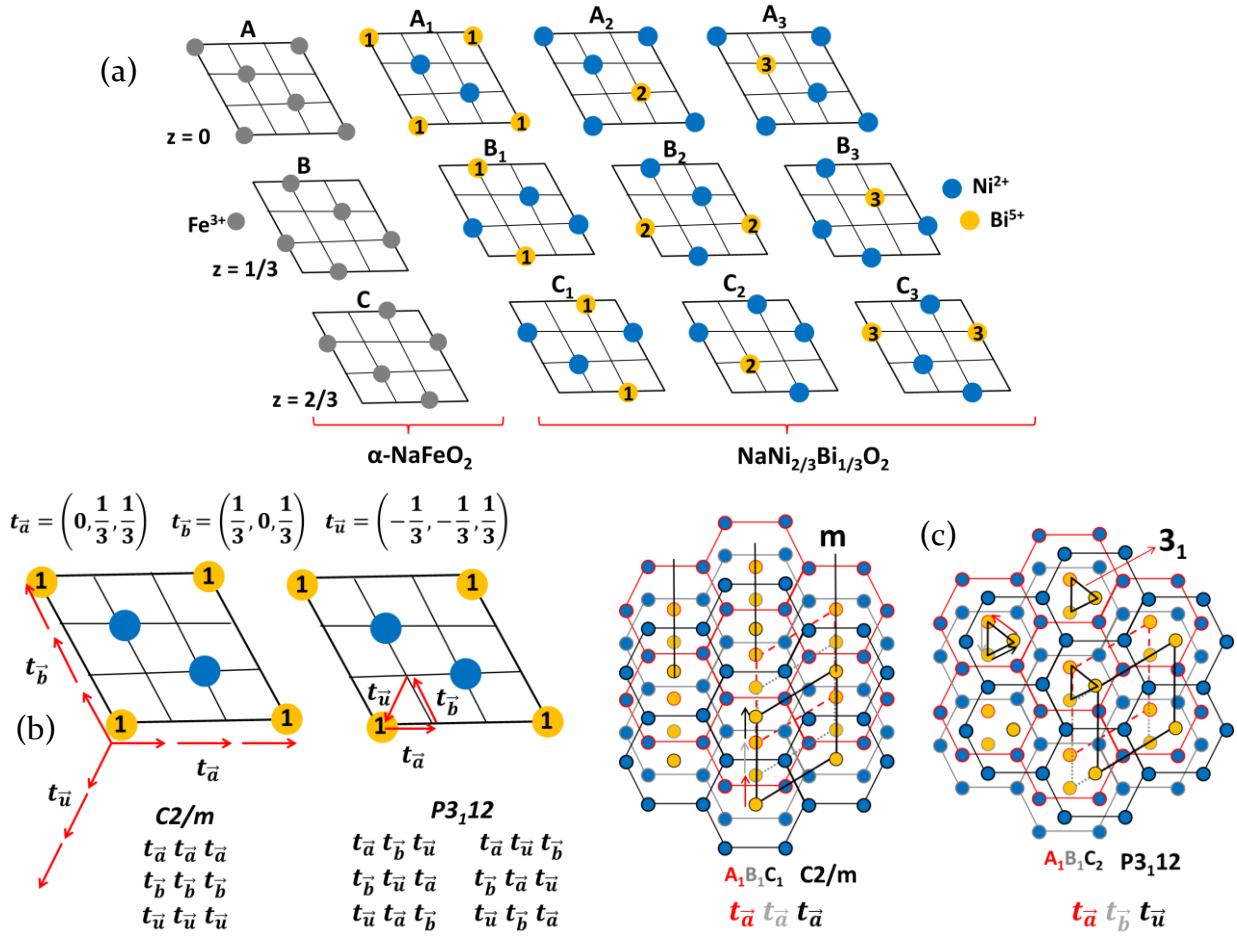

Figure 6.2 (a) Comparison of transition metal site configurations between α-$NaFeO_2$ and honeycomb ordered $Na_3Ni_2BiO_6$. (b) and (c) Two possible stacking configurations (*C2/m* and *$P3_112$*) for the combination of 3 honeycomb ordered Ni/Bi layers, this figure is redrawn based on J. Breger et al[22].

Table 6.1 27 possible stacking sequences for a 3 layered $NaNi_{2/3}Bi_{1/3}O_2$ cell

C2/m	$P3_112$
$t_{\vec{a}}t_{\vec{a}}t_{\vec{a}}$ $t_{\vec{b}}t_{\vec{b}}t_{\vec{b}}$ $t_{\vec{u}}t_{\vec{u}}t_{\vec{u}}$	$t_{\vec{a}}t_{\vec{b}}t_{\vec{u}}$ $t_{\vec{a}}t_{\vec{u}}t_{\vec{b}}$ $t_{\vec{b}}t_{\vec{a}}t_{\vec{u}}$ $t_{\vec{b}}t_{\vec{u}}t_{\vec{a}}$ $t_{\vec{u}}t_{\vec{a}}t_{\vec{b}}$ $t_{\vec{u}}t_{\vec{b}}t_{\vec{a}}$
A1B1C1 A2B2C2 A3B3C3 A1B2C3 A1B3C2 A2B1C3 A2B3C1 A3B1C2 A3B2C1	A1B1C2 A1B1C3 A1B2C1 A1B2C2 A1B3C1 A1B3C3 A2B1C1 A2B1C2 A2B2C1 A2B2C3 A2B3C2 A2B3C3 A3B1C1 A3B1C3 A3B2C2 A3B2C3 A3B3C1 A3B3C2

Interestingly, for an ideal cubic close pack (ccp) stacking without real monoclinic distortion (when monoclinic β angle is equal to $\pi - \cos^{-1}\frac{a_{mon}}{c_{mon}}$), the monoclinic *C2/m* cell can be redrawn into a larger trigonal cell (Figure 6.3), which will make the comparison between these two stacking configurations (monoclinic v.s. trigonal) more convenient. It should also be noticed that more complicated stacking schemes can be generated if the 3 layered blocks are combined with different ones, resulting in an one dimensional (along stacking direction) stacking faults in this type of material, which is often referred as coloring faults[23]. Although this type of stacking faults have been previously observed in various honeycomb ordered oxides, such as Li_2MnO_3[22] and $NaNi_{2/3}Sb_{1/3}O_2$[12], the detailed faulting schemes are still under debate[16,24]. Therefore, a quantitatively study is in urgent need for clarity.

The present article will focus on understanding and quantifying the coloring faults in "ordered" and "disordered" polymorphs of honeycomb ordered $NaNi_{2/3}Bi_{1/3}O_2$. It is expected that these studies will aid our understanding of other technologically important honeycomb ordered oxides, such as Li_2MnO_3[25] and related Li-rich cathode materials[26,27]. Electrochemical performances of these two polymorphs as cathode materials for rechargeable Na-ion batteries will be addressed in the last part.

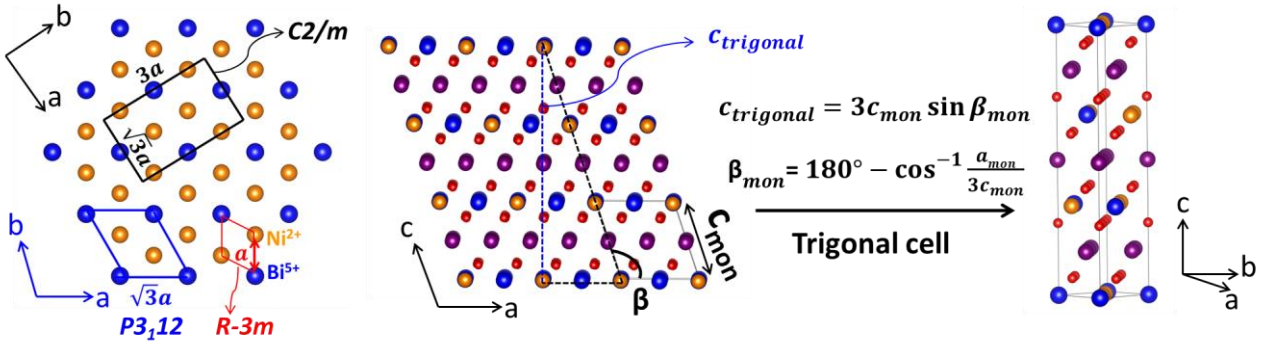

Figure 6.3 (a) two different types of super cell that can be used to describe in plane honeycomb ordering of Ni/Bi. (b) For an ideal ccp stacking without real monoclinic distortion, the monoclinic super cell can be redrawn into a larger trigonal cell.

6.2 Experimental parts

6.2.1 Synthesis of $Na_3Ni_2BiO_6$

The same synthetic method with different starting materials was used to synthesize two polymorphs of powder $Na_3Ni_2BiO_6$. For the first polymorph (which will be referred as "disordered" in the later

sections), stoichiometric amount of anhydrous Na_2CO_3 (EMD, pre-dried), NiO (Sigma-Aldrich, 99.9%) and Bi_2O_3 (Alfa Aesar, >99%) were ball milled in a vibratory mill for 2 hours. A thin layer of the well mixed powder was then placed on an alumina boat. The boat was transferred into a mullite tube inside a horizontal tube furnace (Mellen, SV Series). The sample was heated up to 720 °C with a ramp rate of 200 °C/h, and was held at this temperature for 12 hours before cooling down to room temperate at furnace cooling rate, the whole process was carried out under the flowing of O_2 gas. The obtained dark yellow powder was well ground by using mortar and pestle and then transferred to glass vials and stored in desiccator for further structure and electrochemical characterization. The second polymorph, which will be referred as "ordered" phase, was synthesized at the same conditions as those for the "disordered" phase except that Bi_2O_3 has been replaced by $NaBiO_3$ (CHEM-IMPLEX). The final product for the "ordered" phase was found to be yellow powder.

6.2.2 X-ray diffraction

Laboratory X-ray diffraction data of $Na_3Ni_2BiO_6$ powder samples are collected on a Bruker Advanced D8 diffractometer using Cu K_α radiation from a fine focus X-ray tube ($K_{\alpha1}$ = 1.54053 Å, $K_{\alpha2}$ = 1.54431 Å) The system was operated at a 217.5 mm working radius with a 1D position-sensitive LynxEye Si detector with 192 channels, data was collected between 8° and 100° with a step size of 0.02°/step and a scan speed of 2 second/step. Synchrotron X-ray powder diffraction data was collected at XPD beamline at NSLSII, Brookhaven National Laboratory with a 2D area detector and a wavelength of 0.1878Å. For data collection, powder sample was packed into a 0.8 mm diameter Kapton capillary and rotated at a speed of 1 rad/s. The data collection time was 1s/image and a total of 60 images were collected for one data set. A Ni standard data was also collected and used as calibrant to calibrate the sample to detector distance, beam center position and tilting angles. The as collected image data was calibrated and integrated in the Fit2D software[28]. High resolution synchrotron X-ray diffraction data was collected at 11-BM beamline at Argonne National Laboratory with linear detector and a wavelength of 0.41398 Å, detailed information about the instrument configuration can be found in the beamline homepage. Further refinement of the collected diffraction data was carried out using TOPAS software (Version 4.2. Modeling the stacking faults of "disordered" sample was carried out in two manners: first, a $Na_3Ni_2BiO_6$. supercell constructed from 31 blocks (along c axis) of 3 layered trigonal cells was obtained from counting of corresponded HRTEM images, details can be found in discussion part, this

supercell was used as an initial model for Rietveld refinement, which was also carried out using TOPAS software (Version 4.2); second, a translation vector probability method was utilized, this was carried out using Faults program[29], detailed refinement procedure and results will be presented later.

6.2.3 SEM

Scanning electron microscopy images of as-prepared $Na_3Ni_2BiO_6$ powders were collected on JEOL 7600, to minimize charge effects, the data was collected at high vacuum (pressure) and low voltage (5 KV).

6.2.4 Electrochemistry

Performances of both ordered and disordered samples as cathode materials for Na-ion batteries were evaluated in CR2025 type coin cells. For cathode electrode preparation, active material (ordered or disordered $Na_3Ni_2BiO_6$) were first hand ground for 30 min, and then mixed with acetylene black in a mass ratio of 7:2, the mixture was further ground for about 30 min and then mixed with polyvinylidene difluoride (PVDF) in a mass ratio of 9:1. The mixture was further ground for about 10 min and then appropriate amount of 1-methyl-2-pyrrolidinone (NMP) was added into the mixture to form a thick slurry, this thick slurry was then recovered from the mortar and casted onto an Al foil by using a doctor blade to control the thickness to about 40 μm, the electrode was then dried in a vacuum oven at 100 °C for 12 hours. The dried electrode foil was then punched into ¾'' diameter discs, the active material loading was around 4-5 mg/disc. Metallic sodium was used as anode and saturated $NaClO_4$ in 1:1 (volume ratio) EC/DMC was used as electrolyte. Galvanostatic cycling of corresponded coin cells were carried out at C/30 rate at 20 ° on Lander cycler. Cyclic voltammetry (CV) tests were carried out on Biologic VSP with scan rate of 5 mV/s. Galvanostatic intermediate titration technique (GITT) data of ordered phase was collected on Lander cycler, the cell was charged/discharged for one hour and then relaxed for 15 hours with a totalcharge/discharge rate of about C/320.

6.2.5 X-ray absorption (XAS)

Ni K-edge X-ray absorption (XAS) spectra of ordered and disordered phase were collected at X-18A beamline at NSLS, Brookhaven National Laboratory and BL2-2 of the Stanford Synchrotron Radiation Lightsource, SLAC National Accelerator Laboratory in a transmission model. The beam intensity was detuned to 60% to minimize the high-order harmonics. Reference spectrum of Ni foil was collected

simultaneous as energy calibrant. XANES and EXAFS spectra were first processed using the Athena software package[30]. AUTOBK code was used to normalize corresponded absorption coefficient. The corresponded EXAFS signal $\chi(k)$ was further weighted by k^3 to emphasize the signer character and then Fourier transferred into real space. Fitting of EXAFS data was carried out using Artemis software package[30], initial model from *R-3m, C2/m* and $P3_112$ were used to generate specific atomic pairs by using FEFF6 package[31], fittings were carried out between 1.0 Å and 3.5 Å in real space.

6.2.6 Pair distribution function (PDF)

X-ray pair distribution function (PDF) was collected at XPD beamline at NSLSII, Brookhaven National Laboratory, with a wavelength of 0.1878 Å. Powder samples was packed into a 0.8 mm Kapton capillary and mounted onto a goniometer and rotated at a speed of 1 rad/s. A ccd camera was used as 2D area detector, the sample to detector distance was set to about 300 mm. Standard Ni powder was used as calibrant and an empty Kapton scan was used as background. A data collection speed of 1 image/second was used with a total of 60 images/data set. Fit2D software[28] was used to convert the recorded 2D images into 1D diffraction patterns. The obtained diffraction data was further converted into pair distribution function using PDFgetX3[32]. Fitting of corresponded PDF data was carried out in PDFgui software [33] with initial crystal structure model obtained from Rietveld refinement of corresponded diffraction data. PDF pattern was divided into two different regions, one from 1.2 Å to 16 Å and the other from 16 Å to 30 Å, to evaluate the short range (~ 1 block of 3 layered cell) and medium range (~ 2 blocks of 3 layered cell) structures, Q_{broad} and Q_{damp} was fixed to the value obtained from refinement of Ni standard sample. Atomic positions and isotropic atomic displacements were refined simultaneously until the refinement converged.

6.3 Results and discussion

6.3.1 Synthesis of "ordered" and "disordered" $Na_3Ni_2BiO_6$

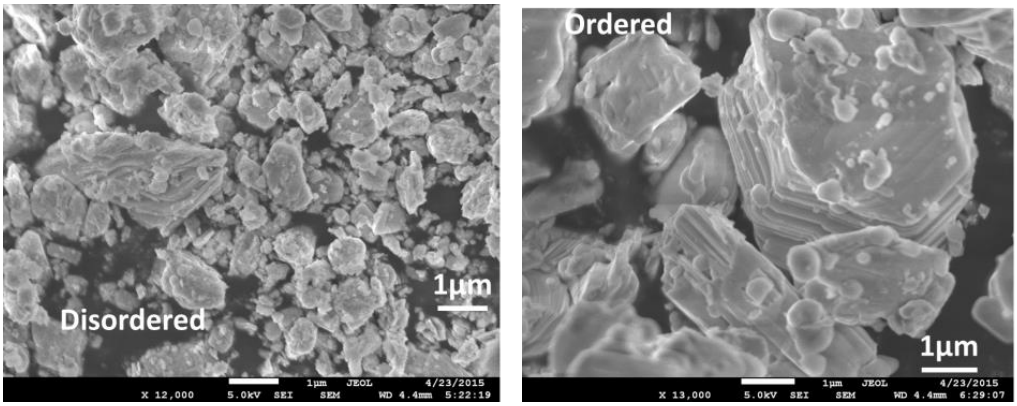

Figure 6.4 SEM images of samples synthesized from Bi_2O_3 (left, disordered) and $NaBiO_3$ (right, ordered).

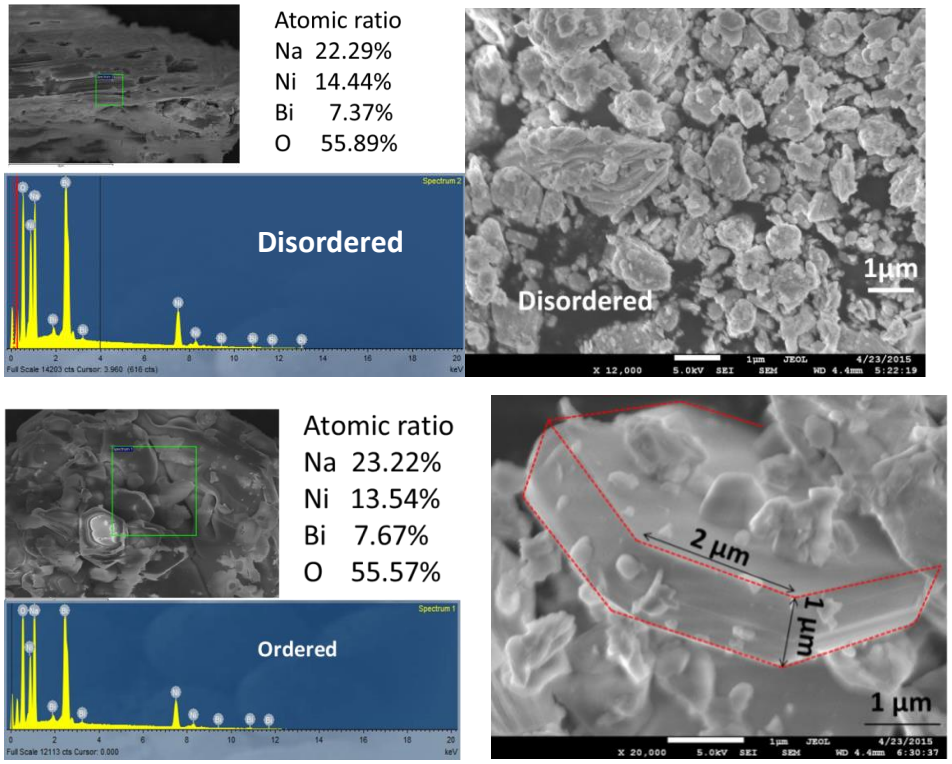

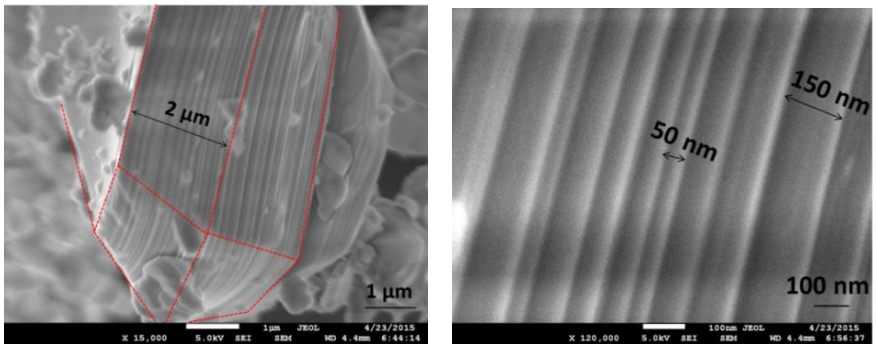

Figure 6.5 (Top) SEM images and EDX spectra of "disodered" $Na_3Ni_2BiO_6$. (Bottom) SEM images and EDX spectra of "ordered" $Na_3Ni_2BiO_6$, which clearly showed the stacking of multiple layers of hexagonal shaped plates.

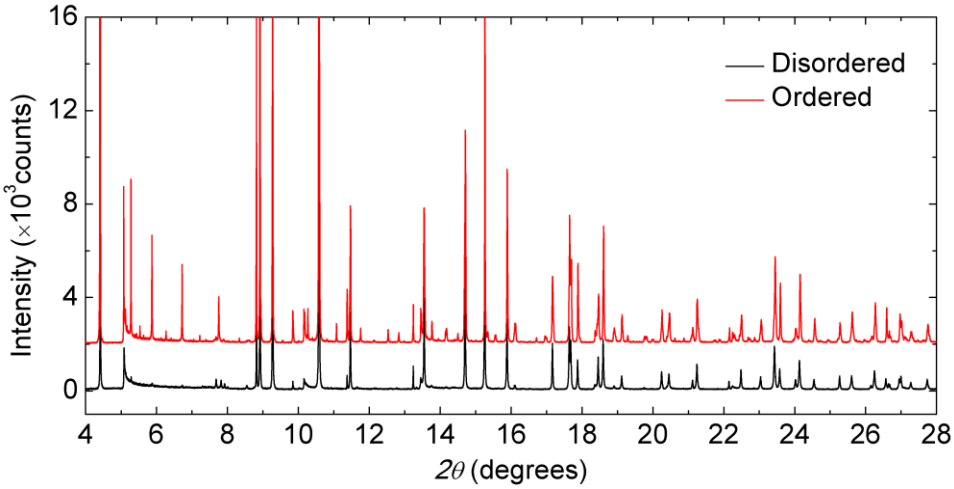

Figure 6.6 Synchrotron XRD data of disordered (black) and ordered (red) $Na_3Ni_2BiO_6$.

Two different polymorphs of $Na_3Ni_2BiO_6$ can be synthesized at the same reaction conditions when different Bi sources are used. The sample synthesized from Bi_2O_3 (disordered) was found to be dark yellowish powder while the one synthesized from $NaBiO_3$ (ordered) was brighter yellow colored. SEM images and EDX patterns of these two samples are shown in Figure 6.5. Although these two samples were prepared at the same temperature, their morphologies are substantially different. The sample synthesized from Bi_2O_3 lacks facets and has particle sizes varying from hundreds of nanometers to several microns. In contrast, the sample synthesized from $NaBiO_3$ is well crystallized with large hexagonal shaped plates which have vertical striations in thickness ranging from tens to hundreds of

nanometers, as can be seen in Figure 6.5. The enhanced crystallinity of the sample synthesized from $NaBiO_3$ suggests the difference of ordering is more likely to be kinetic instead of thermodynamic.

Based on X-ray diffraction data (Figure 6.6) of these two polymorphs, *R-3m* subcell predicts the location of the intense peaks in both ordered (synthesized from $NaBiO_3$) and disordered (synthesized from Bi_2O_3) phases, and these major peaks also have similar relative intensities in both polymorphs. However, significant difference arises from the super lattice peak regions. The XRD data of the sample synthesized from $NaBiO_3$ showed well-defined super lattice peaks, while the one synthesized from Bi_2O_3 only showed a broad diffuse scattering peak with very weak super lattice peak character. For clarity, from here on, we will name the sample with well-defined super lattice diffraction peaks (synthesized from $NaBiO_3$) the "ordered" phase while the one with broad diffuse diffraction peaks (synthesized from Bi_2O_3) the "disordered" phase. Interestingly, both "ordered" and "disordered" phases were synthesized at the same condition (same annealing temperature and time, same cooling rate etc.), and they also showed quite similar sodium concentration as confirmed by corresponded EDX data (Figure 6.5). Therefore, this "ordered" – "disordered" difference is unlikely to be driven by sodium concentration variation as previously reported for $Na_3Ni_2SbO_6$[12] and Li_4FeSbO_6[34].

6.3.2 Structure of "ordered" $Na_3Ni_2BiO_6$

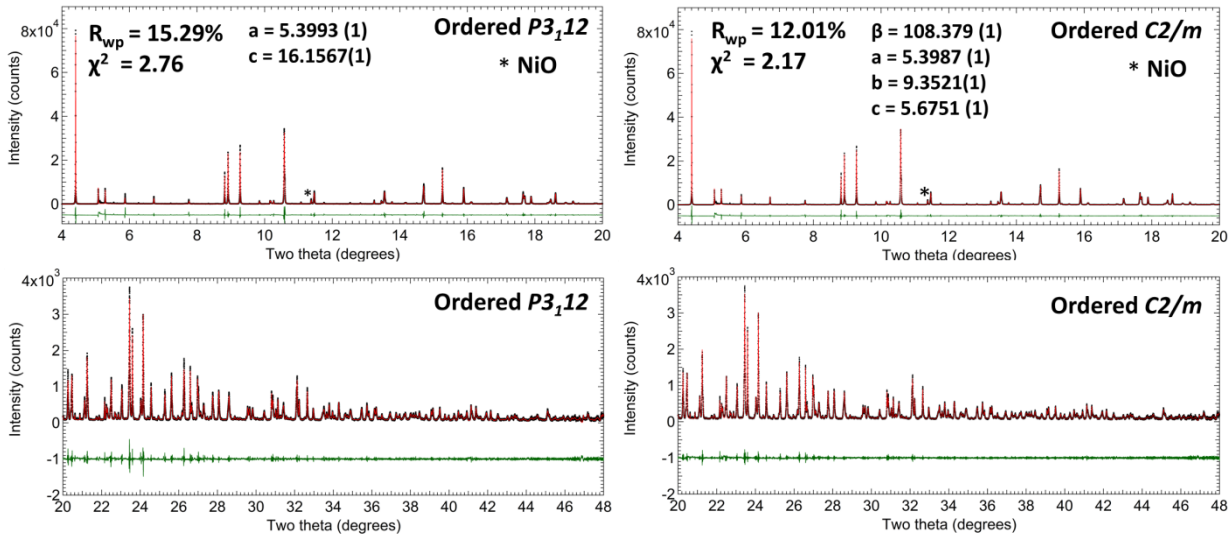

Figure 6.7 Le Bail fits of synchrotron XRD data of "ordered" $Na_3Ni_2BiO_6$ with *C2/m* and *$P3_112$* model.

The XRD pattern of the "ordered" $Na_3Ni_2BiO_6$ showed well-defined super lattice diffraction peaks, as can be seen in Figures 6.6 to 6.8, indicating that a normal super structure model is adequate to describe the structure. Therefore, both monoclinic stacked *C2/m* model and trigonal stacked $P3_112$ model are used in Le Bail fits[35]. The refinement results are shown in Figure 6.7. It has been found that *C2/m* model can fit the pattern substantially better than $P3_112$ model, as can be judged from the corresponded difference curves and R_{wp} values. This has been further confirmed by the refined β angle (108.379(1)°) of the *C2/m* model, which varies substantially from the ideal angle ($= \pi - \cos^{-1}\frac{a_{mon}}{c_{mon}} =$ 108.488°) of a corresponded pseudo trigonal unit cell. Therefore, *C2/m* model was chosen for further Rietveld refinement.

It should be noted that a Ni/Bi site mixing is introduced and refined during Rietveld refinement. This is not a real site mixing but instead reflects the influence of stacking faults in violating the translational expected for the ideal average structure[13,23]. Based on refinement result shown in Table 6.2, a total of 12 % Ni^{2+}/Bi^{5+} mixing are needed to provide the best fit. In the previous report[13], a 18% mixing was reported, suggesting that different preparations have different degrees of order, as is expected for a kinetically limited process. This refinement result indicates the existence of substantial fraction of stacking faults even within the "ordered" $Na_3Ni_2BiO_6$. Interestingly, a close inspection of the diffraction pattern between 4.8° and 8.4° reveals the existence of a series of weak diffraction peaks that cannot be indexed by a single 3 layered block. Instead, 6 layered and 18 layered cells are required to fully index all minor diffraction peaks, indicating more complicated stacking schemes existed within the as-prepared "ordered" sample. These large superstructures provide additional evidence for stacking faults, which are expected to statistically give rise to a variety of local stacking sequences.

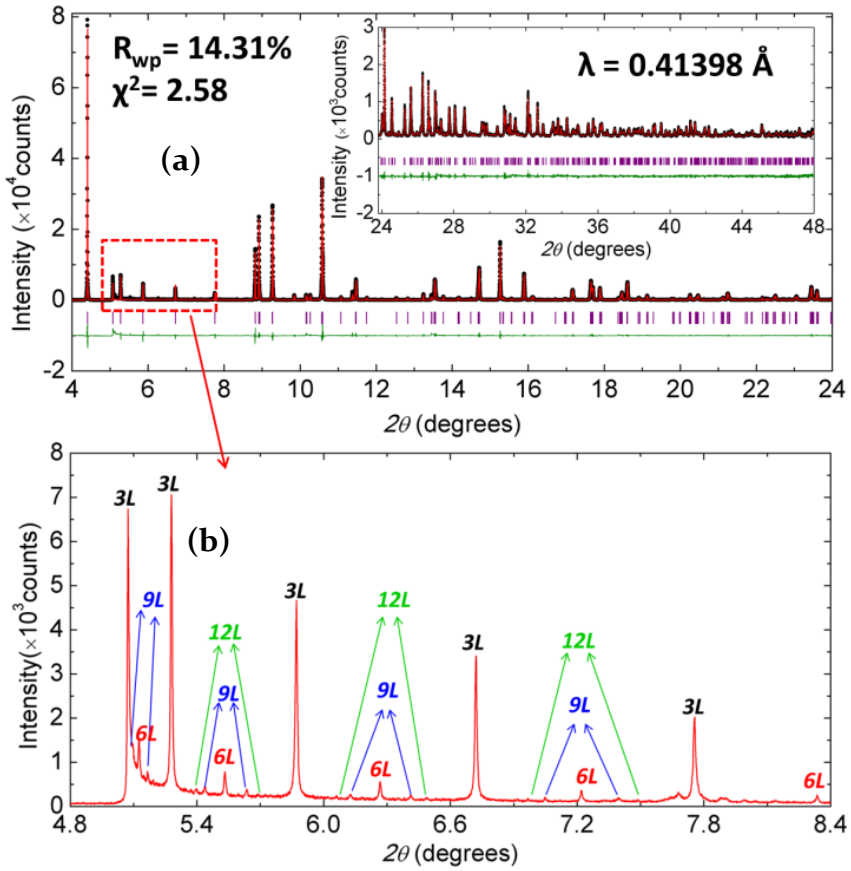

Figure 6.8 (a) Rietveld refinement of synchrotron XRD data of "ordered" $Na_3Ni_2BiO_6$ with *C2/m* model. (b) Enlarged region showed extra diffraction peaks that are associated with 6 (a × b× 2c) and 18 (a × b× 6c) layered super structure.

Table 6.2 Crystal structure of "ordered" $Na_3Ni_2BiO_6$ from Rietveld refinement of synchrotron XRD data (λ = 0.41398 Å).

S.G. C2/m a = 5.3989(1) Å b = 9.3525(1) Å c = 5.6751(1) Å β = 108.380(1) °						
Atom	Wyck.	*x*	*y*	*z*	Occ.	B_{iso} (Å^2)
Bi1	2a	0	0.5	0	0.749(1)	0.3
Ni1	2a	0	0.5	0	0.251(1)	0.3
Bi2	4g	0	0.1656(1)	0	0.126(1)	0.3
Ni2	4g	0	0.1656(1)	0	0.874(1)	0.3
Na1	2d	0	0	0.5	1	0.25(5)
Na2	4h	0	0.6674(4)	0.5	1	1.30(4)
O1	4i	0.2324(9)	0	0.2088(7)	1	0.28(7)
O2	8j	0.2379(7)	0.3328(4)	0.2036(4)	1	0.20(4)

Electron diffraction and high resolution TEM (HRTEM) can provide comprehensive structure information of different regions of the sample. Electron diffraction patterns were taken for a hexagonal plate, as can be seen in Figure 7a – 7d. They clearly show that the diffraction spots collected along $[001]_p$ zone axis cannot be fully indexed with a simple R-3m space group (α-$NaFeO_2$). Instead, a $\sqrt{3}$ a× $\sqrt{3}$ a super cell is needed to fully index extra diffraction spots, confirming that Ni^{2+} and Bi^{5+} is well ordered within the honeycomb layer. The diffraction peaks in $[100]_p$ zone also showed well defined periodicity without obvious streaking along *c*-axis, indicating that honeycomb ordered Ni/Bi layers are well stacked along c-axis direction with a periodicity of 3 layers. Since both monoclinic stacking (*C2/m*) and trigonal stacking ($P3_112$) should result in well-ordered honeycomb layers along *c*-axis with periodicity of three layers, it would be difficult to distinguish them by simply examining electron diffraction patterns. Therefore, HRTEM images are collected for clarity. By carefully examining these two types of stacking configurations (*C2/m* versus $P3_112$) along different direction, it has been found that projection along $[010]_p$ direction (or *b*-axis direction) would be most suitable viewing direction to distinguish these two types of stacking, as demonstrated in Figure 6.10. It can be seen that for *C2/m* type stacking, all Bi atoms will project onto either the diagonal or the edge of c (or c*) axis; whereas for the $P3_112$ type stacking, one Bi atom will project into a zig-zag manner due to the existence of 3_1- fold along c axis direction. It can be seen in Figure 6.9e that one selected region (20.5 nm ×10.5 nm) is perfectly monoclinic *C2/m* stacked. In the second region (13.7 nm ×13.7 nm, Figure 6.9f), there is a small portion of trigonal stacked ($P3_112$) regions although majority parts are *C2/m* stacked. This result is consistent with the presence of stacking faults as shown in our Rietveld refinement of synchrotron XRD data. Higher synthetic temperature and longer annealing time may help to further reduce the stacking faults, but it would be slow to fully diminish this type of layer mismatch. It is worth to note that $Na_3Ni_2BiO_6$ will decompose at temperatures higher than 800 ℃.

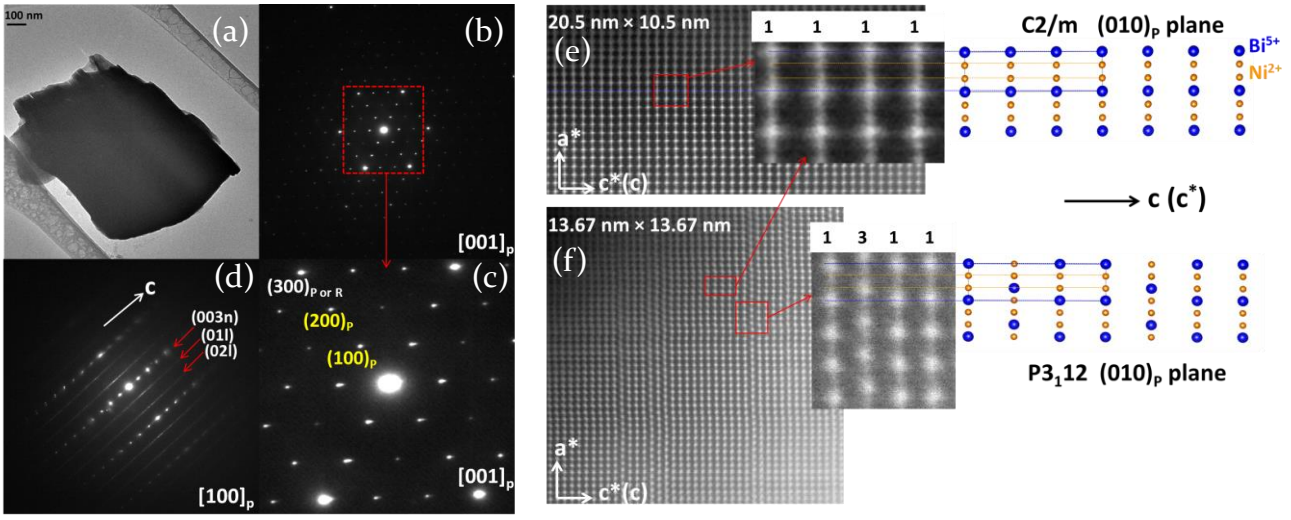

Figure 6.9 (a)-(d) SAED of "ordered" $Na_3Ni_2BiO_6$, electron diffraction were taken on $[100]_p$ and $[001]_p$ zone axis direction. (e)-(f) HRTEM images of two different regions of "ordered" $Na_3Ni_2BiO_6$, Bi atoms are appeared as big white spots whereas Ni atoms are much weaker. It can be seen that Ni/Bi honeycomb layers are well stacked in *C2/m* manner in (d) region, but small portion of *P3₁2* type stacking existed in (e) region.

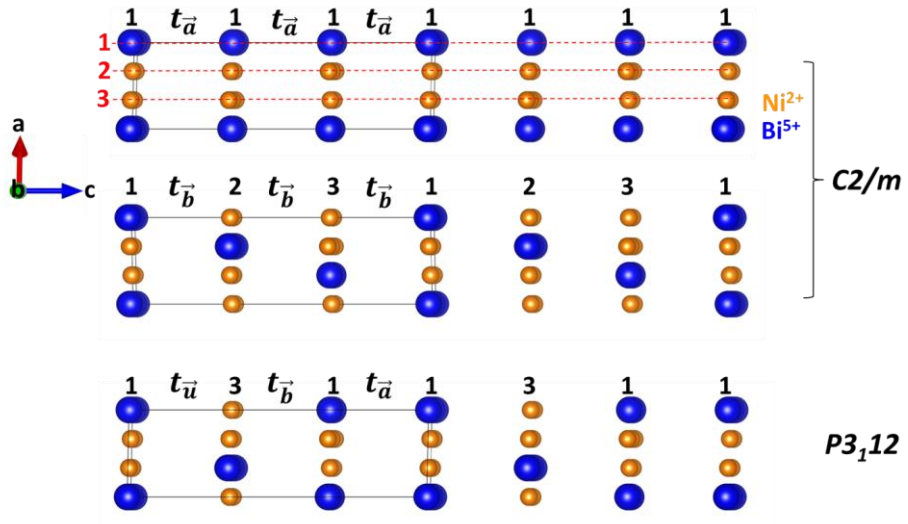

Figure 6.10 Top, two *C2/m* stacking configurations (111 and 123) viewed along b-axis direction in trigonal configuration, it should be noticed that other *C2/m* stacking sequences will show the same stacking character with only a rotation of the mirror plane. Bottom, two *P3₁12* stacking configurations (131) viewed along b-axis direction, the zig-zag distribution of Bi atoms (blue) is due to the existence of 3_1-fold along c axis direction. All Na and O atoms are ommited for clearance.

6.3.3 Structure of "disordered" $Na_3Ni_2BiO_6$

The XRD pattern of "disordered" $Na_3Ni_2BiO_6$ does not exhibit well-defined super lattice diffraction peaks, but instead has very broad asymmetrical diffuse peaks. This indicates disorder in the as-prepared "disordered" sample. It should be noticed that this disorder may arise from either the disorder of Ni/Bi within honeycomb layer or from the stacking disorder of well-ordered honeycomb ordered layers along c axis direction (number faults). One way to examine the in plane honeycomb ordering is by probing the local structure of the as-prepared compound. Thus, Ni K-edge EXAFS data was collected with corresponded fittings with three different structure models shown in Figure 6.11, it can be seen that models (*C2/m* or *P3₁12*) with in plane Ni/Bi honeycomb ordering can fit the spectrum better than that of a random Ni/Bi distribution model (*R-3m*). All three models effective fit the Ni-O first shell, indicating that NiO_6 octahedra is essentially well maintained. However, difference arises for the fitting of the second and third shells: R-3m model is not adequate to model these Ni-Ni, Ni-Bi and Ni-Na shells; While the ordered *C2/m* and *P3₁12* can fit these peaks well, indicating Ni/Bi is essentially well ordered within the honeycomb layer of this "disordered" polymorph.

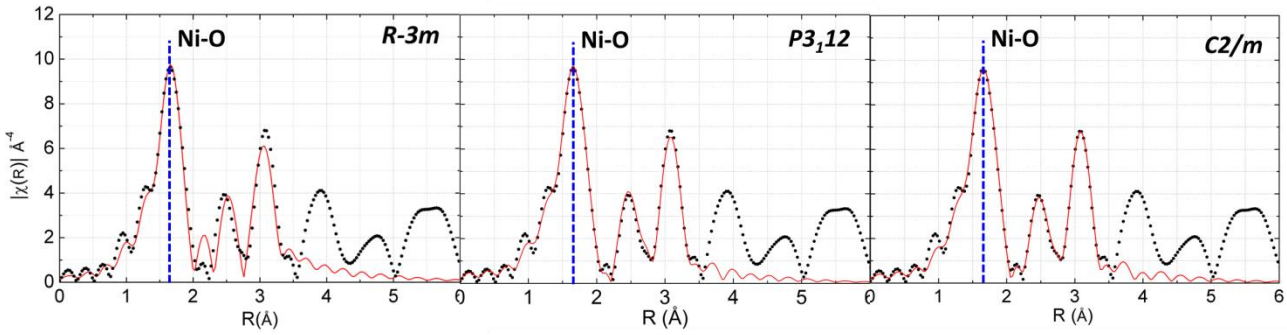

Figure 6.11 Fit of Ni K-edge EXAFS data of "disordered" $Na_3Ni_2BiO_6$ with Ni/Bi randomly distributed *R-3m* model, Ni/Bi honeycomb ordered *P3₁12* and *C2/m* models. All three models can provide essentially good fit for the first Ni-O shell. However, only the honeycomb ordered *P3₁12* and C2/m can provide adequate fit for the second and third shells.

EXAFS is a powerful elemental selective tool to probe local structures. However, it can only provide structure information up to several angstroms due to the nature of this technique. Whereas pair distribution function (PDF) can provide structure information up to tens of angstroms, and thus can provide more accurate local and intermediate structural information. Considering the huge difference of X-ray scattering factors between Ni and Bi, it shall be relatively easy to distinguish Ni/Bi

ordering/disordering by analyzing corresponded X-ray scattering data. Thus, high quality X-ray PDF data of disordered sample was collected at XPD beam line at NSLSII, detailed data collection information can be found in the experimental part. Similar to EXAFS fitting, three different structure models were used to fit the PDF pattern up to 16 Å (~ a cell length in trigonal configuration with three honeycomb layers), as can be seen in Figure 6.12. It clearly shows that *C2/m* and *P3$_1$12* with honeycomb ordered Ni-Bi layer provides better fit than that of *R-3m* with randomly distributed Ni/Bi. Interestingly, it can be seen the biggest difference among these fittings arises from the peak at about 5.3 Å: *C2/m* and *P3$_1$12* with in plane honeycomb ordered Ni/Bi can fit this peak quite well, whereas *R-3m* model fails to capture the full intensity. This ~5.3 Å peak is associated with the second nearest metal-metal pairs (Ni/Bi or Na-Na) within the ab plane, which is also equal to the unit cell parameter (a = b = 5.3Å) of the $\sqrt{3}a \times \sqrt{3}a$ supper cell in trigonal configuration. For PDF modeling, we used the following equation to calculate the *reduced pair distribution function* (G(r)) from an initial structural model[36] :

$$G(r) = \frac{1}{r}\sum_{m}\sum_{n}\frac{f_m f_n}{< f >^2}\,\delta(r - r_{mn}) - 4\pi r\rho_0$$

Where f_m and f_n are the corresponded X-ray forming factor of the *m*th and *n*th atom, <f> is the average X-ray scattering factor of all atoms in the formula, r_{mn} is the distance between the *m*th and *n*th atom, ρ_0 is the number density of atoms and δ is the Dirac delta function. For the specific case here, Na-Na pairs should contribute equally in all three cases (*R-3m*, *C2/m* and *P3$_1$12*), thus, only Ni/Bi pairs will be counted. Therefore, f_m and f_n should be f_{Bi} and f_{Ni} separately, r_{mn} should be the distance for second nearest Ni/Bi pairs. The X-ray scattering factor of Bi (f_{Bi}) is much larger (considering the Z contrast, ~3 times should be a good approximation) than that of Ni (f_{Ni}), thus the total $f_m f_n$ term in honeycomb ordered configuration should be proportional to ($1/3\ f_{Bi}^2 + 2/3\ f_{Ni}^2$), which should be much larger than that of ($1/9\ f_{Bi}^2 + 4/9\ f_{Ni}^2 + 4/9\ f_{Ni}f_{Bi}$) in a randomly distributed *R-3m* model. Therefore, the calculated *G(r)* value for this ~5.3 Å peak from an *R-3m* model should be much weaker than that from honeycomb ordered *C2/m* or *P3$_1$12* model, which is indeed what we have observed. This result confirms that Ni/Bi is honeycomb ordered within the "disordered" $Na_3Ni_2BiO_6$. This has been further confirmed by the appearance of $\sqrt{3}a \times \sqrt{3}a$ super structure diffraction spots in corresponded TEM SAED pattern, as can be seen in Figure 12.

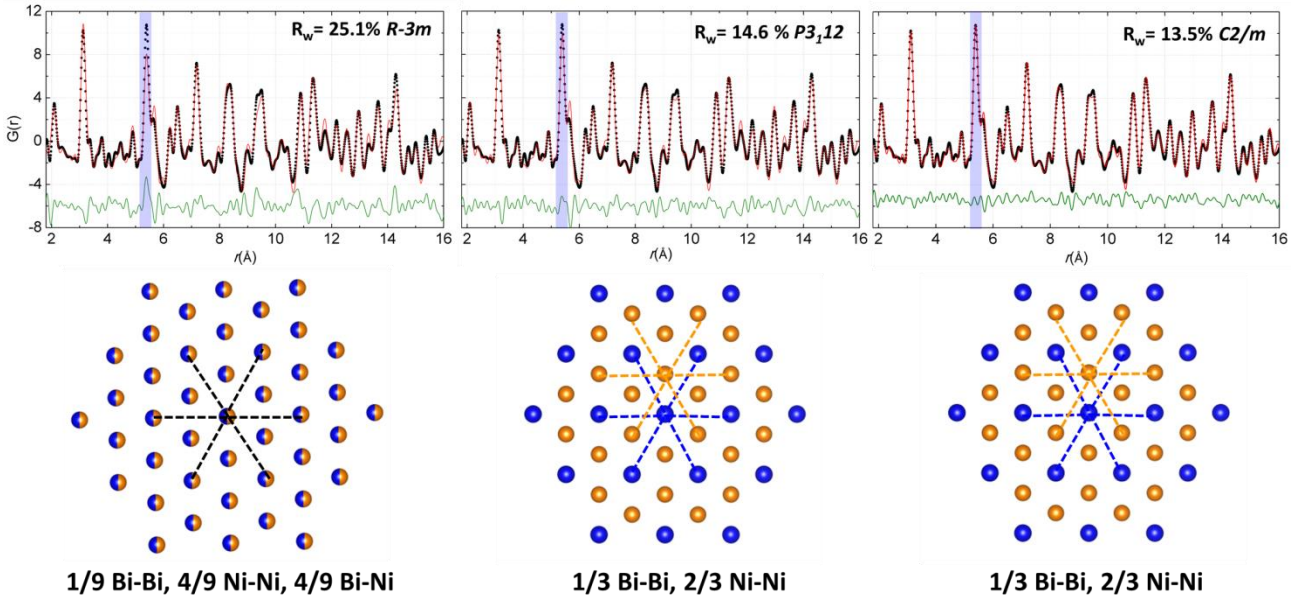

Figure 6.12 (Top) Fitting of local (1.8Å t0 16Å) PDF data of "disordered" $Na_3Ni_2BiO_6$ with randomly distributed R-3m model, Ni/Bi honeycomb ordered *$P3_112$* and *C2/m* models. The most obvious difference arises from the highlighted peak at r ~ 5.9 Å (the a and b lattice parameter , *$P3_112$* and *C2/m* models can provide adequate fit for this peak while the *R-3m* model cannot. (Bottom) Schematic illustration of Ni/Bi arrangements in randomly distributed *R-3m* and honeycomb ordered *C2/m* and *$P3_112$* models. For *R-3m* model, there is a probability of 1/9 Bi-Bi pairs, 4/9 Ni-Ni pairs and 4/9 Ni-Bi pairs, whereas there are only Bi-Bi and Ni-Ni pairs in honeycomb ordered models with the ratio of 1:2.

Excluding the in plane Ni/Bi disordering, the disordered in this material is then most likely to be caused by the stacking disordered of honeycomb ordered layers along stacking direction. Thus, intermediate (up to several unit cells) to long range (up to tens of unit cells) structure study is required for further understanding of this type of disordering. The long range X-ray PDF data (up to 30 Å) is shown in Figure 6.13. It can be seen that neither of these three model (*R-3m, C2/m or $P3_112$)* can provide sufficient fit for this data, indicating the existence of more complicated stacking schemes even within a dimension of 2 trigonal cells (or 6 honeycomb layers). Further insights can be gained from synchrotron XRD data, shown in Figure 6.13. Similarly to the treatment of intermediate ranged PDF, all three different stacking models were used to fit the XRD pattern. It can be seen that *R-3m* can only capture intensity from the major symmetrical diffraction peaks, while *C2/m or $P3_112$* showed supper

lattice diffraction peaks that can only partially cover the intensity of asymmetrical diffuse scattering peaks. However, none of these models can provide adequate fit for the whole diffraction pattern. To carry out physically meaningful modeling of this staking disorder, it is necessary to first understand the origin of the formation of these diffuse scattering peaks.

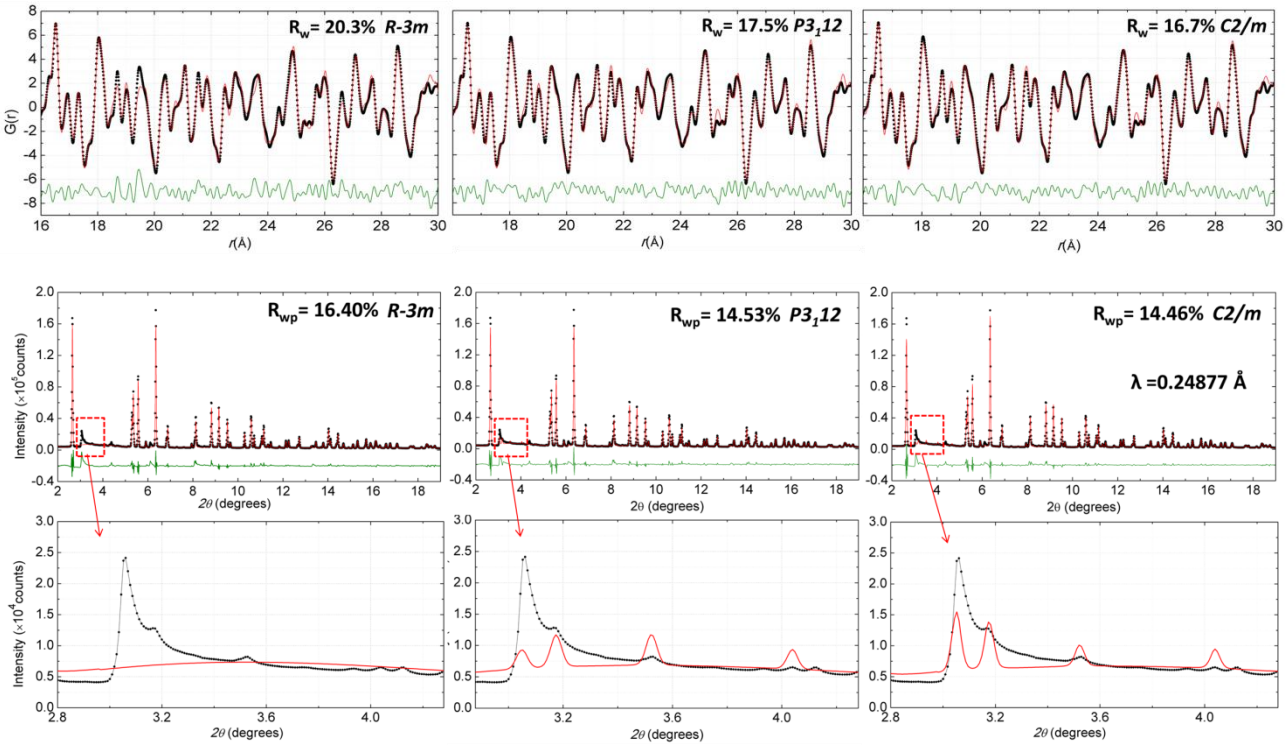

Figure 6.13 (Top) fitting of the intermediate range (16 Å to 30 Å) PDF data of "disordered" $Na_3Ni_2BiO_6$ with randomly distributed *R-3m* model, Ni/Bi honeycomb ordered *P3₁12* and *C2/m* models. (Bottom) fitting of synchrotron XRD data of "disordered" $Na_3Ni_2BiO_6$, enlarged regions show the fitting of related diffuse diffraction peaks associated with stacking disorder. None of these three models can provide adequate fit for the intermediate range PDF data or long range XRD diffraction data.

The $[001]_p$ zone axis TEM SAED pattern is shown in Figure 6.14, it can be clearly seen that all (0kl) (k ≠3n) indexed diffraction spots are merged into streak lines, indicating that there is almost no coherence of honeycomb ordered Ni/Bi layers along c axis. However, the (0k3n) (for l=3n) diffractions spots are still well behaved, indicates that three layered O3-$NaFeO_2$ basic unit cell is well preserved. Therefore, the disorder should be arisen from the combination of different 3 layered honeycomb blocks, which is demonstrated in Figure 6.16. To further validate this conclusion, HRTEM images are collected for several different regions of $[100]_p$ zone axis, as can be seen in Figures 6.14 and 6.15. Similar

counting strategies are applied here as that for the "ordered" sample (Figure 6.9 and Figure 6.10). For the first region with a dimension of 13.67 nm × 13.67 nm, a stacking sequence of 123321121113131211222212312 was identified; for another 20.50 nm × 20.50 nm region, the stacking sequence is found to be 132121221323122233133323231331111131231. The third region (13.67 nm × 13.67 nm) has a stacking sequence of 131132123111223222121232233, as can be seen in supporting information Figure 6.15. These counted sequences provide the possibility to interpret the correlation length by examining the propagation of translation vectors. Recall the three possible translation vectors between each two layers, e.g. $t_{\vec{a}}$, $t_{\vec{b}}$ and $t_{\vec{u}}$. Thus, a probability of 29.5% $t_{\vec{a}}$, 39.9% $t_{\vec{b}}$ and 30.6% $t_{\vec{u}}$ can be mapped out. The translation vectors do not show obvious long range correlations though they are not fully random.

Two strategies can be used to model this type of structure disorder by using scattering techniques: one way is to model the disorder in real space, as exemplified by PDF or EXAFS; the other is to carry out modeling in reciprocal space, such as using Diffax to model stacking faults in layered oxides[22,37]. Here, we choose the reciprocal method for the consideration that stacking (number) faults in honeycomb-ordered materials showed layer recursive nature, which will simplify the analysis into one dimension in reciprocal space. Diffax software[36] has been widely used to model stacking faults in layered compounds, which can provide qualitative disorder simulation but by no means of quantitative analysis. Here, we will use the Faults program[26] incorporated into Fullprof suite[37] to quantitatively model stacking (number) faults in the as-prepared "disordered" $Na_3Ni_2BiO_6$. Faults software utilized the core engine of Diffax but it also enables the simultaneous refinement of translation vector probabilities, background, peak shape and other structure related information, such as atomic positions, occupation and thermal displacements etc. It also provides two different methods to model the stacking sequences: explicit and recursive. For the explicit method, the intensity is calculated from a specified layer sequence, e.g. a defined large super cell. This method can be used to model diffraction patterns from a known model such as that from TEM counting. For the recursive method, the diffraction intensity is calculated from the combination of all possible stacking sequences and weighted by the corresponded probability that sequence will occur. This method can be used to quantitatively refine stacking faults in layered compound.

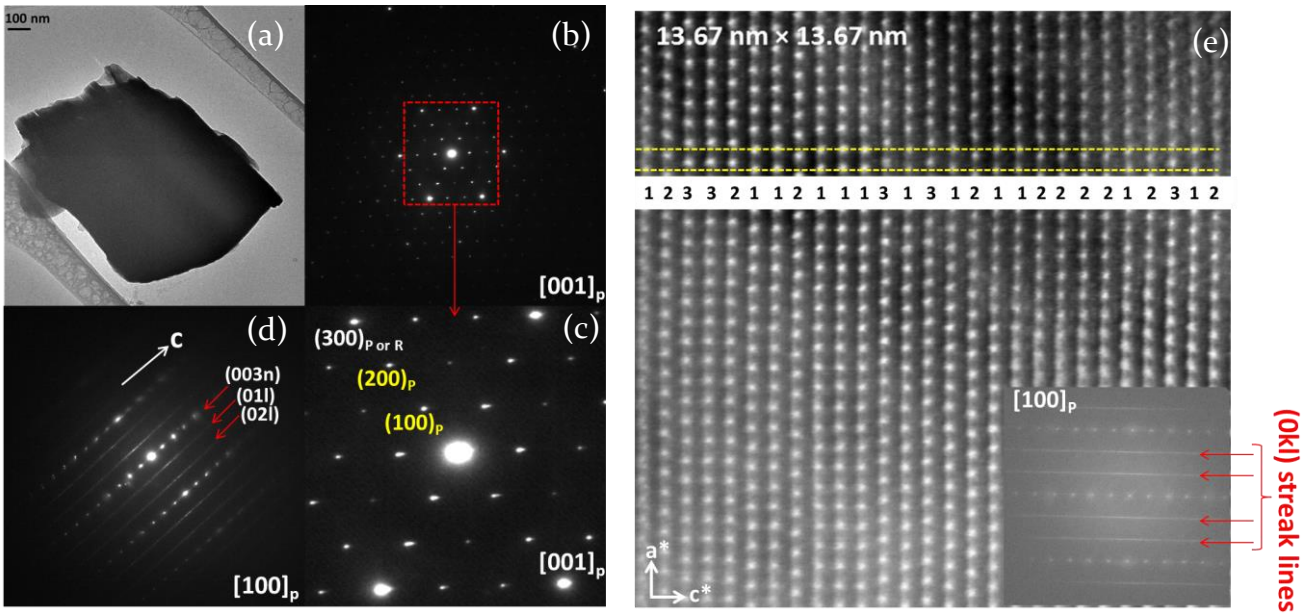

Figure 6.14 (a)-(d) SAED of "disordered" $Na_3Ni_2BiO_6$ along $[100]_p$ and $[001]_p$ zone axis direction. (e) HRTEM images of selected region of "disordered" $Na_3Ni_2BiO_6$, Bi atoms are appeared as big white spots. Insertion in (e) is the Fast Fourier transformed (FFT) HRTEM image.

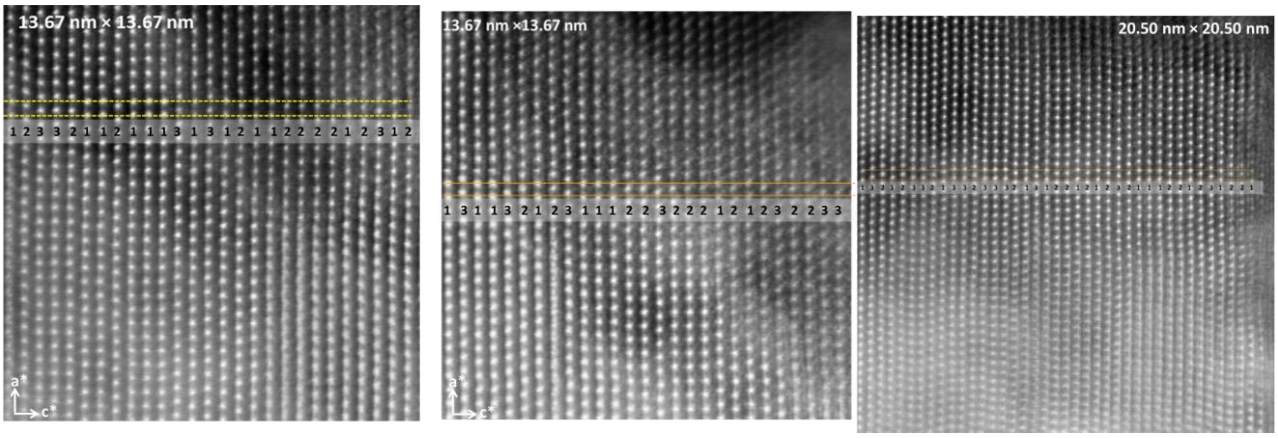

Figure 6.15 Stacking sequences of three different regions of the as-prepared "disordered" $Na_3Ni_2BiO_6$.

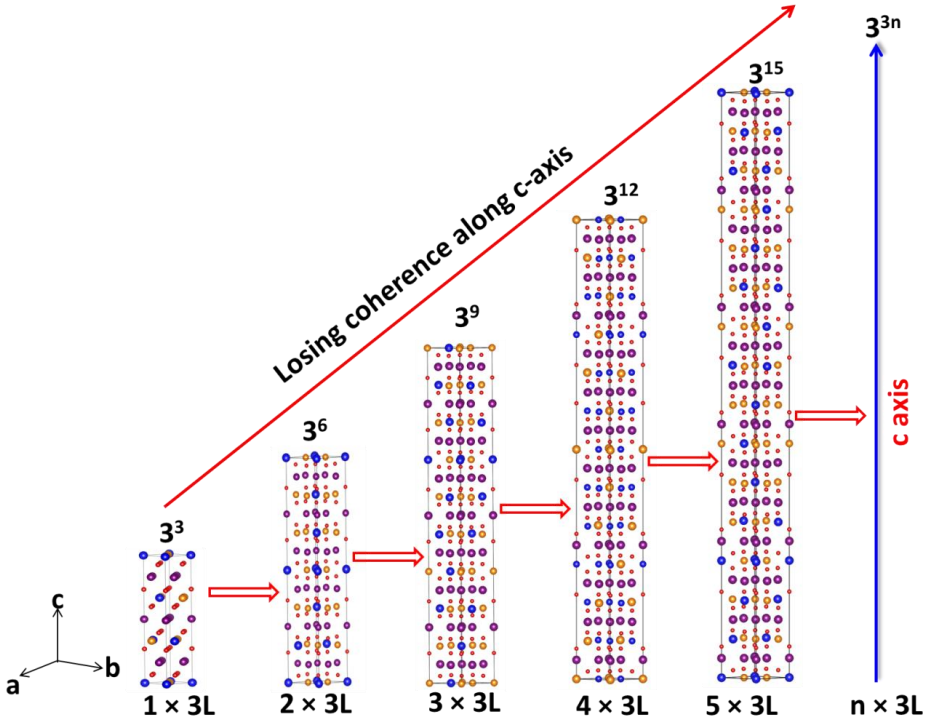

Figure 6.16 Schematic illustration of the formation of stacking (coloring) faults in $Na_3Ni_2BiO_6$.

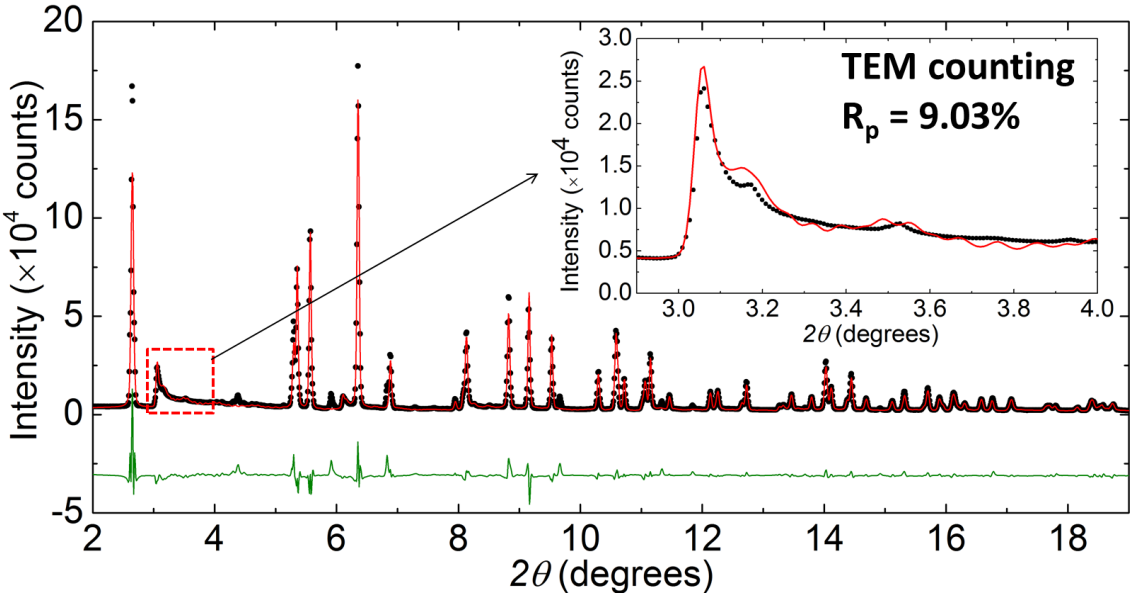

Figure 6.17 Rietveld refinement of synchrotron XRD data of "disordered" $Na_3Ni_2BiO_6$ with the statistical model obtained from counting Ni/Bi arrangements in HRTEM images.

Based on the counting result of HRTEM, a super cell which contains 93 honeycomb layers (~50 nm) was constructed and was used as an initial structure model for the refinement in Faults software in an explicit manner. The refinement result is shown in Figure 6.17. Substantial improvement has been observed for the fitting, especially for those broad diffuse diffraction peaks. However, this model is still not adequate, some characters of the diffuse diffraction peaks are still missing or over estimated. This can be attributed to the relatively small HRTEM counting region (~50 nm), which may not well represent the whole sample. Therefore, a better statistical model is needed.

Further understanding of layer stacking nature is required to build a better statistical model to describe this heavily number faulted sample. As mentioned previously, there are 3n possible stacking sequences for a unit cell with n honeycomb-ordered layers. It is obviously impracticable to explicit test all possible stacking sequences. Fortunately, a recursive nature exists for the honeycomb-ordered layer propagation, as can be seen in Figure 6.18. The three distinct sequences (ones start with 1, 2 or 3 layer types, position indices refer to Figure 6.2) are actually embedded into each other. If the layer correlation is purely local, which is a reasonable approximation for this heavily faulted sample (based on TEM counting), the analysis can be simplified into a single layer with the three possible translation vectors that propagate it to the next layer. Therefore, only 6 independent probabilities (9 probabilities with constrain $P_1 + P_2 + P_3 = 1$) are needed to statistically describe the possible stacking sequences, which should be the combination (3×3) of the existing probabilities of three different layer types (1, 2 and 3) and the probabilities of three different translation vectors ($t_{\vec{a}}$, $t_{\vec{b}}$ and $t_{\vec{u}}$) between each two layers.

Equal layer probability ($P_1 = P_2 = P_3 = 33.3\%$), meaning that the existing probability of type 1 layer is the same as type 2 layer and the same as type 3 layer, is a good start point. Though this is not an ideal model, it should be a good approximation for systems with strong local correlations. This model was then used to refine corresponded XRD data in Faults, an essentially good fit can be achieved after the refinement converged, as can be seen in Figure 6.19. The refinement result indicates that stacking sequences contains 26.8 % $t_{\vec{a}}$, 39.9 % $t_{\vec{b}}$ and 33.2 % $t_{\vec{u}}$. This is quite similar to the TEM counting result with 29.6% $t_{\vec{a}}$, 39.7% $t_{\vec{b}}$ and 30.6% $t_{\vec{u}}$. Though this equal layer probability ($P_1 = P_2 = P_3$) model can adequately fit the broad diffuse diffraction peak, the weak super lattice diffraction peaks are still not well modeled (red arrow in Figure 6.19), indicating the layer correlation is not purely local and there exists longer range correlation regions. One way to probe this longer range correlation is by tuning

the existing probabilities of three layer types (P1 ≠ P2 ≠ P3). Therefore, a model with 9 probabilities (6 independent variables) was used for the refinement. Obvious improvements were achieved for the fitting especially for the weak super lattice peaks (red arrow in Figure 6.20). The refined probabilities are 42.6% for type 1 layer, 31.6% for type 2 layer and 25.8% for type 3 layer.

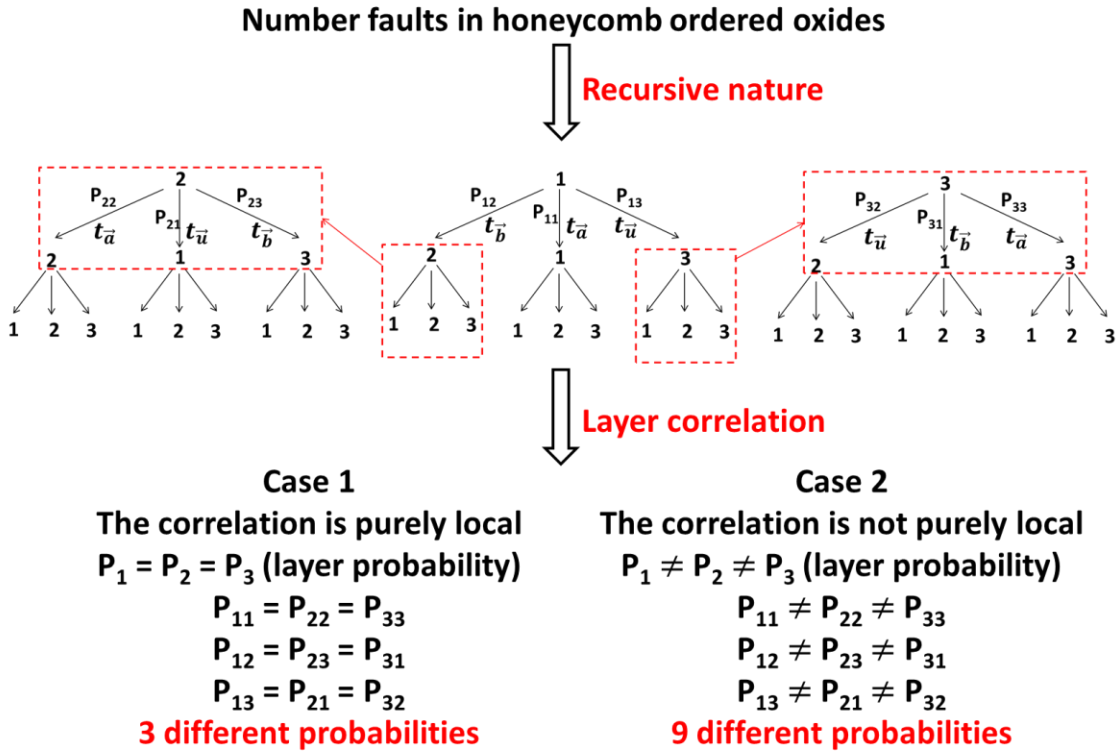

Figure 6.18 Recursive nature of layer (1,2 and 3 types) stacking in honeycomb-ordered $Na_3Ni_2BiO_6$.

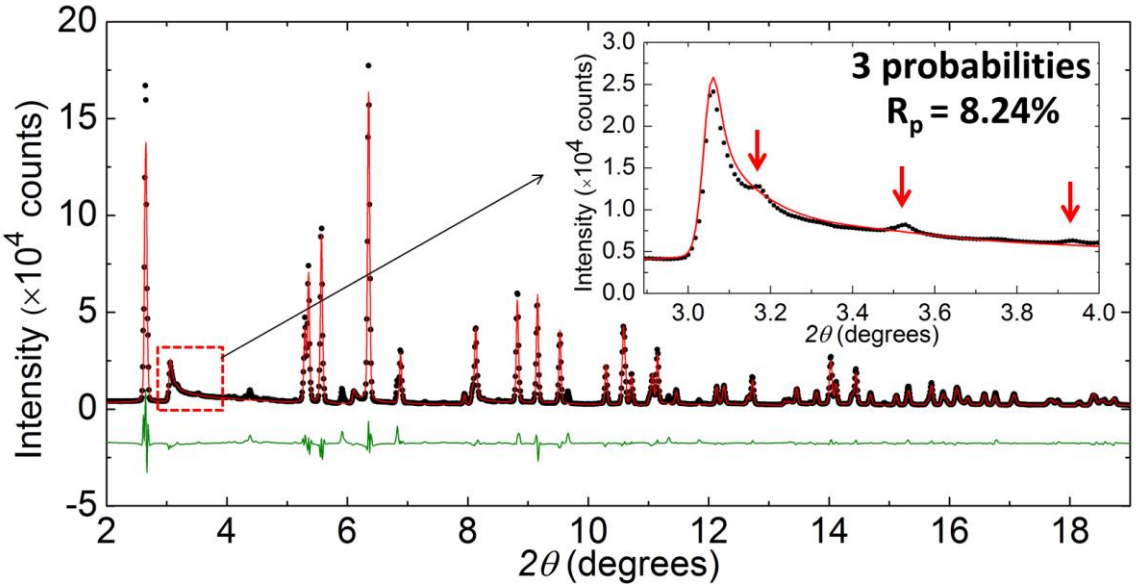

Figure 6.19 Rietveld refinement of synchrotron XRD data of "disordered" $Na_3Ni_2BiO_6$ with the equal layer ($P_1 = P_2 = P_3$) probability model.

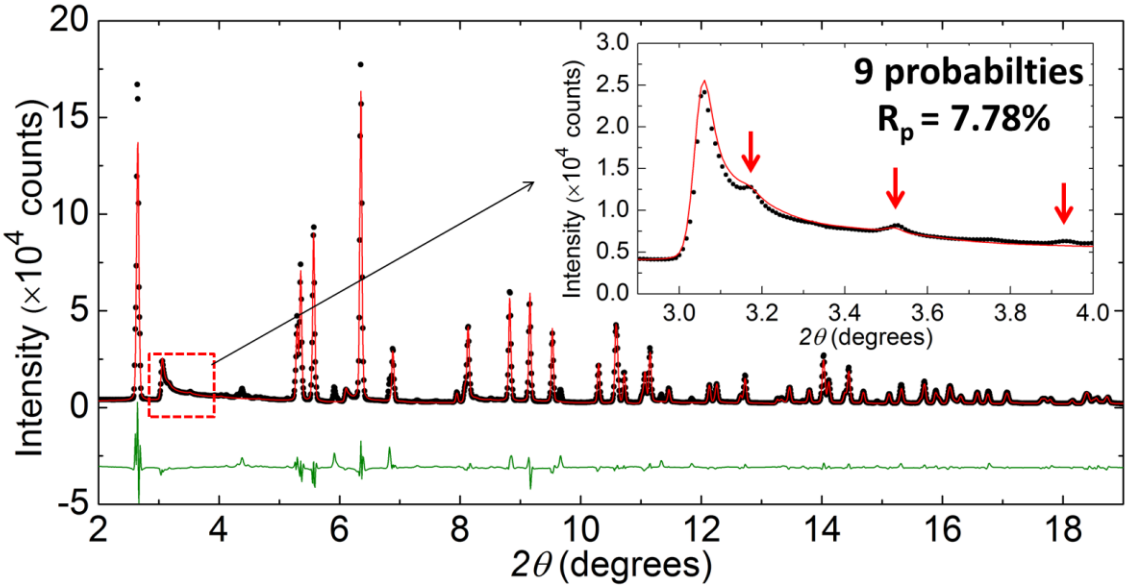

Figure 6.20 Rietveld refinement of synchrotron XRD data of "disordered" $Na_3Ni_2BiO_6$ with the non-equal layer ($P_1 \neq P_2 \neq P_3$) probability model.

Table 6.3 Refined translation vector probabilities between each two layers for the equal layer probability model and non-equal probability model.

	P_1	P_2	P_3
P_1	0.268	0.399	0.332
P_2	0.332	0.268	0.399
P_3	0.399	0.332	0.268

	P1	P2	P_3
P_1	0.513	0.337	0.150
P_2	0.313	0.185	0.502
P_3	0.421	0.441	0.138

6.3.4 Electrochemical performance as cathodes for rechargeable Na-ion batteries.

Galvanostatic charge/discharge curve of "ordered" and "disordered" samples are quite similar, as can be seen in Figure 6.21 and Figure 6.22, however, we reproducibly found that "ordered" phase showed higher discharge capacity and higher columbic efficiency than the disordered phase, presumably due to the stronger side reaction of disordered phase with electrolyte since this sample has larger surface due to the much smaller particle sizes. Thus, we will focus on the electrochemistry study of the "ordered" sample. The first 10 charge and discharge curves between 2.4 V and 3.8 V are shown in Figure 6.21a, an initial discharge capacity of 104 mAh/g with good capacity retention can be achieved at C/30 rate. Based on *ex situ* Ni K-edge XAENES shown in Figure 6.23, it can be seen that only Ni^{2+}/Ni^{3+} was utilized during charge/discharge, leading to the limited theoretical capacity of 110 mAh/g. From the corresponded cyclic voltammetry (CV) curves (Figure 6.21c), it can be seen that two different redox plateaus existed during initial charge process with one centered at 3.38 V and the other at 3.55 V; during initial discharge, there are three distinct redox peaks, one at 3.45 V, another at 3.18 V and the third one at 3.10 V. Interestingly, an over potential of about 0.05 V has been observed during the initial charge process, which is very likely to be associated with the relative sluggish sodium mobility of fully stoichiometry $Na_3Ni_2BiO_6$. Similar over potential was also observed in $Na_3Ni_2SbO_6$[12] and can be

effectively removed by introducing sodium vacancies into the structure. Similar characteristics have been observed in the GITT charge/discharge curve (Figure 6.21d). However, it should be noticed that the voltage, which can be treated as thermodynamic equilibrium voltage in GITT experiment, of the third discharge plateau in GITT curve is almost the same as that of the second discharge plateau, in clear contrast to the situation of a normal Galvanostatic discharge curve (Figure 6.21a). This result indicates that kinetic, very likely to be associated with ionic diffusivity, is retarded after 0.6 Na^+ reinserted into $Na_2Ni_2BiO_6$ (~ 70 mAh/g). Further study of structure evolution (i.e. Na^+ - vacancy ordering etc.) during Na^+ intercalation and deintercalation is required to fully understand these features, which falls out of the scope of current work and will be reported elsewhere.

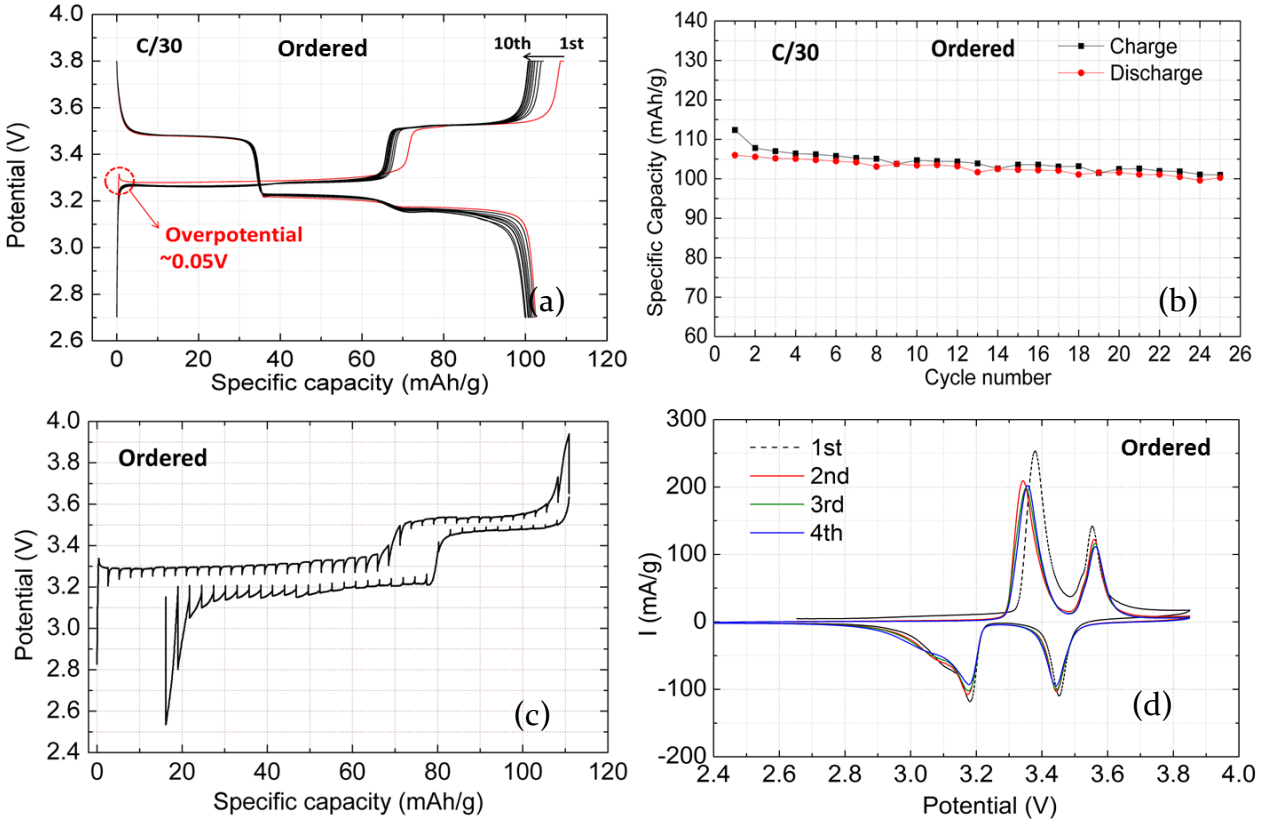

Figure 6.21 (a) First 10 charge/discharge curves of ordered $Na_3Ni_2BiO_6$ (v.s. Na^+/Na) at C/30 rate. (b) Cyclability of ordered $Na_3Ni_2BiO_6$ at C/30 rate. (c) GITT of ordered $Na_3Ni_2BiO_6$ at C/320 (charge/discharge for 30 min and then relax for 15 hours) (d) cyclic voltammetry curves of $Na_3Ni_2BiO_6$ (v.s. Na^+/Na) with 5 mV/s scanning rate.

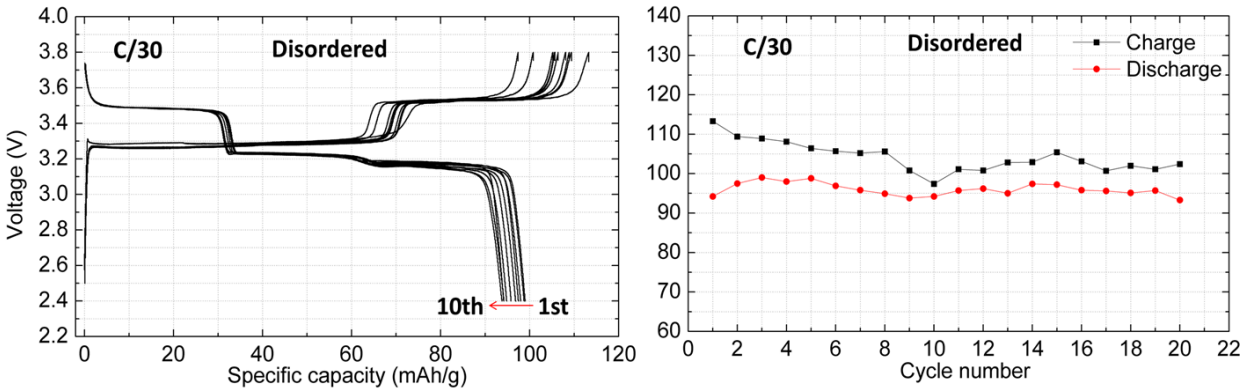

Figure 6.22 Left, first ten charge/discharge curves of "disordered" $Na_3Ni_2BiO_6$ versus Na^+/Na at C/30 rate. Right, Cyclability of "disordered" $Na_3Ni_2BiO_6$ at C/30 rate.

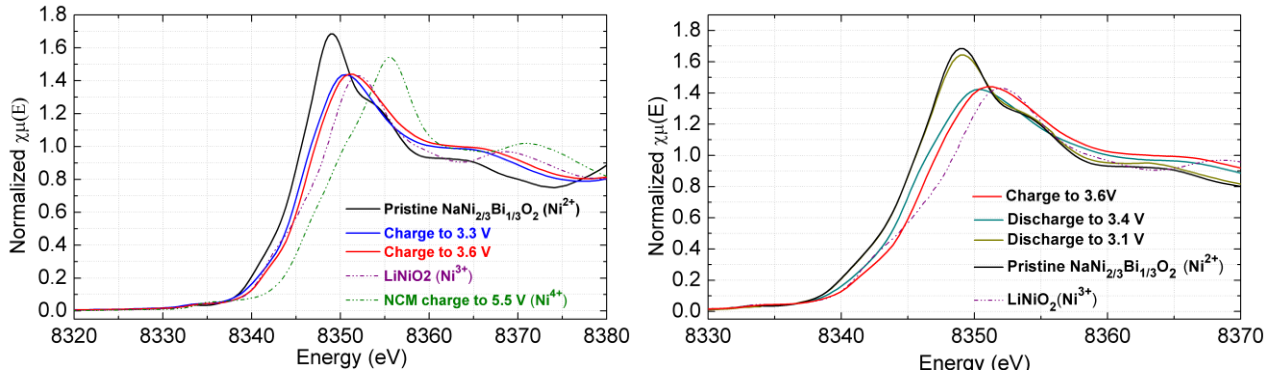

Figure 6.23 Left, Ni K-edge XANES spectra of pristine $Na_3Ni_2BiO_6$ (black), sample charged to 3.3 V (blue) and 3.6 V (red). Right, Ni K-edge XANES spectra of sample discharged to 3.4 V (dark cyan) and 3.1 V (dark yellow).

6.4 Conclusion

Ordered and disordered polymorphs of $Na_3Ni_2BiO_6$ were successfully synthesized. It has been found that Ni^{2+}/Bi^{5+} honeycomb ordering was well preserved in both "ordered" and "disordered" phases. The difference between these two polymorphs arises from different stacking configurations of the well-ordered Ni^{2+}/Bi^{5+} honeycomb layers along stacking direction. The ordered polymorph can be best described by using *C2/m* space group although small portion of intergrowth of *C2/m* and $P3_112$ existed. For disordered polymorph, based on HRTEM counting, a 3_1 blocks supercell model that contains 12 *C2/m* and 19 $P3_112$ blocks is found to be reasonable statistic model for structure description. A quantitative analysis of stacking (number) faults in this structure type has been carried out, similar faulting probabilities have been found from the TEM counting and synchrotron XRD refinements.

Ordered polymorph showed higher discharge capacity (~105 mAh/g) than the disordered polymorph (~90 mAh/g) as cathode for sodium ion batteries. It is believed that the present methods used to modeling and quantifying coloring faults will also be useful for understanding the structure of other technologically important honeycomb ordered oxides.

References

(1) Mizushima, K.; Jones, P. C.; Wiseman, P. J.; Goodenough, J. B. *Mater. Res. Bull.* **1980**, *15*, 783.
(2) Braconnier, J. J.; Delmas, C.; Fouassier, C.; Hagenmuller, P. *Mater. Res. Bull.* **1980**, *15*, 1797.
(3) Whittingham, M. S. *Prog. Solid State Chem.* **1978**, *12*, 41.
(4) Ozawa, K. *Solid State Ionics* **1994**, *69*, 212.
(5) Pan, H. L.; Hu, Y. S.; Chen, L. Q. *Energy & Environmental Science* **2013**, *6*, 2338.
(6) Shannon, R. D.; Prewitt, C. T. *Acta Crystallographica Section B-Structural Crystallography and Crystal Chemistry* **1969**, *B 25*, 925.
(7) Zhou, Y.; Ding, J.; Nam, K. W.; Yu, X.; Bak, S.-M.; Hu, E.; Liu, J.; Bai, J.; Li, H.; Fu, Z. *J. Mater. Chem. A* **2013**, **1**, 11130-11134
(8) Komaba, S.; Takei, C.; Nakayama, T.; Ogata, A.; Yabuuchi, N. *Electrochem. Commun.* **2010**, *12*, 355.
(9) Takeda, Y.; Nakahara, K.; Nishijima, M.; Imanishi, N.; Yamamoto, O.; Takano, M.; Kanno, R. *Mater. Res. Bull.* **1994**, *29*, 659.
(10) Ma, X. H.; Kang, K. S.; Ceder, G.; Meng, Y. S. *J. Power Sources* **2007**, *173*, 550.
(11) Yuan, D. D.; Liang, X. M.; Wu, L.; Cao, Y. L.; Ai, X. P.; Feng, J. W.; Yang, H. X. *Adv. Mater.* **2014**, *26*, 6301.
(12) Ma, J.; Bo, S. H.; Wu, L. J.; Zhu, Y. M.; Grey, C. P.; Khalifah, P. G. *Chem. Mater.* **2015**, *27*, 2387.
(13) Seibel, E. M.; Roudebush, J. H.; Wu, H.; Huang, Q. Z.; Ali, M. N.; Ji, H. W.; Cava, R. J. *Inorg. Chem.* **2013**, *52*, 13605.
(14) Smirnova, O. A.; Nalbandyan, V. B.; Petrenko, A. A.; Avdeev, M. *J. Solid State Chem.* **2005**, *178*, 1165.
(15) Viciu, L.; Huang, Q.; Morosan, E.; Zandbergen, H. W.; Greenbaum, N. I.; McQueen, T.; Cava, R. J. *J. Solid State Chem.* **2007**, *180*, 1060.
(16) Politaev, V. V.; Nalbandyan, V. B.; Petrenko, A. A.; Shukaev, I. L.; Volotchaev, V. A.; Medvedev, B. S. *J. Solid State Chem.* **2010**, *183*, 684.
(17) Berthelot, R.; Schmidt, W.; Muir, S.; Eilertsen, J.; Etienne, L.; Sleight, A. W.; Subramanian, M. A. *Inorg. Chem.* **2012**, *51*, 5377.
(18) Greaves, C.; Katib, S. M. A. *Mater. Res. Bull.* **1990**, *25*, 1175.
(19) Strobel, P.; Lambertandron, B. *J. Solid State Chem.* **1988**, *75*, 90.
(20) Seibel, E. M.; Roudebush, J. H.; Ali, M. N.; Ross, K. A.; Cava, R. J. *Inorg. Chem.* **2014**, *53*, 10989.
(21) Delmas, C.; Fouassier, C.; Hagenmuller, P. *Physica B & C* **1980**, *99*, 81.
(22) Breger, J.; Jiang, M.; Dupre, N.; Meng, Y. S.; Shao-Horn, Y.; Ceder, G.; Grey, C. P. *J. Solid State Chem.* **2005**, *178*, 2575.
(23) Roudebush, J. H.; Andersen, N. H.; Ramlau, R.; Garlea, V. O.; Toft-Petersen, R.; Norby, P.; Schneider, R.; Hay, J. N.; Cava, R. J. *Inorg. Chem.* **2013**, *52*, 6083.
(24) Boulineau, A.; Croguennec, L.; Delmas, C.; Weill, F. *Chem. Mater.* **2009**, *21*, 4216.
(25) Robertson, A. D.; Bruce, P. G. *Chem. Mater.* **2003**, *15*, 1984.
(26) Thackeray, M. M.; Dekock, A.; Rossouw, M. H.; Liles, D.; Bittihn, R.; Hoge, D. *J. Electrochem. Soc.* **1992**, *139*, 363.
(27) Lu, Z. H.; Beaulieu, L. Y.; Donaberger, R. A.; Thomas, C. L.; Dahn, J. R. *J. Electrochem. Soc.* **2002**, *149*, A778.

(28)Hammersley, A. P.; Svensson, S. O.; Hanfland, M.; Fitch, A. N.; Hausermann, D. *High Pressure Research* **1996**, *14*, 235.
(29) Casas-Cabanas, M.; Rodriguez-Carvajal, J.; Palacin, M. R. *Z. Kristallogr.* **2006**, 243.
(30) Ravel, B.; Newville, M. *J Synchrotron Radiat* **2005**, *12*, 537.
(31) Zabinsky, S. I.; Rehr, J. J.; Ankudinov, A.; Albers, R. C.; Eller, M. J. *Physical Review B* **1995**, *52*, 2995.
(32) Juhas, P.; Davis, T.; Farrow, C. L.; Billinge, S. J. L. *J. Appl. Crystallogr.* **2013**, *46*, 560.
(33) Farrow, C. L.; Juhas, P.; Liu, J. W.; Bryndin, D.; Bozin, E. S.; Bloch, J.; Proffen, T.; Billinge, S. J. L. *Journal of Physics-Condensed Matter* **2007**, *19*, 33.
(34) McCalla, E.; Abakumov, A.; Rousse, G.; Reynaud, M.; Sougrati, M. T.; Budic, B.; Mahmoud, A.; Dominko, R.; Van Tendeloo, G.; Hermann, R. P.; Tarascon, J. M. *Chem. Mater.* **2015**, *27*, 1699.
(35) Lebail, A.; Duroy, H.; Fourquet, J. L. *Mater. Res. Bull.* **1988**, *23*, 447.
(36)Egami, T.; Billinge, S. J. L., *Underneath the Bragg-Peaks: Structural Analysis of Complex Materials*, *Plenum, Oxford, 2003.*
(37)Treacy, M. M. J.; Newsam, J. M.; Deem, M. W. *Proceedings of the Royal Society of London Series a-Mathematical Physical and Engineering Sciences* **1991**, *433*, 499.
(38) Rodriguezcarvajal, J. *Physica B* **1993**, *192*, 55.

References

Chapter 1

(1) Nagaura, T.; Tozawa, K. *Prog. Batteries Solar Cells* **1990**, *9*, 209.
(2) Armand, M.; Tarascon, J. M. *Nature* **2008**, *451*, 652.
(3) Linden, D.; Reddy, T. B.; McGraw-Hill: 2002.
(4) Tarascon, J. M.; Armand, M. *Nature* **2001**, *414*, 359.
(5) Pan, H. L.; Hu, Y. S.; Chen, L. Q. *Energy & Environmental Science* **2013**, *6*, 2338.
(6) Shannon, R. D.; Prewitt, C. T. *Acta Crystallographica Section B-Structural Crystallography and Crystal Chemistry* **1969**, *B 25*, 925.
(7) http://pubs.usgs.gov/fs/2002/fs087-02/.
(8) Whittingham, M. S. *Prog. Solid State Chem.* **1978**, *12*, 41.
(9) Thompson, A. H.; Whittingham, M. S. *Mater. Res. Bull.* **1977**, *12*, 741.
(10) Whittingham, M. S. *Science* **1976**, *192*, 1126.
(11) Whittingham, M. S. *J. Electrochem. Soc.* **1976**, *123*, 315.
(12) Whittingham, M. S. *Chem. Rev.* **2014**, *114*, 11414.
(13) Mizushima, K.; Jones, P. C.; Wiseman, P. J.; Goodenough, J. B. *Mater. Res. Bull.* **1980**, *15*, 783.
(14) Guilmard, M.; Pouillerie, C.; Croguennec, L.; Delmas, C. *Solid State Ionics* **2003**, *160*, 39.
(15) Ohzuku, T.; Makimura, Y. *Chem. Lett.* **2001**, 744.
(16) Delmas, C.; Fouassier, C.; Hagenmuller, P. *Physica B & C* **1980**, *99*, 81.
(17) Goodenough, J.; Thackeray, M.; David, W.; Bruce, P. *Revue de Chimie minerale* **1984**, *21*, 435.
(18) Thackeray, M.; David, W.; Bruce, P.; Goodenough, J. *Mater. Res. Bull.* **1983**, *18*, 461.
(19) Thackeray, M. M.; David, W. I. F.; Bruce, P. G.; Goodenough, J. B. *Mater. Res. Bull.* **1983**, *18*, 461.
(20) Thackeray, M.; Johnson, P.; De Picciotto, L.; Bruce, P.; Goodenough, J. *Mater. Res. Bull.* **1984**, *19*, 179.
(21) Ohzuku, T.; Ariyoshi, K.; Yamamoto, S.; Makimura, Y. *Chem. Lett.* **2001**, 1270.
(22) Ariyoshi, K.; Iwakoshi, Y.; Nakayama, N.; Ohzuku, T. *J. Electrochem. Soc.* **2004**, *151*, A296.
(23) Colbow, K.; Dahn, J.; Haering, R. *J. Power Sources* **1989**, *26*, 397.
(24) Ohzuku, T.; Ueda, A.; Yamamoto, N. *J. Electrochem. Soc.* **1995**, *142*, 1431.
(25) Lu, Z.; MacNeil, D.; Dahn, J. *Electrochem. Solid-State Lett.* **2001**, *4*, A191.
(26) Thackeray, M. M.; Johnson, C. S.; Vaughey, J. T.; Li, N.; Hackney, S. A. *J. Mater. Chem.* **2005**, *15*, 2257.
(27) Strobel, P.; Lambertandron, B. *J. Solid State Chem.* **1988**, *75*, 90.
(28) Breger, J.; Jiang, M.; Dupre, N.; Meng, Y. S.; Shao-Horn, Y.; Ceder, G.; Grey, C. P. *J. Solid State Chem.* **2005**, *178*, 2575.
(29) Boulineau, A.; Croguennec, L.; Delmas, C.; Weill, F. *Chem. Mater.* **2009**, *21*, 4216.
(30) Padhi, A. K.; Nanjundaswamy, K. S.; Goodenough, J. B. *J. Electrochem. Soc.* **1997**, *144*, 1188.
(31) Manthiram, A.; Goodenough, J. *J. Solid State Chem.* **1987**, *71*, 349.
(32) Manthiram, A.; Goodenough, J. *J. Power Sources* **1989**, *26*, 403.
(33) Goodenough, J. B.; Hong, H. Y. P.; Kafalas, J. A. *Mater. Res. Bull.* **1976**, *11*, 203.
(34) Hong, H. Y. P. *Mater. Res. Bull.* **1976**, *11*, 173.

(35) Yao, Y. F. Y.; Kummer, J. T. *Journal of Inorganic & Nuclear Chemistry* **1967**, *29*, 2453.
(36) Reiff, W.; Zhang, J.; Torardi, C. *J. Solid State Chem.* **1986**, *62*, 231.
(37) Torardi, C.; Prince, E. *Mater. Res. Bull.* **1986**, *21*, 719.
(38) NADIRI, A.; Delmas, C.; Salmon, R.; Hagenmuller, P. *Revue de chimie minérale* **1984**, *21*, 537.
(39) Delmas, C.; Cherkaoui, F.; Nadiri, A.; Hagenmuller, P. *Mater. Res. Bull.* **1987**, *22*, 631.
(40) Delmas, C.; Nadiri, A. *Mater. Res. Bull.* **1988**, *23*, 65.
(41) Delmas, C.; Nadiri, A.; Soubeyroux, J. *Solid State Ionics* **1988**, *28*, 419.
(42) Nanjundaswamy, K.; Padhi, A.; Goodenough, J.; Okada, S.; Ohtsuka, H.; Arai, H.; Yamaki, J. *Solid State Ionics* **1996**, *92*, 1.
(43) Masquelier, C.; Padhi, A.; Nanjundaswamy, K.; Goodenough, J. *J. Solid State Chem.* **1998**, *135*, 228.
(44) Islam, M. S.; Driscoll, D. J.; Fisher, C. A.; Slater, P. R. *Chem. Mater.* **2005**, *17*, 5085.
(45) Morgan, D.; Van der Ven, A.; Ceder, G. *Electrochem. Solid-State Lett.* **2004**, *7*, A30.
(46) Huang, H.; Yin, S.-C.; Nazar, L. s. *Electrochem. Solid-State Lett.* **2001**, *4*, A170.
(47) Yamada, A.; Chung, S.-C.; Hinokuma, K. *J. Electrochem. Soc.* **2001**, *148*, A224.
(48) Ravet, N.; Chouinard, Y.; Magnan, J.; Besner, S.; Gauthier, M.; Armand, M. *J. Power Sources* **2001**, *97*, 503.
(49) Chung, S.-Y.; Bloking, J. T.; Chiang, Y.-M. *Nat. Mater.* **2002**, *1*, 123.
(50) Armand, M.; Michot, C.; Ravet, N.; Simoneau, M.; Hovington, P. *There is no corresponding record for this reference*.
(51) Nytén, A.; Abouimrane, A.; Armand, M.; Gustafsson, T.; Thomas, J. O. *Electrochem. Commun.* **2005**, *7*, 156.
(52) Dominko, R.; Conte, D. E.; Hanzel, D.; Gaberscek, M.; Jamnik, J. *J. Power Sources* **2008**, *178*, 842.
(53) Gong, Z.; Li, Y.; Yang, Y. *Electrochem. Solid-State Lett.* **2006**, *9*, A542.
(54) Gong, Z.; Li, Y.; Yang, Y. *J. Power Sources* **2007**, *174*, 524.
(55) Masquelier, C.; Croguennec, L. *Chem. Rev. (Washington, DC, U. S.)* **2013**, *113*, 6552.
(56) Nishimura, S.-i.; Hayase, S.; Kanno, R.; Yashima, M.; Nakayama, N.; Yamada, A. *J. Am. Chem. Soc.* **2008**, *130*, 13212.
(57) Boulineau, A.; Sirisopanaporn, C.; Dominko, R.; Armstrong, A. R.; Bruce, P. G.; Masquelier, C. *Dalton Trans.* **2010**, *39*, 6310.
(58) Sirisopanaporn, C.; Boulineau, A.; Hanzel, D.; Dominko, R.; Budic, B.; Armstrong, A. R.; Bruce, P. G.; Masquelier, C. *Inorg. Chem.* **2010**, *49*, 7446.
(59) Yamada, A.; Iwane, N.; Harada, Y.; Nishimura, S. i.; Koyama, Y.; Tanaka, I. *Adv. Mater. (Weinheim, Ger.)* **2010**, *22*, 3583.
(60) Bo, S.-H.; Wang, F.; Janssen, Y.; Zeng, D.; Nam, K.-W.; Xu, W.; Du, L.-S.; Graetz, J.; Yang, X.-Q.; Zhu, Y. *J. Mater. Chem.* **2012**, *22*, 8799.
(61) Barker, J.; Gover, R. K. B.; Burns, P.; Bryan, A.; Saidi, M. Y.; Swoyer, J. L. *J. Power Sources* **2005**, *146*, 516.
(62) Barker, J.; Gover, R. K. B.; Burns, P.; Bryan, A. *Electrochemical and Solid State Letters* **2005**, *8*, A285.
(63) Recham, N.; Chotard, J. N.; Dupont, L.; Delacourt, C.; Walker, W.; Armand, M.; Tarascon, J. M. *Nat. Mater.* **2010**, *9*, 68.
(64) Zhou, Y. N.; Ding, J. J.; Nam, K. W.; Yu, X. Q.; Bak, S. M.; Hu, E. Y.; Liu, J.; Bai, J. M.; Li, H.; Fu, Z. W.; Yang, X. Q. *Journal of Materials Chemistry A* **2013**, *1*, 11130.

(65) Komaba, S.; Takei, C.; Nakayama, T.; Ogata, A.; Yabuuchi, N. *Electrochem. Commun.* **2010**, *12*, 355.
(66) Berthelot, R.; Carlier, D.; Delmas, C. *Nat. Mater.* **2011**, *10*, 74.
(67) Yabuuchi, N.; Kubota, K.; Dahbi, M.; Komaba, S. *Chem. Rev. (Washington, DC, U. S.)* **2014**, *114*, 11636.
(68) Yabuuchi, N.; Kajiyama, M.; Iwatate, J.; Nishikawa, H.; Hitomi, S.; Okuyama, R.; Usui, R.; Yamada, Y.; Komaba, S. *Nat. Mater.* **2012**, *11*, 512.
(69) Zaghib, K.; Trottier, J.; Hovington, P.; Brochu, F.; Guerfi, A.; Mauger, A.; Julien, C. *J. Power Sources* **2011**, *196*, 9612.
(70) Sun, A.; Beck, F. R.; Haynes, D.; Poston, J. A.; Narayanan, S.; Kumta, P. N.; Manivannan, A. *Materials Science and Engineering: B* **2012**, *177*, 1729.
(71) Kim, H.; Park, I.; Seo, D.-H.; Lee, S.; Kim, S.-W.; Kwon, W. J.; Park, Y.-U.; Kim, C. S.; Jeon, S.; Kang, K. *J. Am. Chem. Soc.* **2012**, *134*, 10369.
(72) Sanz, F.; Parada, C.; Rojo, J.; Ruiz-Valero, C. *Chem. Mater.* **2001**, *13*, 1334.
(73) Moreau, P.; Guyomard, D.; Gaubicher, J.; Boucher, F. *Chem. Mater.* **2010**, *22*, 4126.
(74) Breger, J.; Dupre, N.; Chupas, P. J.; Lee, P. L.; Proffen, T.; Parise, J. B.; Grey, C. P. *J. Am. Chem. Soc.* **2005**, *127*, 7529.
(75) Makimura, Y.; Ohzuku, T. *J. Power Sources* **2003**, *119*, 156.
(76) Warren, B. E. *X-ray Diffraction*; Courier Corporation, 1969.
(77) Giacovazzo, C.; Monaco, H.; Viterbo, D.; Scordari, F.; Gilli, G.; Zanotti, G.; Catti, M. *Acta Cryst* **1993**, *49*, 373.
(78) Willis, B. T. M.; Carlile, C. J. *Experimental neutron scattering*; Oxford Univ. Press, 2009.
(79) Young, R. A. *Cryst. Res. Technol.* **1995**, *30*.
(80) Rietveld, H. M. *J. Appl. Crystallogr.* **1969**, *2*, 65.
(81) Debye, P. *The Journal of Physical Chemistry* **1947**, *51*, 18.
(82) Welberry, T. R. *Diffuse x-ray scattering and models of disorder*; Oxford Univ. Press Oxford, 2004; Vol. 16.
(83) Treacy, M.; Newsam, J.; Deem, M. In *Proceedings of the Royal Society of London A: Mathematical, Physical and Engineering Sciences*; The Royal Society: 1991; Vol. 433, p 499.
(84) Hendricks, S.; Teller, E. *The Journal of Chemical Physics* **1942**, *10*, 147.
(85) Egami, T.; Billinge, S. J. *Underneath the Bragg peaks: structural analysis of complex materials*; Elsevier, 2003; Vol. 16.
(86) McGreevy, R. L. *J. Phys.: Condens. Matter* **2001**, *13*, R877.
(87) Koningsberger, D.; Prins, R. *X-ray absorption: principles, applications, techniques of EXAFS, SEXAFS, and XANES* **1988**.
(88) Rehr, J.; Ankudinov, A. *Coord. Chem. Rev.* **2005**, *249*, 131.

Chapter 2

(1) Liu, J.; Chang, D. H.; Whitfield, P.; Janssen, Y.; Yu, X. Q.; Zhou, Y. N.; Bai, J. M.; Ko, J.; Nam, K. W.; Wu, L. J.; Zhu, Y. M.; Feygenson, M.; Amatucci, G.; Van der Ven, A.; Yang, X. Q.; Khalifah, P. *Chem. Mater.* **2014**, *26*, 3295.
(2) Pan, H. L.; Hu, Y. S.; Chen, L. Q. *Energy & Environmental Science* **2013**, *6*, 2338.
(3) Palomares, V.; Serras, P.; Villaluenga, I.; Hueso, K. B.; Carretero-Gonzalez, J.; Rojo, T. *Energy & Environmental Science* **2012**, *5*, 5884.
(4) Kim, S. W.; Seo, D. H.; Ma, X. H.; Ceder, G.; Kang, K. *Advanced Energy Materials* **2012**, *2*, 710.
(5) Braconnier, J. J.; Delmas, C.; Fouassier, C.; Hagenmuller, P. *Mater. Res. Bull.* **1980**, *15*, 1797.
(6) Delmas, C.; Fouassier, C.; Hagenmuller, P. *Physica B & C* **1980**, *99*, 81.
(7) Braconnier, J. J.; Delmas, C.; Hagenmuller, P. *Mater. Res. Bull.* **1982**, *17*, 993.
(8) Didier, C.; Guignard, M.; Denage, C.; Szajwaj, O.; Ito, S.; Saadoune, I.; Darriet, J.; Delmas, C. *Electrochemical and Solid State Letters* **2011**, *14*, A75.
(9) Komaba, S.; Takei, C.; Nakayama, T.; Ogata, A.; Yabuuchi, N. *Electrochem. Commun.* **2010**, *12*, 355.
(10) Zhou, Y. N.; Ding, J. J.; Nam, K. W.; Yu, X. Q.; Bak, S. M.; Hu, E. Y.; Liu, J.; Bai, J. M.; Li, H.; Fu, Z. W.; Yang, X. Q. *Journal of Materials Chemistry A* **2013**, *1*, 11130.
(11) Caballero, A.; Hernan, L.; Morales, J.; Sanchez, L.; Pena, J. S.; Aranda, M. A. G. *J. Mater. Chem.* **2002**, *12*, 1142.
(12) Berthelot, R.; Carlier, D.; Delmas, C. *Nat. Mater.* **2011**, *10*, 74.
(13) Yabuuchi, N.; Kajiyama, M.; Iwatate, J.; Nishikawa, H.; Hitomi, S.; Okuyama, R.; Usui, R.; Yamada, Y.; Komaba, S. *Nat. Mater.* **2012**, *11*, 512.
(14) Moreau, P.; Guyomard, D.; Gaubicher, J.; Boucher, F. *Chem. Mater.* **2010**, *22*, 4126.
(15) Lee, K. T.; Ramesh, T. N.; Nan, F.; Botton, G.; Nazar, L. F. *Chem. Mater.* **2011**, *23*, 3593.
(16) Goodenough, J. B.; Hong, H. Y. P.; Kafalas, J. A. *Mater. Res. Bull.* **1976**, *11*, 203.
(17) Delmas, C.; Cherkaoui, F.; Nadiri, A.; Hagenmuller, P. *Mater. Res. Bull.* **1987**, *22*, 631.
(18) Plashnitsa, L. S.; Kobayashi, E.; Noguchi, Y.; Okada, S.; Yamaki, J. *J. Electrochem. Soc.* **2010**, *157*, A536.
(19) Jian, Z. L.; Zhao, L.; Pan, H. L.; Hu, Y. S.; Li, H.; Chen, W.; Chen, L. Q. *Electrochem. Commun.* **2012**, *14*, 86.
(20) Barker, J.; Saidi, M. Y.; Swoyer, J. L. *Electrochem. Solid-State Lett.* **2003**, *6*, A1.
(21) Gover, R.; Bryan, A.; Burns, P.; Barker, J. *Solid State Ionics* **2006**, *177*, 1495.
(22) Chihara, K.; Kitajou, A.; Gocheva, I. D.; Okada, S.; Yamaki, J. *J. Power Sources* **2013**, *227*, 80.
(23) Ellis, B. L.; Makahnouk, W. R. M.; Makimura, Y.; Toghill, K.; Nazar, L. F. *Nat. Mater.* **2007**, *6*, 749.
(24) Recham, N.; Chotard, J. N.; Dupont, L.; Djellab, K.; Armand, M.; Tarascon, J. M. *J. Electrochem. Soc.* **2009**, *156*, A993.
(25) Chen, H. L.; Hao, Q.; Zivkovic, O.; Hautier, G.; Du, L. S.; Tang, Y. Z.; Hu, Y. Y.; Ma, X. H.; Grey, C. P.; Ceder, G. *Chem. Mater.* **2013**, *25*, 2777.
(26) Barpanda, P.; Oyama, G.; Ling, C. D.; Yamada, A. *Chem. Mater.* **2014**, *26*, 1297.
(27) Liu, J.; Yu, X. Q.; Hu, E. Y.; Nam, K. W.; Yang, X. Q.; Khalifah, P. G. *Chem. Mater.* **2013**, *25*, 3929.
(28) Conanec, R.; Feldmann, W.; Marchand, R.; Laurent, Y. *J. Solid State Chem.* **1996**, *121*, 418.

(29) Feldmann, W. *Zeitschrift Fur Chemie* **1987**, *27*, 182.
(30) Feldmann, W. *Zeitschrift Fur Chemie* **1987**, *27*, 100.
(31) Zatovsky, I. V.; Vorobjova, T. V.; Domasevitch, K. V.; Ogorodnyk, I. V.; Slobodyanik, N. S. *Acta Crystallogr., Sect. E: Struct. Rep. Online* **2006**, *62*, 32.
(32) Liu, J. unpublished results
(33) Lee, M. S.; Kang, J. K.; Kim, S. J. *Bull. Korean Chem. Soc.* **2012**, *33*, 2083.
(34) Yao, Y. F. Y.; Kummer, J. T. *Journal of Inorganic & Nuclear Chemistry* **1967**, *29*, 2453.
(35) Hammersley, A. P.; Svensson, S. O.; Hanfland, M.; Fitch, A. N.; Hausermann, D. *High Pressure Research* **1996**, *14*, 235.
(36) Hu, E.; Bak, S.-M.; Liu, J.; Yu, X.; Zhou, Y.; Ehrlich, S. N.; Yang, X.-Q.; Nam, K.-W. *Chem. Mater.* **2014**, *26*, 1108.
(37) Neuefeind, J.; Feygenson, M.; Carruth, J.; Hoffmann, R.; Chipley, K. K. *Nuclear Instruments & Methods in Physics Research Section B-Beam Interactions with Materials and Atoms* **2012**, *287*, 68.
(38) Ravel, B.; Newville, M. *J Synchrotron Radiat* **2005**, *12*, 537.
(39) Rodriguez-carvajal, J.; Gonzalez-Platas, J. *Acta Crystallographica Section A* **2002**, *A58*, C87.
(40) Adams, S. *Acta Crystallographica Section B-Structural Science* **2001**, *57*, 278.
(41) Momma, K.; Izumi, F. *J. Appl. Crystallogr.* **2008**, *41*, 653.
(42) Thangadurai, V.; Adams, S.; Weppner, W. *Chem. Mater.* **2004**, *16*, 2998.
(43) Adams, S. *J. Solid State Electrochem.* **2010**, *14*, 1787.
(44) Adams, S.; Rao, R. P. *Physica Status Solidi a-Applications and Materials Science* **2011**, *208*, 1746.
(45) Janssen, Y.; Middlemiss, D. S.; Bo, S. H.; Grey, C. P.; Khalifah, P. G. *J. Am. Chem. Soc.* **2012**, *134*, 12516.
(46) Kresse, G.; Furthmuller, J. *Physical Review B* **1996**, *54*, 11169.
(47) Blochl, P. E. *Physical Review B* **1994**, *50*, 17953.
(48) Dudarev, S. L.; Botton, G. A.; Savrasov, S. Y.; Humphreys, C. J.; Sutton, A. P. *Physical Review B* **1998**, *57*, 1505.
(49) Sanchez, J. M.; Ducastelle, F.; Gratias, D. *Physica A* **1984**, *128*, 334.
(50) Van der Ven, A.; Thomas, J. C.; Xu, Q. C.; Swoboda, B.; Morgan, D. *Physical Review B* **2008**, *78*.
(51) Wood, R. M.; Palenik, G. J. *Inorg. Chem.* **1999**, *38*, 3926.
(52) Ohzuku, T.; Ueda, A.; Yamamoto, N. *J. Electrochem. Soc.* **1995**, *142*, 1431.
(53) Neudecker, B. J.; Weppner, W. *J. Electrochem. Soc.* **1996**, *143*, 2198.
(54) Aono, H.; Sugimoto, E. *J. Am. Ceram. Soc.* **1996**, *79*, 2786.
(55) Brown, I. D. *Chem. Rev. (Washington, DC, U. S.)* **2009**, *109*, 6858.
(56) Van der Ven, A.; Bhattacharya, J.; Belak, A. A. *Acc. Chem. Res.* **2013**, *46*, 1216.
(57) Liu, J. unpublished results
(58) Ong, S. P.; Jain, A.; Hautier, G.; Kang, B.; Ceder, G. *Electrochem. Commun.* **2010**, *12*, 427.
(59) Reinert, A. A.; Payne, C.; Wang, L. M.; Ciston, J.; Zhu, Y. M.; Khalifah, P. G. *Inorg. Chem.* **2013**, *52*, 8389.
(60) Hewett, C. L.; Cheng, Y. B.; Muddle, B. C.; Trigg, M. B. *J. Eur. Ceram. Soc.* **1998**, *18*, 417.
(61) Delacourt, C.; Poizot, P.; Tarascon, J.-M.; Masquelier, C. *Nat. Mater.* **2005**, *4*, 254.

Chapter 3

(1) Whittingham, M. S. *Chem. Rev.* **2014**, *114*, 11414.
(2)Hautier, G.; Jain, A.; Ong, S. P.; Kang, B.; Moore, C.; Doe, R.; Ceder, G. *Chem. Mater.* **2011**, *23*, 3495.
(3) Ohzuku, T.; Makimura, Y. *Chem. Lett.* **2001**, 744.
(4)Lu, Z. H.; MacNeil, D. D.; Dahn, J. R. *Electrochemical and Solid State Letters* **2001**, *4*, A191.
(5)Zhong, Q. M.; Bonakdarpour, A.; Zhang, M. J.; Gao, Y.; Dahn, J. R. *J. Electrochem. Soc.* **1997**, *144*, 205.
(6) Amine, K.; Tukamoto, H.; Yasuda, H.; Fujita, Y. *J. Electrochem. Soc.* **1996**, *143*, 1607.
(7) Cushing, B. L.; Goodenough, J. B. *J. Solid State Chem.* **2001**, *162*, 176.
(8) Gaubicher, J.; Wurm, C.; Goward, G.; Masquelier, C.; Nazar, L. *Chem. Mater.* **2000**, *12*, 3240.
(9) Nishimura, S.; Nakamura, M.; Natsui, R.; Yamada, A. *J. Am. Chem. Soc.* **2010**, *132*, 13596.
(10) Tamaru, M.; Barpanda, P.; Yamada, Y.; Nishimura, S.; Yamada, A. *J. Mater. Chem.* **2012**, *22*, 24526.
(11) Sun, M. L.; Rousse, G.; Abakumov, A. M.; Saubanere, M.; Doublet, M. L.; Rodriguez-Carvajal, J.; Van Tendeloo, G.; Tarascon, J. M. *Chem. Mater.* **2015**, *27*, 3077.
(12) Saidi, M. Y.; Barker, J.; Huang, H.; Swoyer, J. L.; Adamson, G. *Electrochemical and Solid State Letters* **2002**, *5*, A149.
(13) Huang, H.; Yin, S. C.; Kerr, T.; Taylor, N.; Nazar, L. F. *Adv. Mater.* **2002**, *14*, 1525.
(14) Gaubicher, J.; Le Mercier, T.; Chabre, Y.; Angenault, J.; Quarton, M. *J. Electrochem. Soc.* **1999**, *146*, 4375.
(15) Kerr, T. A.; Gaubicher, J.; Nazar, L. F. *Electrochemical and Solid State Letters* **2000**, *3*, 460.
(16) Dupre, N.; Gaubicher, J.; Le Mercier, T.; Wallez, G.; Angenault, J.; Quarton, M. *Solid State Ionics* **2001**, *140*, 209.
(17) Chen, H. L.; Hao, Q.; Zivkovic, O.; Hautier, G.; Du, L. S.; Tang, Y. Z.; Hu, Y. Y.; Ma, X. H.; Grey, C. P.; Ceder, G. *Chem. Mater.* **2013**, *25*, 2777.
(18) Wen, B. H.; Chernova, N. A.; Zhang, R. B.; Wang, Q.; Omenya, F.; Fang, J.; Whittingham, M. S. *Chem. Mater.* **2013**, *25*, 3513.
(19) Liu, J.; Chang, D. H.; Whitfield, P.; Janssen, Y.; Yu, X. Q.; Zhou, Y. N.; Bai, J. M.; Ko, J.; Nam, K. W.; Wu, L. J.; Zhu, Y. M.; Feygenson, M.; Amatucci, G.; Van der Ven, A.; Yang, X. Q.; Khalifah, P. *Chem. Mater.* **2014**, *26*, 3295.
(20) Liu, J.; Yu, X. Q.; Hu, E. Y.; Nam, K. W.; Yang, X. Q.; Khalifah, P. G. *Chem. Mater.* **2013**, *25*, 3929.
(21) Rietveld, H. M. *J. Appl. Crystallogr.* **1969**, *2*, 65.
(22) Lebail, A.; Duroy, H.; Fourquet, J. L. *Mater. Res. Bull.* **1988**, *23*, 447.
(23) Hu, E.; Bak, S.-M.; Liu, J.; Yu, X.; Zhou, Y.; Ehrlich, S. N.; Yang, X.-Q.; Nam, K.-W. *Chem. Mater.* **2014**, *26*, 1108.
(24) Seel, J. A.; Dahn, J. R. *J. Electrochem. Soc.* **2000**, *147*, 892.
(25) Liu, J.; Whitfield, P.; Saccomanno, M.; Bo, S.-H.; Hu, E.; Yu, X.; Bai, J.; Grey, C.; Yang, X.-Q.; Khalifah, P.
(26) Zatovsky, I. V.; Vorobjova, T. V.; Domasevitch, K. V.; Ogorodnyk, I. V.; Slobodyanik, N. S. *Acta Crystallogr., Sect. E: Struct. Rep. Online* **2006**, *62*, 32.
(27) Massiot, D.; Conanec, R.; Feldmann, W.; Marchand, R.; Laurent, Y. *Inorg. Chem.* **1996**, *35*, 4957.

(28) Conanec, R.; Feldmann, W.; Marchand, R.; Laurent, Y. *J. Solid State Chem.* **1996**, *121*, 418.
(29) Conanec, R.; Lharidon, P.; Feldmann, W.; Marchand, R.; Laurent, Y. *Eur. J. Solid State Inorg. Chem.* **1994**, *31*, 13.
(30) Feldmann, W. *Zeitschrift Fur Chemie* **1987**, *27*, 100.
(31) Feldmann, W. *Zeitschrift Fur Chemie* **1987**, *27*, 182.
(32) Wood, R. M.; Palenik, G. J. *Inorg. Chem.* **1999**, *38*, 3926.
(33) Brown, I. D.; Altermatt, D. *Acta Crystallographica Section B-Structural Science* **1985**, *41*, 244.
(34) Li, J. Y.; Yao, W. L.; Martin, S.; Vaknin, D. *Solid State Ionics* **2008**, *179*, 2016.
(35) Padhi, A. K.; Nanjundaswamy, K. S.; Goodenough, J. B. *J. Electrochem. Soc.* **1997**, *144*, 1188.
(36) Jian, Z. L.; Zhao, L.; Pan, H. L.; Hu, Y. S.; Li, H.; Chen, W.; Chen, L. Q. *Electrochem. Commun.* **2012**, *14*, 86.
(37) Hu, L. B.; Zhang, Z. C.; Amine, K. *Electrochem. Commun.* **2013**, *35*, 76.
(38) Zhang, Z. C.; Hu, L. B.; Wu, H. M.; Weng, W.; Koh, M.; Redfern, P. C.; Curtiss, L. A.; Amine, K. *Energy & Environmental Science* **2013**, *6*, 1806.
(39) Ellis, B. L.; Makahnouk, W. R. M.; Makimura, Y.; Toghill, K.; Nazar, L. F. *Nat. Mater.* **2007**, *6*, 749.
(40) Barker, J.; Saidi, M. Y.; Swoyer, J. L. *J. Electrochem. Soc.* **2004**, *151*, A1670.
(41) Barker, J.; Gover, R. K. B.; Burns, P.; Bryan, A. *J. Electrochem. Soc.* **2007**, *154*, A307.
(42) Rui, X. H.; Li, C.; Chen, C. H. *Electrochim. Acta* **2009**, *54*, 3374.
(43) Shannon, R. D.; Prewitt, C. T. *Acta Crystallographica Section B-Structural Crystallography and Crystal Chemistry* **1969**, *B 25*, 925.

Chapter 4

(1) Liu, J.; Yu, X. Q.; Hu, E. Y.; Nam, K. W.; Yang, X. Q.; Khalifah, P. G. *Chem. Mater.* **2013**, *25*, 3929.
(2) Mizushima, K.; Jones, P. C.; Wiseman, P. J.; Goodenough, J. B. *Mater. Res. Bull.* **1980**, *15*, 783.
(3) Ohzuku, T.; Ueda, A.; Nagayama, M. *J. Electrochem. Soc.* **1993**, *140*, 1862.
(4) Ohzuku, T.; Makimura, Y. *Chem. Lett.* **2001**, 642.
(5) Guilmard, M.; Pouillerie, C.; Croguennec, L.; Delmas, C. *Solid State Ionics* **2003**, *160*, 39.
(6) Thackeray, M.; David, W.; Bruce, P.; Goodenough, J. *Mater. Res. Bull.* **1983**, *18*, 461.
(7) Lu, Z.; MacNeil, D.; Dahn, J. *Electrochem. Solid-State Lett.* **2001**, *4*, A191.
(8) Manthiram, A.; Goodenough, J. B. *J. Power Sources* **1989**, *26*, 403.
(9) Manthiram, A.; Goodenough, J. B. *J. Solid State Chem.* **1987**, *71*, 349.
(10) Padhi, A. K.; Nanjundaswamy, K. S.; Goodenough, J. B. *J. Electrochem. Soc.* **1997**, *144*, 1188.
(11) Masquelier, C.; Croguennec, L. *Chem. Rev.* **2013**, *113*, 6552.
(12) Islam, M. S.; Driscoll, D. J.; Fisher, C. A.; Slater, P. R. *Chem. Mater.* **2005**, *17*, 5085.
(13) Ellis, B. L.; Makahnouk, W. R. M.; Makimura, Y.; Toghill, K.; Nazar, L. F. *Nat. Mater.* **2007**, *6*, 749.
(14) Barker, J.; Gover, R. K. B.; Burns, P.; Bryan, A.; Saidi, M. Y.; Swoyer, J. L. *J. Power Sources* **2005**, *146*, 516.
(15) Petricek, V.; Dusek, M.; Palatinus, L. *Z. Kristallogr.* **2014**, *229*, 345.
(16) Ravel, B.; Newville, M. *J Synchrotron Radiat* **2005**, *12*, 537.

(17) Lebail, A.; Duroy, H.; Fourquet, J. L. *Mater. Res. Bull.* **1988**, *23*, 447.
(18) Shannon, R. D.; Prewitt, C. T. *Acta Crystallographica Section B-Structural Crystallography and Crystal Chemistry* **1969**, *B 25*, 925.
(19) Brese, N. E.; Okeeffe, M. *Acta Crystallographica Section B-Structural Science* **1991**, *47*, 192.
(20) Oszlanyi, G.; Suto, A. *Acta Crystallographica Section A* **2004**, *60*, 134.

Chapter 5

(1) Heitnerw.C; Albuyaro.A *Isr. J. Chem.* **1964**, *2*, 266.
(2) Inoue, Y.; Suzuki, S.; Goto, H. *Bull. Chem. Soc. Jpn.* **1964**, *37*, 1547.
(3) Albertss.J *Acta Chem. Scand.* **1966**, *20*, 1689.
(4) Aiello, R.; Barrer, R. M. *Journal of the Chemical Society a -Inorganic Physical Theoretical* **1970**, 1470.
(5) Yao, Y. F. Y.; Kummer, J. T. *Journal of Inorganic & Nuclear Chemistry* **1967**, *29*, 2453.
(6) Bear, I. J.; Mumme, W. G. *Chem. Commun. (Cambridge, U. K.)* **1968**, 609.
(7) Okeeffe, M. *Science* **1973**, *180*, 1276.
(8) Goodenough, J. B.; Hong, H. Y. P.; Kafalas, J. A. *Mater. Res. Bull.* **1976**, *11*, 203.
(9) Hong, H. Y. P. *Mater. Res. Bull.* **1976**, *11*, 173.
(10) England, W. A.; Goodenough, J. B.; Wiseman, P. J. *J. Solid State Chem.* **1983**, *49*, 289.
(11) Kataoka, K.; Awaka, J.; Kijima, N.; Hayakawa, H.; Ohshima, K.; Akimoto, J. *Chem. Mater.* **2011**, *23*, 2344.
(12) Armstrong, A. R.; Bruce, P. G. *Nature* **1996**, *381*, 499.
(13) Delmas, C.; Braconnier, J. J.; Hagenmuller, P. *Mater. Res. Bull.* **1982**, *17*, 117.
(14) Gaubicher, J.; Wurm, C.; Goward, G.; Masquelier, C.; Nazar, L. *Chem. Mater.* **2000**, *12*, 3240.
(15) Liu, J.; Yu, X. Q.; Hu, E. Y.; Nam, K. W.; Yang, X. Q.; Khalifah, P. G. *Chem. Mater.* **2013**, *25*, 3929.
(16) Lee, M. S.; Kang, J. K.; Kim, S. J. *Bull. Korean Chem. Soc.* **2012**, *33*, 2083.
(17) Massiot, D.; Conanec, R.; Feldmann, W.; Marchand, R.; Laurent, Y. *Inorg. Chem.* **1996**, *35*, 4957.
(18) Conanec, R.; Feldmann, W.; Marchand, R.; Laurent, Y. *J. Solid State Chem.* **1996**, *121*, 418.
(19) Feldmann, W. *Zeitschrift Fur Chemie* **1987**, *27*, 100.
(20) Liu, J.; Yu, X.; Hu, E.; Nam, K.-W.; Yang, X.-Q.; Khalifah, P. G. *Chem. Mater.* **2013**.
(21) Neuefeind, J.; Feygenson, M.; Carruth, J.; Hoffmann, R.; Chipley, K. K. *Nuclear Instruments & Methods in Physics Research Section B-Beam Interactions with Materials and Atoms* **2012**, *287*, 68.
(22) Liu, J.; Whitfield, P.; Saccomanno, M.; Bo, S.-H.; Hu, E.; Yu, X.; Bai, J.; Grey, C.; Yang, X.-Q.; Khalifah, P. In preparation.
(23) Petricek, V.; Dusek, M.; Palatinus, L. *Z. Kristallogr.* **2014**, *229*, 345.
(24) Farrow, C. L.; Juhas, P.; Liu, J. W.; Bryndin, D.; Bozin, E. S.; Bloch, J.; Proffen, T.; Billinge, S. J. L. *Journal of Physics-Condensed Matter* **2007**, *19*.
(25) Zatovsky, I. V.; Vorobjova, T. V.; Domasevitch, K. V.; Ogorodnyk, I. V.; Slobodyanik, N. S. *Acta Crystallogr., Sect. E: Struct. Rep. Online* **2006**, *62*, 32.
(26) Conanec, R.; Lharidon, P.; Feldmann, W.; Marchand, R.; Laurent, Y. *Eur. J. Solid State Inorg. Chem.* **1994**, *31*, 13.

(27) Liu, J.; Chang, D. H.; Whitfield, P.; Janssen, Y.; Yu, X. Q.; Zhou, Y. N.; Bai, J. M.; Ko, J.; Nam, K. W.; Wu, L. J.; Zhu, Y. M.; Feygenson, M.; Amatucci, G.; Van der Ven, A.; Yang, X. Q.; Khalifah, P. *Chem. Mater.* **2014**, *26*, 3295.
(28) Kamaya, N.; Homma, K.; Yamakawa, Y.; Hirayama, M.; Kanno, R.; Yonemura, M.; Kamiyama, T.; Kato, Y.; Hama, S.; Kawamoto, K.; Mitsui, A. *Nat. Mater.* **2011**, *10*, 682.
(29)Murugan, R.; Thangadurai, V.; Weppner, W. *Angewandte Chemie-International Edition* **2007**, *46*, 7778.
(30) Thangadurai, V.; Kaack, H.; Weppner, W. J. F. *J. Am. Ceram. Soc.* **2003**, *86*, 437.
(31) Zhao, Y. S.; Daemen, L. L. *J. Am. Chem. Soc.* **2012**, *134*, 15042.
(32) Shannon, R. D.; Prewitt, C. T. *Acta Crystallographica Section B-Structural Crystallography and Crystal Chemistry* **1969**, *B 25*, 925.
(33) Oszlanyi, G.; Suto, A. *Acta Crystallographica Section A* **2004**, *60*, 134.
(34) Palatinus, L.; Chapuis, G. *J. Appl. Crystallogr.* **2007**, *40*, 786.
(35) Celestian, A. J.; Parise, J. B.; Goodell, C.; Tripathi, A.; Hanson, J. *Chem. Mater.* **2004**, *16*, 2244.
(36) Celestian, A. J.; Kubicki, J. D.; Hanson, J.; Clearfield, A.; Parise, J. B. *J. Am. Chem. Soc.* **2008**, *130*, 11689.

Chapter 6

(1) Mizushima, K.; Jones, P. C.; Wiseman, P. J.; Goodenough, J. B. *Mater. Res. Bull.* **1980**, *15*, 783.
(2) Braconnier, J. J.; Delmas, C.; Fouassier, C.; Hagenmuller, P. *Mater. Res. Bull.* **1980**, *15*, 1797.
(3) Whittingham, M. S. *Prog. Solid State Chem.* **1978**, *12*, 41.
(4) Ozawa, K. *Solid State Ionics* **1994**, *69*, 212.
(5) Pan, H. L.; Hu, Y. S.; Chen, L. Q. *Energy & Environmental Science* **2013**, *6*, 2338.
(6) Shannon, R. D.; Prewitt, C. T. *Acta Crystallographica Section B-Structural Crystallography and Crystal Chemistry* **1969**, *B 25*, 925.
(7) Zhou, Y.; Ding, J.; Nam, K. W.; Yu, X.; Bak, S.-M.; Hu, E.; Liu, J.; Bai, J.; Li, H.; Fu, Z. *J. Mater. Chem. A* **2013**, **1**, 11130-11134
(8) Komaba, S.; Takei, C.; Nakayama, T.; Ogata, A.; Yabuuchi, N. *Electrochem. Commun.* **2010**, *12*, 355.
(9) Takeda, Y.; Nakahara, K.; Nishijima, M.; Imanishi, N.; Yamamoto, O.; Takano, M.; Kanno, R. *Mater. Res. Bull.* **1994**, *29*, 659.
(10) Ma, X. H.; Kang, K. S.; Ceder, G.; Meng, Y. S. *J. Power Sources* **2007**, *173*, 550.
(11) Yuan, D. D.; Liang, X. M.; Wu, L.; Cao, Y. L.; Ai, X. P.; Feng, J. W.; Yang, H. X. *Adv. Mater.* **2014**, *26*, 6301.
(12) Ma, J.; Bo, S. H.; Wu, L. J.; Zhu, Y. M.; Grey, C. P.; Khalifah, P. G. *Chem. Mater.* **2015**, *27*, 2387.
(13) Seibel, E. M.; Roudebush, J. H.; Wu, H.; Huang, Q. Z.; Ali, M. N.; Ji, H. W.; Cava, R. J. *Inorg. Chem.* **2013**, *52*, 13605.
(14) Smirnova, O. A.; Nalbandyan, V. B.; Petrenko, A. A.; Avdeev, M. *J. Solid State Chem.* **2005**, *178*, 1165.
(15) Viciu, L.; Huang, Q.; Morosan, E.; Zandbergen, H. W.; Greenbaum, N. I.; McQueen, T.; Cava, R. J. *J. Solid State Chem.* **2007**, *180*, 1060.

(16) Politaev, V. V.; Nalbandyan, V. B.; Petrenko, A. A.; Shukaev, I. L.; Volotchaev, V. A.; Medvedev, B. S. *J. Solid State Chem.* **2010**, *183*, 684.
(17) Berthelot, R.; Schmidt, W.; Muir, S.; Eilertsen, J.; Etienne, L.; Sleight, A. W.; Subramanian, M. A. *Inorg. Chem.* **2012**, *51*, 5377.
(18) Greaves, C.; Katib, S. M. A. *Mater. Res. Bull.* **1990**, *25*, 1175.
(19) Strobel, P.; Lambertandron, B. *J. Solid State Chem.* **1988**, *75*, 90.
(20) Seibel, E. M.; Roudebush, J. H.; Ali, M. N.; Ross, K. A.; Cava, R. J. *Inorg. Chem.* **2014**, *53*, 10989.
(21) Delmas, C.; Fouassier, C.; Hagenmuller, P. *Physica B & C* **1980**, *99*, 81.
(22) Breger, J.; Jiang, M.; Dupre, N.; Meng, Y. S.; Shao-Horn, Y.; Ceder, G.; Grey, C. P. *J. Solid State Chem.* **2005**, *178*, 2575.
(23) Roudebush, J. H.; Andersen, N. H.; Ramlau, R.; Garlea, V. O.; Toft-Petersen, R.; Norby, P.; Schneider, R.; Hay, J. N.; Cava, R. J. *Inorg. Chem.* **2013**, *52*, 6083.
(24) Boulineau, A.; Croguennec, L.; Delmas, C.; Weill, F. *Chem. Mater.* **2009**, *21*, 4216.
(25) Robertson, A. D.; Bruce, P. G. *Chem. Mater.* **2003**, *15*, 1984.
(26) Thackeray, M. M.; Dekock, A.; Rossouw, M. H.; Liles, D.; Bittihn, R.; Hoge, D. *J. Electrochem. Soc.* **1992**, *139*, 363.
(27) Lu, Z. H.; Beaulieu, L. Y.; Donaberger, R. A.; Thomas, C. L.; Dahn, J. R. *J. Electrochem. Soc.* **2002**, *149*, A778.
(28)Hammersley, A. P.; Svensson, S. O.; Hanfland, M.; Fitch, A. N.; Hausermann, D. *High Pressure Research* **1996**, *14*, 235.
(29) Casas-Cabanas, M.; Rodriguez-Carvajal, J.; Palacin, M. R. *Z. Kristallogr.* **2006**, 243.
(30) Ravel, B.; Newville, M. *J Synchrotron Radiat* **2005**, *12*, 537.
(31) Zabinsky, S. I.; Rehr, J. J.; Ankudinov, A.; Albers, R. C.; Eller, M. J. *Physical Review B* **1995**, *52*, 2995.
(32) Juhas, P.; Davis, T.; Farrow, C. L.; Billinge, S. J. L. *J. Appl. Crystallogr.* **2013**, *46*, 560.
(33) Farrow, C. L.; Juhas, P.; Liu, J. W.; Bryndin, D.; Bozin, E. S.; Bloch, J.; Proffen, T.; Billinge, S. J. L. *Journal of Physics-Condensed Matter* **2007**, *19*, 33.
(34) McCalla, E.; Abakumov, A.; Rousse, G.; Reynaud, M.; Sougrati, M. T.; Budic, B.; Mahmoud, A.; Dominko, R.; Van Tendeloo, G.; Hermann, R. P.; Tarascon, J. M. *Chem. Mater.* **2015**, *27*, 1699.
(35) Lebail, A.; Duroy, H.; Fourquet, J. L. *Mater. Res. Bull.* **1988**, *23*, 447.
(36)Egami, T.; Billinge, S. J. L., *Underneath the Bragg-Peaks: Structural Analysis of Complex Materials, Plenum, Oxford, 2003.*
(37)Treacy, M. M. J.; Newsam, J. M.; Deem, M. W. *Proceedings of the Royal Society of London Series a-Mathematical Physical and Engineering Sciences* **1991**, *433*, 499.
(38) Rodriguezcarvajal, J. *Physica B* **1993**, *192*, 55.